Precise Satellite Orbit Determination with Particular Application to ERS-1

by

Maria Joana Afonso Pereira Fernandes

A Thesis submitted for the degree of
Doctor of Philosophy
of the University of London

June 1993

Department of Photogrammetry and Surveying
University College London
Gower Street, London

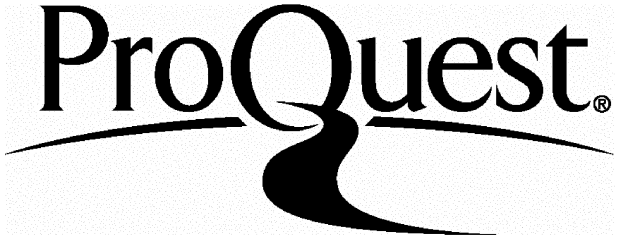

To my parents

Abstract

The motivation behind this study is twofold. First to assess the accuracy of ERS-1 long arc ephemerides using state of the art models. Second, to develop improved methods for determining precise ERS-1 orbits using either short or long arc techniques.

The SATAN programs, for the computation of satellite orbits using laser data were used. Several facilities were added to the original programs: the processing of PRARE range and altimeter data, and a number of algorithms that allow more flexible solutions by adjusting a number of additional parameters.

The first part of this study, before the launch of ERS-1, was done with SEASAT data. The accuracy of SEASAT orbits computed with PRARE simulated data has been determined. The effect of temporal distribution of tracking data along the arc and the extent to which altimetry can replace range data have been investigated.

The second part starts with the computation of ERS-1 long arc solutions using laser data. Some aspects of modelling the two main forces affecting ERS-1's orbit are investigated. With regard to the gravitational forces, the adjustment of a set of geopotential coefficients has been considered. With respect to atmospheric drag, extensive research has been carried out on determining the influence on orbit accuracy of the measurements of solar fluxes ($F_{10.7}$ indices) and geomagnetic activity (Kp indices) used by the atmospheric model in the computation of atmospheric density at satellite height.

Two new short arc methods have been developed: the Constrained and the Bayesian method. Both methods are dynamic and consist of solving for the 6 osculating elements. Using different techniques, both methods overcome the problem of normal matrix ill-conditioning by constraining the solution. The accuracy and applicability of these methods are discussed and compared with the traditional non-dynamic TAR method.

Acknowledgements

A number of people have contributed in many different ways to make the completion of this thesis possible. I wish to thank the following for their guidance and support.

Prof. I. J. Dowman and Dr. J. C. Iliffe, who supervised this project. I wish to express my sincere gratitude to both of them for their great cooperation, and for always being so readily at hand during my numerous visits to UCL. Prof. R. Nunes and Prof. J. Osório, who were my supervisors in Portugal, for their advice and support.

The Portuguese research institution Junta Nacional de Investigação Científica e Tecnológica (JNICT) for funding this project.

Dr. A. Sinclair from RGO for the introduction to the SATAN programs and releasing of data at the beginning of this project, and Dr. G. Appleby who kindly provided ERS-1 data and other relevant information. I also wish to acknowledge Dr. P. Moore from Aston University for his help on the discussion of some topics and provision of data, Dr. Joanna Haig at Imperial College and Dr. Montenegro at Instituto Geofísico for their cooperation.

RAE for supplying the SEASAT altimetry data, Prof. Balmino and Dr. Biancale from GRGS Toulouse, and Dr. Rajasenan from DGFI in Germany for providing the GRIM models.

The staff of the Department of Photogrammetry and Surveying, but in particular to James Pearson for his ever ready help on the use of the computers.

My colleagues in Portugal, Dr. Luisa Bastos, Jorge Carneiro and Mª João Rodrigues for their patience and much help given in discussing several topics. I would also like to thank Ana Morgado, Francelina Neto, Dr. Christine Clark and Dr. Adrian Clark for their collaboration.

My friends Liliane Carter from Imperial College, for her generous hospitality, and Regina Baptista for her affectionate support at the beginning of this study.

I would also like to thank my relatives, in particular my parents and my sisters. Finally my husband Ovídio and my son Nuno for their unconditional support and understanding, and for giving me the strength and the courage to carry on during the most difficult stages of this project.

Table of Contents

List of Figures

List of Tables

Glossary

NASA	- National Aeronautics and Space Administration
BIH	- Bureau International de l'Heure
CIO	- Conventional International Origin
CIS	- Conventional Inertial System
CTS	- Conventional Terrestrial System
DORIS	- Doppler Orbitography and Radiopositioning Integrated by Satellite
ERP	- Earth Rotation Parameters
ET	- Ephemeris Time
FK5	- Star Fundamental Catalogue No 5
GAST	- Greenwich Apparent Sidereal Time
GMST	- Greenwich Mean Sidereal Time
GSFC	- Goddard Space Flight Center
IAG	- International Association of Geodesy
IAU	- International Astronomical Union
IERS	- International Earth Rotation Service
IPMS	- International Polar Motion Service
JD	- Julian Date
JPL	- Jet Propulsion Laboratory
LLR	- Lunar Laser Ranging
MERIT	- Monitor Earth Rotation and Intercompare the Techniques of Observation and Analysis
MJD	- Modified Julian Date
PAF	- Processing and Archive Facility
PRARE	- Precise Range and Range Rate Equipment
RGO	- Royal Greenwich Observatory
SATAN	- SATellite ANalysis programs
SLR	- Satellite Laser Ranging
TAI	- International Atomic Time
TDB	- Barycentric Dynamical Time
TDT	- Terrestrial Dynamical Time
UTC	- Coordinated Universal Time
VLBI	- Very Long Baseline Interferometry

Chapter 1

Introduction

Since the advent of the first satellites carrying radar sensors, precise orbits have become a requisite for the effective exploitation of data generated by the instruments on board these spacecraft. For the first European Space Agency remote sensing satellite (ERS-1) this is a major requirement. Launched in July 1991, ERS-1 is the forerunner of a new generation of space missions aiming to make a substantial contribution to the scientific study and understanding of our environment. Circling the Earth in a near polar orbit, it provides global and repetitive observations of the environment using advanced microwave techniques.

Amongst other instruments ERS-1 carries a Radar Altimeter, which measures the height of the satellite relative to the ocean surface with an accuracy of better than 10 cm. To use these data for geodetic and oceanographic applications, the satellite's position, in particular its radial component, should be known with an accuracy close to that of the altimeter measurement itself.

The experience gained with SEASAT showed that for altimetric satellites, global ephemerides at decimetre level are possible only if a precise tuned gravity field model is available. In the absence of such a model this accuracy can only be achieved over regions of intensive tracking using short arc techniques.

The present global gravity field models were derived from tracking data from a number of satellites. Although they claim to be global, indeed they are tailored to the satellites used in their solution. When applied to the computation of other satellites' orbits with different orbital parameters, some coefficients, in particular high degree resonant coefficients, may cause significant perturbations. The failure of PRARE (Precise Range and Range Rate Equipment), a new tracking system especially designed for ERS-1, due to the fatal damage of the instrument soon after launch, highly compromised the development of a tailored gravity field model for ERS-1. Without PRARE, the only tracking data available are laser data, which in general are sparse and with poor geographical distribution.

In addition to the gravitational forces, surface forces, in particular atmospheric drag, cause large errors on ERS-1 ephemerides. This is due to the fact that part of the ERS-1

mission is taking place during a period of high solar activity, making the effects of atmospheric drag more significant.

Through the German Processing and Archive Facility (PAF), ESA provides precise ERS-1 orbit restitution as an on-line product. Two products have been announced: a preliminary solution to be available within ten days of data collection, and a precise orbit generated after six months. The quoted accuracy of these solutions is given in Table 1.1 (Doherty, 1992).

Table 1.1
Accuracy of ERS-1 orbits provided by ESA

	Preliminary	**Precise**
along-track	8.00 m	2.00 m
across-track	2.00 m	0.60 m
radial	1.50 m	0.40 m

ERS-1 generates a series of near real time products. To analyse these products, the user community requires orbital information with suitable accuracy, usually better than the preliminary solution mentioned above and as close as possible to real time.

The motivation behind this thesis is therefore twofold:

- To assess the accuracy of ERS-1 long arc solutions (typically of three days) using the state of the art models.

- To develop improved methods for determining precise ERS-1 orbits, using either short or long arc techniques.

In this development two main factors are considered. On one hand the solution obtained should be as precise as possible, by modelling all known forces affecting a satellite's motion. On the other hand, it is aimed to determine solutions that do not depend on data that are only available a long time after data collection. In other words the solution should be as close as possible to real time.

The software used is the SATAN software package written at the Royal Greenwich Observatory, designed for the computation of satellite orbits using laser data. Several facilities were added to the original programs, including the processing of PRARE range

and altimeter data, and a number of algorithms that allow more flexible solutions by adjusting a number of additional parameters.

At the beginning of this study ERS-1 tracking data were not yet available. Because it is extremely difficult to simulate altimeter data in a realistic way, and given the similarity between the two satellites, the first part of this study was done with SEASAT data. The tracking data types used were actual altimeter measurements and PRARE simulated data. The fact that PRARE will not be able to contribute to the tracking of ERS-1 does not invalidate these results, as PRARE ranges are very similar to laser data. The latter still have the advantage that the accuracy of most of the present lasers is better than the assumed PRARE accuracy (7 cm). Despite the delay in the launch of ERS-1, some tracking data were nevertheless available in time to be processed in this project. The last part of this study was concerned with the computation of ERS-1's orbit by processing its own data.

This thesis is divided into 11 chapters, each one describing a specified topic.

Chapters 2 to 7 describe the necessary background for satellite orbit determination, the mathematical tools and developed algorithms. To compute a satellite orbit, it is necessary to relate positions of objects on the Earth (station coordinates, geoid) with objects in space (the satellite, objects in the solar system); a correct understanding of the relationships between all these quantities is therefore necessary. These relationships, concerning time and reference systems commonly used in orbit determination, are described in chapter 2. Chapter 3 describes the main characteristics of the SATAN software package used in this study, with emphasis on the new algorithms implemented in the programs. A summary of previous studies related to orbit determination for altimetric satellites similar to ERS-1 is presented in chapter 4. Chapter 5 describes and compares SEASAT and ERS-1 orbits and sensors, with emphasis on the parameters that are relevant for orbit determination. The methodologies used for the processing of PRARE and altimeter data are described in chapters 6 and 7 respectively. The method used for simulating PRARE data is described, as well as the new algorithm developed in this study for the processing of altimeter data.

The SEASAT results for the long arc ephemerides are the subject of chapter 8. First, the accuracy of SEASAT orbits using laser and simulated PRARE data is determined. Second, the effect of temporal distribution of the tracking data along the arc is investigated, by using several configurations with only a few passes from one or two PRARE stations. Then altimetry data were added to these range data and the extent to which altimetry can replace range data was determined.

The only suitable ERS-1 tracking data available for this study were laser data. The altimeter data available were a fast delivery product, with an accuracy not appropriate for tracking purposes. The ERS-1 results are described in chapter 9. This study starts with the computation of ERS-1 orbits using laser data and the state of the art models for this satellite. Then some aspects of modelling the two main forces affecting ERS-1's orbit are investigated. With regard to the gravitational forces, the adjustment of a selected set of geopotential coefficients is investigated. With respect to atmospheric drag, extensive research was carried out on determining the influence on orbit accuracy from actual measurements of solar flux ($F_{10.7}$ indices) and geomagnetic activity (Kp indices), used by the atmospheric model to compute density at satellite height.

Chapter 10 presents the research carried out on the development of short arc techniques. The motivation for this study is the fact that most of the applications do not require a precise ephemeris over a long arc, but only within a limited region. Two new short-arc methods are developed in this study. Both methods are dynamic and involve solving for the 6 initial osculating elements. Solving for these 6 elements usually leads to ill-conditioned solutions with high correlations between the solved-for parameters. The first method, the so-called "constrained" method, overcomes this problem by applying constraints to the solved-for parameters. These constraints are dependent on station configuration. The second method, called the "Bayesian" method, uses the covariance matrix from a previous "a priori" solution, usually a long arc, in a Bayesian least square scheme to constrain the short arc. These two methods are also compared with the traditional non-dynamic TAR method, whereby corrections to a previous long arc solution, along the three directions, along-track (T), across-track (A) and radial (R), are solved for and applied to obtain a corrected satellite track.

Finally the main conclusions and recommendations are presented in chapter 11.

ERS-1 orbits computed with state of the art models yield rms range residuals of 1.5 metres. Two main forces were found to be responsible for these large residuals. During periods of quiet geomagnetic activity the main errors are from gravitational origin, while for periods of strong geomagnetic perturbations, the main source of orbit error is due to drag mismodelling.

The time lag introduced in the geomagnetic Kp indices (TLKP) was found to have a strong influence on the orbit adjustment. A difference of 2 hours in the TLKP causes the rms of fit to laser ranges to vary from 1.6 m to only 0.4 m. Hence the use of Kp data with an appropriately adjusted time lag is essential for precise orbit determination.

The influence of solar flux indices was found to be of slight importance since the adjustment of daily drag coefficients will absorb any existing bias in the indices. As a

consequence of this result, predicted values of the solar flux can be used by just modelling the long wavelength component of their variation, without significantly degrading the solution. This prediction can be important if rapid ephemerides are required.

Results with altimeter data for SEASAT have shown that this data type can fill gaps of range data as long as two days, provided at least one pass of range data exists at the end of the arc. Altimetry is therefore a very useful tracking data type for interpolating, but not for extrapolating range data.

The two short arc methods developed in this study produced very precise orbits. For arcs of up to 30 minutes the accuracy of these solutions is at decimetre level. For longer arcs, up to one orbital revolution, the accuracy gradually diminishes as the length of the arc increases.

Chapter 2

Earth Rotation, Time and Reference Systems

2.1 Introduction

In satellite orbit determination two types of reference systems are required. The equations of motion are usually written in a quasi-inertial system so that positions and velocities refer to this system. Positions of the bodies within the solar system affecting the satellite's motion are also given in an inertial system. However the effect of the Earth's gravitational attraction, or the positions of the ground tracking stations, are described in a terrestrial system. Consequently a correct understanding of these reference systems and the transformation between them is required. The transformation between an inertial and a terrestrial system involves a correct modelling of the Earth's motion relative to fixed space.

This chapter reviews the background to the reference systems used in this study and to the related earth rotation parameters and time systems used in orbit determination.

2.2 Earth Rotation

The ecliptic is the mean orbit plane of the Earth's movement around the sun; it moves slowly due to planetary perturbations. The attractions of the sun and the moon on the oblate mass distribution of the Earth cause a movement of the Earth's axis of rotation around the pole of the moving ecliptic. The long period part of this motion is called precession. It is a slow circular motion of the pole with respect to the inertial space with a period of about 25,700 years. Superimposed on precession, there is a short period motion with periods from 14 days to 18.6 years known as nutation (Figure 2.1).

Both movements are described by the motion of the instantaneous equator and equinox with respect to the fixed equator and equinox of a given epoch. When the effects of nutation are removed, the resultant fictitious equator and equinox are called the mean equator and equinox of that epoch. When the effects of nutation are included, they are referred to as the true equator and equinox of the date.

Precession changes the celestial longitude of a point on the Earth by about 50 arcsec per year. Nutation affects both celestial longitude and celestial latitude with a maximum amplitude of about 20 arcsec.

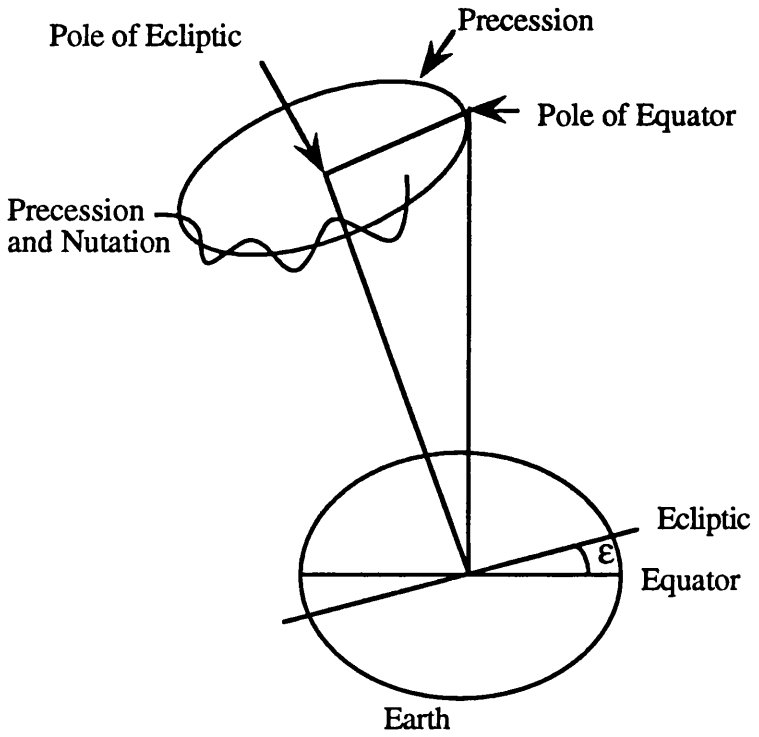

Figure 2.1 - Precession and Nutation

In addition to this forced movement, the pole of the Earth has a free motion called polar motion. As defined by the International Earth Rotation Service (IERS), this is the motion of the celestial ephemeris pole (the axis of maximum moment of inertia) with respect to a reference point fixed to the Earth's crust (IERS, 1992). This reference point is usually selected to be near the average position of the true pole over a certain time interval, usually 6 years, and is called the mean terrestrial pole of that interval.

Polar motion includes a strong periodic component with a period of 14 months ("Chandler term"), another component with an annual period, and a secular trend towards west. Usually this motion is described in terms of cartesian coordinates (xp,yp) expressed in seconds of arc (Moritz, 1979). The origin of such a system is at the adopted conventional pole, the **x** axis along the Greenwich Meridian, and the **y** axis along longitude 90°W (Figure 2.2).

Until 1987, both IPMS (International Polar Motion Service) and BIH (Bureau International de l'Heure) published polar coordinates. In 1988, the IPMS and the earth rotation section of the BIH were replaced by the IERS, which is now responsible for providing the information necessary to define a Conventional Terrestrial System (CTS) and a Conventional Inertial System (CIS).

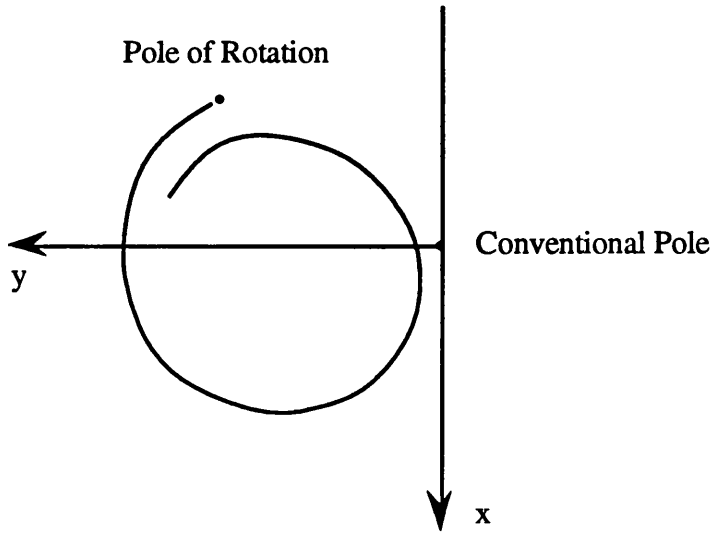

Figure 2.2 - Polar Motion

Since 1968, the pole used to define the Conventional Terrestrial System has been the mean pole of the period 1900-1905, also known as the average 1903 pole or the Conventional International Origin (CIO). The CIO frame was initially defined by the adopted values of the astronomic latitude of 5 observatories of the IPMS, all around the 39° 08' parallel. Initially, polar motion was determined from latitude and/or time observations of stars at a number of observatories. More recently, techniques like VLBI, and lunar and satellite laser ranging observations, are being used to determine Earth Rotation Parameters (ERP), including polar motion.

2.3 Time systems

2.3.1 Dynamical time

Dynamical time is the uniform timescale that governs the motions of bodies in a gravitational field, the independent argument in the equations of motion of a body according to some particular gravitational theory.

There are two types of dynamical time (King et al., 1985):

• Barycentric Dynamical Time (TDB) is measured in the most nearly inertial system to which we have access through gravitational theory, which has its origin at the barycentre of the solar system. A clock fixed on the Earth will exhibit periodic variations as large as 1.6 milliseconds with respect to TDB due to the motion of the Earth in the sun's gravitational field. However, in describing the orbital motion of a near Earth satellite we do not need to use TDB, nor account for these relativistic effects, since both the satellite and the earth itself are subject to nearly the same perturbations.

• Terrestrial Dynamical Time (TDT) is the system used for satellite orbit computations as observed from the Earth. It is a uniform timescale for motion within the Earth's gravity field. It has the same rate as an atomic clock on the Earth. This was previously called Ephemeris Time (ET).

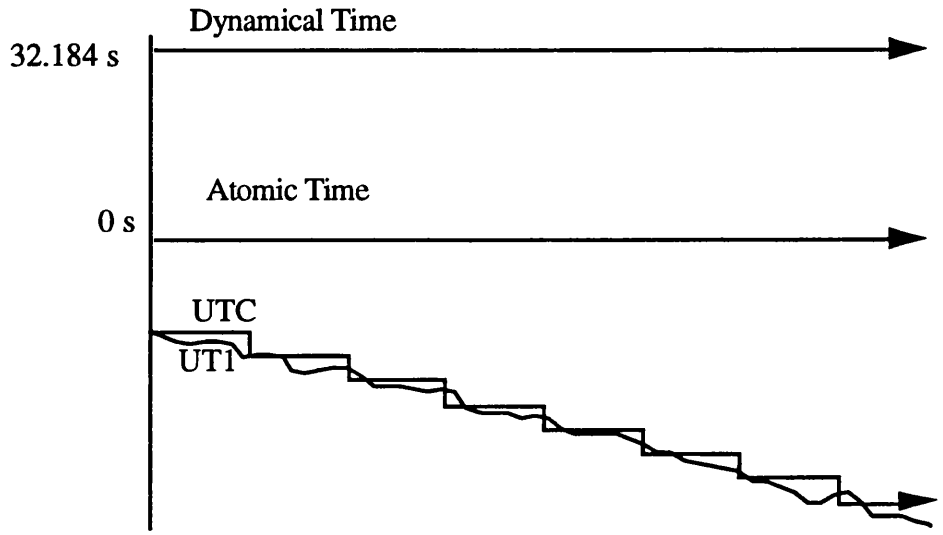

Figure 2.3 - Relationship between different time systems. Adapted from (King et al., 1985).

2.3.2 Atomic time

International Atomic Time (TAI) is the fundamental timescale for all the Earth's time keeping. It results from analysis by the BIH until March 1985, and since then by the Bureau International des Poids et Mesures, of data from atomic standards of many countries. Its unit is the International System of Units (SI) second. It is a continuous timescale and serves as the practical definition of TDT:

$$TDT = TAI + 32.184\ s \qquad (2.1)$$

The Earth's rotation with respect to the sun is slowing down by a variable amount which, at present, averages about 1 second per year. In order to create a time system that would take this into account, Coordinated Universal Time (UTC) was introduced. It runs at the same rate as TAI, but is decreased by 1 second jumps (leap seconds), when necessary, normally at the end of June or December each year, so that it is kept within one second of UT1. It differs from TAI by an integral number of seconds.

2.3.3 Sidereal time and UT1

The angle of the Earth's rotation with respect to the true equinox of date is called Greenwich Apparent Sidereal Time (GAST) and is usually designated by θ. Another angle is that which describes the Earth's rotation with respect to the mean equinox of date. This is called Greenwich Mean Sidereal Time (GMST) or θ_M. The variation of θ_M is due to the rotation of the Earth (ω) and to the precession of the equinox, described by the angles ψ, φ, and χ (Sinclair, 1987).

$$\dot{\theta}_M = \omega + \dot{\psi}\cos\varphi - \dot{\chi} \tag{2.2}$$

Integrating :

$$\theta_M = \text{constant} + \int_0^t \omega\, dt + \int_0^t (\dot{\psi}\cos\varphi - \dot{\chi})dt \tag{2.3}$$

The second integral is called the "accumulated precession in right ascension" (M) and is given by precession theory. Its value, as given by the IAU (1976) precession model, is:

$$M = 4612".4362\ T + 1".39656\ T^2 - 0".00009267\ T^3 \tag{2.4}$$

with T in centuries from J2000.

The integration of the first integral is more complicated because the rate of rotation of the Earth (ω) is not constant. It varies due to tidal friction (long term variations), to core mantle interaction (medium terms), and to seasonal and atmospheric effects (short terms). Therefore to calculate this integral, a nominal constant value ω_0 and a non-uniform timescale, Universal Time (UT1) are introduced, so that:

$$\int \omega\, dt = \omega_0 . T_{UT1} \tag{2.5}$$

where T_{UT1} is a time interval on the UT1 scale.

Thus the UT1 definition is (Sinclair, 1987): a non-uniform timescale relative to which the Earth has a numerically constant rotation rate of ω_0 . relative to an inertial frame.

UT1 is calculated by :

$$UT1 = UTC + \Delta UT1 \tag{2.6}$$

where $\Delta UT1 = UT1\text{-}UTC$ is determined from actual measurements. It is computed and published by the IERS.

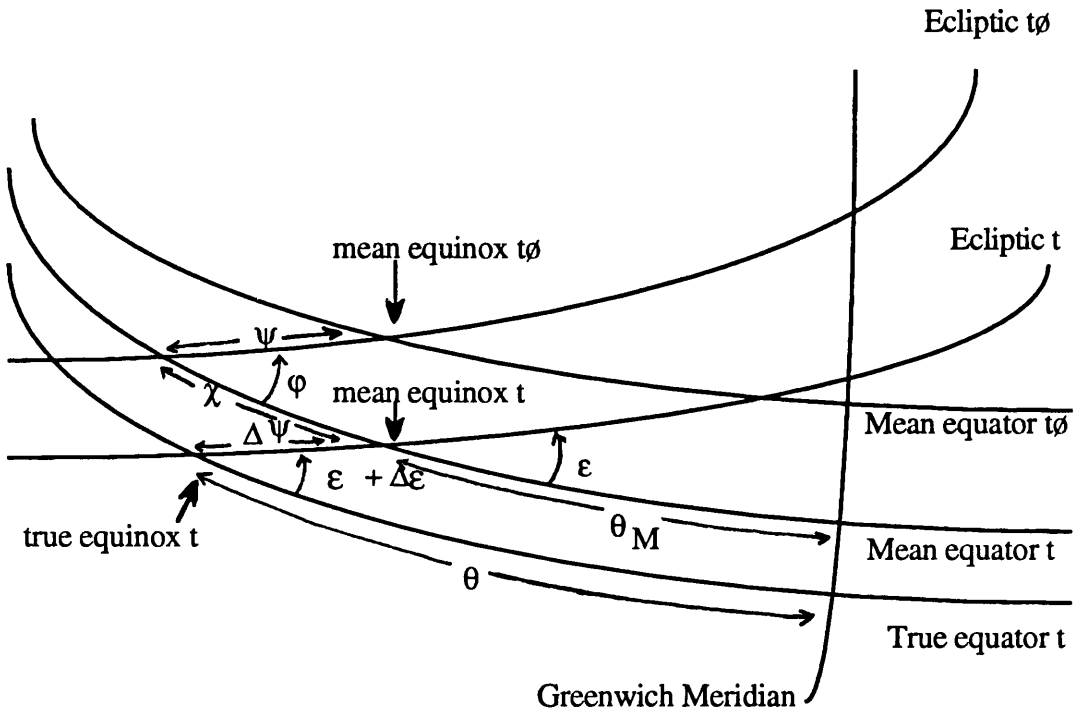

Figure 2.4 - Nutation and Sidereal time. Extracted from (Sinclair, 1987).

The new expression for GMST adopted by the International Astronomic Union (IAU) in 1982 is:

$$GMST = UT1 + 6^h\,41^m\,50^s.54841 + 8640184^s.812866\,T + 0^s.093104\,T^2 - 6^s.2 \times 10^{-6}\,T^3 \tag{2.7}$$

$$T = [\,JD(UT1) - 2451545.0\,] / 36525\,.$$

In these expressions UT1 is the time of day on the UT1 scale from 0h, and JD(UT1) also includes the fractional part of the day.

Finally, GAST is calculated by applying to GMST the nutation effect (known as the equation of the equinox):

$$GAST = GMST + \Delta\psi \cos(\varepsilon + \Delta\varepsilon) \qquad (2.8)$$

$\Delta\psi$ and $\Delta\varepsilon$ are the nutation in longitude and obliquity respectively (see section 2.4.3).

2.4 Reference Systems

When dealing with problems of orbit determination, two types of reference systems are usually required: an Earth-fixed or terrestrial and a space-fixed or inertial. If this idea is very simple, in practice the realisation of such systems and the establishment of the transformations between them is a complex task. In general, each observational technique uses different realisations of both the terrestrial and inertial frames. Since the realisation of the MERIT project (Melbourne et al., 1983), an attempt has been made to use the same frames (Mueller, 1981), (Wilkins and Mueller, 1986).

2.4.1 Celestial Systems

Ideally a celestial system should be inertial (move through space with a constant translational velocity but without rotation) or at least quasi-inertial (without rotational motion but its origin may have acceleration). The requirement for an inertial frame is that this is the frame in which Newton's laws hold, and any rotation of the frame will appear as an unmodelled coriolis force on the satellite (Sinclair, 1987).

An example of a quasi-inertial frame is a system whose direction with respect to the stars remains unchanged and whose origin is at the Earth's centre of mass, as the Earth has a curvilinear non-uniform motion around the sun (Moritz, 1979). Such systems are realised in practice by various techniques such as: VLBI to extragalactic radio sources, observations to the stars, to moon or the planets and artificial satellite tracking. The most accurate are the systems determined by VLBI in which the system is attached to extragalactic radio sources.

By resolution of the International Association of Geodesy (IAG) and the International Astronomical Union (IAU), the Conventional Inertial System (CIS) used after 1 January

1984 is defined by the mean equator and equinox at 12 h TDB on 1 January 2000 (Julian Date 2451545.0), designated J2000.

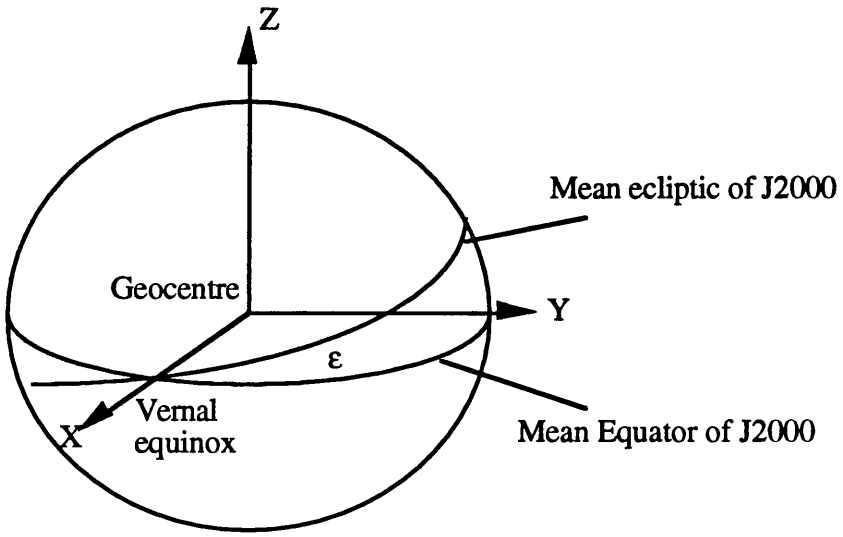

Figure 2.5 - J2000 Conventional Inertial System (CIS)

2.4.2 Terrestrial Systems

A conventional terrestrial system is defined by a set of adopted station coordinates. It moves and rotates, in some average sense, with the Earth (Mueller, 1988).

The Conventional Terrestrial System (CTS) is defined with the **z** axis towards the CIO pole and the **x** axis on the intersection of the equator with the Greenwich Meridian.

The definition of the CIO and of the Greenwich Meridian was initially based on the adopted coordinates of the five International Latitude Service (ILS) stations making astronomic zenith observations. These were assumed to be motionless relative to each other, and without variations in their respective verticals relative to the Earth. Later the BIH and more recently the IERS have tried to maintain the same frame for a much larger number of instruments that are also making UT1 determinations at a much greater number of locations around the world. The new techniques of SLR, LLR, Doppler and VLBI have all attempted to maintain the same frame by forcing their polar motion series to fit into the BIH series. The present CTS is conceptually defined similarly to the CIO-BIH system, i.e., it is attached to observatories located on the surface of the Earth. The main difference is that these can no longer be assumed motionless with respect to each

other. The IERS is the entity responsible for the definition and realisation of the CTS, by combination of data provided by space techniques presently participating to IERS, namely VLBI, LLR and SLR (Boucher and Altamini, 1992).

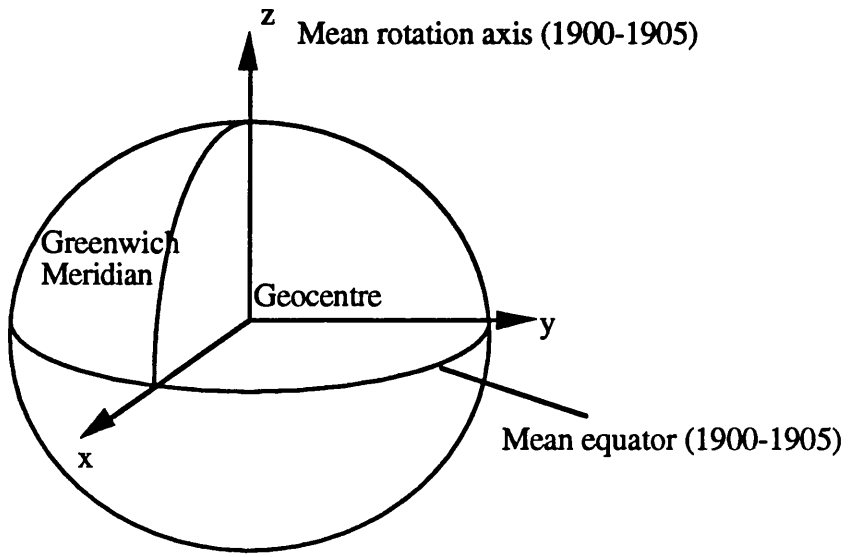

Figure 2.6 - Conventional Terrestrial System (CTS)

2.4.3 Transformation between CIS and CTS

The relationship between the CIS and the CTS systems is established by an appropriate modelling of the precession, nutation, polar motion and UT1-UTC. The first two are modelled theoretically because they are forced movements; the last two are determined from direct measurements.

The transformation between the two systems is usually performed in four main steps (Figure 2.7).

Using vector notation :

$$\begin{bmatrix} x \\ y \\ z \end{bmatrix}_{CTS} = S \,.\, N \,.\, P. \begin{bmatrix} X \\ Y \\ Z \end{bmatrix}_{CIS} \tag{2.9}$$

or inversely

$$\begin{bmatrix} X \\ Y \\ Z \end{bmatrix}_{CIS} = P^T . N^T . S^T \begin{bmatrix} x \\ y \\ z \end{bmatrix}_{CTS} \tag{2.10}$$

where

- [x,y,z] is the position vector in the CTS.
- [X,Y,Z] is the position vector in the CIS.
- P is the rotation matrix accounting for precession between J2000 and the required epoch.

$$P = R_3(-z_A)\, R_2(\theta_A)\, R_1(-\zeta_A) \tag{2.11}$$

The matrices R_1, R_2 and R_3 are rotations about the X, Y and Z axis respectively. These are orthogonal matrices $\left(R^{-1} = R^T\right)$ of the form:

$$R_1(\alpha) = \begin{bmatrix} 1 & 0 & 0 \\ 0 & \cos\alpha & \sin\alpha \\ 0 & -\sin\alpha & \cos\alpha \end{bmatrix} \quad R_2(\alpha) = \begin{bmatrix} \cos\alpha & 0 & -\sin\alpha \\ 0 & 1 & 0 \\ \sin\alpha & 0 & \cos\alpha \end{bmatrix} \quad R_3(\alpha) = \begin{bmatrix} \cos\alpha & \sin\alpha & 0 \\ -\sin\alpha & \cos\alpha & 0 \\ 0 & 0 & 1 \end{bmatrix} \tag{2.12}$$

The rotation angles as given by the IAU,(1976) Theory of Precession, are :

$$\begin{aligned} \zeta_A &= (2306''.2181 + 1''.39656T - 0''.000139T^2)t + (0''.30188 - 0''.000344T)t^2 \\ &\quad + 0''.017998t^3 \\ z_A &= (2306''.2181 + 1''.39656T - 0''.000139T^2)t + (1''.09468 + 0''.000066T)t^2 \\ &\quad + 0''.018203t^3 \\ \theta_A &= (2004''.3109 - 0''.85330T - 0''.000217T^2)t + (-0''.42665 - 0''.000217T)t^2 \\ &\quad - 0''.041833t^3 \end{aligned} \tag{2.13}$$

T = [JD (base epoch) - 2451545.0] / 36525

is the interval in Julian Centuries (36525 days of TDB or TAI), between J2000 and the base epoch.

t = [JD (current date) - JD (base epoch)] / 36525

is the interval in Julian centuries between base epoch and current date. Usually base epoch is J2000, so T=0 and t = [JD (current date) - 2451545.0] / 36525

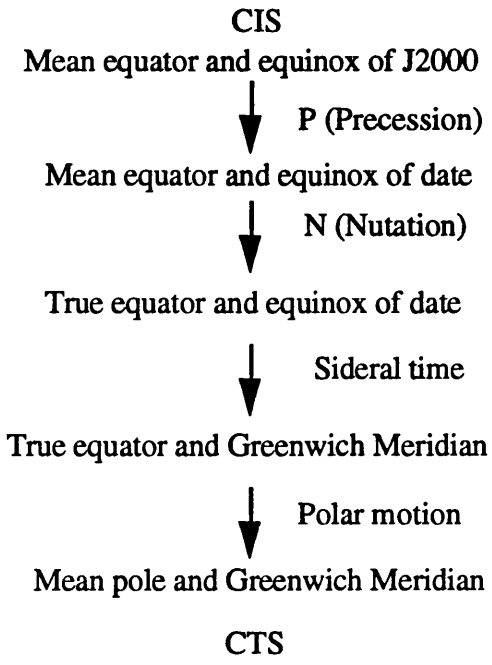

Figure 2.7 - Schematic representation of the transformation between the CIS and the CTS

- N is the rotation matrix accounting for nutation for the required epoch

$$N = R_1(-\varepsilon - \Delta\varepsilon)\, R_3(-\Delta\psi)\, R_1(\varepsilon) \qquad (2.14)$$

$$\varepsilon = 23^\circ\, 26'\, 21''.448 - 46''.8150\, T - 0''.00059\, T^2 + 0''.001813\, T^3 \qquad (2.15)$$

is the obliquity of the ecliptic. It varies between 22°.14 and 24°.43 with a period of 41.000 years.

T = [JD (date) - 2451545.0] / 36525

$\Delta\psi$ and $\Delta\varepsilon$ are given by the nutation theory as sums of many periodic terms. The Theory of Nutation adopted by the IAU (1980) is based on the Wahr (1981) model.

- S is the rotation matrix accounting for Earth rotation

$$S = R_2(-xp).\ R_1(-yp)\ .\ R_3(\theta) \qquad (2.16)$$

(xp,yp) are polar motion components defining the angular separation of the **z** axis of the CTS with the axis of the Earth for which the nutation (N) is computed. In the IAU (1980) nutation model this axis is the axis of maximum moment of inertia. The correspondent pole is referred as the Celestial Ephemeris Pole and differs from the instantaneous axis of rotation by small quasi-diurnal terms. The polar motion angles are computed and distributed by the IERS. θ is Greenwich Apparent Sidereal Time (GAST) and is calculated as indicated in section 2.3.3.

Chapter 3

Orbit Computation

3.1 Introduction

Satellite orbit computation is a complex exercise requiring expert knowledge in a wide range of subjects, from celestial mechanics to numerical analysis. The development of computer programs for the computation of satellite ephemerides is therefore a difficult and time consuming exercise. Large software packages have been developed at specialised centres such as the GEODYN program at the Goddard Space Flight Center (GSFC). However a very large computer is needed to run GEODYN, and setting up and running the program involves a considerable amount of effort. The software employed at University College London is the satellite analysis (SATAN) package of programs written by A. T. Sinclair and G. M. Appleby at the Royal Greenwich Observatory (RGO). This is a much more compact package of programs which run on a much smaller computer. During this project they were implemented on a μVAX 2000 computer, with a single precision of 7 to 8 figures and a double precision of 16 decimal places.

This package was used as a starting point for this thesis, and was subsequently adapted and expanded to meet the specific needs of this project. This chapter gives a brief description of this software, with more detailed information on the new algorithms added to the programs.

3.2 The SATAN Programs and Software Development

The SATAN package consists of two main programs: ORBIT and RGODYN (Sinclair and Appleby, 1986). The first computes satellite position and velocity at specified dates by numerical integration of the equations of motion. The second determines corrections to the parameters that define the orbit by fitting it to laser observations.

Throughout this study several facilities were introduced into the programs:

- Solution for multiple drag coefficients

- Solution for orbital elements of initial position and velocity instead of cartesian coordinates

- Solution for a user selected set of geopotential coefficients

- Possibility of applying constraints to the solve-for parameters
- Bayesian least squares solution in addition to conventional least squares
- Processing of PRARE range data
- Processing of altimeter data

3.2.1 Program ORBIT

Program ORBIT performs the numerical integration of the equations of motion (Sinclair, 1988):

$$\ddot{\vec{r}} = f(\vec{r}, \dot{\vec{r}}, t) = \ddot{\vec{r}}_g + \ddot{\vec{r}}_b + \ddot{\vec{r}}_d + \ddot{\vec{r}}_{rp} + \ddot{\vec{r}}_{tides} \qquad (3.1)$$

where

$\ddot{\vec{r}}_g$ - acceleration due to the Earth's gravitational field

$\ddot{\vec{r}}_b$ - acceleration due to third bodies (sun, moon and planets)

$\ddot{\vec{r}}_d$ - acceleration due to atmospheric drag

$\ddot{\vec{r}}_{rp}$ - acceleration due to radiation pressure

$\ddot{\vec{r}}_{tides}$ - acceleration due to solid earth and ocean tides

The integration method used is an eighth order Gauss-Jackson method with an iterative starting scheme. Given the position and velocity at an initial time t_1, the starting scheme calculates the position and velocity for the next 8 points t_2, ... , t_9. For a subsequent time t_{10}, the position and velocity are calculated as functions of the previous nine values and the total acceleration at time t_{10}.

The step length is fixed for each integration. This limits the use of the programs to satellites of low eccentricity. For each satellite, the step length should be selected to give the required accuracy. It has to be short enough to cope with the short period perturbations caused by the high order tesseral harmonics of the gravitational field.

The celestial reference frame used for the integration is the equator and equinox of J2000. However, the acceleration due to the gravitational field has to be calculated in a terrestrial reference frame (the real equator of the Earth, as defined by the geopotential coefficients). So, at every step of integration, the satellite position is transformed to the terrestrial reference frame and the acceleration is evaluated. The acceleration is then transformed to the J2000 frame for the numerical integration. The rotation matrices used in the

transformation between the two systems are those of the FK5 system: IAU (1976) precession, IAU (1980) nutation, and IAU (1982) sidereal time as described in section 2.4.3.

The timescale used is an atomic timescale that is equal to UTC at the starting epoch of integration (called ATC). So ATC is calculated by subtracting from TAI the leap seconds that occurred until the starting epoch, but if a leap second occurs during the span of the integration, it will not be applied.

The program also calculates the partial derivatives of satellite position and velocity with respect to the solve-for parameters that affect the orbit. These partial derivatives are necessary for subsequent use in RGODYN to fit the orbit to observations. In its original form the program included the calculation of the partial derivatives with respect to the initial state position and velocity vectors, a drag coefficient and its rate of change, solar radiation coefficient and the product GM. The main modifications introduced into this program were the implementation of the solution for multiple drag coefficients and for a selected set of geopotential coefficients.

The force model used, described in section 3.3, is the recommended one in project MERIT standards (Melbourne et al., 1983), and includes effects due to :

- The Earth's gravitational field
- Gravitational attraction of the sun, moon and the planets
- Atmospheric drag
- Radiation pressure
- The solid Earth and ocean tides

3.2.2 Program RGODYN

For most of the applications, the accuracy achieved when computing an orbit by simple integration of the equations of motion is not sufficiently good. This is due to the inability of the force model to describe accurately the forces that act on a satellite. In practice, the satellite is tracked from a number of stations on the Earth, and orbital parameters are estimated by fitting the orbit to observations.

In its initial form, RGODYN performed the adjustment of the orbit to laser observations only. The processing of PRARE range and altimeter data has been added to the program, allowing any combination of the three data types. The program takes each observation (O) in time, computes a corresponding quantity (C), according to initial conditions, and forms the "O-C" residuals. In addition, it computes the partial derivatives of the observed quantity with respect to the solve-for parameters, and adds their contribution to

the normal equations. After all observations have been processed, the normal equations are solved to derive corrections to the initial parameters. In this way, an updated set of parameters is determined.

The least squares procedure implemented in RGODYN was the traditional method of "observation equations" described in section 3.4.1. This algorithm assumes that there is no "a priori" information on the initial set of parameters. When such information exists, it may be used to help to constrain the new solution. Hence, the Bayesian Least Squares technique described in section 3.4.3 was also implemented in the program.

The new formulae implemented in RGODYN for the partial derivatives of PRARE Range and altimeter data with respect to satellite parameters are presented in section 3.5. The algorithms for the computation of the computed (C) values are described in chapter 6 for PRARE and laser range data, and in chapter 7 for altimeter data.

3.3 The Force Model

3.3.1 The Earth's Gravitational Field

The Earth's gravity field, expressed as a potential, the geopotential, W, at a point (r, φ, λ), can be written as:

$$W = V + \Phi \tag{3.2}$$

Φ is the centrifugal potential, due to the Earth's rotation, which for points outside the Earth is nil.

For a satellite at a distance **r** the only component of W that needs to be considered is the gravitational potential V. The distribution of density within the Earth departs considerably from radial symmetry. Therefore, gravitational attraction varies with latitude and longitude, in addition to the geocentric distance (Sinclair, 1988):

$$V = \frac{GM}{r} - \frac{GM}{r} \sum_{\ell=2}^{\infty} J_\ell \left[\frac{r_o}{r}\right]^\ell P_\ell[\sin\phi] + \tag{3.3}$$

$$+ \frac{GM}{r} \sum_{\ell=2}^{\infty} \sum_{m=1}^{\ell} K_{\ell m} \left[C_{\ell m} \cos m\lambda + S_{\ell m} \sin m\lambda \right] \left[\frac{r_o}{r}\right]^\ell P_{\ell m}[\sin\phi]$$

where:

G - universal gravitational constant

M - mass of the Earth

ϕ - geocentric latitude

λ - longitude

r - geocentric distance to the satellite

P_ℓ, $P_{\ell m}$ - Legendre and associated Legendre polynomials

J_ℓ - zonal coefficients

$C_{\ell m}$, $S_{\ell m}$ - normalised tesseral coefficients

r_0 - equatorial radius of the Earth

$K_{\ell m}$ - normalising factor ($m \neq 0$)

and

$$K_{\ell m} = \sqrt{\frac{(\ell - m)!\, 2\,(2\ell + 1)}{(\ell + m)!}} \tag{3.4}$$

An alternative notation is to omit the zonal terms explicitly, and include them in the tesserals by summing from m=0 to ℓ. Then,

$$J_\ell = - K_{\ell 0} \cdot C_{\ell 0} \tag{3.5}$$

$$K_{\ell 0} = \sqrt{2\ell + 1} \tag{3.6}$$

The J's represent the variation of the gravitational field with latitude; the C's and the S's with latitude and longitude. The predominant effects are from the lower order zonal harmonics. The largest asymmetries are due to the equatorial bulge and the pear shape of the Earth.

In the SATAN programs, the Earth's gravitational potential is input as a set of normalised coefficients which can be specified to any degree and order.

The satellite acceleration due the Earth's gravitational field is:

$$\ddot{\vec{r}}_g = \left[\frac{\partial V}{\partial X}, \frac{\partial V}{\partial Y}, \frac{\partial V}{\partial Z}\right] \tag{3.7}$$

In program ORBIT the computation of $\ddot{\vec{r}}_g$ follows a method by Merson and Odell (1975) and modified by Sinclair (1988). Merson and Odell derived expressions for the

acceleration caused by the gravity field using a set of axes in which the XY plane is the true equator of date, and the X axis points towards the equinox of 1950.0. Sinclair rewrote Merson's formulae by redefining the system of axes so that the X,Y plane is the earth fixed equatorial plane, and the X axis points towards the Greenwich meridian. Using this system of axes the acceleration due the gravity field can be written as:

$$\begin{cases} \ddot{X}_g = -AX + \beta \\ \ddot{Y}_g = -AY - \gamma \\ \ddot{Z}_g = -AZ + B \end{cases} \tag{3.8}$$

where

$$A = \frac{GM}{r^3}\left[1 - \sum_{\ell=2}^{\infty} J_\ell \left[\frac{r_o}{r}\right]^\ell P_{\ell+1}^{(1)} + \sum_{\ell=2}^{\infty}\sum_{m=1}^{\ell} K_{\ell m}\left[\frac{r_o}{r}\right]^\ell P_{\ell+1}^{(m+1)}\left(C_{\ell m}\alpha_m + S_{\ell m}\beta_m\right)\right]$$

$$\beta = \frac{GM}{r^2}\left[\sum_{\ell=2}^{\infty}\sum_{m=1}^{\ell} m K_{\ell m}\left[\frac{r_o}{r}\right]^\ell P_\ell^{(m)}\left(C_{\ell m}\alpha_{m-1} + S_{\ell m}\beta_{m-1}\right)\right] \tag{3.9}$$

$$\gamma = \frac{GM}{r^2}\left[\sum_{\ell=2}^{\infty}\sum_{m=1}^{\ell} m K_{\ell m}\left[\frac{r_o}{r}\right]^\ell P_\ell^{(m)}\left(C_{\ell m}\beta_{m-1} - S_{\ell m}\alpha_{m-1}\right)\right]$$

$$B = \frac{GM}{r^2}\left[-\sum_{\ell=2}^{\infty} J_\ell \left[\frac{r_o}{r}\right]^\ell P_\ell^{(1)} + \sum_{\ell=2}^{\infty}\sum_{m=1}^{\ell} K_{\ell m}\left[\frac{r_o}{r}\right]^\ell P_\ell^{(m+1)}\left(C_{\ell m}\alpha_m + S_{\ell m}\beta_m\right)\right]$$

In these formulae all the symbols are as described in equation (3.3) except for:

$$\begin{aligned} \alpha_m &= \cos^m\phi \cos m\lambda \\ \beta_m &= \cos^m\phi \sin m\lambda \end{aligned} \tag{3.10}$$

The coefficients α_m , β_m are computed by recurrence relations. The $P_\ell^{(m)}$ are functions of $\sin\phi$ but differ from the associated Legendre polynomials $P_{\ell m}(\sin\phi)$. They are defined as:

$$P_\ell^{(m)}(\sin\phi) = \frac{P_{\ell m}(\sin\phi)}{\cos^m\phi} \tag{3.11}$$

and computed using a method described by Sinclair (1988).

3.3.2 The Direct Attraction of the Sun, Moon and the Planets

The Earth is not the only body to affect satellites' motion. The sun, the moon and the planets also affect satellites' orbits. The direct attraction of the moon is the most significant effect. Although the sun is more massive, it is also much farther and therefore its effect is less.

The perturbing acceleration due to a "third body" is (King et al., 1985) :

$$\ddot{\vec{r}}_b = Gm_b \left[\frac{\vec{r}_b - \vec{r}}{|\vec{r}_b - \vec{r}|^3} - \frac{\vec{r}_b}{r_b^3} \right] \qquad (3.12)$$

where

$\vec{r}_b$ - geocentric position vector of the third body

$\vec{r}$ - geocentric position vector of the satellite

m_b - mass of the third body

The geocentric position vectors of the sun, moon and the planets are calculated by interpolation on ephemerides published by the Jet Propulsion Laboratory (JPL).

The programs include perturbations by the Sun, Moon, Venus, Mars, Jupiter and Saturn.

3.3.3 Atmospheric Drag

Atmospheric drag is a force which arises from the friction between the satellite surface and the surrounding atmosphere. Due to this effect, the satellite loses energy which results in secular changes in the semi-major axis **a** and in the mean anomaly **M**.

For low satellites such as ERS-1 or SEASAT, the drag acceleration is given by:

$$\ddot{\vec{r}}_d = -\frac{1}{2} C_d \rho \frac{A}{m} \vec{V}_{rel}^{\,2} \frac{\vec{V}}{V} \qquad (3.13)$$

where:

ρ - atmospheric density

C_d - drag coefficient

$\vec{V}$ - satellite velocity

$\vec{V}_{rel}$ - satellite velocity relative to the atmosphere = $\vec{V} - \vec{V}_{atm}$

A - satellite cross sectional area

m - satellite mass

Since the air density decreases rapidly as height above the Earth increases, the effect of air drag is predominant at low altitudes. A satellite in an orbit of appreciable eccentricity is mostly affected within a small section of the orbit where it is closest to the Earth. To a first approximation therefore, the effect of air drag is to retard the satellite as it passes the perigee, with the result that it does not swing out so far from the Earth at the subsequent apogee (King-Hele, 1964). From this perturbation results that the apogee height is reduced while the perigee height remains almost constant, and so the orbit becomes more circular.

For satellites at heights below 500 km this is the dominant of the surface forces. Above this height, radiation pressure makes itself felt, and above 700 km it may become more important than atmospheric drag. Actually, these figures vary with the phase of the solar cycle, since the atmosphere expands or contracts with solar activity. At sunspot minimum, the effect of radiation pressure becomes comparable with that of atmospheric drag at about 600 km, while at sunspot maximum it does not become so below 1100 km (Jacchia, 1965).

Several difficulties exist in modelling the drag force (Moore, 1987):

- The effective cross-sectional area is very difficult to describe as most of the satellites have irregular shape.

- To know the velocity of the atmosphere relative to the satellite, it is necessary to know the velocity of the atmosphere relative to the geocentre. The atmosphere rotates west-to-east with some north-south rotation.

- Various atmospheric density models of increasing complexity have been derived. The density of the atmosphere at satellite height varies due to a variety of phenomena. The main types of variations are a diurnal and an annual variation and variations due to solar and geomagnetic activity. This subject is discussed further in section 9.4.2.

The original SATAN programs used a linear model for modelling the drag coefficient, i.e., it included a constant C_d and its rate of change $\dot{C}_d$:

$$\ddot{\vec{r}}_d = -\frac{1}{2}\left(C_d + \dot{C}_d\right)\rho\,\frac{A}{m}\,\vec{V}_{rel}^{\,2}\,\frac{\vec{V}}{V} \qquad (3.14)$$

The option to solve for multiple drag coefficients has been introduced into the programs. The algorithm is explained in section 3.6. Atmospheric density is computed using

Jacchia's atmospheric model (Jacchia, 1972), with an efficient procedure for its evaluation (Oliver, 1982).

3.3.4 Radiation Pressure

The radiation incident on a satellite produces a repulsive pressure upon its impact on the spacecraft equal to the difference between the incident and reflected momentum flux. This radiation can be the directly emitted solar radiation, the radiation reflected by the Earth and its atmosphere (albedo) or the infrared radiation (IR) emitted by the Earth and its atmosphere. The dominant effect is from the direct solar radiation.

The acceleration due to the direct solar radiation pressure is given by Melbourne et al., (1983):

$$\ddot{\vec{r}}_{drp} = \nu P_s C_r \frac{A}{m} \frac{\vec{r} - \vec{r}_s}{|\vec{r} - \vec{r}_s|^3} \tag{3.15}$$

where:

ν – eclipse factor
- $\nu = 0$ when the satellite is in the Earth's shadow
- $\nu = 1$ when it is in sunlight
- $0 < \nu < 1$ if it is in the penumbra region.

P_S - solar radiation pressure constant = 4.5605×10^{-6} Newton/m^2

C_r - reflectivity coefficient depending on the reflective properties of the satellite

A - cross sectional area of the satellite on which radiation falls

$\vec{r}_s$, $\vec{r}$ - geocentric position vector of the sun and the satellite

m - satellite mass

Passage through Earth's shadow is modelled using a cylindrical model for a spherical Earth. A penumbra effect is included by using a sinusoidal shadow function.

A first order model for the Earth's albedo and infrared radiation pressures is given by McCarthy and Martin (1977). According to this model, the acceleration on the satellite due to radiation from an Earth's surface element dS is (Wakker et al., 1983a):

$$\ddot{\vec{r}}_{albedo+ir} = \left[C_r \gamma P_s \cos\theta + P_{ir} \right] \frac{\cos\alpha}{\pi} \frac{A}{m} \frac{\vec{r} - \vec{r}_{se}}{|\vec{r} - \vec{r}_{se}|^3} dS \tag{3.16}$$

where:

C_r - direct solar radiation scaling factor

γ - albedo of the surface element

P_S - solar radiation pressure constant

P_{ir} - force exerted by the infrared radiation emitted by the surface element (emitted flux/velocity of light)

θ - angle between the surface element's normal and the sun

α - angle between the surface normal and the satellite

A - satellite's cross-sectional area (as viewed from the Earth's surface element)

m - satellite mass

$\vec{r}_{se}$, $\vec{r}$ - geocentric position vector of the surface element, and the satellite

The values of P_{ir} and γ at a surface element are interpolated from tables based on Haar and Suomi (1971). The total acceleration produced on the satellite is computed by integrating the equation over the whole Earth surface visible to the satellite. This is done by dividing the visible surface into 13 different area elements grouped about the sub-satellite point. The contributions of these areas are summed to yield the total acceleration due to albedo and IR radiation.

The effects of radiation pressure are most visible on the semi-major axis, **a**, and eccentricity **e**, but, unlike atmospheric drag, can either increase or decrease the orbital parameters. The effect is dominant for satellites at heights above 1000 km.

One of the main difficulties found in modelling the effects of radiation pressure is the computation of the area to mass ratio because the area exposed to the radiation for non-spherical satellites varies along the orbit.

Effects of direct solar radiation pressure, Earth's albedo and infrared radiation are included in program ORBIT.

3.3.5 The Solid Earth and Ocean Tides

In section 3.3.2, it was explained how the gravitational attraction of the sun and moon causes the precession and nutation movements, which are movements of the Earth as a whole. Because the Earth is not perfectly rigid, the changes in the attractions of the disturbing bodies also produce small movements or tides which vary from place to place. The joint attractions of the sun and the moon cause displacements of the matter in the interior, oceans and atmosphere of the Earth. These tidal deformations cause a periodic rearrangement of the Earth's mass, which in turn alters the Earth's gravitational attraction, inducing additional accelerations on a near Earth satellite.

Solid Earth tides

The potential exerted at a point on the Earth's surface by an external body at a distance r_b from the geocentre is (Melchior, 1978):

$$U = Gm_b \sum_{n=2}^{\infty} \frac{r_o^n}{r_b^{n+1}} P_n (\cos \theta) \qquad (3.17)$$

θ - angle between the geocentric position vector of the point and the geocentric position vector of the perturbing body

r_o - Earth radius

r_b - geocentric distance of the perturbing body

m_b - mass of the perturbing body

Considering only the second order term,

$$U_2 = Gm_b \frac{r_o^2}{r_b^3} P_2 (\cos \theta) \qquad (3.18)$$

For a purely elastic Earth, the deformations due to tides cause a variation in the Earth's gravitational potential equal to:

$$\Delta V = k_2 U_2 \qquad (3.19)$$

where k_2 is the nominal second degree Love number.

The Love numbers (h and k) are dimensionless parameters introduced by Love in 1909 in the theory of spherical elasticity. In 1912, Shida introduced a third number ℓ. These three numbers allow a very practical representation of all deformation phenomena produced by a potential which can be developed in spherical harmonics (Melchior, 1978).

At the satellite (geocentric distance **r**) the potential due to the tidal deformation is given by Dirichlet's theorem:

$$\Delta V = \left[\frac{r_o}{r}\right]^3 k_2 U_2 = \frac{k_2}{2} \frac{Gm_b}{r^3} \frac{r_o^5}{r_b^3} (3\cos^2\theta - 1) \qquad (3.20)$$

The higher order terms in the potential have little influence on the satellite because their amplitude quickly decreases with $\left[\frac{r_o}{r_b}\right]^{n+1}$.

The perturbing acceleration due to the tidal induced potential ΔV, caused by either the sun or the moon, is equal to grad (ΔV) and is given by King et al. (1985):

$$\ddot{\vec{r}}_{et} = \frac{k_2 G m_b}{2 r_b^3} \frac{r_o^5}{r^4} \left[(3 - 15 \cos^2\theta) \frac{\vec{r}}{r} + 6 \cos\theta \frac{\vec{r}_b}{r_b} \right] \qquad (3.21)$$

Using this simple model, the total acceleration due to solid Earth tides is obtained by writing this equation for the sun and the moon and adding the two accelerations.

Actually, Love numbers are not constant but depend on frequency due to resonant effects produced by the Earth's liquid core. So, in the expression of ΔV, k_2 should be replaced by a set of coefficients k_{2m} multiplying the different frequencies. The effects due to frequency dependence of Love numbers are usually expressed in terms of corrections to the Earth's gravitational potential coefficients.

The model implemented on the programs is the MERIT recommended model for solid Earth tides (Melbourne et al., 1983, Appendix 5). The effect is calculated in two steps: first, the perturbed acceleration is computed considering a frequency independent k_2, using equation 3.21; secondly, corrections for the error that arises from using k_2 are applied to the geopotential coefficients.

Ocean tides

The effect due to oceanic tides is more complicated to model than for solid Earth tides. Schwiderski (1980) gives one such model in which the tidal constituents are expressed in terms of spherical harmonics. This is the MERIT recommended model for ocean tides and it is implemented as periodical variations in the geopotential coefficients (Melbourne et al., 1983, Appendix 6).

Station tidal displacement

The total displacement of a station on the Earth's surface due to the solid Earth tides is computed using Wahr's theory, where only the second degree tides are needed for a centimetre level precision (Melbourne et al., 1983). This formulation uses frequency independent Love and Shida numbers. The formula for the vector displacement is (Melbourne et al., 1983):

$$\Delta\vec{r} = \sum_{j=2}^{3} \frac{m_j}{M} \frac{r^4}{r_j^3} \left[\left[3 l_2 (\vec{r}_j \cdot \vec{r}) \right] \frac{\vec{r}_j}{r_j} + \left[3 \left(\frac{h_2}{2} - l_2 \right) (\vec{r}_j \cdot \vec{r})^2 - \frac{h_2}{2} \right] \frac{\vec{r}}{r} \right] \qquad (3.22)$$

m_j - mass of moon (j=2) or the sun (j=3).

M - mass of the Earth

$\vec{r}_j$ - geocentric position vector of the moon or sun

$\vec{r}$ - geocentric position vector of the station

h_2 - nominal second degree Love number = 0.6090

l_2 - nominal Shida number = 0.0852

The station's tidal displacement is of the order of 50 cm. Hence it has to be modelled and applied when processing the tracking data acquired at a particular station. This formula gives the deformation to about 2 cm precision. A correction can be applied to account for the error introduced by using frequency independent Love numbers. This correction is maximum at 45° latitude, with an amplitude of 1.3 cm (Melbourne et al., 1983). Therefore it is neglected in this study.

3.4 Least Squares

3.4.1 Observation equations

The procedure of the best estimation of orbital parameters by least squares is explained (Cross, 1983).

Let us consider the theoretical relationship between the observed quantities and the parameters:

$$f(X') = \ell' \tag{3.23}$$

ℓ' - vector of the true values of the quantities to be observed (e.g. range)

$\mathbf{X}'$ - vector of the true values of the parameters to estimate (e.g. orbital parameters).

In practice there is no access to these true values, but only to approximate values $\mathbf{X_o}$ (calculated) and ℓ (observed) of $\mathbf{X}'$ and ℓ' respectively. Hence corrections $\mathbf{x}$ and $\mathbf{v}$ have to be determined, so that:

$$\begin{aligned} X' &= X_o + x \\ \ell' &= \ell + v \end{aligned} \tag{3.24}$$

Note the use of capital letters to mean parameters (**X**) and lower case letters to mean corrections to the parameters (**x**). This notation was followed for simplicity to avoid the use of differential notation for corrections.

The relationship between parameters and observations can be rewritten:

$$f(X_o + x) = \ell + v \tag{3.25}$$

Usually these equations are not linear. Linearisation can be obtained by expanding **f** in a Taylor series and retaining only the first order terms:

$$f(X_o) + \frac{\partial f}{\partial X} . x = \ell + v \tag{3.26}$$

or :

$$\frac{\partial f}{\partial X} . x = [\ell - f(X_o)] + v \tag{3.27}$$

In matrix form

$$A\ x = b + v \tag{3.28}$$

where **A** is the matrix of the partial derivatives (for **m** observations and **n** parameters):

$$A = \begin{bmatrix} \frac{\partial f_1}{\partial x_1} & \frac{\partial f_1}{\partial x_2} & \cdots & \frac{\partial f_1}{\partial x_n} \\ \frac{\partial f_2}{\partial x_1} & \frac{\partial f_2}{\partial x_2} & \cdots & \frac{\partial f_2}{\partial x_n} \\ \cdots & \cdots & \cdots & \cdots \\ \frac{\partial f_m}{\partial x_1} & \frac{\partial f_m}{\partial x_2} & \cdots & \frac{\partial f_m}{\partial x_n} \end{bmatrix} \qquad f = \begin{bmatrix} f_1 \\ f_2 \\ \cdots \\ f_m \end{bmatrix} \tag{3.29}$$

and **b** is the vector of the "observed minus calculated" residuals:

$$b = \ell - f(X_o) \tag{3.30}$$

The least squares estimate for **x** is defined as the solution which minimises:

$$v^T W v = \text{minimum} \tag{3.31}$$

where $W = C_\ell^{-1}$ and C_ℓ is the covariance matrix of the observations. For uncorrelated observations, W is simply a diagonal weight matrix:

$$W = \text{diag.}(w_1, w_2, \ldots, w_m) \tag{3.32}$$

$$w_i = \frac{\sigma_o^2}{\sigma_i^2}$$

σ_i - standard deviation of observation i

σ_o - standard deviation of unit weight, usually unknown

The least squares solution for $\mathbf{x}$, $\hat{\mathbf{x}}$, is given by the solution of the normal equations:

$$(A^T W A)\,\hat{x} = A^T W b \tag{3.33}$$

which is:

$$\hat{x} = (A^T W A)^{-1}\, A^T W b \tag{3.34}$$

The symmetric matrix $N = A^T W A$ is called the normal equations matrix.

The residuals after the fitting process are given by:

$$\hat{v} = A\,\hat{x} - b \tag{3.35}$$

The sum of the squares of the weighted residuals after fitting can easily be computed by:

$$\hat{v}^T W \hat{v} = b^T W b - \hat{x}^T N\, \hat{x} \tag{3.36}$$

The covariance matrix for the parameters is:

(3.37)

$$C_{\hat{x}} = \sigma_o^2\, N^{-1} = \begin{bmatrix} \sigma_1^2 & \sigma_{12} & \ldots & \sigma_{1n} \\ \sigma_{21} & \sigma_2^2 & \ldots & \sigma_{2n} \\ \ldots & \ldots & \ldots & \ldots \\ \sigma_{n1} & \sigma_{n2} & \ldots & \sigma_n^2 \end{bmatrix}$$

The covariance matrix for the residuals is:

$$C_{\hat{v}} = \sigma_o^2\,(W^{-1} - A\, N^{-1} A^T) \tag{3.38}$$

The covariance matrix for the estimated observed quantities is:

$$C_{\hat{\ell}} = \sigma_o^2 (A\, N^{-1} A^T) = \sigma_o^2\, W^{-1} - C_{\hat{v}} \tag{3.39}$$

Standard error of unit weight:

$$\sigma_o^2 = \frac{\hat{v}^T W \hat{v}}{m-n} \tag{3.40}$$

Orbit determination is usually an iterative process where the procedure explained above is repeated the number of times necessary for the corrections to become negligible. In fact, at step 1 we have:

$$\begin{aligned} b_o &= \ell - f(X_o) \\ \hat{x}_1 &= (A^T W A)^{-1} A^T W b_o \\ X_1 &= X_o + \hat{x}_1 \end{aligned} \tag{3.41}$$

and at step n:

$$\begin{aligned} b_{n-1} &= \ell - f(X_{n-1}) \\ \hat{x}_n &= (A^T W A)^{-1} A^T W b_{n-1} \\ X_n &= X_{n-1} + \hat{x}_n \end{aligned} \tag{3.42}$$

3.4.2 Observation equations with added constraints

The method explained in the previous section applies when, for each equation, there is only one observed quantity (e.g. range or range-rate) and all the parameters are assumed to be independent. If some of the parameters are not independent but are subject to **r** equations of condition, which in the linear form are written as:

$$C\,x = d \tag{3.43}$$

the least squares solution for **x** is the solution of the normal equations (Allan, 1993)

$$\begin{bmatrix} A^TWA & C^T \\ C & 0 \end{bmatrix} \begin{bmatrix} x \\ k \end{bmatrix} = \begin{bmatrix} A^TWb \\ d \end{bmatrix} \tag{3.44}$$

where k are auxiliary parameters, the Lagrange multipliers. The standard error of unit weight becomes

$$\sigma_o^2 = \frac{\hat{v}^T W v}{m-n+r} \tag{3.45}$$

where (m - n + r) is the number of redundant observations. This algorithm is used in Chapter 10 to apply constraints to parameters in short arc solutions.

3.4.3 Bayesian Least Squares

The procedure explained in section 3.4.1, the so-called traditional Least Squares, assumes that there is no particular information on the initial set of parameters $\mathbf{X_o}$. However, sometimes these parameters come from a previous solution with an associated covariance matrix, and it may be useful to use this "a priori" information to constrain the new solution.

Let $\mathbf{X_o}$ be the initial set of parameters, $\mathbf{B_X}$ the associated "a priori" covariance matrix and $W_X=B_X^{-1}$.

The Bayesian solution for $\mathbf{X}$ is the solution for which

$$v^T W v + (X - X_o)^T W_X (X - X_o) = \text{minimum} \qquad (3.46)$$

In statistical terms, the Bayesian solution is the solution which maximises the "a posteriori" density function (Eddy et al., 1990)

$$p(X/\ell) = \frac{p(X) \cdot p(\ell/X)}{p(\ell)} \qquad (3.47)$$

where

$p(\ell)$ - probability density function for data vector ℓ

$p(\ell/X)$ - conditional density function for data vector ℓ, given that vector X has occurred

$p(X)$ - "a priori" probability density function for parameter vector X

$p(X/\ell)$ - "a posteriori" conditional probability density function for parameter vector X, given that vector data ℓ has occurred.

Maximising $p(X/\ell)$ is equivalent to maximising the product $p(X) . p(\ell/X)$, because $p(\ell)$ is a constant valued function.

Assuming that $p(X)$ and $p(X/\ell)$ are normal distributions:

$$p(X) = \frac{\det W_X}{2p^n} \exp\left[-\frac{1}{2} (X_o - X)^T W_X (X_o - X)\right] \qquad (3.48)$$

$$p(\ell/X) = \frac{\det W}{2\,p^{m}} \exp\left[-\frac{1}{2} v^{T} W v\right] \tag{3.49}$$

where all quantities are as defined above, **n** is the number of parameters, **m** the number of observations and $W = C^{-1}$ (C - covariance matrix of the observations ℓ).

So, maximising the a posteriori density function $p(X/\ell)$ is equivalent to maximising the product $p(X)\,.\,p(\ell/X)$ and thus, to minimise:

$$v^{T} W v \;+\; (X_o - X)^{T}\; W_X\; (X_o - X) \tag{3.50}$$

Considering an iterative process, we have at step **n**:

$$\begin{aligned} b_{n-1} &= \ell - f(X_{n-1}) \\ v &= A\;x_n \;-\; b_{n-1} \end{aligned} \tag{3.51}$$

The Bayesian solution for X_n is the solution for which

$$v^{T} W v \;+\; (X_n - X_o)^{T}\; W_X\; (X_n - X_o) \;=\; \text{minimum} \tag{3.52}$$

and is given by

$$\hat{x}_n = [\,A^{T} W A \;+ W_X\,]^{-1}\;\; [\,A^{T} W\, b_{n-1} \;+ W_X\,(\,X_o - X_{n-1})\,] \tag{3.53}$$

$$X_n = X_{n-1} + \hat{x}_n$$

The covariance matrix for the parameters is:

$$C_{\hat{x}} = \sigma_o^{2}\left[\,A^{T}WA + W_X\right]^{-1} \tag{3.54}$$

and the standard error of unit weight is:

$$\sigma_o^{2} = \frac{\hat{v}^{T} W \hat{v} + (\,X_n - X_o)^{T} W_X (\,X_n - X_o)}{m - n} \tag{3.55}$$

3.5 Partial derivatives

In order to form the normal equations, the partial derivatives of the observed quantities with respect to the solve-for parameters have to be computed for all data types.

If ℓ is an observed quantity at time **t**, and **p** is a satellite solve-for parameter, usually ℓ is a function of **p** through satellite state vector $\vec{Q} = [\, X, Y, Z, \dot{X}, \dot{Y}, \dot{Z} \,]$ at time **t**, i.e. there are functions **g** and **h** such that :

$$\begin{aligned} \ell &= h(\vec{Q}) \\ \vec{Q} &= g(p) \end{aligned} \tag{3.56}$$

The computation of

$$\frac{\partial \ell}{\partial p} = \frac{\partial \ell}{\partial \vec{Q}} \cdot \frac{\partial \vec{Q}}{\partial p} \tag{3.57}$$

can then be separated in two parts: the part which is independent of the data type , $\frac{\partial \vec{Q}}{\partial p}$, and the part which is different for each data type, $\frac{\partial \ell}{\partial \vec{Q}}$.

Unless specified, it is assumed that all coordinates are referred to an inertial system which in the case of program RGODYN is the J2000 system.

3.5.1 Partials of satellite position and velocity with respect to solve-for parameters

The partial derivatives of satellite position and velocity at a given time **t**, with respect to various parameters, $\frac{\partial \vec{Q}}{\partial p}$, are computed by program ORBIT by numerical integration.

Considering the equations of motion in the form,

$$\begin{aligned} \ddot{X} &= f_1(X, Y, Z, \dot{X}, \dot{Y}, \dot{Z}, p_i, t) \\ \ddot{Y} &= f_2(X, Y, Z, \dot{X}, \dot{Y}, \dot{Z}, p_i, t) \\ \ddot{Z} &= f_3(X, Y, Z, \dot{X}, \dot{Y}, \dot{Z}, p_i, t) \end{aligned} \tag{3.58}$$

the differential equations for the partials are derived by forming the partial derivatives of the equations of motion and rearranging (Sinclair, 1988) :

$$\frac{d^2}{dt^2}\left[\frac{\partial X}{\partial p_i}\right] = \left[\frac{\partial f_1}{\partial p_i}\right]_{exp} + \frac{\partial f_1}{\partial X}\frac{\partial X}{\partial p_i} + \frac{\partial f_1}{\partial Y}\frac{\partial Y}{\partial p_i} + \frac{\partial f_1}{\partial Z}\frac{\partial Z}{\partial p_i} + \frac{\partial f_1}{\partial \dot{X}}\frac{\partial \dot{X}}{\partial p_i} + \frac{\partial f_1}{\partial \dot{Y}}\frac{\partial \dot{Y}}{\partial p_i} + \frac{\partial f_1}{\partial \dot{Z}}\frac{\partial \dot{Z}}{\partial p_i}$$

$$\frac{d^2}{dt^2}\left[\frac{\partial Y}{\partial p_i}\right] = \left[\frac{\partial f_2}{\partial p_i}\right]_{exp} + \frac{\partial f_2}{\partial X}\frac{\partial X}{\partial p_i} + \frac{\partial f_2}{\partial Y}\frac{\partial Y}{\partial p_i} + \frac{\partial f_2}{\partial Z}\frac{\partial Z}{\partial p_i} + \frac{\partial f_2}{\partial \dot{X}}\frac{\partial \dot{X}}{\partial p_i} + \frac{\partial f_2}{\partial \dot{Y}}\frac{\partial \dot{Y}}{\partial p_i} + \frac{\partial f_2}{\partial \dot{Z}}\frac{\partial \dot{Z}}{\partial p_i} \qquad (3.59)$$

$$\frac{d^2}{dt^2}\left[\frac{\partial Z}{\partial p_i}\right] = \left[\frac{\partial f_3}{\partial p_i}\right]_{exp} + \frac{\partial f_3}{\partial X}\frac{\partial X}{\partial p_i} + \frac{\partial f_3}{\partial Y}\frac{\partial Y}{\partial p_i} + \frac{\partial f_3}{\partial Z}\frac{\partial Z}{\partial p_i} + \frac{\partial f_3}{\partial \dot{X}}\frac{\partial \dot{X}}{\partial p_i} + \frac{\partial f_3}{\partial \dot{Y}}\frac{\partial \dot{Y}}{\partial p_i} + \frac{\partial f_3}{\partial \dot{Z}}\frac{\partial \dot{Z}}{\partial p_i}$$

The computation of the partials of **f** with respect to X,Y,Z is done using formulae described by Sinclair (1988). For every solve-for parameter the explicit partial derivatives $\left[\frac{\partial f_j}{\partial p_i}\right]_{exp}$ must also be calculated. The partials of position and velocity with respect to the required parameters are then obtained by integrating these equations. Since the dependence of **f** on velocity is weak, usually only the partials with respect to position are computed. These partials are only needed to low accuracy because the correction procedure is only accurate to first order.

In the original programs, the parameters considered were the start vector in terms of cartesian coordinates $\vec{Q}_0 = [\, X_0, Y_0, Z_0, \dot{X}_0, \dot{Y}_0, \dot{Z}_0 \,]$, the constant GM and the drag and solar radiation coefficients. Two major modifications have been introduced into the programs: solution for a selected set of geopotential coefficients and for the start vector in terms of orbital elements instead of cartesian coordinates.

Solution for start vector in terms of orbital elements

Solving for the start vector in cartesian coordinates is the usual practice, especially when using numerical methods to integrate the equations of motion. However, sometimes it is convenient to solve for the start vector in terms of orbital elements, instead of cartesian coordinates, as correlations between the parameters are more meaningful.

Let $\vec{E}_0$ be the start vector in terms of orbital elements :

$$\vec{E}_0 = (a_0 , e_0 , i_0 , M_0 , \omega_0 , \Omega_0) \qquad (3.60)$$

where a - semi-major axis
e - eccentricity
i - inclination
M - mean anomaly
ω - argument of perigee
Ω - right ascension of ascending node

For near circular orbits there is a high correlation between M and ω, and in this case it may be advantageous to use the following equivalent set of elements :

$$\vec{E}_0 = (a_0 , e_0 , i_0 , M_0 + \omega_0 , \omega_0 , \Omega_0) \qquad (3.61)$$

In any case

$$\frac{\partial \vec{Q}}{\partial \vec{E}_0} = \frac{\partial \vec{Q}}{\partial \vec{Q}_0} \cdot \frac{\partial \vec{Q}_0}{\partial \vec{E}_0} \qquad (3.62)$$

$\frac{\partial \vec{Q}}{\partial \vec{Q}_0}$ is computed by numerical integration as explained above.

The formulae for $\frac{\partial \vec{Q}_0}{\partial \vec{E}_0}$ in the case $\vec{E}_0 = (a_0 , e_0 , i_0 , M_0 , \omega_0 , \Omega_0)$, the usual 6 orbital elements, are well known from Kaula (1966). When the modified set of parameters given in (3.61) is used, the matrix of the partial derivatives $\frac{\partial \vec{Q}_0}{\partial \vec{E}_0}$ in equation (3.62) have a slightly different form.

Let **A** be the matrix of the partial derivatives of the start vector in terms of position and velocity $\vec{Q}_0 = [X_0, Y_0, Z_0, \dot{X}_0, \dot{Y}_0, \dot{Z}_0]$ with respect to the 6 osculating orbital elements $\vec{E}_0 = (a_0 , e_0 , i_0 , M_0 , \omega_0 , \Omega_0)$:

$$A = \begin{bmatrix} \frac{\partial X}{\partial a} & \frac{\partial X}{\partial e} & \frac{\partial X}{\partial i} & \frac{\partial X}{\partial M} & \frac{\partial X}{\partial \omega} & \frac{\partial X}{\partial \Omega} \\ \frac{\partial Y}{\partial a} & \frac{\partial Y}{\partial e} & \frac{\partial Y}{\partial i} & \frac{\partial Y}{\partial M} & \frac{\partial Y}{\partial \omega} & \frac{\partial Y}{\partial \Omega} \\ \frac{\partial Z}{\partial a} & \frac{\partial Z}{\partial e} & \frac{\partial Z}{\partial i} & \frac{\partial Z}{\partial M} & \frac{\partial Z}{\partial \omega} & \frac{\partial Z}{\partial \Omega} \\ \frac{\partial \dot{X}}{\partial a} & \frac{\partial \dot{X}}{\partial e} & \frac{\partial \dot{X}}{\partial i} & \frac{\partial \dot{X}}{\partial M} & \frac{\partial \dot{X}}{\partial \omega} & \frac{\partial \dot{X}}{\partial \Omega} \\ \frac{\partial \dot{Y}}{\partial a} & \frac{\partial \dot{Y}}{\partial e} & \frac{\partial \dot{Y}}{\partial i} & \frac{\partial \dot{Y}}{\partial M} & \frac{\partial \dot{Y}}{\partial \omega} & \frac{\partial \dot{Y}}{\partial \Omega} \\ \frac{\partial \dot{Z}}{\partial a} & \frac{\partial \dot{Z}}{\partial e} & \frac{\partial \dot{Z}}{\partial i} & \frac{\partial \dot{Z}}{\partial M} & \frac{\partial \dot{Z}}{\partial \omega} & \frac{\partial \dot{Z}}{\partial \Omega} \end{bmatrix} \qquad (3.63)$$

The subscript "o" was omitted in the matrix to avoid heavy notation. The corresponding matrix **B** of the partial derivatives of $\vec{Q}_o = [\, X_o, Y_o, Z_o, \dot{X}_o, \dot{Y}_o, \dot{Z}_o \,]$ with respect to $\vec{E}_o = (a_o, e_o, i_o, M_o + \omega_o, \omega_o, \Omega_o)$ is:

$$A = \begin{bmatrix} \frac{\partial X}{\partial a} & \frac{\partial X}{\partial e} & \frac{\partial X}{\partial i} & \frac{\partial X}{\partial M} & \frac{\partial X}{\partial \omega} - \frac{\partial X}{\partial M} & \frac{\partial X}{\partial \Omega} \\ \frac{\partial Y}{\partial a} & \frac{\partial Y}{\partial e} & \frac{\partial Y}{\partial i} & \frac{\partial Y}{\partial M} & \frac{\partial Y}{\partial \omega} - \frac{\partial Y}{\partial M} & \frac{\partial Y}{\partial \Omega} \\ \frac{\partial Z}{\partial a} & \frac{\partial Z}{\partial e} & \frac{\partial Z}{\partial i} & \frac{\partial Z}{\partial M} & \frac{\partial Z}{\partial \omega} - \frac{\partial Z}{\partial M} & \frac{\partial Z}{\partial \Omega} \\ \frac{\partial \dot{X}}{\partial a} & \frac{\partial \dot{X}}{\partial e} & \frac{\partial \dot{X}}{\partial i} & \frac{\partial \dot{X}}{\partial M} & \frac{\partial \dot{X}}{\partial \omega} - \frac{\partial \dot{X}}{\partial M} & \frac{\partial \dot{X}}{\partial \Omega} \\ \frac{\partial \dot{Y}}{\partial a} & \frac{\partial \dot{Y}}{\partial e} & \frac{\partial \dot{Y}}{\partial i} & \frac{\partial \dot{Y}}{\partial M} & \frac{\partial \dot{Y}}{\partial \omega} - \frac{\partial \dot{Y}}{\partial M} & \frac{\partial \dot{Y}}{\partial \Omega} \\ \frac{\partial \dot{Z}}{\partial a} & \frac{\partial \dot{Z}}{\partial e} & \frac{\partial \dot{Z}}{\partial i} & \frac{\partial \dot{Z}}{\partial M} & \frac{\partial \dot{Z}}{\partial \omega} - \frac{\partial \dot{Z}}{\partial M} & \frac{\partial \dot{Z}}{\partial \Omega} \end{bmatrix} \qquad (3.64)$$

This form of the start vector in terms of the 6 modified osculating elements is used in Chapter 10 in short arc computations.

Adjustment of geopotential coefficients

As explained above, the inclusion of more solve-for parameters requires the computation of the explicit partial derivatives of the acceleration **f** in equation (3.58) with respect to

these parameters. In the case of the geopotential coefficients these partials are derived by differentiating equations (3.8) with respect to each coefficient:

Partials with respect to zonals J_ℓ :

$$\begin{aligned}
\frac{\partial f_1}{\partial J_\ell} &= -\frac{\partial A}{\partial J_\ell} X \\
\frac{\partial f_2}{\partial J_\ell} &= -\frac{\partial A}{\partial J_\ell} Y \\
\frac{\partial f_3}{\partial J_\ell} &= -\frac{\partial A}{\partial J_\ell} Z + \frac{\partial B}{\partial J_\ell}
\end{aligned} \tag{3.65}$$

Partials with respect to tesserals $C_{\ell m}$

$$\begin{aligned}
\frac{\partial f_1}{\partial C_{\ell m}} &= -\frac{\partial A}{\partial C_{\ell m}} X + \frac{\partial \beta}{\partial C_{\ell m}} \\
\frac{\partial f_2}{\partial C_{\ell m}} &= -\frac{\partial A}{\partial C_{\ell m}} Y - \frac{\partial \gamma}{\partial C_{\ell m}} \\
\frac{\partial f_3}{\partial C_{\ell m}} &= -\frac{\partial A}{\partial C_{\ell m}} Z + \frac{\partial B}{\partial C_{\ell m}}
\end{aligned} \tag{3.66}$$

Similar expressions hold for the partials with respect to $S_{\ell m}$, by just replacing $C_{\ell m}$ by $S_{\ell m}$ in the above equations.

Denoting by H the common factor:

$$H = \frac{GM}{r^3} \left[\frac{r_o}{r}\right]^\ell \tag{3.67}$$

the partials of A, B, β and γ with respect to each coefficient can be expressed as:

$$\frac{\partial A}{\partial J_\ell} = -H \; P_{\ell+1}^{(1)}$$

$$\frac{\partial B}{\partial J_\ell} = -H \; r \; P_\ell^{(1)}$$

$$\frac{\partial A}{\partial C_{\ell m}} = H \; K_{\ell m} \; P_{\ell+1}^{(m+1)} \alpha_m \qquad \frac{\partial A}{\partial S_{\ell m}} = H \; K_{\ell m} \; P_{\ell+1}^{(m+1)} \beta_m \tag{3.68}$$

$$\frac{\partial B}{\partial C_{\ell m}} = H \; r \; K_{\ell m} \; P_\ell^{(m+1)} \alpha_m \qquad \frac{\partial B}{\partial S_{\ell m}} = H \; r \; K_{\ell m} \; P_\ell^{(m+1)} \beta_m$$

$$\frac{\partial \beta}{\partial C_{\ell m}} = H\ r\ m\ K_{\ell m}\ P_{\ell}^{(m)} \alpha_{m-1} \qquad \frac{\partial \beta}{\partial S_{\ell m}} = H\ r\ m\ K_{\ell m}\ P_{\ell}^{(m)} \beta_{m-1}$$

$$\frac{\partial \gamma}{\partial C_{\ell m}} = \frac{\partial \beta}{\partial S_{\ell m}} \qquad \frac{\partial \gamma}{\partial S_{\ell m}} = - \frac{\partial \beta}{\partial C_{\ell m}}$$

These partials are first computed in the terrestrial system and then transformed into the J2000 system by using the appropriate transformation.

3.5.2 Partials of the observed quantity with respect to satellite position

In this study, three different tracking data types were used: laser, PRARE and altimeter observations. These data types are described in Chapters 6 (laser and PRARE) and Chapter 7 (altimetry). This section gives the formulae for the partial derivatives of these quantities with respect to satellite position. All the partials with respect to satellite velocity are zero, since none of these observed quantities is a function of velocity.

Partials of Range (Laser or PRARE)

Range vector from station T to satellite S :

$$\vec{R} = \vec{S} - \vec{T} \tag{3.69}$$

$$\vec{S} = [\, X_S, Y_S, Z_S \,]$$

$$\vec{T} = [\, X_T, Y_T, Z_T \,]$$

Range distance :

$$R = [\, (X_S - X_T)^2 + (Y_S - Y_T)^2 + (Z_S - Z_T)^2 \,]^{1/2} \tag{3.70}$$

Partials of range with respect to satellite cartesian coordinates:

$$\frac{\partial R}{\partial X_S} = \frac{X_S - X_T}{R}$$

$$\frac{\partial R}{\partial Y_S} = \frac{Y_S - Y_T}{R} \tag{3.71}$$

$$\frac{\partial R}{\partial Z_S} = \frac{Z_S - Z_T}{R}$$

Partials of altimeter height

Partials of **h** with respect to satellite geocentric coordinates X, Y, Z :

$$\begin{cases} \dfrac{\partial h}{\partial X} = \cos\varphi \cos\lambda \\ \dfrac{\partial h}{\partial Y} = \cos\varphi \sin\lambda \\ \dfrac{\partial h}{\partial Z} = \sin\varphi \end{cases} \qquad (3.72)$$

where φ is geodetic latitude and λ is longitude.

These expressions give the partials in the terrestrial system. To compute them in the J2000 system the required transformation has to be applied. Note that these expressions are precise, not just approximate. The demonstration of these formulae, derived by the author of this thesis, is presented in Appendix A.

3.6 Multiple Drag Coefficients

It has been current practice in long arc solutions, if enough tracking data are available, to solve for multiple drag coefficients instead of a single coefficient for the whole arc. This greatly improves the orbital fit by absorbing some of the along-track error.
The use of multiple drag coefficients instead of a single coefficient involves two main aspects:

i) redefinition of the formula for the acceleration due to the drag force

ii) computation of the partial derivatives of satellite position and velocity with respect to each coefficient.

i) In the case of a single coefficient, the acceleration due to drag force can be written as (see equation 3.13):

$$\ddot{\vec{r}}_d = C_d \cdot \vec{D} \qquad (3.73)$$

where

$$\vec{D} = -\frac{1}{2}\rho \frac{A}{m} \vec{V}_{rel}^{\,2} \frac{\vec{V}}{V} \qquad (3.74)$$

Let us consider an arc **A** , with start and end dates t_0 and t_n respectively, which is divided into **n** arcs A_l :

$$A = [t_o, t_n]$$

$$A_i = [t_{i-1}, t_i] \ , \quad i=1,N \tag{3.75}$$

so that a different drag coefficient C_d^i applies for each arc A_i.

C_d can now be considered a vector of length **n** :

$$C_d = \left(C_d^1, C_d^2, \ldots, C_d^n \right) \tag{3.76}$$

and the formula for the acceleration due to drag becomes a function of **n** branches:

$$\ddot{\vec{r}}_d = \begin{cases} C_d^1 . \vec{D} & t \in A_1 \\ C_d^2 . \vec{D} & t \in A_2 \\ \quad \ldots\ldots & \\ C_d^n . \vec{D} & t \in A_n \end{cases} \tag{3.77}$$

Therefore, at every step of the integration of the equations of motion, the corresponding C_d is used. The fact that acceleration is now a discontinuous function does not mean that the resulting satellite position and velocity will have sharp variations at the discontinuity points. This is a consequence of the numerical integration method itself. In the case of Gauss-Jackson method, at every step, satellite position and velocity are a function of acceleration at that time, plus function values at the previous 9 steps. Therefore a sharp change on the acceleration due to a change of the drag coefficient leads to smooth changes in position and velocity.

ii) The computation of the partial derivatives is not so simple. As the equations of motion are solved by numerical integration, at every step, satellite position and velocity are a function of not only the parameters that define the orbit at that time but also, in an implicit form, of all parameters that have affected the orbit since the beginning of the arc. As explained in section 3.5.1 the partial derivatives of satellite position and velocity with respect to the solve-for parameters (including C_d) are computed by numerical integration (equation 3.59). For each drag coefficient there is an equation of the form:

$$\frac{\partial f}{\partial C_d^i} = \left[\frac{\partial f}{\partial C_d^i}\right]_{explicit} + \left[\frac{\partial f}{\partial C_d^i}\right]_{implicit} \tag{3.78}$$

To set up these equations the explicit partial derivatives $\left[\frac{\partial f}{\partial C_d}\right]_{explicit}$ must be computed.

According to equation 3.77 they are :

$$\left[\frac{\partial f}{\partial C_d^i}\right]_{explicit} = \begin{cases} \vec{D} & t \in A_i \\ 0 & t \notin A_i \end{cases} \tag{3.79}$$

To compute the implicit dependence one only need to include the partials with respect to position. This is because the dependence of **f** on velocity is very weak and, as the correction procedure is of first order, the partials are only needed at low accuracy (Sinclair, 1988). This implicit dependence is computed as:

$$\left[\frac{\partial f}{\partial C_d^i}\right]_{implicit} = \begin{cases} \dfrac{\partial f}{\partial X}\dfrac{\partial X}{\partial C_d^i} + \dfrac{\partial f}{\partial Y}\dfrac{\partial Y}{\partial C_d^i} + \dfrac{\partial f}{\partial Z}\dfrac{\partial Z}{\partial C_d^i} & t \in A_j \text{ for } j \le i \\ 0 & t \in A_j \text{ for } j > i \end{cases} \tag{3.80}$$

Therefore, for each arc A_i :

$$\frac{\partial f}{\partial C_d} = \left[\left[\frac{\partial f}{\partial C_d^1}\right]_{imp}, \left[\frac{\partial f}{\partial C_d^2}\right]_{imp}, \ldots, \left[\frac{\partial f}{\partial C_d^{i-1}}\right]_{imp}, \left[\frac{\partial f}{\partial C_d^i}\right]_{imp+exp}, 0, \ldots, 0 \right] \tag{3.81}$$

In other words, at every step of the integration **t**, inside arc A_i, the implicit dependence of **f** with respect to each drag coefficient C_d^j is computed as:

- if $j > i$ $\dfrac{\partial f}{\partial C_d^j}$ is null as f does not depend at all on C_d^j.
- if $j = i$ then $\dfrac{\partial f}{\partial C_d^j}$ is fully computed, both the explicit and the implicit components, as **f** is an explicit function of C_d^j
- if $j < i$ then on $\dfrac{\partial f}{\partial C_d^j}$ only the implicit part has to be computed, as **f** is only an implicit function of C_d^j, due to the fact that C_d^j has affected the function on previous steps.

As the partial derivatives themselves are computed by numerical integration, the problem arises of how to change the computation from explicit to implicit and vice-versa when changing the arc, since the integration method used (Gauss-Jackson) needs an iterative

starting scheme. During this study, intensive research was done on how to implement this algorithm with the addition of minimal computational effort. Here the main conclusions are presented.

	C_d^1	C_d^2	C_d^3
Arc 1	E	I Ø	I Ø
Arc 2	I	E	I Ø
Arc 3	I	I	E

A

	C_d^1	C_d^2	C_d^3
Arc 1	E	Ø	Ø
Arc 2	I	↑ E	Ø
Arc 3	I	I	↑ E

B

Figure 3.1 - Schematic representation of two equivalent algorithms for implementing the solution for multiple drag coefficients.

To simplify the schematic representation of the algorithm, let us suppose that the number of drag coefficients to solve for along the arc is 3. Two different algorithms were found to be equivalent. Figure 3.1 describes these algorithms. In this figure the following symbolic representation was used :

E - the partial derivatives are computed considering both the explicit and the implicit parts.

I - only the implicit part was computed

I Ø - although the implicit part is computed (because it is needed as starting values for subsequent arcs), it is not output (the output is zero).

↑ - the computation is restarted at the beginning of the arc. When this symbol does not appear, the change from implicit to explicit and vice-versa is done without using the starting procedure, i.e., the integration continues normally only with different formulae.

Results show that it is irrelevant whether the integration is restarted at the beginning of each arc or continued sequentially. Algorithm A is faster than B because the starting procedure is slower than the Gauss-Jackson integrator. Considering the computation time and simplicity of the algorithm, the adopted model which was implemented in the programs was model A.

3.7 Conclusions

This chapter has described the main features of the SATAN programs and some of the modifications that have been introduced during this project. Additional algorithms developed in this study for processing PRARE range and altimeter data are described in chapters 6 and 7 respectively. These programs were used in all the research work carried out during this project which is described in chapters 8 to 10.

Chapter 4

Background to orbit determination for altimetric satellites

4.1 Introduction

This chapter summarises the background to techniques that have been used in the computation of the orbit of low orbiting remote sensing satellites.

Orbit computation for low satellites such as ERS-1 is usually performed by means of two types of solutions: short arcs and long arcs. These two solutions have different requirements and possess different characteristics with respect to a number of points:

- spanning interval
- amount and distribution of tracking data
- accuracy of dynamic models
- accuracy of tracking stations

Typically a short arc covers a time interval of a few minutes, less than one orbital revolution. For a low polar orbit a long arc should encompass at least 3 days, unless there are plenty of well distributed tracking data along the arc. This is because the ground track pattern of low orbiting polar satellites repeats itself after a time interval close to 3 days. Therefore this is the minimum time for the satellite to go through all the perturbations due to the Earth's gravitational field except resonance. If a shorter interval is used, an artificially good fit to data can be achieved but, away from tracked areas, the solution may have large errors.

For short arcs, the amount and distribution of tracking data along the arc are crucial. These will determine the stability of the solution, as well as the number and type of parameters to adjust. The precision of these solutions is that of the tracking data, and they are highly inaccurate away from the fitted arc. The type of dynamic model used is of slight importance, since the model errors are absorbed in the fitting process.

The most important factor for long arcs is the accuracy of the dynamic model, i.e. how well it describes the forces that act on the satellite and their variability. Their accuracy is limited by the accuracy of the model used, in particular the gravity field and atmospheric drag models. These are smooth solutions that, in principle, are of similar accuracy at all

parts, even where not fitted to data. The amount and distribution of the tracking data used is of minor importance.

Sinclair (1985) considers a third type of solution: medium arcs from 10 minutes to one revolution. These solutions achieve a precision of fit only slightly worse than that of the tracking data, but they depend to some extent on the orbit model used. The amount and distribution of data are still as important as in short arcs, the accuracy of the tracking stations being less important.

Orbit solutions can still be classified as dynamical and non-dynamical.

A dynamical solution usually consists of an iterative process. First an orbit is computed by numerical integration using a model for the forces that act on the satellite. During the next step some of the parameters that define the force model are adjusted by fitting the orbit to observations. These improved parameters are then used to compute an improved orbit.

A non-dynamical method determines corrections to a computed orbit in such a way that the corrected track of the satellite is no longer an exact solution of the equations for its motion. Examples of non-dynamical methods are the TAR method described in section 4.2 and crossover analysis of altimetry data (section 4.5).

4.2 Short arcs

Short arc computations require the use of special techniques. The quality of the solution is strongly dependent on the number and type of parameters to adjust.

To compute an orbit over a short arc up to 10 minutes, Sinclair (1985, 1989) considers two methods:

• Method 1: To generate an orbit by numerical integration and fit it only to the data points of the short arc by solving for the 6 parameters of the start vector at some convenient close starting epoch. This method may lead to very high correlations between the solved-for parameters. An alternative is to first determine a long arc orbit that includes the short arc, and then fit the long arc orbit to the short arc data points by solving for corrections to the 6 osculating orbital elements at some epoch. This gives virtually identical results with the advantage that constraints can be applied to them more meaningfully. In both methods, it is found that the gravity field, and the models for drag and radiation pressure used, have no influence on the quality of the solution.

• Method 2: To determine a long arc orbit and fit it to the short arc data points by solving for corrections along the three following directions: along-track (T), across-track (A) and radial (R), the so-called TAR corrections.

A good fit to the short arc data points can be obtained by both methods, but the solution can sometimes be spurious.

The TAR corrections can be represented as simple constants, linear variations with time, or periodic variations of the orbital period. The best way of representing the corrections seems to be the last method. The advantage of using TAR corrections is that correlations related to the configuration of the track relative to the stations are more apparent, and can be controlled by limiting the number of parameters. The disadvantage is that the corrected track is no longer an exact solution of the equations for its motion.

Using the TAR method, Sinclair (1989) researched the type of configuration the network of the tracking stations should have to give an accuracy of less than 10 cm over a short arc. The configuration required is either:

• Two stations, close to the ground track of the satellite, one at each end of the arc.
• Four stations, two at each end of the arc, preferably on either side of the track, with significantly different minimum zenith angles.

If range data from a single pass of a station are used, then very high corrections are found between various solved-for parameters.

Hauck and Herzberger (1986) and Hauck (1988) used similar techniques for short arc solutions where station coordinates were simultaneously solved. They used two methods: the first is similar to method 1 described above; the second method solves for 4 corrections to the following parameters: T, R, inclination and ascending node.

For short arc solutions, the coordinates of the tracking stations have to be accurately known. The tracking data only locate the satellite relative to the stations. Hence its location relative to the centre of the Earth is dependent on knowing the station coordinates. Errors in the latitude and longitude of the stations will cause errors in the position of the satellite of the same order in the T and R directions, the effect on R being smaller (Sinclair, 1989). However, an error in the height of the station will cause errors of the same order in the radial component.

On a simulation study for ERS-1, Wakker et al.(1983a) found that a radial accuracy of better than 10 cm can be achieved for an arc of about 15 minutes that is tracked intensively by several laser or PRARE stations, but the errors increase rapidly away from this region. The results also show that, for these short arcs, the gravity model errors lead

to only very small orbit errors of less than 4 cm, and that the surface model errors have almost a negligible effect on orbit accuracy. The dominant error in this case is the station coordinates error.

4.3 Medium arcs

Sinclair (1985) investigated how a short arc technique could be extended to longer arcs, up to half a revolution. He used an artificial method whereby two orbits were computed for the satellite Starlette (height 960 km and inclination 49.8°) using two different gravity models, GEM10B and PGS1331. GEM10B is a general purpose geopotential model developed by GSFC, complete to degree and order 36, while PGS1331 is a tuned gravity field for Starlette. The GEM10B orbit was fitted to the PGS1331 orbit in 2 ways: by fitting at points every 0.3 minutes along the whole arc, and by fitting at points every 0.3 minutes along the first and last 9 minutes of the arc. This latter method was intended to simulate a situation where the arc would be tracked by stations at each end of the arc. It was found that the first method gives rather strange results, completely different from the effect of fitting to range data, giving radial errors larger than the along-track and across-track errors. The second method gives a better overall result with an rms radial error of 6 cm to 57 cm, depending on arc length.

For these medium arcs, if the arc is well determined at the ends, there will be an error within it due to the limitations of the orbital model. These errors will not be as large as in long-arc solutions, because the long-period errors of the model, and those close to the orbital period, will be absorbed by the fitting process.

Short and medium arc computations can be very useful for ERS-1. Due to the limitations in the existing force models for this satellite, this may be the only alternative if very precise positions are required. In this study intensive research has been done on the development of alternative short and medium arc methods. These results are presented in Chapter 10.

4.4 Long arcs

Generally, long arc solutions are less influenced by data distribution but are very dependent on the accuracy of the force models being used, especially the models for the gravity field, atmospheric drag and radiation pressure. Together with the start vector, drag and solar radiation coefficients are usually adjusted in the orbit computation process.

Studies being done for Starlette (Sinclair, 1985) suggest that to obtain an orbit that achieves close to the optimum radial accuracy of the model being used at all parts, the amount and distribution of tracking data is not critical but should cover at least 3 days, should be very well distributed geographically (i.e. from all continents), and should include 15 or more passes. For arcs longer than 8 days, the accuracy gradually deteriorates, and the use of single solved-for coefficients for drag and radiation pressure becomes inadequate. Generally, for arcs longer than 3 days, or arcs covering a period of strongly enhanced solar and geomagnetic activity, multiple daily drag coefficients should be used. The adjustment of multiple drag coefficients will absorb any slowly varying along-track orbit error due for example to mismodelling of geopotential coefficients.

For long arc solutions the main source of orbit error is the gravity field model. At present, the best gravity models for orbit determination seem to be the GEMTn series (Table 4.1). GEMT1 is a general purpose model, derived from satellite only tracking data from 17 satellites, complete to degree and order 36 (Marsh et al., 1988).

The accuracy of a geopotential model is limited by two types of modelling errors:

- commission errors due to mismodelling of the coefficients.
- omission errors due to fact that each model is truncated at a particular degree and order.

The commission error for GEMT1 is 1.60 m. GEMT2 uses data from 31 satellites, is complete to degree and order 36 and contains more than 600 coefficients above degree 36, up to degree 50, to better accommodate zonal, low order, and satellite resonant terms. The commission error for GEMT2 is 1.30 m for the 36x36 portion of the field and 1.41 m for the full model (Marsh et al., 1990a).

Gravity models derived from satellite data only are limited by the fact that the available data do not cover all the relevant inclinations and semi-major axes. Such models possess heavily correlated coefficient values, and will be unsuitable for the computation of orbits of satellites with other different parameters (Zandbergen et al., 1988).

For irregularly shaped satellites like ERS-1 or SEASAT the cross-sectional area for atmospheric drag or radiation pressure has large variations. For these satellites it is important that these areas are modelled accurately. Wakker et al. (1983a) show that the modelling of the variable cross-sectional area of SEASAT considerably affects the orbit solution.

Table 4.1
Summary of geopotential models used in this study

Geopotential model	Degree	RMS Commission error of the geoid (m)	Data utilised in the models
GEMT1	36	1.60	Data from 17 satellites including SEASAT
GEMT2	50 (incomplete) Complete to degree 36	1.30 - for the 36x 36 portion of the model 1.41 - for the whole model	Data from 31 satellites including SEASAT and GEOSAT
OSU89A OSU89B	360	0.32 - for the portion of the field common to GEMT2 0.60 - for the whole model	GEMT2 model + 1°x 1° gravity anomalies + SEASAT and GEOS3 altimetry
GRIM4_C2	50	0.54	Data from 29 satellites including SEASAT, GEOSAT and SPOT2 (DORIS) + 1°x 1° gravity anomalies + SEASAT and GEOS3 altimetry

SEASAT orbits

To assess the accuracy to be expected for ERS-1 orbit, and given the similarity between the two satellites, the SEASAT orbit has been extensively computed by a number of investigators. These studies reveal the progress that has been achieved on force modelling and data processing during the last decade.

The SEASAT orbit used in the Geophysical data records had errors of the order of 1.5 m.

For arcs from 3 to 6 days' length, Wakker et al. (1983b) determined SEASAT orbits using adjustable daily drag coefficients, area tables for atmospheric drag, and the SEASAT tuned gravity field PGS-S4. These orbits exhibit laser range residuals from 0.5 m to 1.23 m and rms values of 0.8 m in radial and across-track direction and 3 m along-track.

Using GEMT1, SEASAT area tables and daily drag coefficients, Wakker et al. (1987) obtained solutions with rms laser residuals of 48 to 62 cm.

Zandbergen et al. (1988) investigated the kind of accuracy that could be achieved by tailoring GEMT1 to SEASAT. In this exercise, crossover data were added to the laser data, because of the sparseness of the latter, and 360 coefficients were solved for. It was found that for 3 day arcs, using this tailored model, the radial orbit error is reduced to 30 cm rms, with laser range residuals from 28 to 45 cm. The same kind of accuracy could be obtained for ERS-1, the only difference being that GEMT1 is already a very accurate model for SEASAT, which is not true for ERS-1.

Using crossover differences, Marsh et al (1990a) predicted a radial error of 28 cm for SEASAT orbits computed with GEMT2.

Chapter 8 describes the work performed during this study on the determination of the SEASAT orbit by using GEMT1 and GEMT2.

ERS-1 simulations:

For ERS-1 several simulation studies have been done.

For arcs of 3 days, assuming a gravity field error model equal to 30% of the differences between GEM10 and GEM10B, Wakker et al. (1983a) estimated a global rms orbit error for ERS-1 of 0.6 m in the radial and across-track components and 2.4 m in along-track. Note that GEM10B (36 x 36 model), contains many coefficients which are not present in GEM10 (22 x 22 model).

For this satellite, long arc solutions are crucially dependent on the existence of a good tuned gravity field model, in which the unmodelled high order resonant coefficients are absorbed by the lower terms. The optimum accuracy of the long-arc orbits computed with this tuned model is expected to be 50-70 cm (rms range residuals). Provided this good tuned field giving rms range residuals of 50 cm is available, the expected rms radial error for ERS-1 is 30 cm (Sinclair, 1985).

The failure of the PRARE tracking system highly compromised the development of a precise tuned field for ERS-1. While this field is not available, the best geopotential models for this satellite are probably the models that include DORIS (Doppler Orbitography and Radiopositioning Integrated by Satellite) data. DORIS is an uplink Doppler tracking system that measures the satellite radial velocity relative to stations located at the Earth (Boucher and Dufour, 1992). It was used for the first time on the French remote sensing satellite SPOT2, a sunsynchronous satellite at 832 km altitude and an inclination of 98.7°. The system includes a dedicated tracking network of 50 fairly

well distributed stations, providing numerous data that can be used for gravity field determination.

Several geopotential models have been derived using DORIS data: GRIM4_S2 and GRIM4_C2 (Biancale et al, 1993), (see Table 4.1) and TEG-2B (Boucher and Dufour, 1992). Since these models include data from SPOT, which has an inclination very similar to that of ERS-1, they should give better results for ERS-1 than the GEMTn models.

Chapter 9 describes the work carried out during this study on the determination of ERS-1 orbit using GEMT2 and GRIM4_C2.

4.5 Use of altimetry as tracking data

Altimeter data alone can only be used to recover the radial component of the orbit error, as they lack information on the across-track component and give extremely weak along-track information. To be used in a global solution, they have to be mixed with other types of data.

With only one laser station no accurate orbit determination is possible, but one or two laser stations together with altimeter data may replace an extensive ground based tracking system (Wakker et al., 1983a). Orbits computed with only one laser station and crossover points are found to be as good as orbits computed with a full network of laser stations (Wakker et al., 1987).

The use of altimeter data to improve global orbit solutions has been investigated by several authors, using either dynamic (Wakker et al, 1987) or non-dynamic (Fernandes, 1988), (Goad et al, 1980), (Wakker et al, 1987) methods. Two main approaches are adopted: the use of altimeter measurements themselves, with appropriate sampling and filtering, and the use of crossover differences (Wakker et al, 1987), (Zandbergen et al, 1988).

Radial orbit errors are not random in nature but geographically correlated. This geographically correlated error is found to be latitude dependent and is believed to be, in an rms sense, half of the total error.

The use of crossover differences has the advantage that they are not affected by the large errors in modelling the mean sea surface (geoid errors). However, they do not allow the recovery of the geographically correlated part of the error because this is cancelled in the differencing process. Although the orbit error is the predominant part, they also contain tidal errors and time dependent oceanic effects (eddies, meanders, rings and atmospheric

storms). In the crossovers, the 1 cycle per revolution portion of the error is unobservable at the northernmost and at the southernmost latitudes but is perfectly observable at the equator. This is related to the way crossovers are formed. Also, crossovers that are formed at extreme latitudes have time lags that are almost exact multiples of one revolution and so there is no observability of the orbit error (Wagner, 1985). For frozen orbits ($\omega \approx \pi/2$, $\dot{\omega} = 0$) like SEASAT and ERS-1 orbits, there are further components of the orbit error that are unobservable in crossover differences: the constant offset, the 2 cycles per revolution term and the periodic zonal terms (Moore and Rothwell, 1990).

The use of filtered residual sea surface heights usually leads to an overestimation of the value of the radial orbit error because it tends to incorporate some geoid errors. On the contrary, crossover residuals lead to an underestimated value as they contain the geographically uncorrelated part of it. By using Legendre functions this geographically correlated error was found to be, for SEASAT, of the order of 50-80 cm radially (Wakker et al., 1987). The correlated and uncorrelated parts of the error are found to be, in an rms sense, of the same order (Zandbergen et al., 1988).

Engelis (1988) and Engelis and Knudsen (1989) used a combined solution where the stationary sea surface topography was simultaneously determined with orbit and long wavelength geoid improvement, by using both residual sea surface heights and crossover discrepancies. In these solutions the errors due to the geopotential are absorbed by the adjustment of geopotential coefficients. It was found that the total radial orbit error had an rms of 1.02 m. The main components of this error are a constant of about 85 cm and the error due to the geopotential, with an rms of about 40 cm. Excluding the constant correction, which is attributed to an error in the semi-major axis of the GRS80 ellipsoid, the rms of the remaining error is of the order of 50 cm. Using this method, the rms of crossover differences was found to go from a previous level of 90 cm to a level of 28 cm after the adjustment.

Marsh et al. (1990b) performed a simultaneous solution for the gravitational field (PGS3520), satellite orbit and the quasi-stationary surface topography using altimeter and conventional tracking data. SEASAT orbits computed in this solution have an estimated radial accuracy of 20 cm rms.

4.6 Spectrum of the orbital error

To establish optimum techniques for short arc determination, or for the analysis of altimetry data, an understanding of the spectrum of the ephemeris error is required.

The major errors are due to the gravity field. The spectrum of these errors can either be determined analytically (Figure 4.1) or by examining the differences of two orbits computed with two different field models (Figure 4.2). The second method is much more practical but lacks information on the part of the error that is common to both solutions.

The frequency spectrum for the gravity model induced orbit error spans resonant (secular), long period, daily, and short period terms of the order of one revolution (Tapley and Rosborough, 1985). Long period and resonant terms are usually absorbed by the solve-for parameters within the orbit determination process, provided that accurate tracking data are used. Consequently, the error in actual ephemerides has mainly short period and daily terms. The remaining error in a satellite ephemeris has a geographically correlated portion that does not average to zero. Using conventional orbit determination methods, this can only be removed from the ephemeris through gravity model improvement or through near continuous tracking.

In particular, the errors of any computed orbit along the TAR directions have a major variation with time that is approximately periodic with a period of one orbital revolution (Figures 4.3 and 4.5). The reason for this is that the osculating elements can in principle be represented as arbitrary constants plus forced periodic and secular terms. Errors in the force model lead to errors that have a wide range of periods, but when they are expressed as TAR variations they are close to the orbital period (Sinclair, 1989). In addition to this, in the orbit determination process, the adjusted parameters will have errors as they absorb errors due to the force model. These errors cause orbit errors which in the TAR directions are exactly 1 cycle per revolution. Along with this dominant 1 cycle per revolution term, the along-track error has a much wider spectrum, with many significant terms of long wavelength.

Engelis (1988) gives a detailed analytical analysis of the radial orbit error. The radial error from gravitational origin has frequencies that are a linear combination of the orbit frequency $\dot{\omega} + \dot{M}$ (one cycle per revolution), the apsidal frequency $\dot{\omega}$ of a complete revolution of the perigee, and the frequency $\dot{\Omega} - \dot{\theta}$ of a complete rotation of the Earth with respect to the precessing orbital plane. This error is mainly periodic with frequencies close to 1 and 2 cycles per revolution with time independent amplitudes, 1 and 2 cycles per revolution with amplitudes linearly increasing with time, many long wavelength terms of frequencies between zero and two cycles per revolution and a constant bias term.

Errors due to initial state errors have the same form and opposite sign to these errors and are a function of the constants of integration. If the observations to the satellite are global and very accurate, these errors can be simultaneously removed during the adjustment of the initial state vector. Similarly, resonant errors are likely to be absorbed by drag

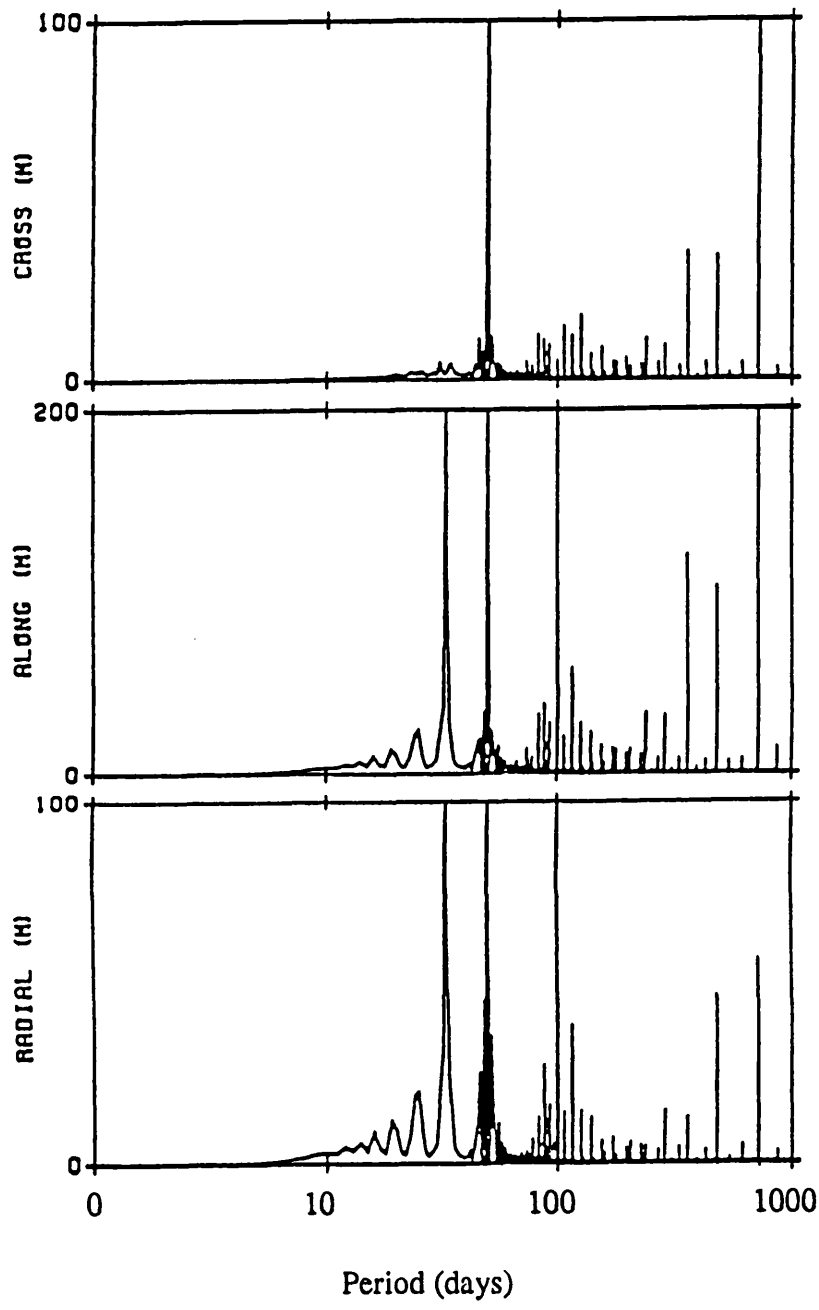

Figure 4.1 - Amplitude spectrum of ERS-1 radial cross-track and along-track gravity field perturbations. Extracted from (Wakker et al, 1983a).

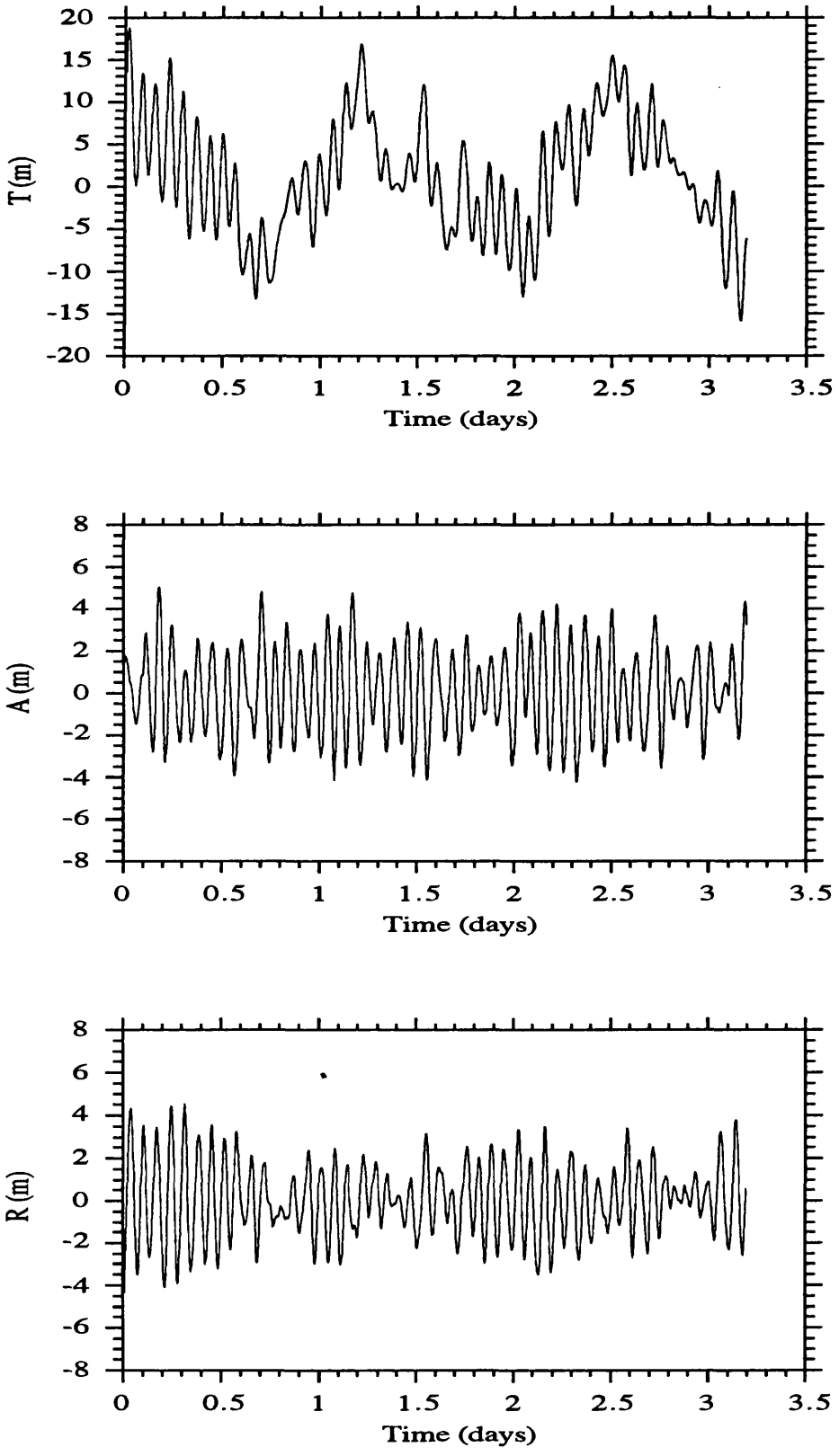

Figure 4.2 - ERS-1 differences along the T A R directions for the GRIM4 C2 versus GEMT2 gravity field models. Computed using the model described in Table 9.1.

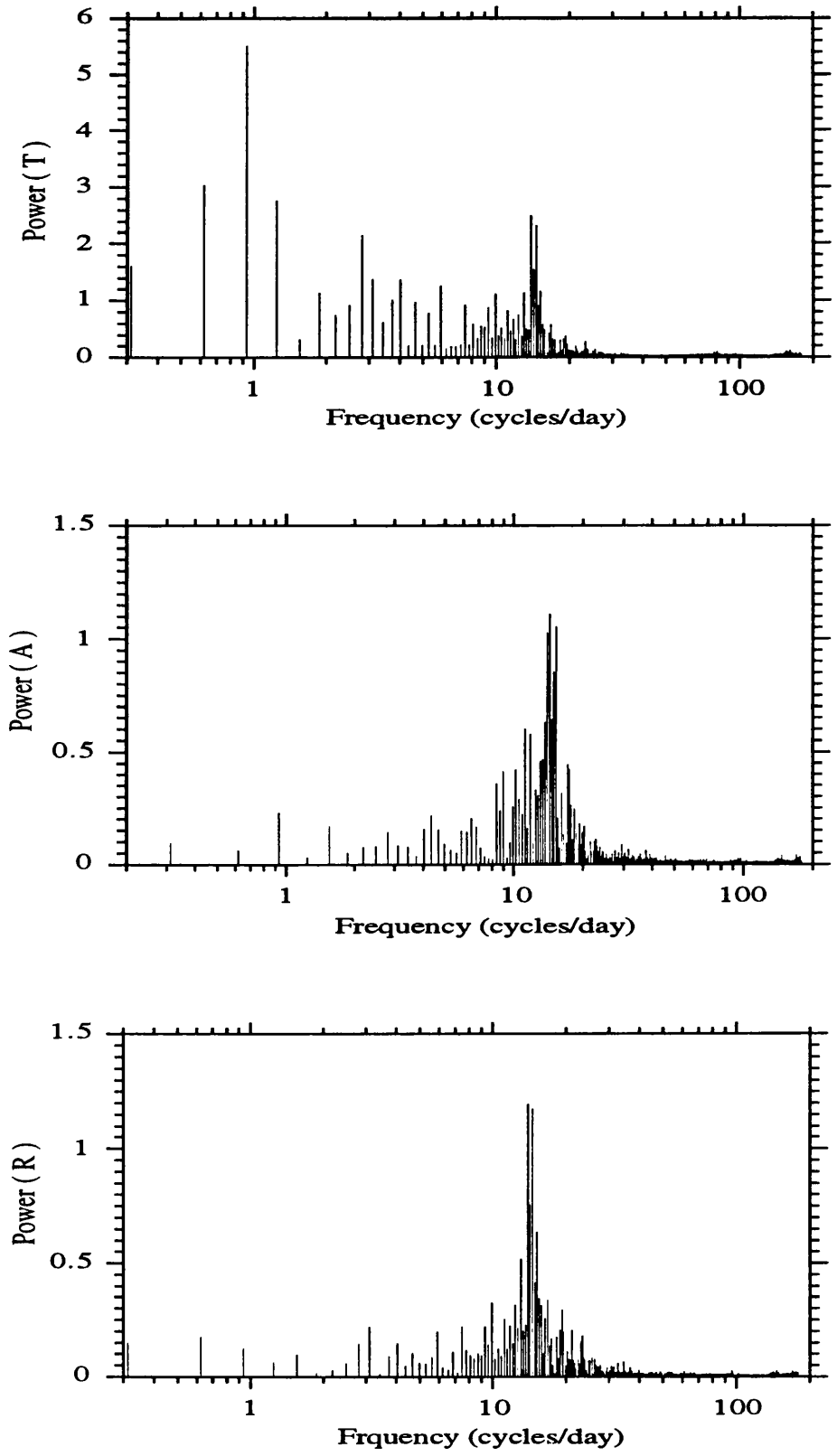

Figure 4.3 Amplitude spectrum of the T A R differences between two ERS-1 orbits (GRIM4 C2 versus GEMT2).

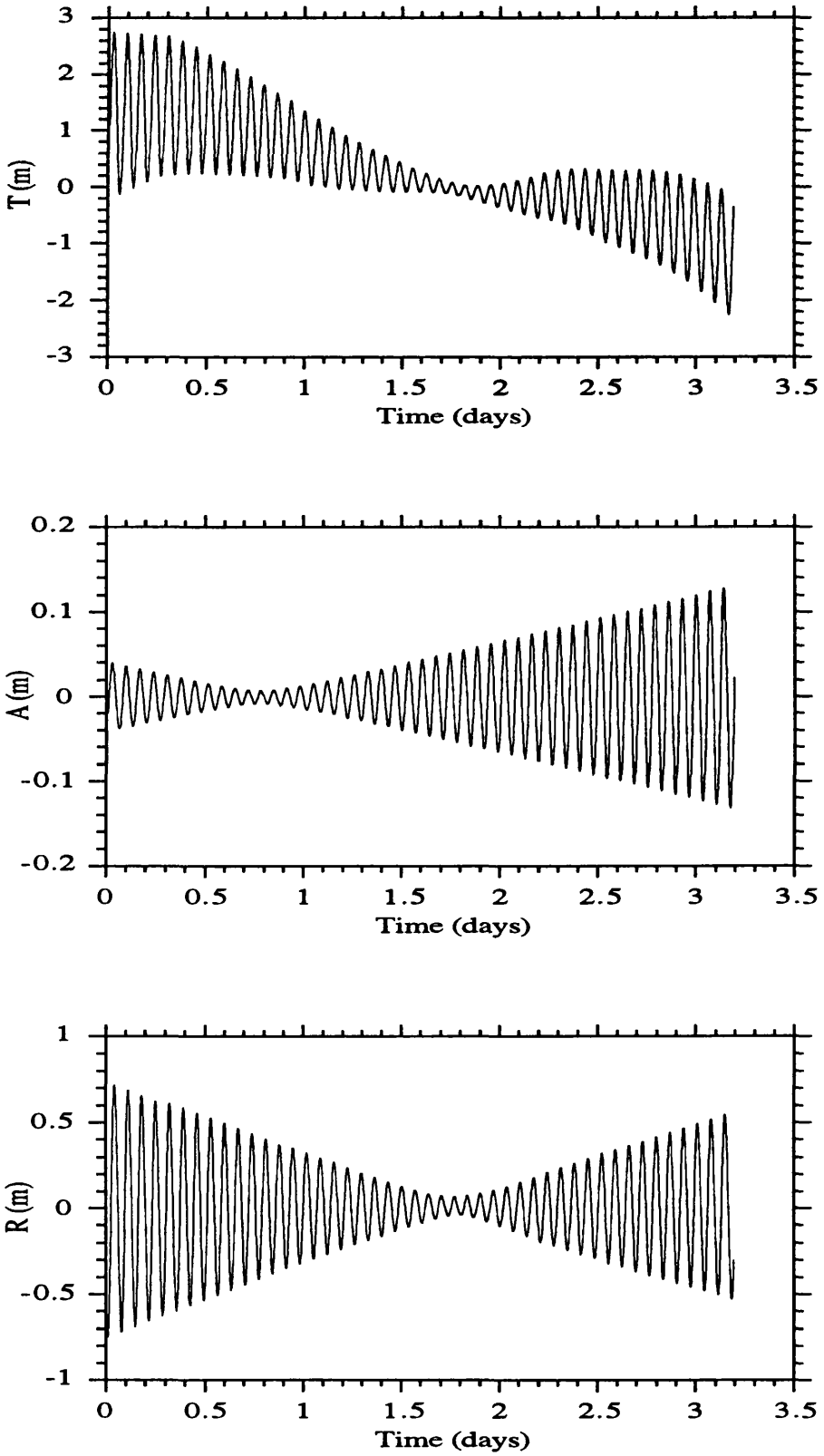

Figure 4.4 - ERS-1 differences along the T A R directions for atmospheric drag modelled with a variable cross-sectional area versus a constant area. Computed using the model described in Table 9.1.

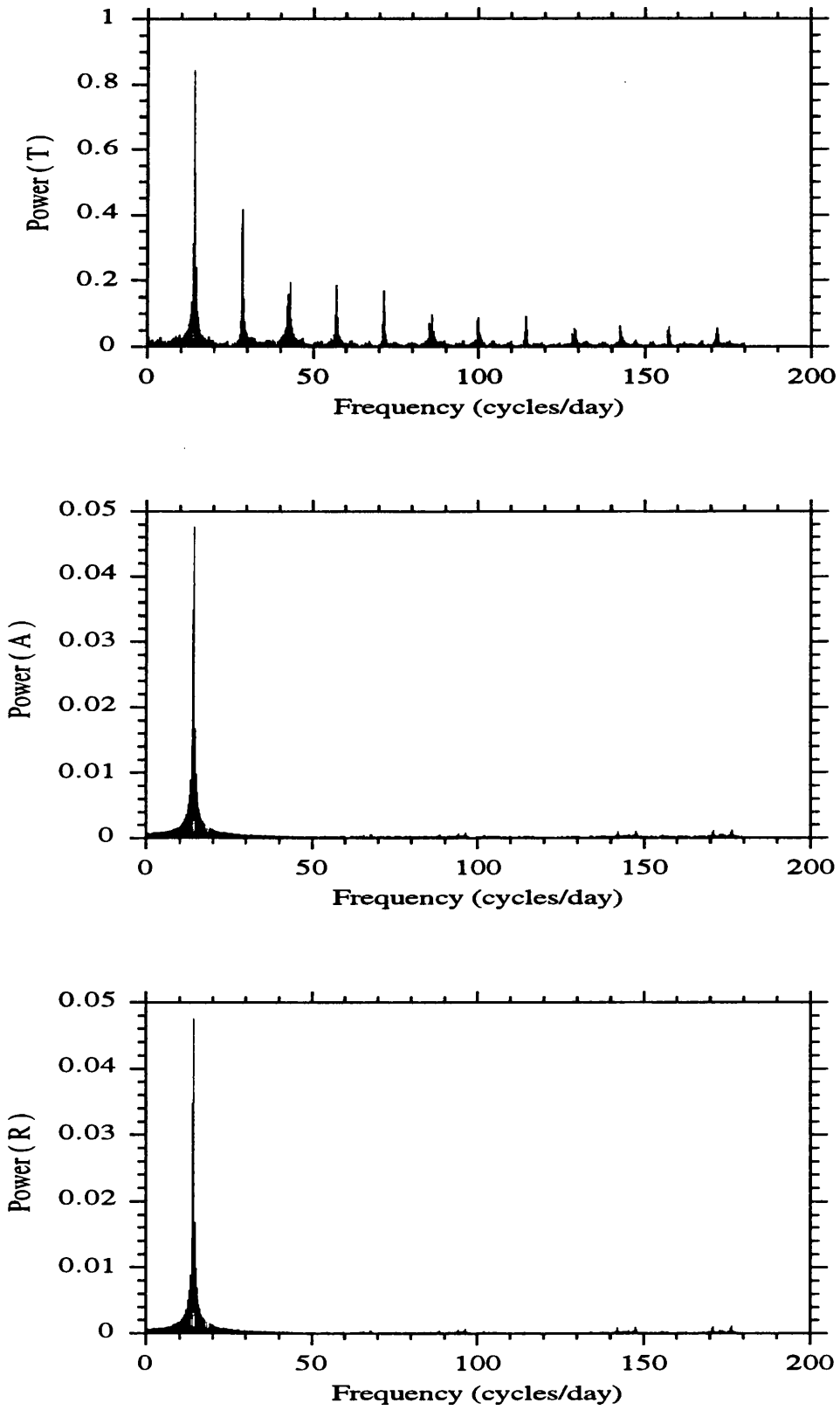

Figure 4.5 Amplitude spectrum of the T A R differences between two ERS-1 orbits (atmospheric drag modelled with a variable cross-sectional area versus a constant area).

parameters that are estimated during the adjustment. In practice, 1 cycle per revolution errors of constant and time dependent amplitudes remain after the adjustment. Residual drag and resonant errors often exhibit a signature (bow-tie pattern) that is zero at the middle of the arc and is maximum at its extremities (Figure 4.4).

Moore and Rothwell (1990) present a detailed analytical analysis of the radial error due to gravitational and non-gravitational origin, with application to altimeter crossover differences. For the gravitational error, the conclusions are similar to the results by Engelis (1988). The error due to air drag is dominated by a quasi secular change in the radial distance **r**, with a small sinusoidal term of increasing amplitude superimposed. For radiation pressure the errors are similar to drag errors but the sinusoidal term is more significant.

If inadequate tracking data are used to determine an orbit, the major discrepancies (compared to the optimum orbit for the force model being used) will be of the orbital period. In particular, the radial error is always close to the orbital period, whether it is caused by an inadequate force model or insufficient data. This is why short arc extrapolations have to be very limited: although the radial error can be made very small locally, within a quarter of a revolution it will have increased to its maximum (Sinclair, 1985).

Chapter 5

ERS-1 and SEASAT

5.1 Introduction

At the time of the beginning of this study, ERS-1 had not yet been launched. SEASAT was the satellite closest to ERS-1 with regard to the type of orbit and characteristics of the measuring instruments, and with easily available data. Therefore, the first part of this study (Chapters 8 and 10) was concerned with the computation of SEASAT's orbit, as a preparation for the subsequent work on the determination of the orbit of ERS-1 (Chapter 9).

This chapter describes and compares the characteristics of these two satellites with respect to the parameters that are relevant for orbit determination.

5.2 ERS-1

5.2.1 Mission objectives

ERS-1 was launched from Kourou, in French Guiana, aboard Ariane flight V44, on 17 July 1991. It is the European Space Agency's first satellite devoted entirely to remote sensing from a polar orbit. It provides global and repetitive observations of the environment using advanced microwave techniques, which enable measurements and imaging to take place independently of weather or sunlight conditions.

The main objectives of the mission are (Duchossois, 1991) and (Francis et al., 1991):

- to increase our understanding of ocean-atmosphere interactions with the aim of deepening our knowledge of climate.
- to determine improved weather and sea-state forecasting.
- study ocean circulation and transfer of energy.
- to determine reliable estimates of the mass balance of the Arctic and Antarctic ice sheets.
- monitor the dynamic coastal processes and pollution.
- improve detection and management of land use change.

• develop land applications such as forest or geological mapping, or crop monitoring and snow and ice studies.

5.2.2 Spacecraft and instruments

The satellite is tailored around a multipurpose platform developed in the framework of the French SPOT programme, with some modifications to meet the unique needs of the ERS-1 mission. The platform provides the major services for the satellite and payload operation, in particular attitude, orbit control, power supply and telecommunications with the ground segment.

The principal constituents of the ERS-1 payload are active microwave instruments. To sense the Earth from a mean altitude of 780 km, powerful radar pulses are needed, to provide sufficient illumination of the Earth's surface and produce detectable echo signals. Therefore the satellite has to be very large with large antennae.

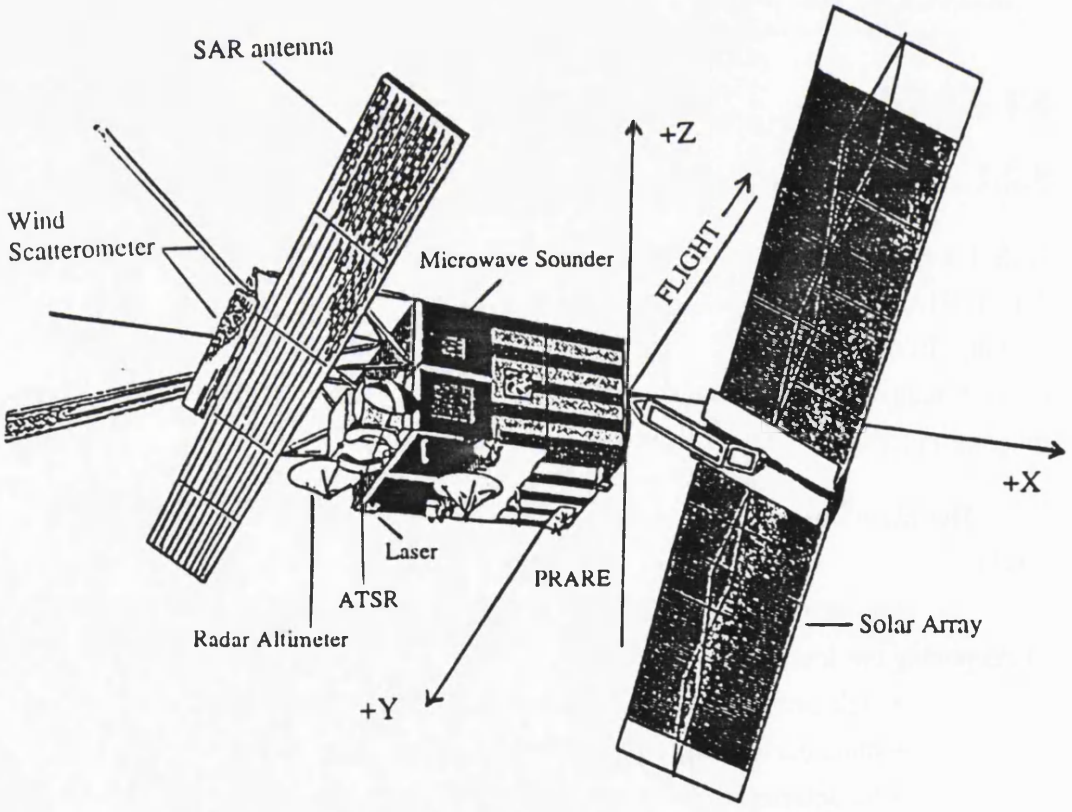

Figure 5.1 - The ERS-1 Spacecraft

The satellite shape is very irregular and complex as shown in Figure 5.1, weighing about 2400 kg and measuring 12m x 12m x 2.5m (ESA, 1992). The main payload support structure has a 2m x 2m base and is some 3m high (Frances et al, 1991). The largest of the sensors, the Synthetic Aperture Radar has a 10 m long antenna.

To generate enough electrical power for all the mission operations a 12m x 2.4 m solar array is included. During the 66 minutes sunlit period of each orbit, the solar array provides electrical power to all the onboard systems. It also charges the spacecraft's batteries, so that they can provide the energy necessary for payload operations during the 34 minutes eclipse period.

To fulfil the objectives of the mission, the satellite carries a set of five main instruments (ESA, 1992):

1 - An Active Microwave Instrument (AMI), operating in C band (5.3 GHz). It can operate in one of the three modes: image mode, wave mode or wind mode. To perform these functions, two separate radar instruments are incorporated:

• A Synthetic Aperture Radar (SAR) which can operate in one of the two modes:

i) **Image mode**, generating two dimensional images, 100 km in width, displaced 250 km to the right of the sub satellite track (Figure 5.2). The SAR 10m x 1m antenna is aligned parallel to the satellite track and has a viewing direction that is offset by 23° from the (-Z) axis towards the (-X) axis. The antenna directs a narrow radar beam onto the Earth's surface. An image is build up from the time delay and strength of the return signals, which depend mostly on the roughness and dielectric properties of the surface and its range from the satellite. The spatial resolution of these images is 30 m in range and between 8 and 30 m in azimuth.

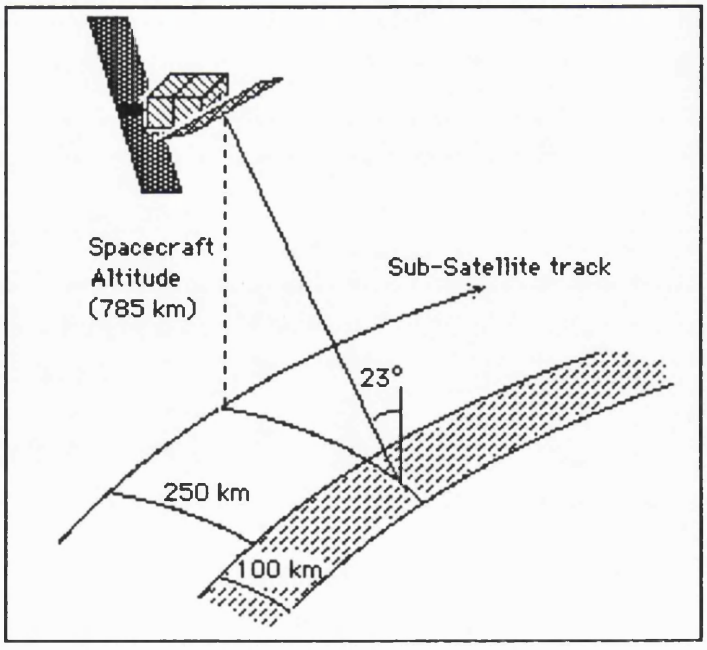

Figure 5.2 - SAR imaging geometry

The SAR's range resolution is obtained from the travel time of the transmit pulse by phase coding the pulse with a linear chirp, and compressing the echo by matched filtering. Azimuth resolution is achieved by recording the phase as well as the amplitude of the echoes along the flight path. The set of the echoes over a flight path of about 800 m will be processed (on the ground) as a single entity, giving a resolution equivalent to a real aperture 800 m in length (the "synthetic aperture" of the radar).

ii) **Wave mode**, to derive wave spectra from small SAR images (5 x 5 km) at intervals of 200 km along track.

• A Wind Scatterometer, to measure wind speed and wind direction over ocean. It uses three sideways looking antennae, one pointing normal to satellite flight path and the other two pointing 45° forward and backwards, respectively. These antennae continuously illuminate a 500 km wide swath providing measurements of radar backscatter from the sea surface on a 25 km grid.

Because of the high data rate generated (100 Mbit/s), the AMI can only operate in the image mode for about 10 minutes per orbit. The wind and wave modes however, are capable of interleaved operation, the so-called wind/wave mode.

2 - A Radar Altimeter (RA), operating in the Ku band (13.7 GHz), with nadir pointing, to measure echoes from ocean and ice surfaces. It has two measurement modes, optimised for measurements over ice and ocean respectively. In the ocean mode it is used to measure altitude, significant wave height and ocean surface wind speed. In the ice mode the instrument operates with a coarser resolution, providing information on ice sheet surface topography and sea/ice boundary. The height measurement precision is less than 10 cm when averaged over 1 second. More detail on this instrument is given in Chapter 7.

3 - An Along Track Scanning Radiometer and Microwave Sounder (ATSR-M), a passive instrument consisting of an advanced four channel infrared radiometer (IRR) and a two channel nadir viewing Microwave Radiometer (MWR), designed to determine:

• Infrared Radiometer: sea surface temperatures; cloud top temperatures; cloud cover and classification; land, sea and ice surface radiance.

• Microwave Sounder: total atmospheric water content; liquid content and rain areas; land and ice surface emissivity.

4 - A Precise Range and Range Rate Equipment (PRARE), an active microwave instrument to allow for precise tracking of the satellite, and ionospheric correction of the altimeter signal. Unfortunately, the PRARE suffered fatal damage to the Random Access

Memory, due to radiation after a few hours of nominal operations. An improved version of PRARE is being built for ERS-2. Chapter 6 gives detailed information on this instrument.

5 - A Laser Retro-Reflector array (LRR), a passive optical device operating in the infrared, to allow for very accurate laser tracking of the satellite from ground stations. It is mounted on the Earth-facing side of the spacecraft and consists of an array of corner cubes, one nadir-looking in the centre, surrounded by an angled ring of eight corner cubes.

5.2.3 Mission phases

The ERS-1 mission is sub-divided into six main phases (ESA, 1992) and (Louet and Francis, 1992):

- orbit acquisition
- commissioning phase
- first ice phase
- multi-disciplinary phase
- second ice phase
- geodetic phase

During each phase, the main parameters and characteristics of the mission are kept unchanged. The transition between different phases is accomplished by a number of manoeuvres to adjust the orbital pattern to the various requirements for ground coverage.

• The Launch and Early Orbit Phase (LEOP) took place during the first two weeks after launch.

• The Commissioning Phase took place during the first 5.5 months of the mission, immediately after the LEOP. During this period the so-called Venice orbit was used, providing a 3-day repeat cycle passing over the city of Venice, selected for the Radar Altimeter's calibration. The main goals during the commissioning phase were to:

- calibrate and validate the on-board instruments
- phase-in and commission the near-real-time ground segment components.

• During the Ice Phases a 3-day repeat orbit is still used, but with a slightly different longitudinal phase, selected especially for the ice experiments to ensure highly repetitive coverage of ice zones during Arctic winters.

Table 5.1
Timetable for ERS-1 mission phases

Phase	Repeat Cycle (days)	Start	End
Commissioning	3	03 / 08 / 91	10 / 12 / 91
First Ice	3	28 / 12 / 91	30 / 03 / 92
Multidisciplinary	35	15 / 04 / 92	31 / 12 / 93
Second Ice	3	01 / 01 / 94	31 / 03 / 94
Geodetic	176	15 / 04 /94	___

• The Multi-disciplinary Phase corresponds to a period where the satellite is in a 35-day repeat cycle orbit. During this period the SAR will be capable of imaging any part of the world within station coverage, and the density of the altimeter tracks increases to give a separation between ground tracks of just 39 km at 60° latitude.

• The Geodetic Phase will take place only at the end of the mission. A repeat cycle of 176 days will be used allowing the acquisition of high density altimeter measurements, aiming at a better determination of the geoid over the oceans.

The timetable for the first mission phases is presented in Table 5.1 (ESA, 1992)

5.2.4 ERS-1 orbit

ERS-1 is in a near circular, polar, sunsynchronous orbit with a mean altitude of 780 km and an inclination of 98.5 degrees. This high inclination has been selected to give the satellite visibility of all areas of the Earth as the planet rotates beneath its orbit.

The characteristics of the three main types of orbits used during the ERS-1 mission are presented in Table 5.2 (ESA, 1992).

For the spacecraft to be in a periodic motion relative to the rotating Earth the satellite orbital period must be a rational fraction **n/m** of the Earth's spin period (Rosengren, 1992). After **m** spacecraft orbits and **n** Earth rotations, the satellite will be back over the same point. For ERS-1 the orbital periods of 3/43 and 35/501 days have been selected.

For the 3-day repeat cycle, at the equator, each successive track is displaced 2796 km west of the previous one. Every day the satellite begins a new cycle of passes, which are displaced 932 km from the previous day cycle (Figure 5.3). The 35-day repeat cycle results in an adjacent crossing of the equator of only 80 km thus allowing a much finer coverage (Figure 5.4). The orbital parameters are maintained to ensure the ground track repeatability to within ±1 km at any point in the orbit.

Table 5.2
ERS-1 Orbit characteristics

	Commissioning Phase	**Ice Phases**	**Multi-disciplinary Phases**
Repeat cycle	3 days	3 days	35 days
Semi-major axis (km)	7153.138	7153.138	7159.496
Inclination	98.516°	98.516°	98.543°
Mean altitude (km)	785	785	782
Orbits per cycle	43	43	501
Ascending node reference	24.36°E	128.02°W	20.96°E
Mean local solar time at descending node (± 1 min.)	10h 30m	10h 30m	10h 30m

The combination of ERS-1 inclination and mean altitude causes the orbit to be retrograde, with a period close to 100 minutes.

Orbital parameters have been selected to provide an orbit in which there is no precession of the perigee, i.e., the argument of the perigee is kept fixed at a mean value of 90°. Such an orbit with a small eccentricity and perigee over the North pole is called a frozen orbit.

The ERS-1 orbit is sun-synchronous, i.e., the precession of the orbit caused by the non-spherical components of the Earth's gravity field, exactly opposes the mean angular rate of the Earth in its orbit around the sun. Consequently the orbital plane will always maintain its position relative to the mean sun, crossing the equator with the descending node at 10:30 am ± 1 minute mean local time.

However the direction of the true sun relative to ERS-1 orbit plane varies along the year due to two main factors. First, the movement of the Sun relative to the Earth takes place in a plane (the ecliptic) which is inclined by 23°.4 relative to the equator. Secondly,

Figure 5.3 - ERS-1 ground tracks for the 3-day repeat orbit.

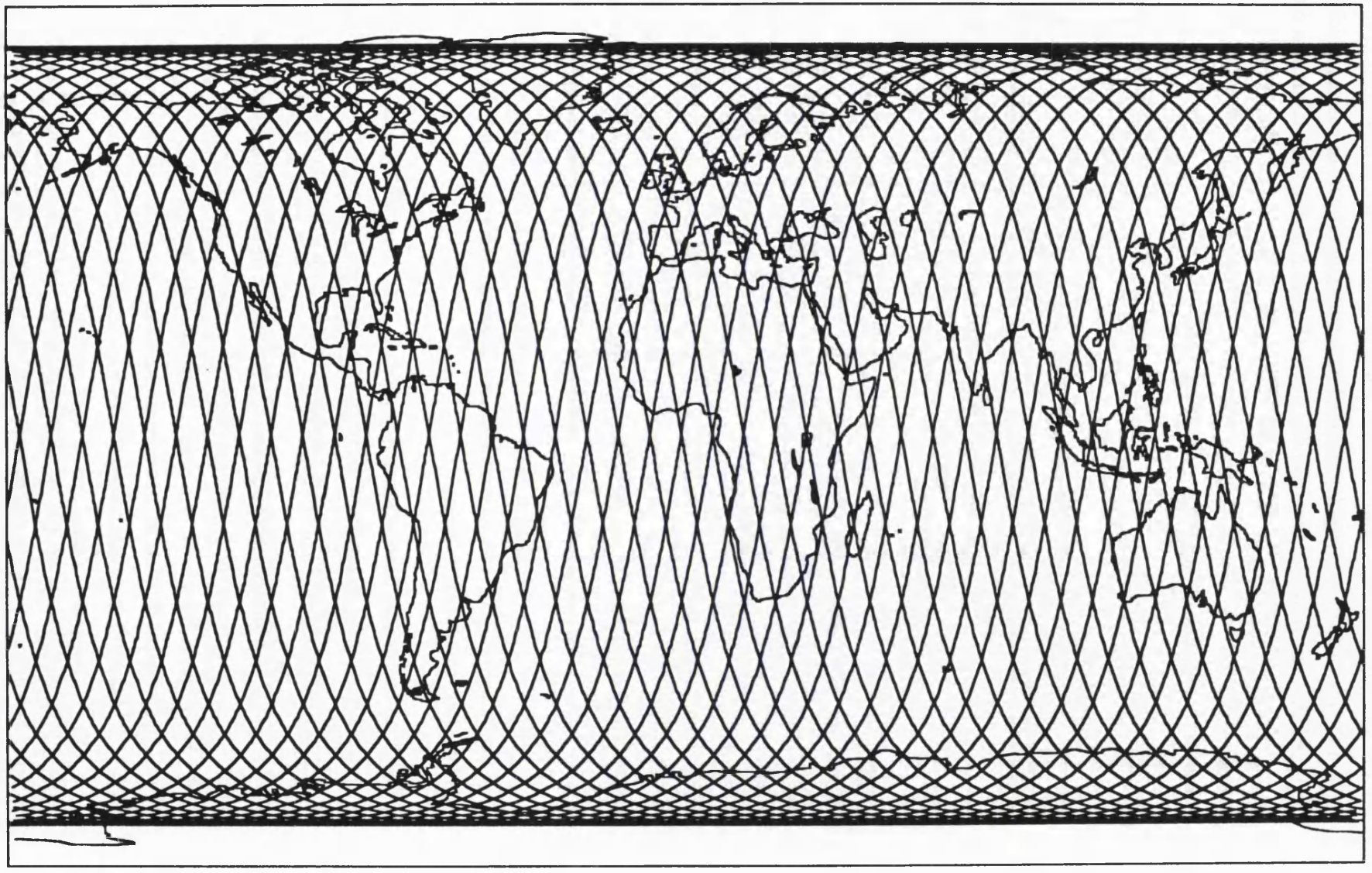

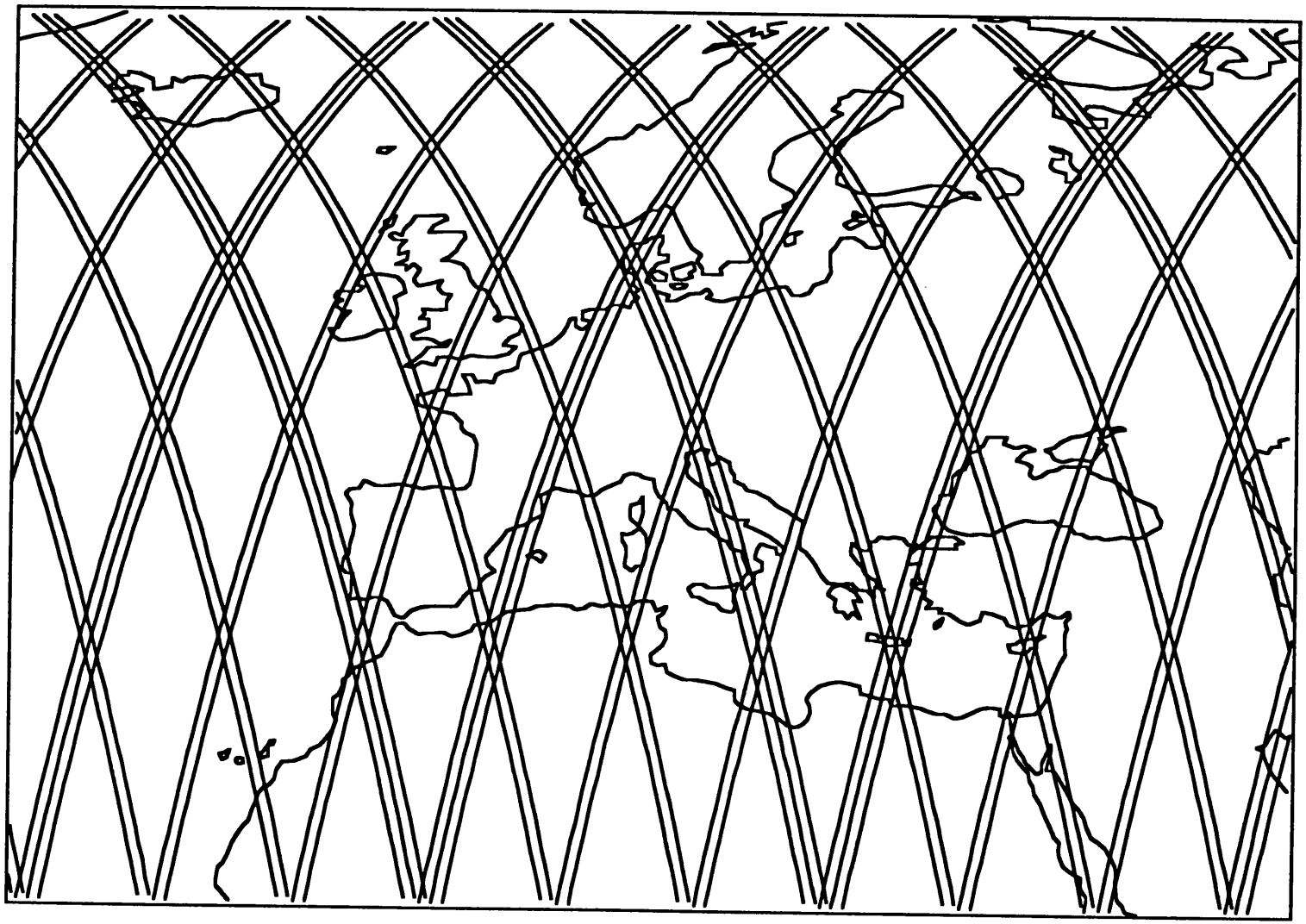

Figure 5.4 - ERS-1 ground tracks over Europe for the 35-day repeat orbit

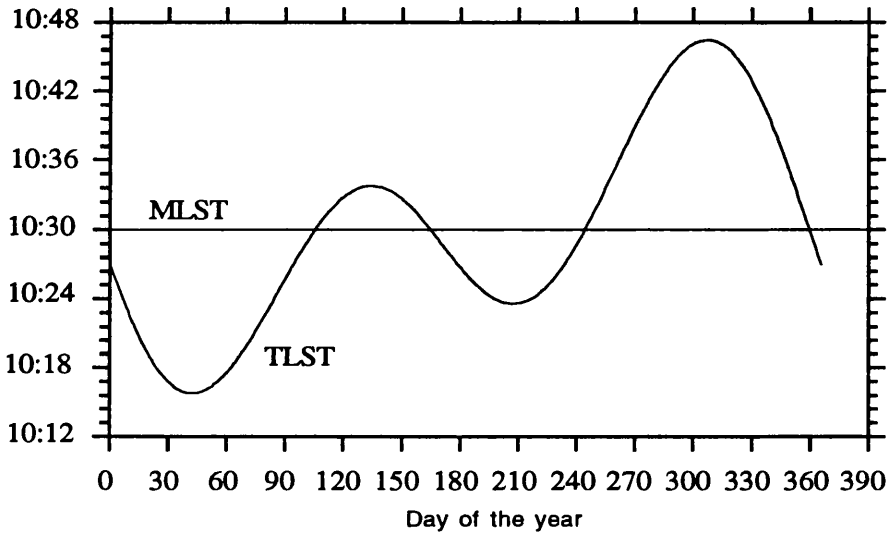

Figure 5.5 - Annual variation of the True Local Solar Time at ERS-1 descending node (in hours).

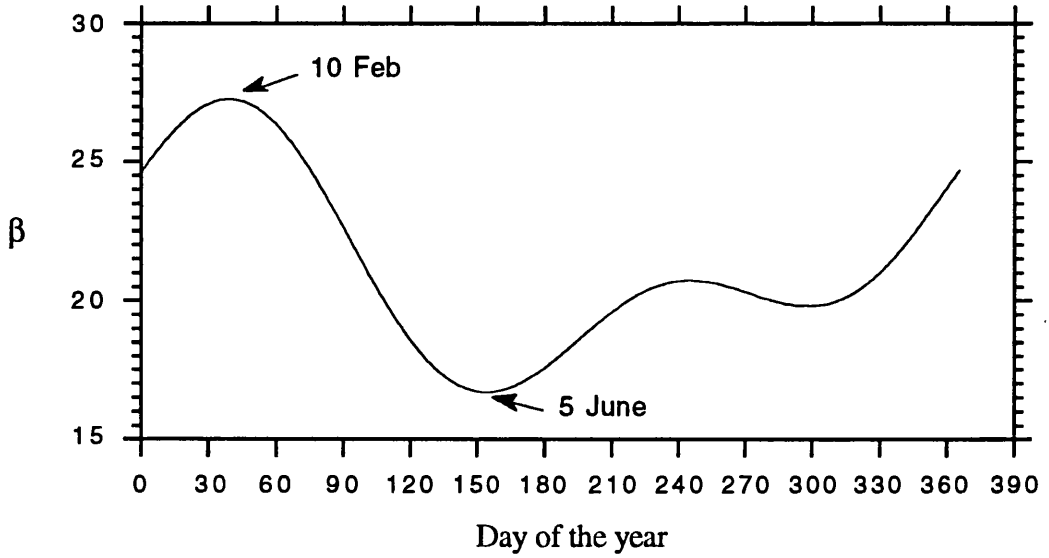

Figure 5.6 - Annual Variation of the angle β between the direction of the Sun and ERS-1 orbit plane (in degrees).

because the velocity of the sun relative to the Earth is not constant, the hour angle of the true sun departs from the hour angle of the mean sun by an amount given by the so called "Equation of Time", which amounts to ±15 minutes. Therefore the true local solar time at the descending node (TLST) is not equal to the constant value of the Mean Local Solar Time (MLST) but has an annual variation of ±15 minutes (Figure 5.5).

$$TLST = MLST + \text{Equation of Time} = 10h\ 30m + \text{Equation of Time}$$

In consequence of these movements the inclination of the sun relative to the ERS-1 orbital plane has an annual variation with minimum 17° at the beginning of June and maximum 27° at the beginning of February (Figure 5.6). Therefore the spacecraft solar array needs only be rotated about one axis (the spacecraft X axis, normal to the orbit plane) to maintain pointing to within 5° of the Sun's direction. During each orbit the solar array rotates through 360° with respect to the satellite, around the X axis, to maintain its Sun pointing. This information is important for the modelling of the cross-sectional areas for atmospheric drag and radiation pressure, as will be discussed in section 9.2.4.

5.2.5 ERS-1 attitude system

ERS-1 is a three-axis stabilised earth pointing spacecraft (Figures 5.1 and 5.7)

The attitude control system orientates the yaw (+Z) axis towards the local vertical (geodetic pointing with respect to the reference ellipsoid) and the pitch (X) axis normal to the instantaneous ground velocity vector (and not normal to the instantaneous orbital velocity vector, as in the previous Earth satellites). The (-Z) axis and therefore the Radar Altimeter and the ATSR-M are directed towards the sub satellite nadir point relative to the Earth's surface (Rosengren, 1992).

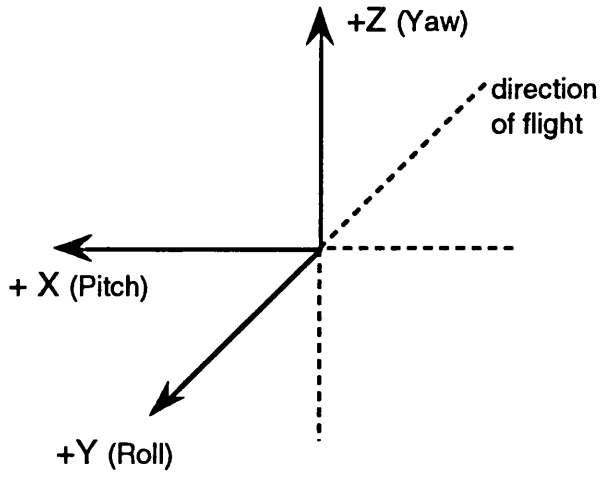

Figure 5.7 - ERS-1 Satellite Fixed Reference System

The (-Y) face of the spacecraft is in the "forward" direction, i.e., the direction of motion of the sub satellite point relative to the Earth's surface. This attitude control technique, called yaw steering mode, has been selected to provide

more favourable conditions for the operation of the AMI in the wind mode. In this way the AMI SAR antenna and AMI wind mode mid-beam boresight are looking towards the zero Doppler line.

The direction of the pitch axis oscillates slightly during each orbit, to keep it oriented normal to the composite ground velocity vector, taking into account the Earth's rotation.

Table 5.3
Attitude accuracy for ERS-1

	Pitch	**Roll**	**Yaw**
Bias and long-term drift	0.11°	0.11°	0.21°
Harmonic and random	0.03°	0.03°	0.07°

The attitude accuracy is as specified in Table 5.3 (ESA, 1986). Absolute rate errors in each platform axis are less than 0.0015 °/sec over all frequencies.

ERS-1 has a range of attitude sensors (Francis et al, 1991). The long term reference in pitch and roll are obtained from an infrared Earth sensor. The yaw steering is obtained once each orbit from a narrow-field sun sensor aligned to point at the sun as the satellite crosses the day/night terminator. The short term attitude and rate reference are obtained from an inertial platform, with a pack of three gyroscopes. In addition the spacecraft possesses two wide-field sun acquisition sensors for use in the initial stages of attitude acquisition, and in safe mode, when the satellite is in sun rather than in Earth pointing (Francis et al, 1991).

5.3 SEASAT

5.3.1 The SEASAT spacecraft and instruments

SEASAT was the first satellite to assess the value of microwave sensors for remote sensing of the oceans. It was launched on June 27, 1978, and operated only until October 10, when a short circuit in the power system occurred.

A simple comparison of Figures 5.1 and 5.8 shows that SEASAT and ERS-1 spacecraft have significantly different shapes. SEASAT was a modified version of the Agena

system that has been extensively used for Earth-orbiting missions (Born et al, 1979). It is basically a cylinder with large appendages. The satellite is about 13 m long and weights about 2195 kg. The largest of the sensors, the SAR antenna is 10.7 m long by 2.2 m wide. The spacecraft includes two 7.4 m^2 solar panels.

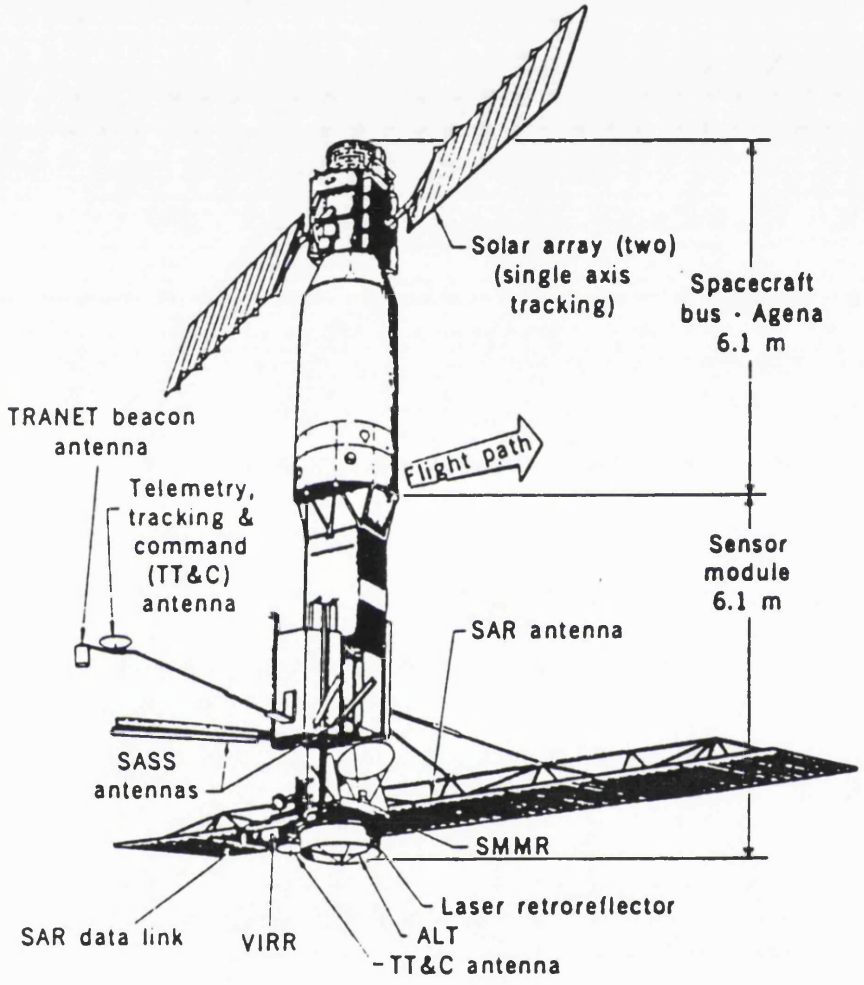

Figure 5.8 - SEASAT Spacecraft. Extracted from (Tapley and Born, 1980).

By comparison, ERS-1 could be described as a box with external payloads and large panels. The dimension of this main box (platform + payload) is 2 m x 2 m x 3 m. The ERS-1 SAR antenna has dimensions (10 m x 1 m) similar to SEASAT SAR, but the solar panels are considerably larger, each covering an area about 14 m^2. Due to its highly irregular shape, ERS-1's cross-sectional area for the surface forces, in particular for atmospheric drag, will exhibit a much wider variability than for SEASAT (cf. section 9.2.4).

The SEASAT spacecraft included five sensors. The first three were active radar instruments, the last two, radiometers:

1 - Radar Altimeter - a nadir viewing instrument to measure altitude above mean sea level, significant wave height and wind speed at nadir. The precision of altitude measurement is about 10 cm for 1 second averaged data. Detailed information on this instrument is given in Chapter 7.

2 - Synthetic Aperture Radar (SAR) - an active imaging system operating in the L band (1.275 GHz) to derive wave spectra. The SAR antenna was oriented along track, which resulted in a ground swath 100 km wide, centred 23° off nadir.

3 - Microwave Scatterometer - an active microwave sensor to measure surface wind speed with an accuracy of ±10 cm, and wind direction with an accuracy of ±20°.

4 - Scanning Multichannel Microwave Radiometer (SMMR) - to determine sea surface temperature, surface wind speed and atmospheric water content.

5 - Visible and IR Radiometer- a passive imaging system to measure sea surface and cloud top temperatures, and to identify cloud, land and water features.

The SEASAT tracking systems included: a unified S band transponder, a TRANET Doppler beacon, and a laser retro-reflector array (Wakker et al, 1983b). A total of 14 laser stations have tracked SEASAT, but some of them produced a reduced set of passes or passes with significant data problems (Wakker et al, 1987).

5.3.2 SEASAT orbit and attitude system

The SEASAT orbit was near circular, with an altitude of about 800 km, a period of 101 minutes and an inclination of 108 degrees.

During the SEASAT mission two orbit cycles were used. From July 3 to August 17 a near 17 day repeat cycle was used, with a semi-major axis of 7166 km, giving an equatorial spacing between adjacent tracks of 165 km. During the period August 18 to September 10 the satellite was manoeuvred into a 3 day repeat cycle orbit, with a semi-major axis of 7172 km, an argument of perigee of 90° (frozen orbit), and an equatorial spacing of 932 km. The satellite remained in this orbit until its failure.

Table 5.4 compares some characteristics of the SEASAT and ERS-1 3-day repeat orbits and ground track patterns. It is obvious that there is a great similarity between these orbits. The major difference is that SEASAT's orbit has a smaller inclination and is not

sun-synchronous. The maximum latitudes covered by SEASAT and ERS-1 are 72° and 81°.5 respectively, showing that ERS-1 allows a better sensing of the polar regions.

Table 5.4
SEASAT and ERS-1 mean orbital elements
for the 3-day orbit

	SEASAT	**ERS-1**
semi-major axis (km)	7169.0	7153.1
inclination (deg)	108.0	98.5
eccentricity	0.0008	1.165×10^{-3}
nodal period (min.)	100.8	100.5
revolutions per day	14 1/3	14 1/3
argument of perigee	90	90
ω rate (°/day)	- 1.7	0
Ω rate (°/day)	2.04	0.986
eq. spacing between successive tracks	2796 km	2796 km
eq. spacing between adjacent tracks	932 km	932 km

One consequence of the 10 degrees difference in the inclination, is that the satellites are sensitive to different coefficients of the geopotential. Therefore a tuned field for SEASAT such as GEMT2 (tuned in the sense that incorporates SEASAT's own data) is not necessarily an accurate model for ERS-1.

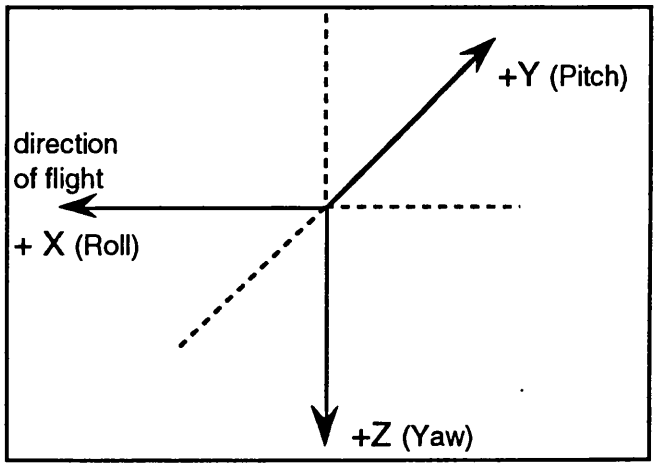

Figure 5.9 - SEASAT Attitude Reference System

The SEASAT attitude reference system (Figure 5.9) is a geodetic, orthogonal reference set (X, Y, Z) with origin at the satellite centre of mass where:

- Z - axis is perpendicular to the reference ellipsoid at the sub-satellite point, positive toward nadir.

- X - axis is defined by $(\vec{r} \times \dot{\vec{r}}) \times \vec{Z}$ where $\vec{r}$ is the radius vector of the satellite toward the geocentre.

- Y - axis completes the right-hand coordinate set.

This attitude system is similar to ERS-1's system when the satellite is in the fine pointing mode.

Chapter 6

PRARE and Laser Data

6.1 PRARE System Description

This chapter describes the PRARE and laser tracking systems and the process used in this study to simulate PRARE data for SEASAT.

PRARE (Precise Range and Range Rate Equipment) is a new tracking system designed to be tested on ERS-1 for the first time (Hartl et al., 1984). Unfortunately, the instrument was damaged by radiation soon after launch and could not be recovered. However, this does not invalidate the study being done on PRARE simulated data, as a new instrument (PRARE-2) is being built for ERS-2.

It is a space-based two-way, two-frequency range and range rate measurement system.

Two microwave signals are sent to Earth from the satellite, one in S band (2.2 GHz), the other in the X band (8.5 GHz). Because the S band signal is more affected by the ionosphere than the X band, it encounters a different time delay. The difference in the time delay, in the reception of the two simultaneously emitted signals, is measured at the ground station. Here it is transmitted to the on board memory where it is used to calculate the ionospheric correction and applied to the data.

At the ground station the X band signal is transposed to 7.2 GHz and retransmitted to the space segment, to determine on board the two-way signal delay. This time delay is used to calculate the two-way slant range between ERS-1 and the ground station. In addition, the received carrier frequency is evaluated in a Doppler counter, to derive the relative velocity of the spacecraft to the ground station (range rate).

Together with the ionospheric delay data, meteorological ground data are also sent with the up-link signal to calculate the tropospheric correction.

The PRARE system consists of three components (Wilmes at al., 1987):

- the space segment -with minimum interface to the spacecraft
- the ground segment - the network of ground tracking stations
- the control segment - the master station for control operations, data transfer to and from the spacecraft payload and for processing of the tracking data.

The ground stations are small transportable units with a parabolic dish antenna of 60 cm diameter. Four ground stations can be served simultaneously. To allow the tracking of more than four stations in any coverage zone, time multiplexing is used. More than 15 PRARE stations were expected to be tracking ERS-1. Due to the system failure all this planning will have to be postponed to ERS-2.

The main advantages of PRARE over conventional systems are:

- the smaller, easily transportable and fully automatic ground stations
- use of very high frequencies which accounts for the extreme accuracy
- use of PN- codes (pseudo random noise) for signal modulation, which brings a high accuracy, operational flexibility and leads to wide band system
- the use of two-way ranging allowing for better compensation for propagation effects
- the use of two frequencies allowing the correction for ionospheric effects
- the all weather capability

The estimated accuracy of PRARE is better than 7 cm for X band ranging and about 0.1 mm/s for range rate measurements (Wilmes at al., 1987).

6.2 PRARE Processing

To first simulate and later process PRARE data, the measurement system has to be accurately modelled.

The PRARE range measurement principle is explained in Figure 6.1.

The pulse is sent from the satellite at time t_1 and arrives at station at time t_2. Here it is transposed to another frequency and sent back at time t_3, reaching the satellite at t_4. In the time taken for this to occur, station and satellite have also moved. The observed quantity is the time difference ($t_4 - t_1$).

Thus, the "observed" one-way range is the quantity R_O :

$$R_O = 0.5 \, (R_1 + R_2) = 0.5 \, (t_4 - t_1) \, . \, c + \text{corrections} \qquad (6.1)$$

where c is the velocity of light.

The "calculated" one-way range is obtained by first computing the time that the pulse takes to go from the satellite to the station, τ_1 , and secondly the time that it takes to reach the satellite on the way back, τ_2.

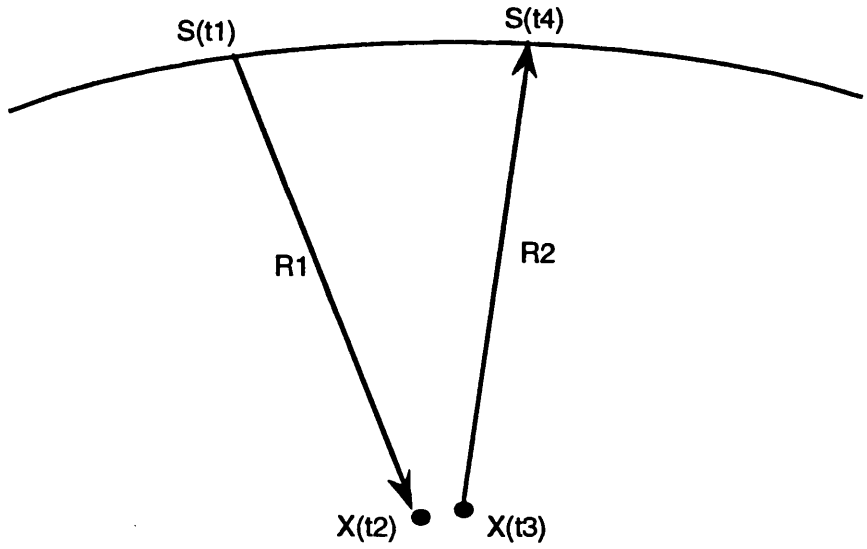

Figure 6.1 - PRARE range measurement principle.

The "Calculated" one-way range, R_C, then becomes:

$$R_C = 0.5 \, (\, R_1 + R_2 \,) = \, 0.5 \, (\, \tau_1 + \tau_2) \, . \, c \qquad (6.2)$$

Calculation of τ_1:

known: $\vec{S}(t_0)$ - satellite position at a tabulated time t_0 (close to t_1), in J2000 frame

$\vec{V}_S \, (t_0)$ - satellite velocity at t_0, in J2000

$\vec{T}$ - station position in the Conventional Terrestrial System

c - speed of light

- compute satellite position at time t_1:

$$\vec{S}(t_1) = \vec{S}(t_0) + \vec{V}_S \, . (\, t_1 - \, t_0 \,)$$

- compute t_2 and station position at t_2, by iteration:
  - compute $NP(t_1)$ - the precession-nutation matrix for time t_1
  - tau(1)=0

  DO j = 1 , 3
    - $t_2 = t_1 + tau(j)$
    - compute $SS(t_2)$ - the Earth rotation matrix for time t_2.

- compute station position in J2000 frame, at time t_2:

$$\vec{T}(t_2) = (NP)^T(t_2).\ SS^T(t_2)\ .\ \vec{T}$$

- apply tides:

$$\vec{T}(t_2) = \vec{T}(t_2) + \text{tides}$$

- $\text{tau}(j+1) = |\ \vec{S}(t_1) - \vec{T}(t_2)\ | / c$

END DO

- $\tau_1 = \text{tau}(3)$

Note that within the DO loop, NP only needs to be calculated once for all j's , because precession and nutation can be considered constant during the measurement time. On the contrary, SS represents the velocity of the station, rotating with the Earth, and thus it has to be calculated for each time.

Calculation of τ_2:

known: $\vec{S}(t_1)$ - satellite position at time t_1 in J2000 frame

$\vec{T}(t_2)$ - station position at time t_2 in J2000

- compute t_4 and satellite position at t_4, by iteration:
  - $\text{tau}(1)=0$
  - DO j = 1 , 3
    - $t_4 = t_2 + \text{tau}(j)$
    - $\text{diff} = t_4 - t_1$
    - $\vec{S} = \vec{S} + \vec{V}s\ .\ \text{diff}$
    - $\text{tau}(j+1) = |\ \vec{S} - \vec{T}\ | / c$
  - END DO
- $\tau_2 = \text{tau}(3)$

- $R_C = 0.5\ (\tau_1 + \tau_2)\ .\ c$

Note that in this computation the station displacement during the time (t_3-t_2) was neglected, which should be very small. This fraction of time is hardware dependent (time taken, at the ground station, to transpose the X band signal from 8.5 to 7.2 GHz) and a correction can be applied if information on its value is provided.

6.3 PRARE Range Data Simulation

For use in this study, PRARE range data were simulated for the SEASAT satellite. Two sets of data were generated, one for using on long arc solutions, with an interval between observations of 30 seconds and another for short arc analysis with an interval of 5 seconds.

Simulation algorithm

A - Long Arcs

1. The period chosen is the 3 day period from 0h September 18 to 0h September 21, 1978, corresponding to the Modified Julian Dates MJD $\in$ [43769.0 , 43772.0].

2. The reference orbit used on this simulation, is a solution computed using all laser data available for the period MJD $\in$ [43769.0 , 43772.25], the field GEMT2, and a step length of 1.25 min. The computation of this reference orbit is described in Chapter 8.

3. A set of 18 well-distributed stations were selected, with assumed approximate positions according to the PRARE programme status at the time of this exercise. The assumed coordinates of these stations on the GRS80 ellipsoid (a = 6378137 m 1/f = 298.257) are presented in Table 6.1. Figure 6.2 shows their geographical distribution.

4. For each station, a set of dates were generated, at 30 seconds interval for the same 3-day period.

5. The reference orbit was used to compute the satellite position at these dates.

6. Using the algorithm described in section 6.2 the two-way slant range from satellite-to-station-to-satellite was computed.

7. To these computed range values, a random number with zero mean and standard deviation of 7 cm (PRARE range accuracy) was added.

8. A minimum elevation angle of 20° was used.

This procedure generated 225 passes for these 18 stations, corresponding to a total of 2639 observations. These data are summarised in Table 6.1. The code used for station number is such that each new PRARE station has a number starting with 3. For stations that are very close to previous laser sites the laser codes were kept.

Table 6.1 - Simulated PRARE Data for long arcs

Station	Symbol	Location	Longitude (° E)	Latitude (°)	Height (m)	Passes	Points
3002	TRO	Trompsø Norway	18.0	70.0	100	19	257
3003	AZO	Azores/Portugal	334.0	38.0	350	9	108
3004	HIG	O'Higgins/Antarctica	303.0	-63.0	100	21	260
3005	FAL	Falkland/UK	300.0	-52.0	100	13	153
3006	BUE	Buenos Aires/Argentina	302.0	-34.0	100	8	99
3009	FOR	Fortaleza/Brazil	321.5	-4.0	10	7	80
3011	GRO	Greenland/Dennmark	316.0	60.0	500	21	235
3013	SVA	Svalbard/Norway	12.0	79.0	100	16	167
3014	HAR	Hartbeesthoes/S. Afr.	27.6	-25.8	1200	8	89
3017	KER	Kerguelen Isl./France	70.0	-49.0	0	12	138
3019	DJA	Djakarta/Indonesia	105.8	-6.3	50	7	79
3020	TOW	Townsville/Australia	146.0	-19.0	100	7	80
3022	FAI	Fairbanks/Alaska	212.4	64.9	200	20	263
3023	MUR	Mc Murdo/Antartica	167.0	-78.0	1000	17	188
3027	ULA	Ulan Bator/Mongolia	107.0	48.0	1500	10	123
7067	BER	Bermuda Island	295.3	32.4	-23	9	97
7121	HUA	Huanine/French Polyn.	209.0	-16.7	47	8	85
7834	WAT	Wettzell/Germany	12.9	49.1	661	13	138

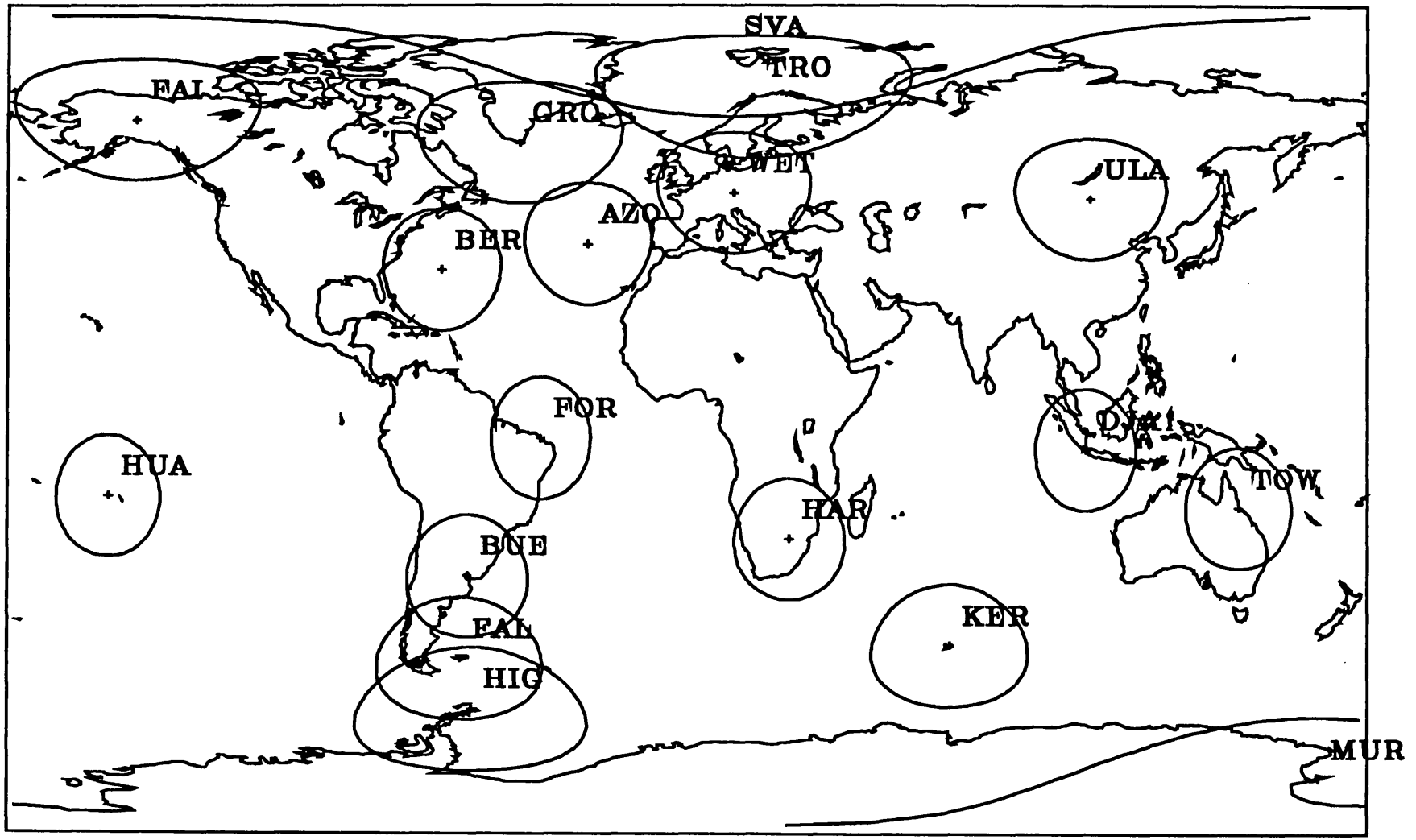

Figure 6.2 - Spatial distribution of PRARE stations for long arcs

Table 6.2 - Simulated PRARE Data for short arcs

Station	Symbol	Location	Longitude (° E)	Latitude (°)	Height (m)	Passes	Points
3002	TRO	Trompsø/Norway	18.0	70.0	100	3	262
3003	AZO	Azores/Portugal	334.0	38.0	350	2	113
3004	HIG	O'Higgins/Antarctica	303.0	-63.0	100	1	67
3005	FAL	Falkland/UK	300.0	-52.0	100	1	87
3006	BUE	Buenos Aires/Argentina	302.0	-34.0	100	1	84
3009	FOR	Fortaleza/Brazil	321.5	-4.0	10	1	88
3011	GRO	Greenland/Denmark	316.0	60.0	500	2	156
3013	SVA	Svalbard/Norway	12.0	79.0	100	3	209
3019	DJA	Djakarta/Indonesia	105.8	-6.3	50	1	87
3020	TOW	Townsville/australia	146.0	-19.0	100	1	76
3023	MUR	Mc Murdo/Antartica	167.0	-78.0	1000	3	204
3027	ULA	Ulan Bator/Mongolia	107.0	48.0	1500	1	120
3028	FS1	False station no 1	145.0	40.0	50	1	37
3029	FS2	False station no 2	120.0	50.0	1000	2	145
3030	FS2	False station no 3	125.0	-5.0	50	1	75
7067	BER	Bermuda Island	295.3	32.4	-23	2	85
7834	WAT	Wettzell/Germany	12.9	49.1	661	1	36

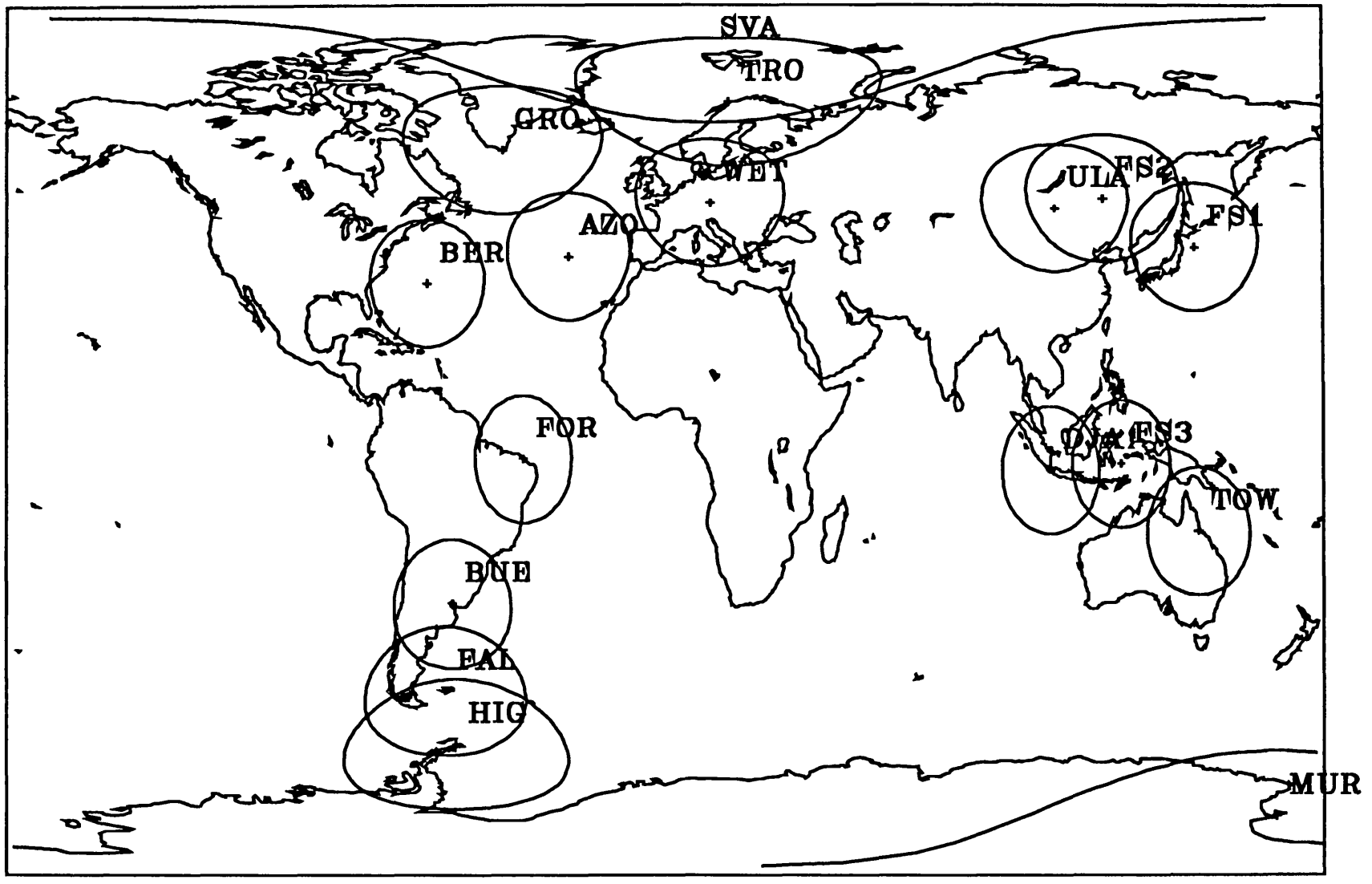

Figure 6.3 - Simulated PRARE stations for short arcs

B - Short arcs

The same procedure was repeated to simulate data for short arc solutions, with the following differences:

1. Period: first 310 minutes of day 43769, corresponding approximately to the first 3 revolutions.

2. The reference orbit used is the same solution used on long arcs, with the difference that a smaller step size of 0.5 minutes was used. This step is more suitable for short arc computation, as it is necessary to interpolate satellite position and velocity at dates only 5 seconds apart.

3. From the previous set of stations, 14 were found to track the satellite during this period. To these 14 stations 3 more were added with convenient locations, to allow certain configurations for test purposes. These stations were called "False stations".

4. An interval between observations of 5 sec was selected.

This procedure generated 27 passes for these 17 stations, corresponding to a total of 1931 observations. These data are summarised in Table 6.2

6.4 Laser Processing

In laser tracking, a short laser pulse is sent by the ground station to the satellite where it is reflected back by corner cubes. The delay time of the pulse is measured and used to derive the range from the satellite to the respective ground station.

Lasers are the most accurate tracking systems so far. Depending on the quality of the systems, they produce measurements with a single shot precision of 1 to 10 cm. The main problem with lasers is that they need clear skies to operate. They are quite expensive, require much maintenance and are not easily transportable.

The laser measurement principle is explained in Figure 6.4. The laser pulse is fired from the station at time t_1, it arrives at satellite at time t_2, is reflected back and reaches the station at t_3. In the time taken for this to occur, station and satellite have moved. The observed quantity is the time difference ($t_3 - t_1$).

The "observed" one-way range is given by:

$$R_0 = 0.5 (R_1 + R_2) = 0.5 (t_3 - t_1) . c + \text{corrections} \qquad (6.3)$$

The computation of the "calculated" one-way range is analogous to the method used for PRARE data. The only difference is that the measurement starts at the station instead of starting at the satellite. Now τ_1 is the time that the pulse takes to go from the station to the satellite and τ_2 the time that it takes to reach the station on the way back.

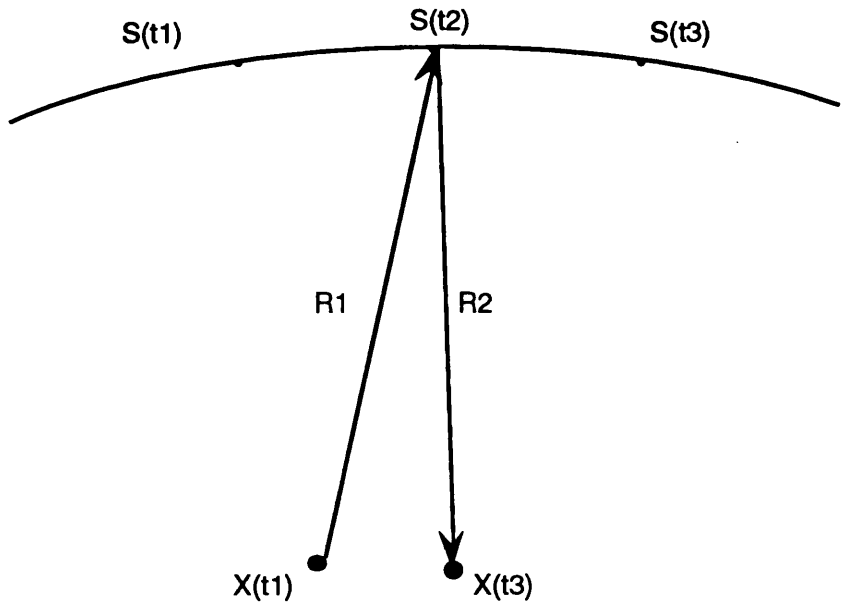

Figure 6.4 - Laser range measurement principle

The "Calculated" one-way range is :

$$R_C = 0.5 \, (\, R_1 + R_2 \,) = \, 0.5 \, (\, \tau_1 + \tau_2) \, . \, c \qquad (6.4)$$

The main correction that needs to be applied to laser observations is a correction for the tropospheric effects. The model currently adopted is the Marini and Murray (1973) formulae which is implemented in RGODYN.

The correction to a one-way range is (McCarthy, 1992):

$$\Delta R \, = \, \frac{f(\lambda)}{f(\varphi, \, h)} \, . \, \frac{A \, + \, B}{\sin E \, + \, \dfrac{B \, / \, (A + B)}{\sin E \, + \, 0.01}} \qquad (6.5)$$

where

$$A = 0.002357\, P_0 + 0.000141\, e_0$$

$$B = (1.084\text{x}10^{-8})\, P_0\, T_0\, K + (4.734\text{x}10^{-8})\, \frac{P_0^2}{T_0}\, \frac{2}{(3-1/K)} \qquad (6.6)$$

$$K = 1.163 - 0.00968 \cos 2\varphi - 0.00104\, T_0 + 0.00001435\, P_0$$

where

ΔR - range correction (metres)

E - true elevation of satellite

P_0 - atmospheric pressure at the laser site (in 10^{-1} kPa, equivalent to millibars)

T_0 - atmospheric temperature at the laser site (degrees Kelvin)

e_0 - water vapour pressure at the laser site (in 10^{-1} kPa, equivalent to millibars)

$f(\lambda)$ - laser frequency parameter (λ = wavelength in micrometres):

$$f(\lambda) = 0.9650 + \frac{0.0164}{\lambda^2} + \frac{0.000228}{\lambda^4} \qquad (6.7)$$

$f(\varphi, h)$ - Laser site function:

$$f(\varphi, h) = 1 - 0.0026 \cos 2\varphi - 0.00031h \qquad (6.8)$$

where φ is the latitude and h is the geodetic height.

In 1991 a number of 40 fixed and mobile SLR stations were participating in the work of the IERS (IERS, 1992). These stations are mainly involved in the tracking of the geodetic satellite Lageos and the Etalon pair of satellites. In addition to the tracking of these satellites, ERS-1 became a high priority target of SLR in 1991 (IERS, 1992). New 1992 SLR targets include TOPEX/Poseidon and Lageos-II. The high quality of the data acquired for the geodetic satellite Lageos (launched in 1976 to an orbit at a height of 5900 km) has revolutionised satellite geodesy. Several research centres have been processing these SLR data, deriving high accuracy solutions for Earth Rotation Parameters and Station Coordinates (Charlot, 1992).

Chapter 7

Altimeter Data

7.1 Introduction

Following the advances in altimeter processing techniques during the last decade, altimeter data have been widely used as a tracking data type. For tracking purposes these data are usually processed by using one of the following techniques:

- the altimeter measurements themselves expressed as residual sea surface heights, with appropriate sampling and filtering to remove the errors from other sources

- crossover differences - altimeter height differences at the intersections of ascending and descending satellite ground tracks.

The advantages and disadvantages of each technique were discussed in section 4.5. In this study the first approach was adopted. An algorithm was developed and implemented in the RGODYN program, to process the residual sea surface heights. This algorithm is a low pass filter making use of Fast Fourier Transforms (FFT).

This chapter describes and compares the SEASAT and ERS-1 altimeters and the algorithm developed in this study to process altimeter data for tracking purposes.

7.2 SEASAT and ERS-1 Radar Altimeters

In 1973 the SKYLAB altimeter was the first to give a continuous, direct measurement of the sea-surface topography. This altimeter was designed for obtaining the radar measurements necessary for designing the future improved instruments. The GEOS-3 altimeter was actually the first globally applied altimeter system. SEASAT was the third in the series of altimetry missions. Since SEASAT several space missions have been planned which included altimeters: GEOSAT in 1985 and more recently ERS-1 and TOPEX-Poseidon.

An altimeter is a nadir pointing radar instrument designed to make precise measurements of the echoes from the surface of the ocean. From these measurements three main quantities can be derived:

- the height from the satellite to the ocean surface
- ocean wave height
- ocean wind speed

This study is only concerned with the height measurement.

The principle of altitude measurement by an altimeter is simple and straightforward. A short pulse is transmitted by the radar toward the surface beneath it at a time t_1. The pulse propagates toward the surface, at a speed **c**, is returned by the surface, and an echo is received by the sensor at a time t_2. The height from the sensor to the ocean surface is therefore a function of the time difference $\Delta t = t_2 - t_1$:

$$h = c\frac{\Delta t}{2} \qquad (7.1)$$

The accuracy of time measurement depends mainly on the duration of the pulse τ. The sharper the radar pulse is, the wider the frequency band required to carry it. The value of τ is determined by the smallest wavelength to be resolved at the sea surface. For SEASAT and ERS-1 altimeters τ is 3 ns giving a minimum resolved wavelength of 0.5 m.

When using such a short pulse the problem arises of how to give it sufficient power so that the strength of the return signal is measurable. This is achieved by a pulse compression (chirp) technique. A filter is applied to the sharp pulse, dispersing it into a much longer pulse T, and the frequency is swept linearly over range f^- to f^+ such that $f^+ - f^- = B$, where B is the signal bandwidth. This expanded chirp pulse carries the same information, but possesses more energy. On return, the reflected dispersed pulse is recompressed by applying an inverse filter, producing an effective pulse width of $\tau = 1/B$. For SEASAT and ERS-1, T = 20 μs, τ = 3 ns and B $\approx$ 300 MHz.

Ideally one would like to have a sharp pulse focused in a small area of the sea so that all the measured area would be simultaneously illuminated. This is the so-called beam-limited geometry. However this would require a very large antenna with serious technological disadvantages. In the present altimeters the pulse-limited geometry is used instead, requiring only an antenna of small diameter ($\approx$ 1m for SEASAT and ERS-1).

The formation of the footprint is explained in Figure 7.1. This is formed when the pulse radiated from the altimeter antenna, as a spherical shell, intersects the ocean surface and produces a transient illuminated area. The leading edge of the pulse will strike the sea first, just beneath the satellite and then move out in a circular front. The trailing edge will do the same a fraction of time later. The illuminated area will be first a circle of growing area and then will become an annulus. The effective area (footprint) whose height is sampled is the illuminated circle just before it becomes an annulus. This area also depends on the wave height.

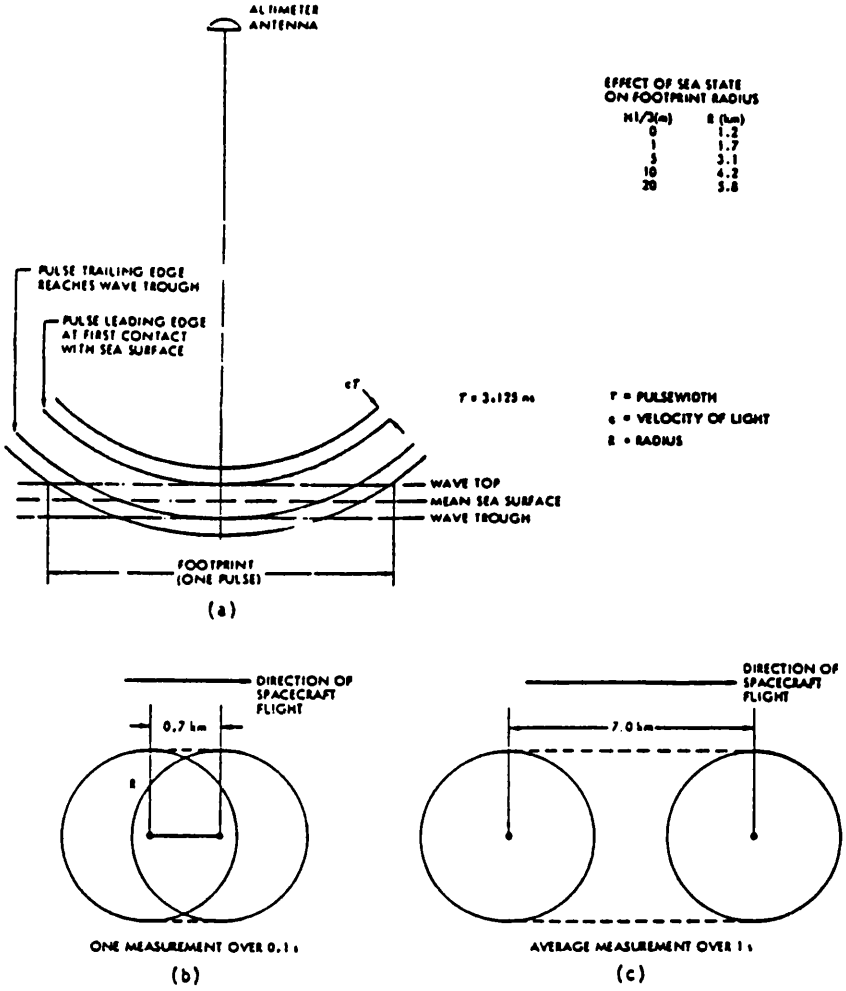

Figure 7.1 - SEASAT altimeter footprint. a) Cross-sectional view; b) and c) Satellite's eye views. Extracted from (JPL, 1980).

For a calm sea, the footprint is a circle of radius (Robinson, 1985):

$$r_{min} = \sqrt{2\,h\,c\,\tau} \tag{7.2}$$

For a rough sea with significant wave height $h_{1/3}$ this radius increases to:

$$r_{max} = \sqrt{2\,h\,c\tau'} \tag{7.3}$$

$$\tau'^{2} = \tau^{2} + \frac{16\,h_{1/3}^{2}\,\ln 2}{c^{2}} \tag{7.4}$$

For SEASAT and ERS-1, $h \approx 780$ km, $\tau = 3$ ns and so $r_{min} = 1.2$ km and $r_{max} = 5$km for $h_{1/3}$=5m. Therefore the swath width varies from 2.4 km for a calm sea up to some 10 to 15 km in high seas.

The return signal is sampled and fitted to a model curve. The shape of the curve varies with wave height, but for the height measurement the quantity of interest is the timing of the mid-point of the leading edge slope (Figure 7.2). By comparing it to the known characteristics of the emitted pulse the travel time can be derived. Curve fitting can lead to errors, but these are reduced by averaging over a certain time interval. For SEASAT the accuracy for 1 second averaged measurements was ≈ 10 cm. For ERS-1 it is expected to be better than 10 cm.

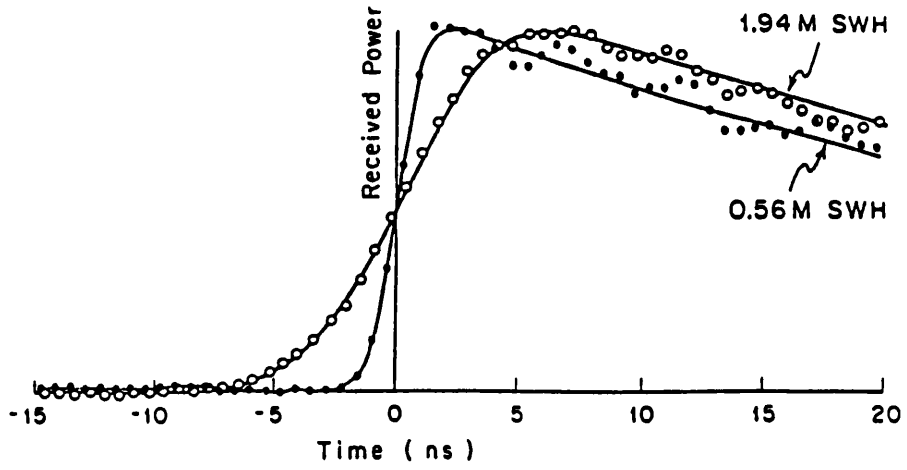

Figure 7.2 - Return pulse curve fitting for two sea states (Stewart, 1985).
SWH=Significant wave height.

During 1 second the satellite travels about 7 km. Therefore the spatial resolution of each measurement is a strip of variable width, depending on sea state, and 7 km length.

The ERS-1 altimeter has two measurement modes, optimised for measurements over ocean and ice respectively. In ice mode the altimeter works at a coarser resolution, to maximise the data return over the ice surfaces.

Table 7.1 compares the main characteristics of the SEASAT altimeter with the ERS-1 altimeter in the ocean mode.

Table 7.1
SEASAT and ERS-1 altimeter characteristics

	SEASAT	**ERS-1**
Radar frequency	13.5 GHz	13.8 GHz
Pulse repetition frequency	1020 Hz	1020 Hz
Chirp pulse length	20 μs	20 μs
Chirp bandwidth	320 MHz	330 MHz
Effective pulse length	3.125 ns	3.0 ns
Antenna diameter	1.0 m	1.2 m
Mass	94 kg	96 kg
DC power	165 W	130 W
Altitude accuracy (1 sec averages)	10 cm	< 10 cm

7.3 Data Modelling

The radar altimeter measures the height of the satellite above the sea surface. To relate this quantity to the satellite position, it must be converted into a height above some reference ellipsoid.

The fundamental relationship between the main quantities involved in satellite altimetry is:

$$h = h_a + N + SST \tag{7.5}$$

where:

h - satellite height above the reference ellipsoid

N - geoid height above the same ellipsoid

SST - sea surface topography (sea height above geoid)

h_a - altimeter measurement corrected for instrument and geophysical effects.

The altimeter data used in this study were SEASAT data as provided in the Geophysical Data Record (GDR) tapes (JPL, 1980). The following corrections, also provided in the tapes for each measured point, were applied to data:

Instrument corrections:

- time tag adjustment - adjusts the time tag so that it refers to the time of signal reflection from the ocean surface.

- attitude (off nadir pointing) - uses attitude information to infer a correction for h due to satellite off-nadir pointing.

- centre of mass reduction.

- wave height - uses telemetered sea state information to correct h for the deviation of sea surface from a specular surface.

Geophysical corrections:

- inverse barometer effect - change in the sea surface height above the geoid due to atmospheric pressure variations.

- tides (solid Earth and ocean) - periodic variations in sea surface height due mainly to the attractions of the moon and the sun.

- atmospheric effects (tropospheric and ionospheric) - an overestimate of the distance due to the reduction in the speed of light through the atmosphere. This can be separated into tropospheric (dry and wet) and ionospheric effects.

Equation 7.5 is a theoretical relationship. In practice only approximate values of these quantities are known, which are in error. So one can write (Figure 7.3):

$$h = h_c + dh = (h_a + dh_a) + (N + dN) + SST \qquad (7.6)$$

where

h_c - "computed" approximate height above ellipsoid
dh - error in the "computed" height (orbit error)
dh_a - residual errors on altimeter measurement
dN - error in the computed geoid height due to inaccuracy of the geoid model
SST - Sea Surface Topography (sea height above geoid)

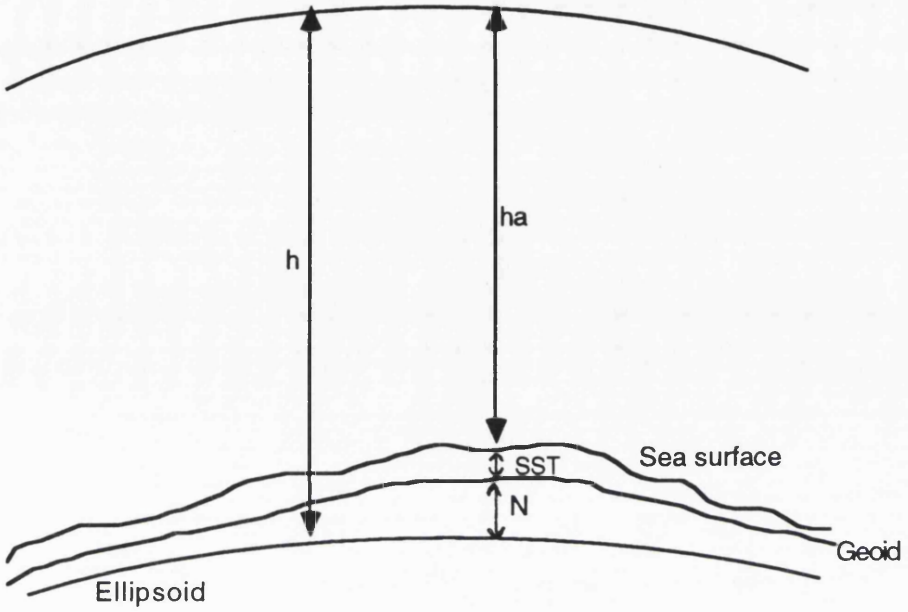

Figure 7.3- Altimeter measurement geometry

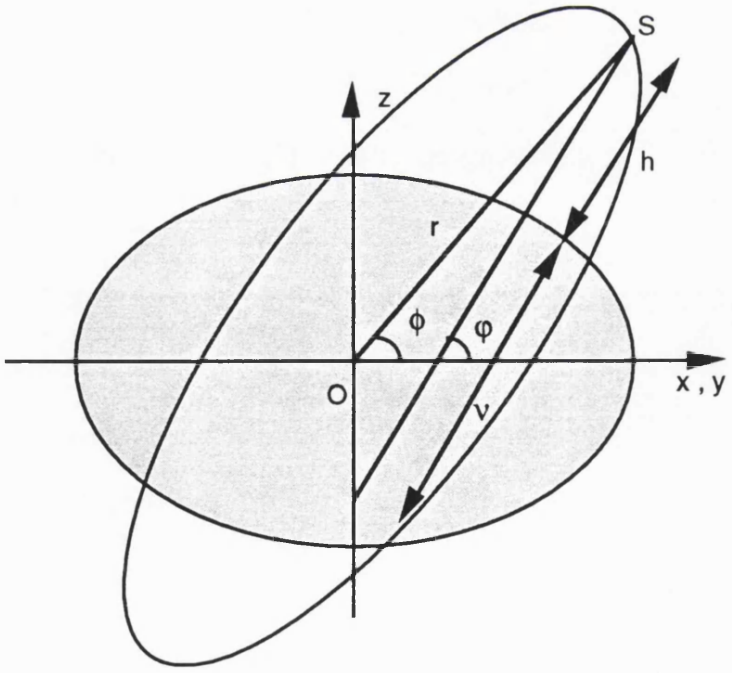

Figure 7.4 - Height above ellipsoid

The "computed" height above the ellipsoid, h_C, can be computed from the satellite geocentric position vector (X, Y, Z) using the relationship between cartesian and geodetic coordinates:

$$\begin{aligned} X &= (\nu + h_c) \cos\varphi \cos\lambda \\ Y &= (\nu + h_c) \cos\varphi \sin\lambda \\ Z &= [\nu (1 - e_E^2) + h_c] \sin\varphi \end{aligned} \qquad (7.7)$$

The subscript E means that these elements are referred to the Earth's ellipsoid and are not to be confused with satellite orbital elements.

The "calculated" h_C is:

$$h_c = \frac{\sqrt{X^2 + Y^2}}{\cos\varphi} - \nu \qquad (7.8)$$

ν is the radius of curvature in prime vertical and φ is the geodetic latitude, which can be computed by iteration using the expressions:

$$\nu = a_E (1 - e_E^2 \sin^2\varphi)^{-1/2} \qquad (7.9)$$

$$\tan\varphi = \frac{Z + e_E^2 \nu \sin\varphi}{\sqrt{X^2 + Y^2}} \qquad (7.10)$$

The iteration can be started using an initial value for φ, given by the spherical approximation ϕ:

$$\tan\phi = \frac{Z}{\sqrt{X^2 + Y^2}} \qquad (7.11)$$

The geoid height above the reference ellipsoid at a point with geodetic coordinates (φ,λ), can be computed from one of the present geopotential models using Brun's formula:

$$N = \frac{T}{\gamma} \qquad (7.12)$$

where T is the disturbing potential:

$$T = - \frac{GM}{r} \sum_{\ell=2}^{\infty} \Delta J_\ell \left[\frac{r_o}{r}\right]^\ell P_\ell[\sin\phi] + \tag{7.13}$$

$$+ \frac{GM}{r} \sum_{\ell=2}^{\infty} \sum_{m=1}^{\ell} K_{\ell m} \left[C_{\ell m} \cos m\lambda + S_{\ell m} \sin m\lambda \right] \left[\frac{r_o}{r}\right]^\ell P_{\ell m}[\sin\phi]$$

All the quantities are as defined in equation (3.3) except for:

$$\Delta J_\ell = J_\ell - J_\ell^{ellip} \tag{7.14}$$

where J_ℓ are the zonals of the geopotential model, and J_ℓ^{ellip} the coefficients defining the normal potential of the reference ellipsoid. γ is the normal gravity at latitude φ.

7.4 Filtering process

The expression for the total altimeter (O-C) residuals can be written in the form:

$$RESID = (h_a + N) - h_c = dh - (dN + dh_a + SST) \tag{7.15}$$

An inspection of this formula shows that these residuals are a sum of errors of different sources (Table 7.3):

- orbit error - as explained in section 4.6, it is mainly long wavelength, the main frequencies being of one and two cycles per revolution.

- SST - the sea surface topography can be as big as 1.5 m, but it is usually less than 0.5 m.

- geoid error - present geoid models are accurate for the longer wavelengths, close to the dominant errors of the satellite ephemeris error, but the errors increase rapidly for the smaller wavelengths. Wakker et al (1987) quote an accuracy for the present models as indicated in Table 7.2.

The adopted approach explores the knowledge that the orbit error is predominantly long wavelength with wavelengths higher than all other error sources. The method developed for this study is a fast algorithm using Fast Fourier Transforms (FFT).

Table 7. 2
Accuracy of present geoid models

λ (km)	accuracy
10,000	< 5 cm
2,000	40 cm
100	1.5 m

To be able to use these observations for orbit determination, it is necessary to find a process of filtering these residuals to eliminate the component of the error that comes from other sources.

Fourier Transform (FT) methods are widely used for spectrum analysis. If the data set is large the classic FT is slow, and FFT should be used instead, the number of computations being reduced from N^2 to N $\log_2(N)$. However the use of FFT requires data to be evenly sampled with a number of points equal to a power of 2.

The altimeter data set does not meet any of these requirements. First, the altimeter measurement is not continuous, mainly due to land gaps. Second, one is usually interested in processing data within a specified interval which can have any number of points, depending on the length of the interval and on the sampling rate used.

The method presented here implements the use of FFT methods to any uneven set of points. It is based on an algorithm developed by Press and Rybicki (1989) to compute the periodogram of unevenly sampled data. The basic idea is to find an evenly spaced data set, with a number of points equal to a power of 2, which produces a spectrum "equivalent" to the spectrum of the original data set. This is done by Press and Rybicki through a process called "extirpolation", similar to an inverse Lagrange interpolation. By this process, each point on the original interval is transformed into a set of evenly spaced function values on an expanded interval, with a number of points of the form 2^k, in such a way that the original points could be obtained by interpolating along these function values. Press and Rybicki implemented this method to compute the FFT and therefore the periodogram of an unevenly spaced data set.

Table 7.3
Typical altimeter error budget
(Tapley et al., 1982)

Type of effect	Source	Amplitude (cm)	Residual after modelling (cm)	Wavelength (km)
altimeter	noise		5	
altimeter	bias	20	2	
sea state	electromagnetic bias + tracker bias	7% swh	3% swh	500 - 1000
ionosphere	free electrons	2-20	3	50 - 10,000
dry troposphere	mass of air	240	1	1000
wet troposphere	water vapour	10 - 40	3	50 - 500
liquid water	clouds, rain	10-100		30-50
ocean tides	moon, sun attraction	100	5	500 - 1000
solid earth tide	moon, sun attraction	20	2	20,000
ocean currents	equatorial	30	?	5000
	western boundary	130	?	100 - 1000
	eastern boundary	30	?	100 - 1000
mesoscale	eddies	25		100
	rings	100		100
	gyres	50		3
geoid	mass distribution of earth	100 m	2 m	2000 - 5000
orbital error	gravity	10 km	140	40,000
	drag	300	30	10,000
	solar radiation	300	30	10,000
	station location	100	10	10,000

During this study this method was further developed to build a complete filtering algorithm. This algorithm was implemented in a FORTRAN subroutine called DFFT (Discrete Fast Fourier Transform) which makes use of a set of other subroutines:

Subroutine SPREAD - "Extirpolates" an array of length N into an expanded array of size NDIM (Press and Rybicki, 1989)

Subroutine SHRINK - Reverses extirpolation made by SPREAD

Subroutine REALFT - Computes the FFT (if the input parameter ISIGN is set to 1) or the inverse FFT (if ISIGN is set to –1) of a real array of size $N = 2^k$ (Press et al, 1986)

The main innovation introduced by this algorithm is the recovery of the lowest frequencies on the original data set (subroutine SHRINK), by a process which inverts the "extirpolation" done by subroutine SPREAD. This way the recovered data set is a smoothed version of the original, after removing the highest frequencies. In this study this algorithm was used for the specific purpose of processing altimeter data, but can also be applied as a low pass filter to any unevenly spaced data set.

7.5 Processing Algorithm

Let (X,Y) be a set of N unevenly spaced points (N any number). X is usually time and Y the values of a measured quantity at the corresponding times (Figure 7.5).

1 - Transform array Y into an equivalent array DATA of size NDIM evenly spaced points, by "extirpolation" (Subroutine SPREAD).

2 - Take FFT of DATA. DATA is transformed from the time domain to the frequency domain (Subroutine REALFT, with ISIGN=1).

3 - Choose an appropriate cut-off frequency (LFREQ) and neglect frequencies above LFREQ.

4 - Take inverse FFT of filtered DATA. DATA, now smoothed is transformed back to the time domain (Subroutine REALFT, with ISIGN=-1).

5 - Go back from smoothed DATA of size NDIM to equivalent YF of size N , which is now a smoothed version of the original Y (Subroutine SHRINK).

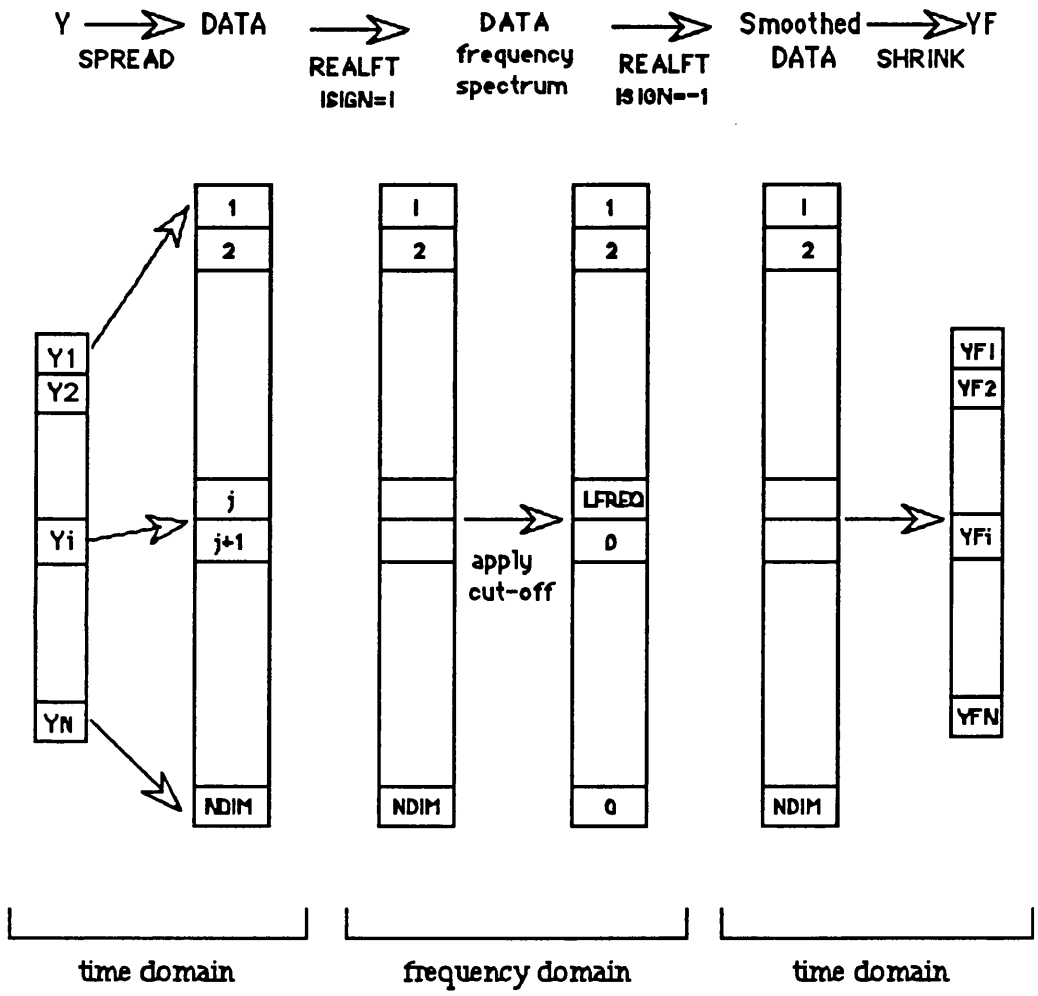

Figure 7.5 - Smoothing algorithm

The filtering process is controlled by a number of parameters. Here the main points are underlined:

1. The size of the expanded array DATA, NDIM is controlled by two parameters:

OFAC - Oversampling factor - Using an OFAC >1 basically has the effect of a better sampling of the spectrum by increasing the number of sampled frequencies.

MACC - Number of interpolation points per 1/4 cycle of highest frequency. Each point on Y is transformed into a number of MACC points on DATA.

2. How to choose LFREQ:

By analogy to the evenly spaced case, an unevenly sampled data array Y of N points, has N/2 independent frequencies. Let L be the length of the interval covered by these N points. Then the frequencies are:

$$f_i = \frac{i}{L} \qquad i = 1,..,\frac{N}{2} \tag{7.16}$$

with corresponding periods

$$p_i = \frac{1}{f_i} = \frac{L}{i} \qquad i = 1,..,\frac{N}{2} \tag{7.17}$$

The maximum frequency $\frac{N}{2L}$ is called the nyquist frequency.

If we could compute directly the FFT of array Y, then it would be easy to choose the appropriate LFREQ as the maximum frequency to retain. However the actual FFT that is computed is the FFT of array DATA of size NDIM and, in this case, there are NDIM/2 independent frequencies. However a close inspection of the algorithm shows that the first N/2 frequencies of DATA are in fact the frequencies of the original data Y.

If i_{max} is the index of the maximum frequency to retain (i_{max} cycles per L) i.e. :

$f_{max} = \frac{i_{max}}{L}$ is the maximum frequency to retain and

$p_{min} = \frac{L}{i_{max}}$ is the minimum period

LFREQ should be

$$LFREQ = i_{max} \times OFAC = \frac{L}{p_{min}} \times OFAC \tag{7.18}$$

The index of the maximum frequency with significance is $\frac{N}{2} \times OFAC$.

• Although the frequencies on the original interval correspond exactly to the first frequencies on the expanded interval, the amplitudes have to be scaled. The need for this comes from the fact that an FFT of size $\frac{NDIM}{2}$ is computed instead of an FFT of size $\frac{N}{2} \times OFAC$. Thus the scale factor to be applied to the amplitudes on the expanded interval to obtain the amplitudes on the original interval is $\frac{NDIM}{N \times OFAC}$.

To test the efficiency of the algorithm two examples are presented.

Example 1

A set of (X , Y) unevenly spaced points was generated where Y is a sinusoidal function of X . To simulate noise existing in real data, to each value of Y was added a random variable NOISE with zero mean and $\sigma = 0.8$. To simulate uneven spacing, 50 points were generated with a spacing between consecutive points of 3 + R, where R is random variable with zero mean and $\sigma = 0.3$.

Number of points: N=50
Length of the interval : L =150
DO i=1,50

$$X_i = 3i + R$$

$$\omega_i = (2\pi / L)X_i$$

$$Y_i = 2.5 + 2\cos(\omega_i) + 3\sin(2\omega_i) + 1.5\sin(6\omega_i) + \text{NOISE}$$

END DO

According to the way these points were generated, there are 3 main frequencies, of 1, 2 and 6 cycles in the interval L. Therefore the index of the maximum frequency to retain is $i_{max} = 6$.

Figure 7.6 illustrates the result when using

OFAC=MACC=2
LFREQ=6 x OFAC =12

In the figure the dots represent the original data points and the continuous line the smoothed version of these data which contains only the 6 largest frequencies. The remaining signal, which contains all the frequencies from 7 to 25 is regarded as noise.
The importance of the oversampling factor OFAC can be illustrated in this figure. Using an oversampling factor of 1 means that the Fourier function (F) will be periodic in the interval L and therefore the smoothed curve will be such that F(1)=F(N). This is a serious constraint that will strongly influence the shape of the smoothing function at both ends of the interval. By applying an OFAC >1 , for example OFAC = 2, the interval L is expanded to 2L and this constraint is then applied to the interval 2L, therefore becoming unnoticed in the original interval.

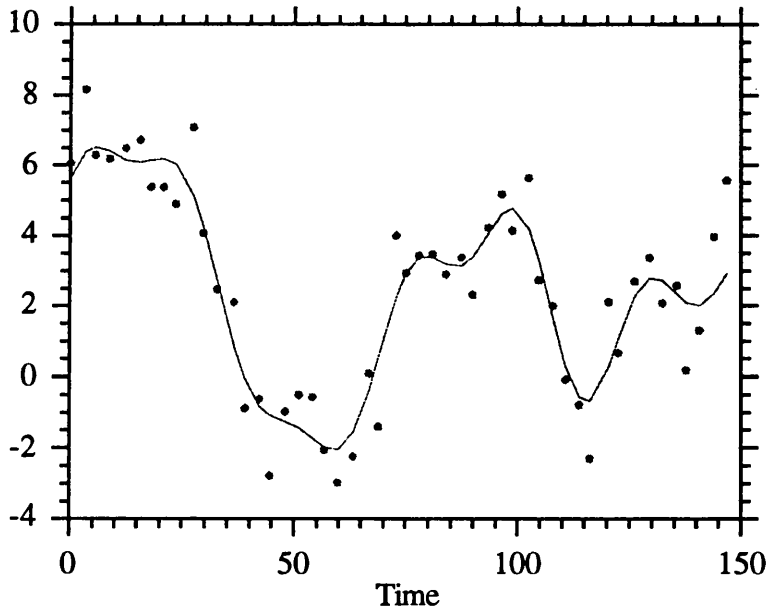

Figure 7.6 - Result of smoothing data in example 1, using OFAC=2, MACC=2, LFREQ=12.

Example 2

In this example a set of actual altimeter residuals is presented. According to equation 7.15 these residuals are computed in the following way:

$$RESID = (h_a + N) - h_c$$

where

h_a - actual SEASAT altimeter measurements after applying all instrument and geophysical corrections, using a sampling interval of 1 minute.

N - geoid undulation computed using OSU89B geopotential model up to degree and order 180 (Rapp and Pavlis, 1990).

h_c - computed satellite height above ellipsoid using an ephemeris where all the forces described in section 3.3 were modelled and the GEMT1 gravity field was used.

The ellipsoid used is the Geodetic Reference System 80 (GRS80) ellipsoid, as recommended in the SEASAT GDR tapes: (a = 6378137 m, 1/f= 298.257).

It was found that using a sampling interval of 1 minute, the original data set of 1 sec measurements is highly reduced without loosing the long wavelength information of the signal. The main advantage of using a large sampling interval is the saving in computing time.

The spectrum of these residuals is shown in Figure 7.7. The two main frequencies correspond to 2 and 1 cycles per revolution with periods of 50 min and 100 min respectively. These are the well known dominant frequencies of the orbit error. Apart from some long period signals, the remaining frequencies with significance have periods smaller than 30 minutes, which can hardly be considered orbit error. At these wavelengths the geoid error becomes as important as the orbit error itself. Therefore it was decided to use a cut-off frequency just above 2 cycles per revolution.

The smoothing algorithm was applied to this data set:

Number of points: N= 2886
Length of the interval L = 4299 minutes (≈ 3 days)
OFAC=2
MACC=1
p_{min} = 48 min
LFREQ = 180

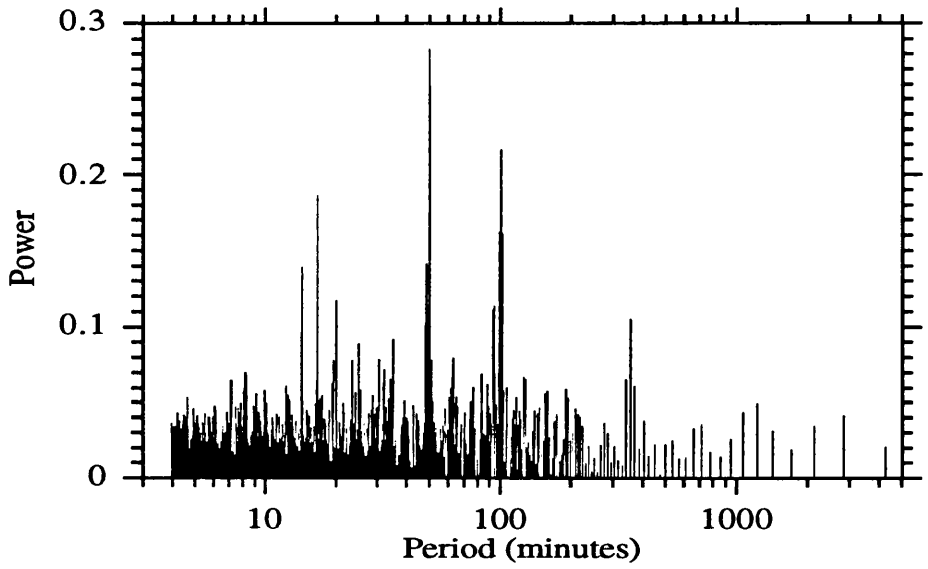

Figure 7.7 - Spectrum of altimeter residuals (example 2)

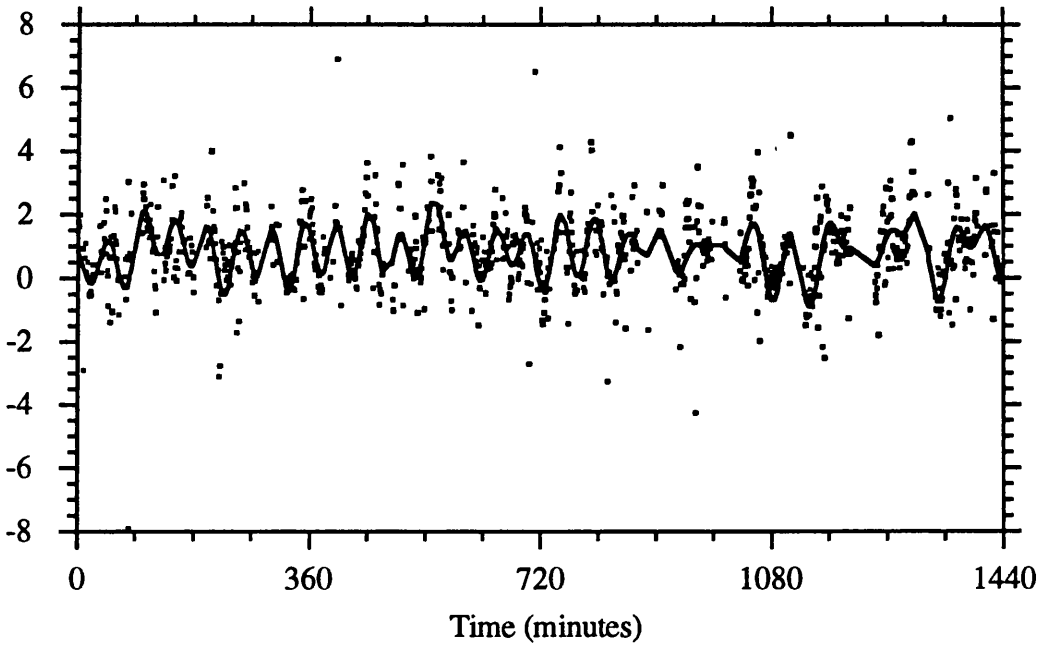

Figure 7.8 - Residuals and smoothed curve (example 2)

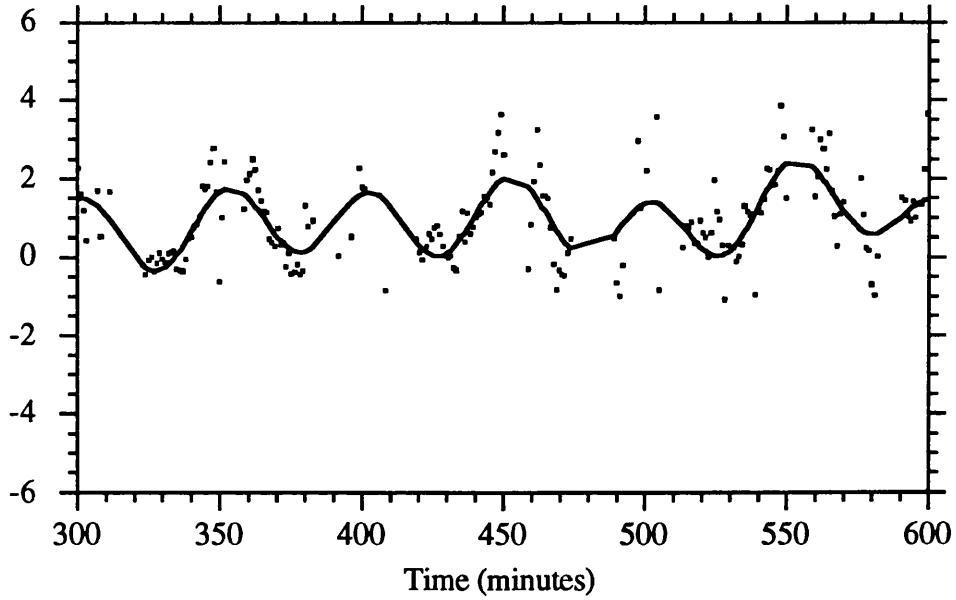

Figure 7.9 - Zoomed section of Figure 7.8

Figures 7.8 and 7.9 illustrate the result. The second figure is a zoomed representation of a section of the first. The 2 cycles per revolution frequency is the dominant signal. The statistics of the plotted values over the whole interval (≈ 3 days) are:

average of total residuals (Y) :	0.88 m
rms total residuals (Y):	1.48 m
rms smoothed residuals (YF):	1.13 m
rms noise (Y-YF) :	0.98 m

These are typical values obtained when processing altimetry data. An important feature of these statistics is the average value of these residuals of approximately 1 m. This is a common feature in all SEASAT solutions and was explained by several investigators as being due to an error of similar value in the semi-major axis of the GRS80 ellipsoid.

If the assumption made above about the spectrum of the errors that constitute the altimeter residuals is correct, then the smoothed curve YF is the orbit error with an rms of 1.13 m.

This algorithm was implemented in program RGODYN to process altimetry data for tracking purposes. This is done in three main steps:

1 - program computes residuals for all observations (Y)

2 - applies smoothing algorithm, using an appropriate cut-off frequency, returning the smoothed residuals (YF).

3 - All the observations are processed again now using YF as the actual altimeter residuals, and the fitting process is completed.

Chapter 8

SEASAT long arcs

8.1 Introduction

The first part of this study, before the launch of ERS-1, was dedicated to the computation of SEASAT's orbit, as a preparation for subsequent application to the determination of the orbit of ERS-1, once its own data became available. The main components of this study, which are the subject of this chapter are:

- to determine the accuracy of SEASAT long arc ephemerides, computed with the SATAN programs implemented at UCL and the state of the art models for this satellite.

- to assess the accuracy of orbits determined with PRARE data.

- to investigate the effect of tracking stations' configuration in the orbit accuracy, by using reduced tracking networks.

- to investigate the potential of altimetry data to replace range data over considerably long time intervals.

The tracking data used were actual SEASAT laser and altimeter measurements and PRARE simulated observations.

8.2 Computational model

This section describes the computational model used in SEASAT solutions. This model is summarised in Table 8.1.

The period chosen for this study is the 3 day period from 0h September 18 to 0h September 21, 1978, corresponding to the Modified Julian Dates MJD $\in$ [43769.0 , 43772.0]. This corresponds to a period during which SEASAT was flying on a 3-day repeat orbit, similar to the ERS-1 orbit used during the commissioning and ice phases.

For long arc analysis, arcs of 3 days' length were selected. This is the minimum length required to obtain a stable solution. This nominal length was chosen due to the large number of tests that were performed. A much larger arc length, such as 6 days, would substantially increase the computing time of each run.

8.2.1 Reference systems

The adopted time scale and reference systems were described in Chapter 2 except for the Terrestrial System where the so-called GEMT1 system was used instead of the BIH/IERS frame. This is the system adopted by the geopotential models GEMT1 and GEMT2. Therefore if these models are utilised in the computations, this system should be adopted as the terrestrial frame where the acceleration due to the Earth's gravity field is computed. The main difference between the BIH and GEMT1 systems is a shift in the pole origin. The GEMT1 system adopts an origin that coincides with the 1979-1984 6-year average pole.

The transformation between BIH and GEMT1 systems is described.

Transformation BIH → GEMT1:

Mueller et al. (1982) establish the relationship between the Earth Rotation Parameters (ERPs) for two different reference systems.

The two celestial (CIS) and two terrestrial (CTS) systems inherent in two different techniques (I and II) are generally not identical. Let the relationship between the two CIS's be

$$\begin{bmatrix} X \\ Y \\ Z \end{bmatrix}^{II}_{CIS} = R_1(\alpha_1)\ R_2(\alpha_2)\ R_3(\alpha_3).\ \begin{bmatrix} X \\ Y \\ Z \end{bmatrix}^{I}_{CIS} \tag{8.1}$$

and similarly the relationship between the two CTS's

$$\begin{bmatrix} x \\ y \\ z \end{bmatrix}^{II}_{CTS} = R_1(\beta_1)\ R_2(\beta_2)\ R_3(\beta_3).\ \begin{bmatrix} x \\ y \\ z \end{bmatrix}^{I}_{CTS} \tag{8.2}$$

where α_i and β_i are small rotation angles about the axes **i** (cf. equation 2.12).

The transformation from CIS to CTS is

$$\begin{bmatrix} x \\ y \\ z \end{bmatrix}^{I}_{CTS} = S^I\ N\ P\ \begin{bmatrix} X \\ Y \\ Z \end{bmatrix}^{I}_{CIS} \tag{8.3}$$

$$\begin{bmatrix} x \\ y \\ z \end{bmatrix}^{II}_{CTS} = S^{II}\ N\ P \begin{bmatrix} X \\ Y \\ Z \end{bmatrix}^{II}_{CIS} \tag{8.4}$$

It is assumed that common nutation (N) and precession (P) matrices are used for both systems (I and II). S is the Earth rotation matrix $S = R_2(-xp).R_1(-yp).R_3(\theta)$, in which xp and yp are the coordinates of the pole, measured in arc seconds, and θ is the Greenwich Sidereal Time (see section 2.4.3).

Substituting the left hand side of equation (8.2) by the right hand side of equation (8.4),

$$R_1(\beta_1)\ R_2(\beta_2)\ R_3(\beta_3).\ \begin{bmatrix} x \\ y \\ z \end{bmatrix}^{I}_{CTS} = S^{II}\ N\ P \begin{bmatrix} X \\ Y \\ Z \end{bmatrix}^{II}_{CIS} \tag{8.5}$$

and replacing $\begin{bmatrix} X \\ Y \\ Z \end{bmatrix}^{II}_{CIS}$ by its equivalent expression given in equation (8.1):

$$R_1(\beta_1)\,R_2(\beta_2)\,R_3(\beta_3) \begin{bmatrix} x \\ y \\ z \end{bmatrix}^{I}_{CTS} = S^{II}N\,P\ R_1(\alpha_1)\ R_2(\alpha_2)\ R_3(\alpha_3) \begin{bmatrix} X \\ Y \\ Z \end{bmatrix}^{I}_{CIS} \tag{8.6}$$

After some manipulation, neglecting second order terms,

$$\begin{bmatrix} x \\ y \\ z \end{bmatrix}^{I}_{CTS} = R_1(-\beta_1 + \alpha_1\cos\theta + \alpha_2\sin\theta)\,R_2(-\beta_2 - \alpha_1\sin\theta + \alpha_2\cos\theta)\,.$$
$$.\ R_3(-\beta_3 + \alpha_3)\,S^{II}N\,P \begin{bmatrix} X \\ Y \\ Z \end{bmatrix}^{I}_{CIS} \tag{8.7}$$

Comparing equations 8.7 and 8.3,

$$S^{I} = R_1(-\beta_1 + \alpha_1\cos\theta + \alpha_2\sin\theta)\,R_2(-\beta_2 - \alpha_1\sin\theta + \alpha_2\cos\theta)\,.$$
$$.\ R_3(-\beta_3 + \alpha_3)\,S^{II} \tag{8.8}$$

Therefore the difference between the pole coordinates of the two systems can be written as:

$$\Delta yp = yp^{II} - yp^{I} = -\beta_1 + \alpha_1\cos\theta + \alpha_2\sin\theta$$
$$\Delta xp = xp^{II} - xp^{I} = -\beta_2 - \alpha_1\sin\theta + \alpha_2\cos\theta \tag{8.9}$$

The parameters for the BIH → GEMT1 transformation can be taken from Marsh et al. (1988):

$$\begin{aligned} \beta 1 &= \ 1.46 \text{ mas} \\ \beta 2 &= -3.80 \text{ mas} \\ \alpha 1 &= -0.22 \text{ mas} \\ \alpha 2 &= \ 0.62 \text{ mas} \end{aligned} \qquad (8.10)$$

In this transformation $\alpha_3 = \beta_3 = 0$, i.e., there is no transformation in the UT1-UTC series. The GEMT1 model adopts the BIH-provided UT1-UTC series with no changes whatsoever (Marsh et al., 1988).

The transformation applied to the BIH polar motion series to refer them to the GEMT1 system was

$$\begin{aligned} yp^{GEMT1} &= yp^{BIH} - \beta_1 + \alpha_1 \cos\theta + \alpha_2 \sin\theta - \bar{y} \\ xp^{GEMT1} &= xp^{BIH} - \beta_2 - \alpha_1 \sin\theta + \alpha_2 \cos\theta - \bar{x} \end{aligned} \qquad (8.11)$$

In these expressions $\bar{x}$ and $\bar{y}$ are the coordinates of the 6 year average pole adopted as GEMT1 origin.

$$\begin{aligned} \bar{x} &= \ 38.2 \text{ mas} \\ \bar{y} &= 280.3 \text{ mas} \end{aligned} \qquad (8.12)$$

Using this transformation the BIH polar motion series is transformed to the so-called "a priori" GEMT1 system, i.e., the reference system initially adopted by GEMT1. However the GEMT1 solution includes the adjustment of the ERPs, including polar potion. After the adjustment it was found that there was a significant shift along the y axis, of approximately 18 mas, between the "a priori" and the adjusted series. The parameters for the transformation between the "a priori" and the "adjusted" series were found to be:

$$\begin{aligned} \beta 1 &= -17.30 \text{ mas} \\ \beta 2 &= \ -2.30 \text{ mas} \\ \alpha 1 &= \ \ 0.13 \text{ mas} \\ \alpha 2 &= \ \ 0.03 \text{ mas} \end{aligned} \qquad (8.13)$$

These parameters were used again in equation (8.9), for the final transformation between the "a priori" and the "adjusted" GEMT1 systems. Throughout this thesis the expression "GEMT1 system" will be used to refer to the "adjusted" system.

Table 8.1
Summary of the computation model used in SEASAT orbits

Period of study	From 0h September 18 to 0h September 21, 1978 MJD ∈ [43769.0 , 43772.0]
Celestial Reference System Terrestrial Reference System	J2000 GEMT1 system
Earth Parameters	a=6378137 m 1/f = 298.257 GM = 398600.436 c = 299792.458 km/s
Laser Station Coordinates	GEMT1 stations
Pole coordinates	BIH coordinates transformed to GEMT1 system
Geopotential	Variable (GEMT1, GEMT2, GRIM4_C2)
Precession	IAU, 1976
Nutation	IAU, 1980
Earth Tides	Wahr, 1980
Ocean tides	Schwiderski, 1980
Atmospheric Drag	Jacchia 1972 atmospheric model A/m = 0.0114 (m^2/kg)
Radiation Pressure	A/m = 0.0114 (m^2/kg)
Ephemerides	JPL DE-2000. Effects of Sun, Moon, Venus, Mars, Jupiter and Saturn included
Adjusted parameters	Start vector, daily drag coefficients, radiation pressure coefficient
Step length for integration	1.25 minutes for long arcs 0.50 minutes for short arcs
Laser data	20° cut-off elevation Marini-Murray tropospheric correction Centre of mass correction

8.2.2 Integration step length

When computing a satellite ephemeris by numerical integration, if a large number of computer runs is to be performed, the integration step length should be as large as possible to reduce the computing time. However it has to be short enough to cope with the short period perturbations due to the Earth's gravity field.

If a geopotential model such as GEMT1 is employed, complete to degree and order 36, the shortest wavelength described by the model is:

$$\lambda_{min} = \frac{40{,}000}{36} \text{ km} \cong 1100 \text{ km} \tag{8.14}$$

According to the sampling theorem, to detect these perturbations the minimum sampling interval has to equal half this wavelength (550 km). The satellite velocity projected onto the Earth's surface is approximately 6.7 km/s. The time taken by the satellite to sweep this distance is

$$t_{min} = \frac{550}{6.7} \text{ s} \cong 82 \text{ s} \tag{8.15}$$

Therefore, for a 36 degree model, a step length of about 75 seconds (1.25 minutes) is adequate.

If a model containing terms up to degree 50 is used, such as GEMT2, the step length should decrease to about 60 seconds. It will be demonstrated that in practice it is not necessary to apply a step length smaller than 1.25 minutes, since the last coefficients in the geopotential model have little influence on the solution.

During this study the effect of step length on orbit computation was investigated, with the aim of establishing the minimum step that should be used for the computation of orbits of satellites such as SEASAT or ERS-1. To do this, a 3-day SEASAT orbit which had been computed using a step = 1.25 minutes, was re-integrated using the same model (GEMT2) and the same starting values but different step lengths. These solutions are named L1, L2, L3 and L4 and are described in Table 8.2. The rms of fit is the same for all solutions: 0.30 metres.

The results show that truncation and convergence errors grow with step length (Table 8.2). These parameters are error estimates associated with the numerical integrator (Sinclair, 1988). Comparing these errors for solution L1 (step = 1.25) and L4 (step = 0.5), the last are about 10^6 smaller.

The differences between these solutions are presented in Table 8.3. The differences between orbits L1 and L2 are also plotted in Figure 8.1. The only component with significance in these differences is the along-track component. The differences in the across-track direction are always negligible. For the larger steps, the radial differences have an rms of about 2 decimetres, but for the smaller steps they are also negligible. The differences in the along-track direction increase linearly with time, the maximum values being reached at the end of the arc. So, orbits integrated with the same initial parameters and force model but different step sizes, have an along-track difference that increases linearly with time. The limit, i.e., the value after which it is not worth decreasing the step any further, is 0.5 minutes. Now when step size is halved (0.25 minutes), the along-track difference after 3 days is 4 cm which is within the accuracy of the observations.

Table 8.2
Orbits computed using the same force model and initial parameters
but different step lengths

Orbit	step (minutes)	number of steps	Max. convergence error (m)	Max. truncation error (m)
L1	1.25	3456	0.5x10-6	0.7x10-2
L2	1.00	4320	0.6x10-7	0.2x10-2
L3	0.50	8640	0.2x10-9	0.3x10-5
L4	0.25	17280	0.6x10-10	1.0x10-9

Table 8.3
Differences between solutions computed with different integration steps

Orbits	Total (m)		T (m)		A (m)		R (m)	
	rms	max	rms	max	rms	max	rms	max
L1 - L2	44.72	77.81	44.72	77.81	0.05	0.08	0.24	0.41
L1 - L3	42.99	74.72	42.99	74.72	0.05	0.07	0.22	0.39
L2 - L3	1.74	3.09	1.74	3.09	0.00	0.01	0.02	0.04
L3 - L4	0.02	0.04	0.02	0.04	0.00	0.00	0.00	0.00
L1 - L3A	0.01	0.03	0.01	0.03	0.00	0.00	0.00	0.01

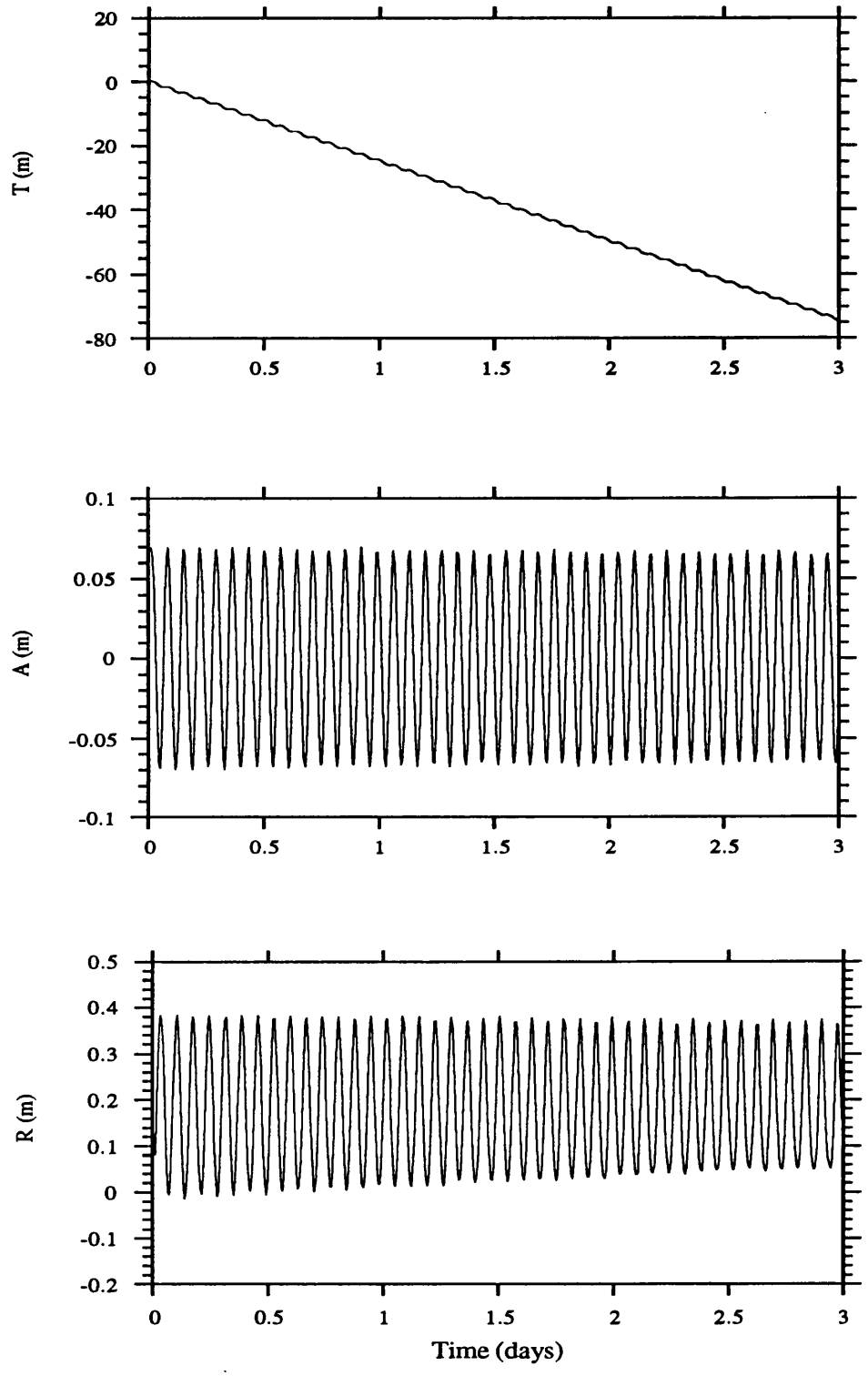

Figure 8.1 - T A R differences between orbits L1 and L3, computed with the same force model and initial parameters but different integration steps (step=1.25 versus step=0.50 minutes).

These results do not imply that one cannot use steps larger than 0.5 min. To prove that, orbit L3 (step = 0.5) was fitted to the same laser tracking data that had been used on the computation of orbit L1 (step = 1.25). This solution is named L3A. The difference between these solutions after fitting is presented in the last row of Table 8.3. Although initially these two orbits (L1 and L3) had a difference which after 3 days reached several metres, as the fitting process progresses they converge, and the final solutions are equivalent. Naturally the solved-for parameters will be different for both solutions, to compensate for the different step lengths.

In conclusion, the step length is an intrinsic characteristic of each solution computed by numerical integration. If an orbit is computed using a given step value, then it must not be changed on further computations involving this solution. A further conclusion is that a step length as large as 1.25 minutes can be employed on the computation of SEASAT orbits with geopotential models up to degree 50, without any appreciable loss of accuracy.

For the reasons explained above, a constant step length of 1.25 minutes was used on all long arc computations.

8.2.3 Centre of mass correction for laser data

The laser data used in SEASAT computations are described in Table 8.4. The positions of the laser stations were directly extracted from the GEMT1 file (Marsh et al. 1987), without need for any transformation.

The corrections applied to these data were the tropospheric correction using the Marini-Murray (1973) formulae and the centre of mass correction. For the first five stations the centre of mass correction was provided with the data (last column of Table 8.4). A simple correction algorithm was applied to the last three stations for which no correction was available.

Figure 5.8 illustrates the spacecraft symmetric shape relative to the satellite Z axis. The laser retro-reflector is positioned at the bottom of the cylinder, with its centre coincident with the base centre of the cylinder. The correction ΔR to be applied to the measured range to refer it to the satellite centre of mass can be written to sufficient approximation as (Figure 8.2):

$$\Delta R = A \cos \theta + B \sin \theta \qquad (8.16)$$

A - Distance between the centre of the laser retro-reflector array and the satellite centre of mass

B - Radius of the laser retro-reflector array

θ - Angle defined by the range direction and the satellite geocentric vector.

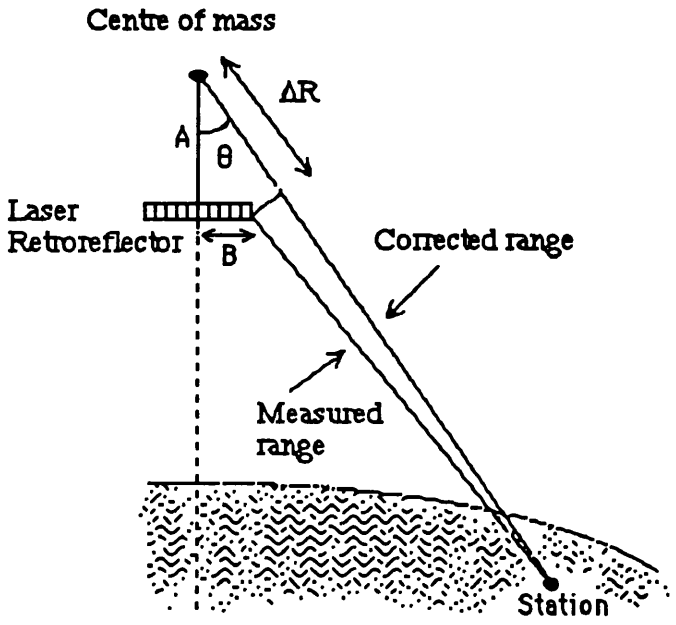

Figure 8.2 - Centre of mass correction for SEASAT laser data.

Using the known corrections (ΔR) for 5 of the stations, constants A and B were determined by least squares. The obtained values are:

$$A = 4.660 \text{ m}$$
$$B = 0.611 \text{ m}$$

These values were then used to compute the centre of mass correction for the three remaining stations (7833, 7903 and 7921) by using equation (8.16). This simple procedure proved to be very efficient, supplanting the need for a more complicated algorithm.

8.3 Solutions with laser data; the Reference Orbit

One of the aims of this study is to assess the feasibility of using reduced sets of tracking data for orbit determination. To determine the accuracy of these solutions the best possible orbit must be computed and used as a reference with which all other solutions could be compared.

It is not possible to make an assessment of the exact error of a computed ephemeris, because the "true" path of the satellite is not known. Two methods are frequently used for estimating the accuracy of a computed solution.

The first is the analysis of the rms of fit to tracking data. As the spatial and temporal coverages of these data are very limited, this method lacks information on areas where no data are available. For long arcs, if the data are well distributed, the solution is usually uniform, which means that the error should be of the same order all over the arc. However, with reduced sets of tracking data, small rms values are a very poor indicator of the accuracy of the orbit over the non tracked parts.

Table 8.4
SEASAT laser data for the period MJD ∈ [43769.00 , 43772.25] - LASER1

Station	Symbol	Location	Longitude (° E)	Latitude (°)	Height (m)	Passes	Points	C.M. corr.
7062	SDI	San Diego, California	243.15912	32.60080	992.1	5	921	Yes
7063	GRB	Greenbelt, Maryland	283.17221	39.02046	22.3	2	377	Yes
7067	BER	Bermuda Island	295.34392	32.35390	-19.3	4	259	Yes
7068	GND	Grand Turk Island	288.86811	21.46057	-15.1	2	57	Yes
7069	PAT	Patrick AFB Florida	279.39429	28.22804	-20.1	4	484	Yes
7833	KOO	Kootwijk, Holland	5.809896	52.17840	93.5	2	31	No
7907	ARE	Arequipa Peru	288.50687	-16.46567	2492.3	5	148	No
7921	HOP	Mount Hopkins Arizona	249.12192	31.68430	2352.9	4	42	No

The second method consists in computing the differences between solutions generated with different models. As both models are non exact, this mainly gives information on the accuracy of the less accurate model and does not detect errors common to both

models. It has however the big advantage of being global, i.e., of giving information about all parts in the arc. These differences are usually expressed along the three components: along-track (T), across-track (A) and radial (R). In this thesis these directions are defined by the unit vectors:

$$\vec{T} = \frac{\dot{\vec{S}}}{|\dot{\vec{S}}|} \qquad \vec{A} = \frac{(\vec{S} \times \dot{\vec{S}})}{|\vec{S} \times \dot{\vec{S}}|} \qquad \vec{R} = \frac{\vec{S}}{|\vec{S}|} \tag{8.17}$$

where $\vec{S}$ is the satellite geocentric position and $\dot{\vec{S}}$ the satellite velocity.

To generate a reference orbit for SEASAT, a solution was computed using all laser data available for the period MJD $\in$ [43769.0 , 43772.25]. The reason for using this slightly longer period of 3.25 days, is because there were no tracking data for the last 6 hours of September 20. This would obviously generate a poorly determined solution at the end of the arc, if a 3-day solution was computed.

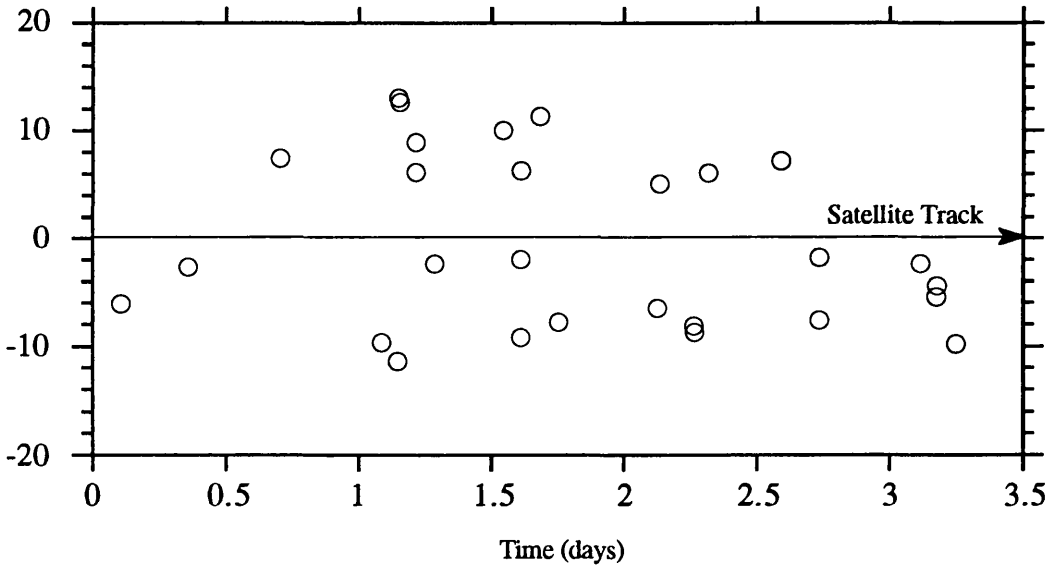

Figure 8.3 - Temporal distribution of SEASAT laser data (LASER1) for the period MJD $\in$ [43769.0 , 43772.25]. Each circle represents one pass. For each pass the Y axis represents the minimum angular distance between the satellite and the tracking station. If the station is on the left or on the right of the satellite track, the angular distance is considered respectively positive or negative.

The laser data available for this 3.25 day period comprise 25 passes from 8 stations. The quality of these data varies from station to station. In this solution the same accuracy was assumed for all stations with a standard deviation of 0.2 m. In the final iteration, considering a rejection level of 2 m and a minimum elevation of 20°, a set of 2319 measurements was processed, distributed as indicated in Table 8.4. This laser data set is referred to as LASER1.

Figure 8.4 illustrates the poor spatial distribution of these stations showing that most of them are located in North America. However the passes are fairly well distributed along the arc, as is illustrated in Figure 8.3.

Table 8.5

SEASAT orbits computed with different geopotential models

Orbits	Tracking data	Model	rms (m)
L1	LASER1	GEMT2	0.30
L5	LASER1	GEMT1	0.46
L6	LASER1	GRIM4_C2	0.29
P1	PRARE1	GEMT1	0.64

Table 8.6

Differences between SEASAT orbits computed with different geopotential models

Orbits	Total (m)		T (m)		A (m)		R (m)	
	rms	max	rms	max	rms	max	rms	max
L1 - L5	1.34	3.62	1.07	3.44	0.72	1.89	0.37	1.05
L1 - L6	0.96	2.47	0.73	2.44	0.57	2.30	0.27	0.98
L1 - P1	1.27	3.45	1.01	3.43	0.67	1.74	0.37	1.11
P1 - L5	0.45	0.88	0.39	0.84	0.20	0.30	0.06	0.09

The geopotential model used to generate this reference orbit was the best available model for SEASAT at the time of these computations: GEMT2. The adjusted parameters were the start position and velocity, the solar radiation coefficient and 3 drag coefficients, one

Figure 8.4 - Spatial distribution of SEASAT laser stations (LASER1) for the period MJD ∈ [43769.0 , 43772.25]

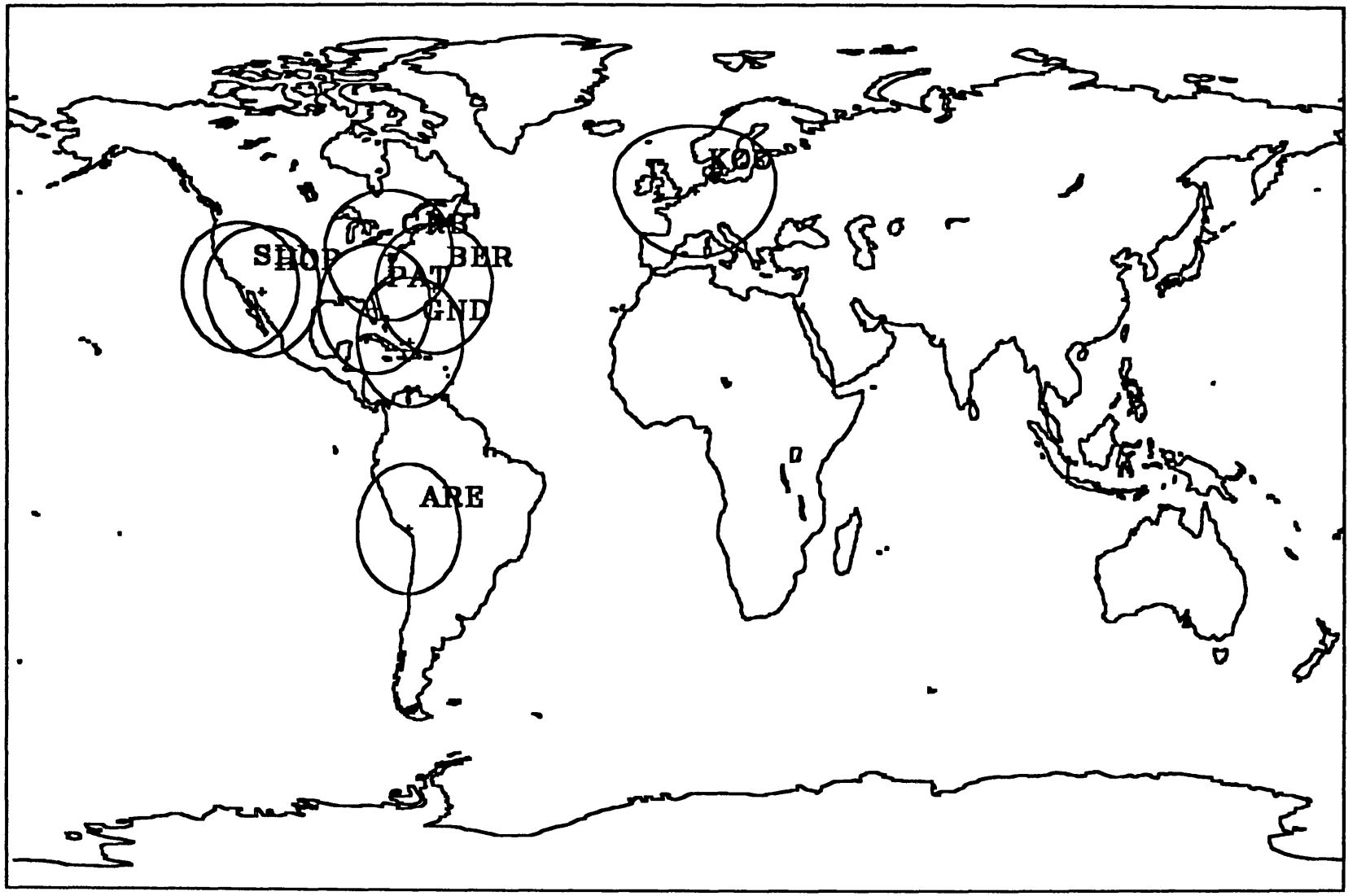

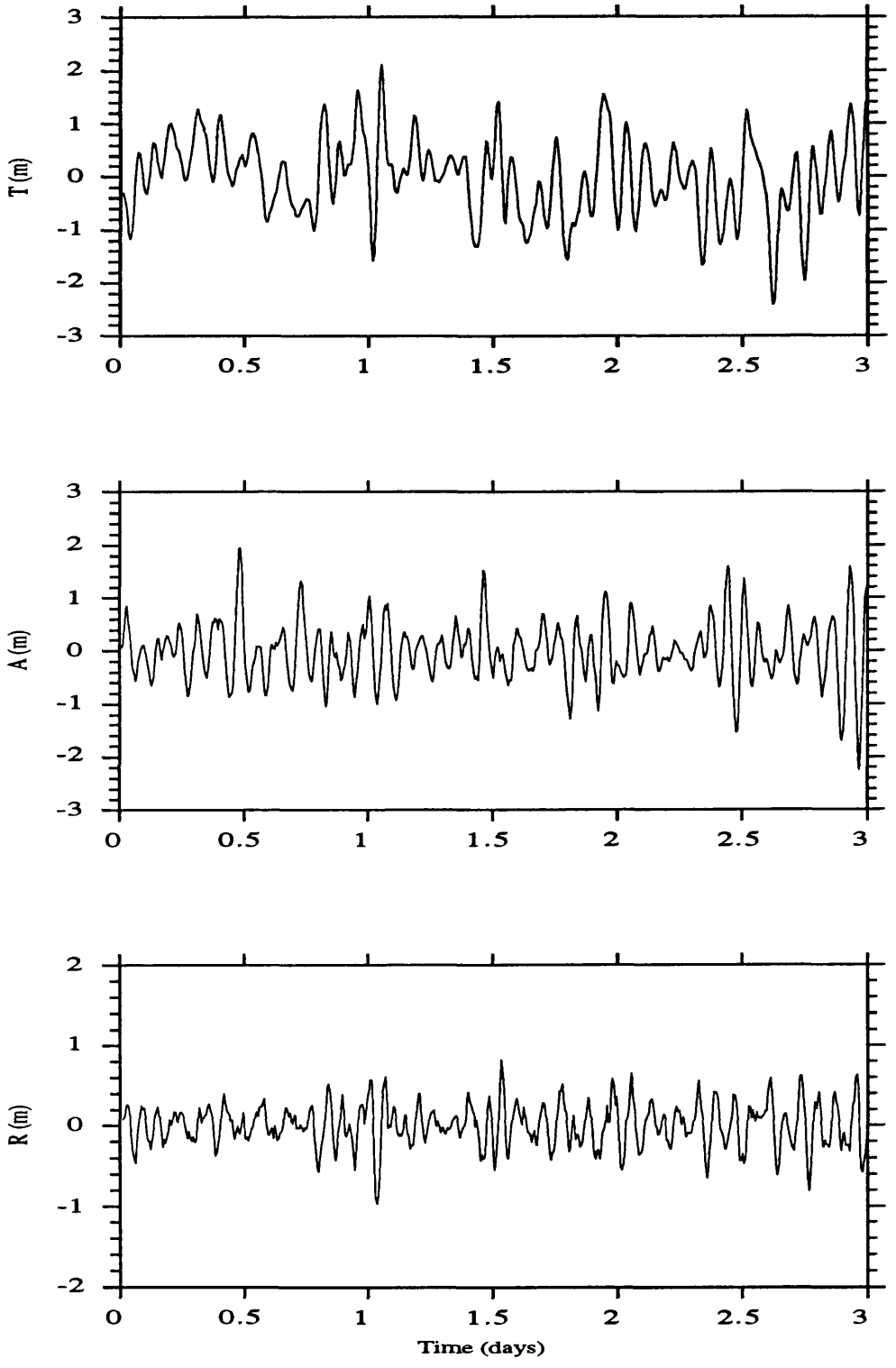

Figure 8.5 - TAR differences between orbits L1 and L6 (GEMT2 versus GRIM4_C2)

for each of the first two days and one for the last 1.25 days. This generated a solution with range rms residuals of 0.30 m. Due to the poor spatial distribution of the tracking data the rms of fit is probably an optimistic indicator of the ephemeris accuracy over the non-tracked parts. The actual global accuracy can be two to three times worse.

To have a more realistic estimate of the accuracy of this solution, the same computation was repeated using two different geopotential models: GEMT1 and GRIM4_C2 (Table 8.5). The differences between these solutions are presented in Table 8.6.

The solutions computed with GEMT2 and GRIM4_C2 have similar accuracy since they possess the same rms of fit. However their differences amount to 0.7, 0.6 and 0.3 m in the TAR directions respectively, with a global rms of 1 metre (Figure 8.5). These figures are a more realistic indicator of the actual accuracy of these ephemerides.

GEMT1 solution (L5) exhibits a larger rms than GEMT2 and GRIM4_C2 orbits, showing that the last two models are more accurate for SEASAT than GEMT1.

These figures are in agreement with published results for SEASAT. Wakker et al. (1987) computed GEMT1 solutions with rms in the range 48 to 62 cm. Using crossover differences, Marsh et al (1990a) predicted a radial error of 28 cm for SEASAT orbits computed with GEMT2. The 30 cm rms in the laser range residuals exhibited by solutions L1 and L6 contain errors in all components and therefore cannot be compared directly with the 28 cm radial error obtained using crossover analysis. However the differences between these two orbits (L1-L6) is of 27 cm in the radial direction which is a clear indication of the actual radial error in these solutions.

Orbit L1 described above will be referred to throughout this chapter as the reference orbit.

8.4 Solutions with PRARE and altimetry data

8.4.1 Solution with a full PRARE network

Having established the accuracy of SEASAT orbits obtained with laser data and various geopotential models, the aim is now to assess the accuracy of solutions computed with PRARE data.

As described in section 6.3, PRARE range observations were simulated for a network of 18 well-distributed stations. The orbit used to generate these observations was the reference orbit L1. This full network of 18 PRARE stations is named PRARE1 (Table 8.7).

Since these PRARE observations were generated using the state of the art geopotential model for SEASAT (GEMT2), in the analysis of these data the same model cannot be used, since any solution computed with the same model would fit exactly to the observations (the rms of fit would be equal to the standard deviation of the observations, 7 cm). Therefore, for the analysis of these PRARE data the GEMT1 geopotential model was used. This procedure was intended to simulate our imperfect knowledge of the gravity field. When comparing orbits computed with these PRARE data and GEMT1 with the reference orbit L1, the errors due to the gravity field are modelled as the differences between GEMT1 and GEMT2. This was believed to be a realistic estimate of the gravity field error for ERS-1. Later on, in Chapter 9, it will be demonstrated that this estimate is too optimistic.

In this analysis, errors due to the surface forces drag and radiation pressure were not considered. Most of the errors due to mismodelling of these forces are in the along-track component and are absorbed by solving for daily drag coefficients.

An orbit was computed using all PRARE1 data and GEMT1 (orbit P1 in Tables 8.5 and 8.6). Since these data are very well distributed in both spatial and temporal dimensions (see Figure 6.2), this solution represents the best SEASAT orbit that can be computed using the GEMT1 model. The rms of fit of this solution is 0.64 m. This rms of fit is greater than the rms of fit of the orbit computed with the same model and LASER1 data (orbit L5). This is a clear indication that a smaller rms of fit does not necessarily mean a better orbit. Although orbit P1 has a larger rms than orbit L5, the global accuracy of the two orbits is comparable since the difference between them (0.45 m rms) is of the order of the rms of fit (Table 8.6).

We can conclude that orbits with PRARE data have the same accuracy as laser orbits. The dominant error in all these solutions is due to errors in the geopotential. The differences between orbits L1 and P1 are an indication of the remaining errors on SEASAT solutions computed with GEMT1, irrespective of station configuration. These are of the order of 1.0, 0.7 and 0.4 m in the T, A and R directions respectively.

8.4.2 Solutions with reduced PRARE networks and altimetry data

In practice the tracking data available have a spatial distribution that is far from the ideal coverage represented by the PRARE1 tracking network. This section describes the research being done on the influence of tracking data distribution in the orbit accuracy and the extent to which altimetry data can be used to replace range data.

Wakker at al. (1983a) have considered the combination of altimetry with laser data, but in these solutions the distribution of the laser data was fairly regular with at least one pass per day. In practice sometimes there are intervals of one day or more during which there are no passes of range data. In the present study the influence of tracking data distribution along the arc is investigated in more detail.

To study the effect of tracking data distribution on the ephemeris accuracy, several configurations with only a few passes from one or two PRARE stations were considered. The reason for using PRARE instead of laser data is because at the time of this study it was expected that PRARE would play an important role in the tracking of ERS-1. According to the simulation process, the standard deviation of these PRARE observations is $\sigma_P = 0.07$ metres.

Results obtained with five of these configurations, named PRARE2 to PRARE6, are presented. These configurations are defined in Table 8.7. The temporal distribution of these data sets is represented in Figures 8.6 to 8.10.

The altimeter data set employed in these computations consists of SEASAT altimeter measurements for the period MJD $\in$ [43769.0 , 43772.0]. Although the original data set contains one measurement every second, to use these data for tracking purposes it is more appropriate to adopt a larger sampling interval. Since we are only interested in retaining the long wavelength component of these measurements, this procedure highly simplifies the data processing without information loss. Two sampling intervals were found to produce the same results: 30 sec and 60 sec. For simplicity a sampling interval of 60 seconds was employed, resulting in a data set of 2901 points covering the 3-day period.

These altimeter data were processed using the algorithm described in Chapter 7. This processing is controlled by a number of parameters:

Oversampling factor (OFAC) - As was explained in the previous chapter, the oversampling factor should be greater than 1. Since the Fourier functions are periodic in the sampled interval (3 days), using an OFAC = 1 causes the orbit error to be exactly equal at the beginning and end of the arc. To avoid this, an OFAC = 2 was used in all computations. This way the original interval is expanded into 6 days, and the periodicity constraint is applied to this interval, becoming undetectable in the original interval.

Cut off frequency (LFREQ) - This was chosen in such a way that the minimum period retained (PMIN) is close to 48 minutes. This is equivalent to using a cut-off frequency of two cycles per revolution. It is found that higher frequencies are corrupted with geoid errors and therefore should not be incorporated in the orbit error.

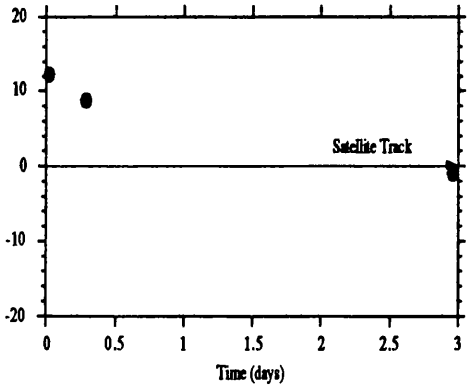

Figure 8.6 - Temporal distribution of PRARE2 data set

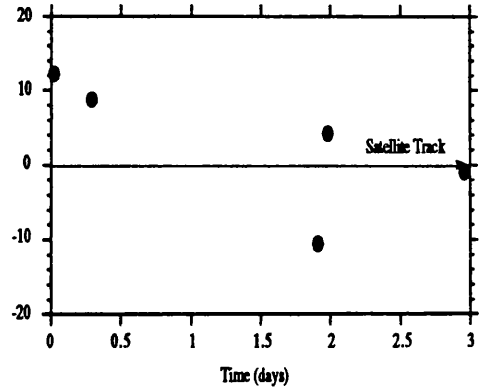

Figure 8.7 - Temporal distribution of PRARE3 data set

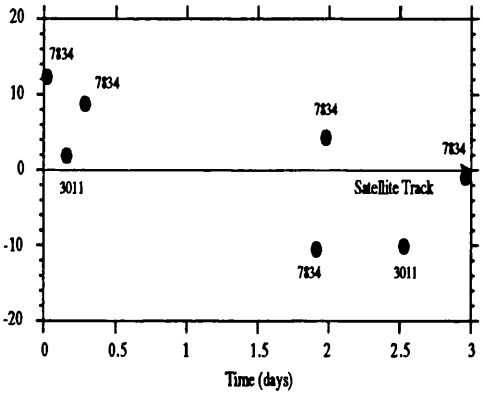

Figure 8.8 - Temporal distribution of PRARE4 data set

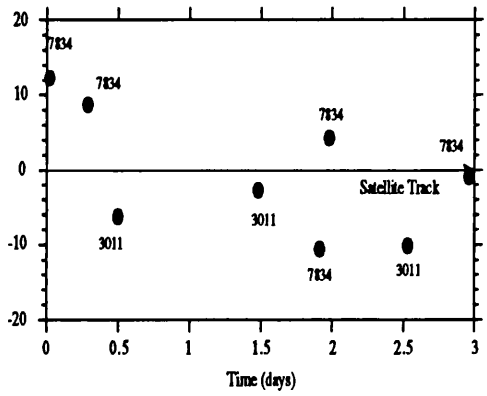

Figure 8.9 - Temporal distribution of PRARE5 data set

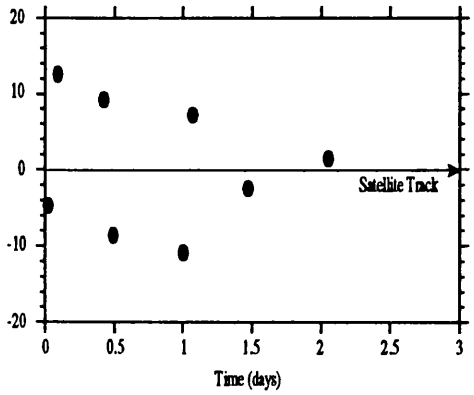

Figure 8.10 - Temporal distribution of PRARE6 data set. In all figures from 8.6 TO 8.10 the Y axis represents the angular distance (in degrees) between satellite and station (see also fig.8.3)

Standard deviation of the altimeter measurements - σ_a - It is very difficult to obtain a realistic estimate of the accuracy of the filtered altimeter measurements when used for tracking purposes. Assuming that the filtering process is correct, one estimate can be the so called altimeter "Noise", computed as the difference between the original altimeter residuals and the filtered residuals. Results suggest a value around 1 metre. In practice it is not relevant if the adopted value is close to the truth. The altimeter standard deviation should be regarded as a scaling factor, which determines the relative weight of these measurements in the final solution, when mixed with PRARE observations with a sigma $\sigma_P = 0.07$ m.

Table 8.7
Tracking data sets used in SEASAT computations for the period
MJD $\in$ [43769.00 , 43772.25]

Name	Description
LASER1	Laser data for 8 stations: 7062, 7063, 7067, 7068, 7069,7833, 7907, 7921
PRARE1	PRARE data for 18 stations
PRARE2	3 passes from PRARE station 7834 - 31 points
PRARE3	5 passes from PRARE station 7834 - 54 points
PRARE4	7 passes from PRARE stations 3011 and 7834 (2 + 5) - 79 points
PRARE5	8 passes from PRARE stations 3011 and 7834 (3 + 5) - 91 points
PRARE6	8 passes from PRARE station 3003 - 94 points
ALT1	Altimeter data - 2901 points at a sampling interval of 60 sec; Geoid computed from OSU89B (Rapp and Pavlis, 1990) considering terms up to degree and order 180

For each of these data sets an orbit was computed using PRARE data only. These solutions are named P2 to P6 (Table 8.8). In the next step altimeter data were added to each PRARE data set resulting in orbits P2A, to P6A.

Table 8.8 summarises the results obtained. For the solutions computed solely with range data, the only solution parameters presented in the table are the rms and maximum values of fit to data. For the solutions computed with range and altimeter data, several altimeter parameters are presented. The fifth column represents the rms of the altimeter residuals after fitting (only the filtered part). This parameter is an indication of the remaining radial

error in the computed solution. The sixth column represents the altimeter Noise (difference between the total and the filtered residuals). This noise parameter is a measure of the accuracy of this tracking data type. The last column shows the average of the total altimeter residuals. Several authors have found that this average has values from about 0.7 m to one metre: 0.75 m (Rapp, 1987), 0.86 m (Marsh et al., 1990b) and 0.90 m (Engelis and Knudsen, 1989). This bias is attributed to an error in the adopted GRS80 ellipsoid (Moritz, 1980). For this reason, in most of the computations, a constant altimeter bias (ALTBIAS) of -0.80 m was applied to all altimeter measurements.

Table 8.8
SEASAT orbits computed with PRARE and Altimetry

Orbit	Tracking data	Altimeter parameters			PRARE residuals (m)		Altimeter residuals (m)		Alt. Noise (m)	Alt. Average (m)
		σ_a (m)	PMIN (min)	ALTBIAS (m)	rms	max	rms	max	rms	
P2	PRARE2		—		0.23	0.51	—		—	—
P2A	PRARE2 + ALT1	0.1	48	-0.80	0.18	0.43	0.71	2.18	0.96	0.11
P3	PRARE3		—		0.11	0.32	—		—	—
P3A	PRARE3 + ALT1	0.3	48	-0.80	0.29	0.61	0.72	2.05	0.96	0.13
P3B	PRARE3 + ALT1	0.3	48	0.00	0.41	0.78	1.07	2.93	0.96	0.87
P3C	PRARE3 + ALT1	1.0	48	-0.80	0.09	0.23	0.82	2.60	0.96	0.18
P4	PRARE4		—		0.15	0.50	—		—	—
P4A	PRARE4 + ALT1	0.3	48	-0.80	0.36	0.82	0.74	2.10	0.96	0.15
P5	PRARE5		—		0.41	1.19	—		—	—
P5A	PRARE5 + ALT1	0.5	48	-0.80	0.43	1.10	0.72	1.99	0.96	0.13
P6	PRARE6		—		0.25	0.81	—		—	—
P6A	PRARE6 + ALT1	0.5	48	-0.80	0.81	2.39	0.71	2.16	0.95	0.10

The results obtained for each tracking configuration are described.

1 - The first configuration (PRARE2) was chosen to be close to the limit of a very poor 3-day arc tracking network. It consists of only three passes of one station (7834) two at the beginning of the arc and one at the end (Figure 8.6). With only these tracking data it

is not possible to compute a solution by solving for all the usual parameters. The normal matrix will be poorly conditioned and several parameters come up with correlations equal to 1. A simple solution is to solve for only the start vector, keeping drag and radiation pressure coefficients constant. This was the procedure used in the computation of orbit P2. The rms of fit of this solution is 0.23 m, but this is only an indication of the accuracy of the orbit in the tracked areas. The global accuracy is very poor as indicated by the differences to the reference orbit (Table 8.9 and Figure 8.11). These differences demonstrate a strong one cycle per revolution signal, with an amplitude of 15 m in the T component and about 4 metres in the A and R components. Such a large amplitude is a clear indication of a very unstable solution. Therefore with such a poor configuration no reliable solution can be obtained.

Table 8.9
Differences between reference and orbits computed with PRARE and Altimetry
(Meaning of orbit names explained in Table 8.8)

Orbits	Total (m)		T (m)		A (m)		R (m)	
	rms	max	rms	max	rms	max	rms	max
L1 - P2	9.17	19.92	8.43	19.77	2.13	4.25	2.92	4.80
L1 - P2A	3.39	7.96	3.21	7.93	1.01	2.53	0.40	1.22
L1 - P3	5.63	12.78	5.41	12.69	0.84	2.15	1.21	2.82
L1 - P3A	1.72	3.70	1.30	3.66	1.06	2.63	0.38	1.24
L1 - P3B	1.74	3.87	1.24	3.71	1.14	2.80	0.44	1.25
L1 - P3C	3.14	6.31	2.91	6.22	1.09	2.72	0.41	1.27
L1 - P4	4.37	9.63	4.17	9.51	0.87	2.20	0.96	2.40
L1 - P4A	1.69	3.68	1.44	3.67	0.82	2.12	0.39	1.26
L1 - P5	1.54	3.60	1.24	3.59	0.83	2.10	0.38	1.13
L1 - P5A	1.46	4.18	1.14	4.18	0.83	2.11	0.38	1.23
L1 - P6	1.88	6.47	1.62	6.43	0.86	2.08	0.40	1.26
L1 - P6A	2.16	7.09	1.93	7.05	0.85	2.07	0.45	1.44

A second orbit (P2A) was then computed by adding altimetry to these three passes of range data. The results are shown in Figure 8.12. To make the comparison of the two orbits (P2 and P2A) easier, the same scale is used in the graphs of Figures 8.11 and 8.12. A similar procedure was adopted for all the other configurations. The improvement

is remarkable particularly in the radial component where the errors decreased from an rms of 2.9 m to 0.4 m. The amplitude of the along-track error was also greatly reduced. The improvement in the A component is the less noticeable, confirming that altimeter data lacks information in this direction.

2 - The second configuration was created by adding two passes to the previous data set, close to the end of the second day (Figure 8.7). There still is a gap of about two days during which there are no tracking data. A solution is now possible (P3) using the conventional solved-for parameters, although correlations as high as 0.9 still exist between some of the parameters. The differences to the reference orbit are still very large amounting to 5.4, 0.8 and 1.2 m in the T, A and R directions respectively (Figure 8.13). The amplitude of these differences is now smaller than on the previous solution (P2). The main signature in these differences is the big increase in the T component errors, in the area of the arc where no tracking data are available, revealing that the accuracy of the solution is not uniform along the arc.

As before, an orbit was computed by adding altimetry to the PRARE3 data (orbit P3A). As shown in Figure 8.14, the altimeter data are strong enough to make the previous along-track pattern disappear, making the solution uniform along the whole arc.

To illustrate the influence of the altimeter standard error and the altimeter bias in the solution, two more solutions are presented for this configuration: P3B and P3C. These solutions are identical to P3A except for:

P3B - no altimeter bias was applied (ALTBIAS = 0)

P3C - Altimeter sigma σ_a =1 m

Comparing solution P3B with P3A we see that the averages of the altimeter residuals differ by about 0.8 m (last column of Table 8.8). The fact that the fitting process does not absorb this constant bias, indicates that this bias is not an orbit error. This is further illustrated in the differences between these two ephemerides (Figure 8.15). If this bias were part of the orbit error then it would be absorbed and these orbits computed using different bias would have a constant shift in the radial component. These results justify the use of a constant altimeter bias in all other solutions.

Comparing orbits P3A and P3C we see the influence of the altimeter sigma in the solution. The value of σ_a =1 m is certainly closer to the true accuracy of the altimeter data than the value σ_a = 0.3 m. However the influence of altimeter data in the solution in the first case is not strong enough to balance the lack of range data. In fact it is found that

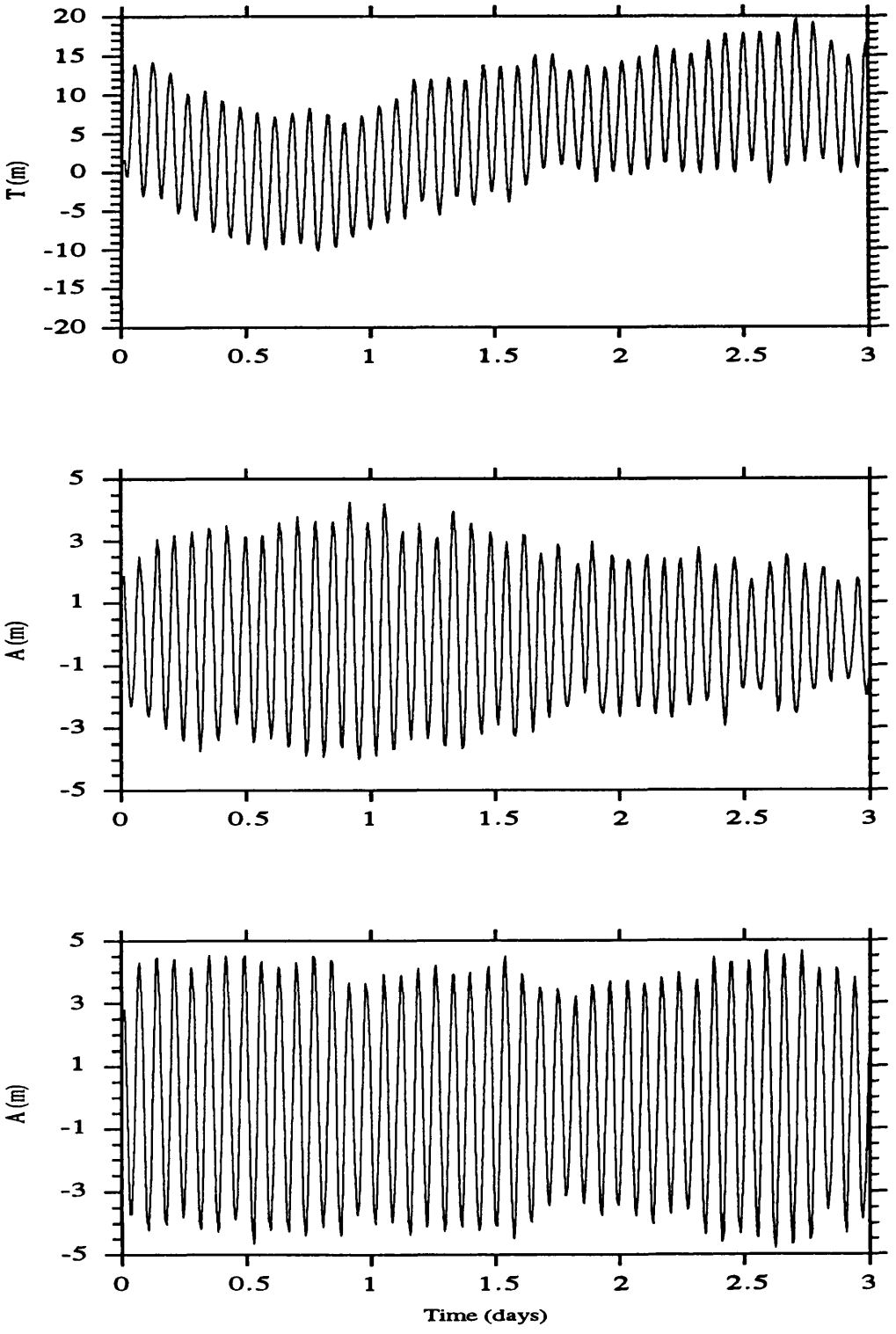

Figure 8.11 - TAR differences between orbits L1 and P2.

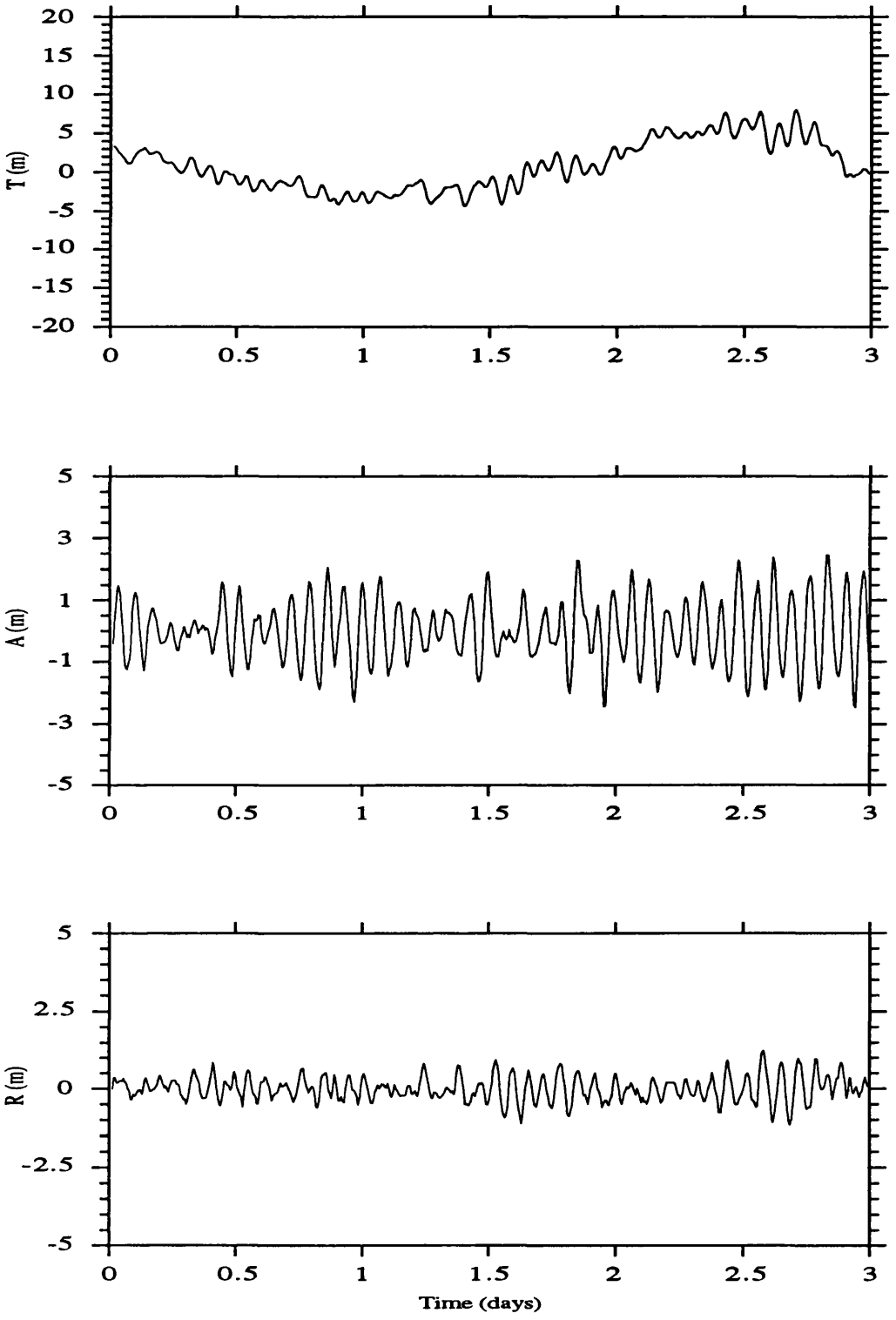

Figure 8.12 - TAR differences between orbits L1 and P2A.

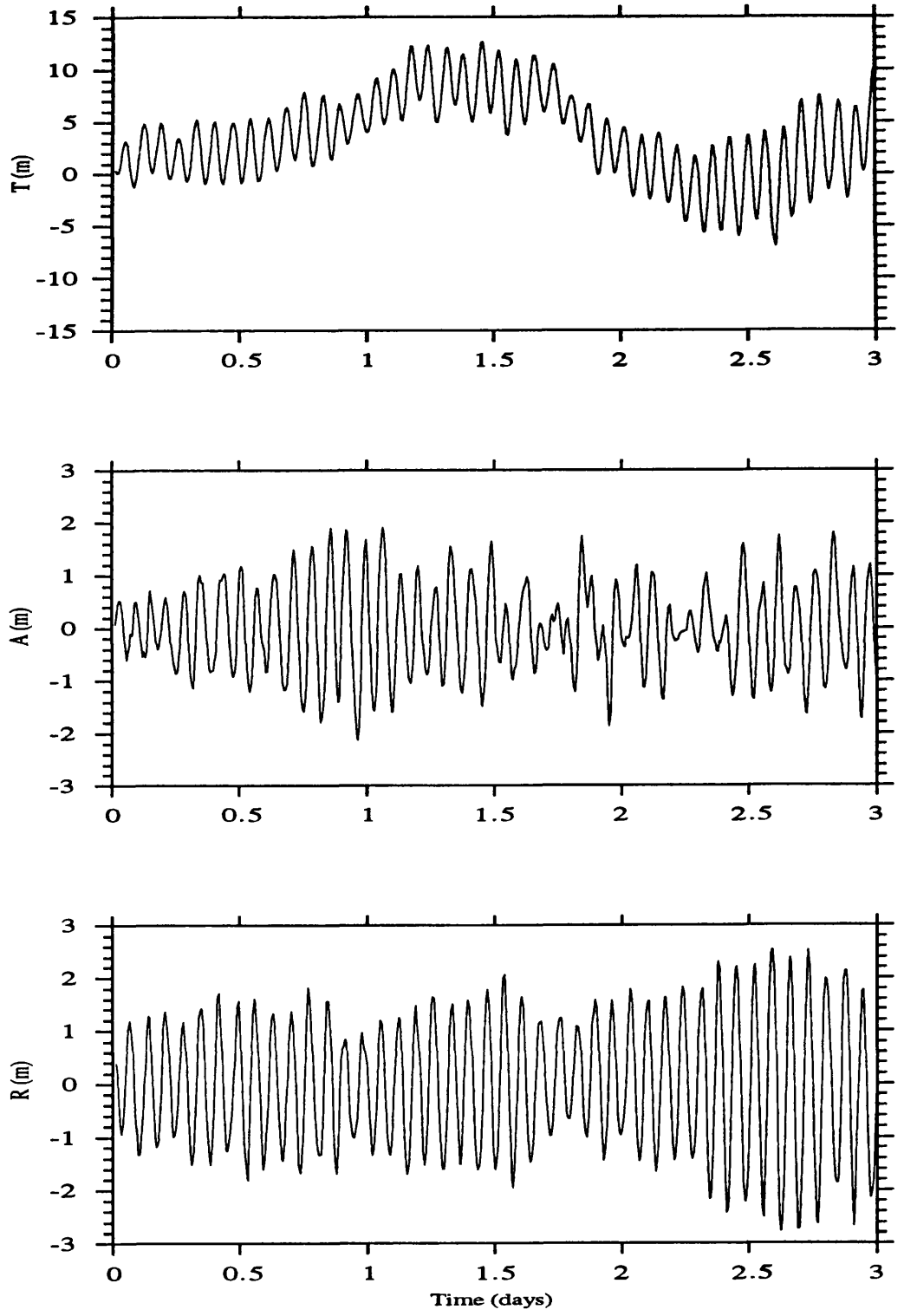

Figure 8.13 - TAR differences between orbits L1 and P3.

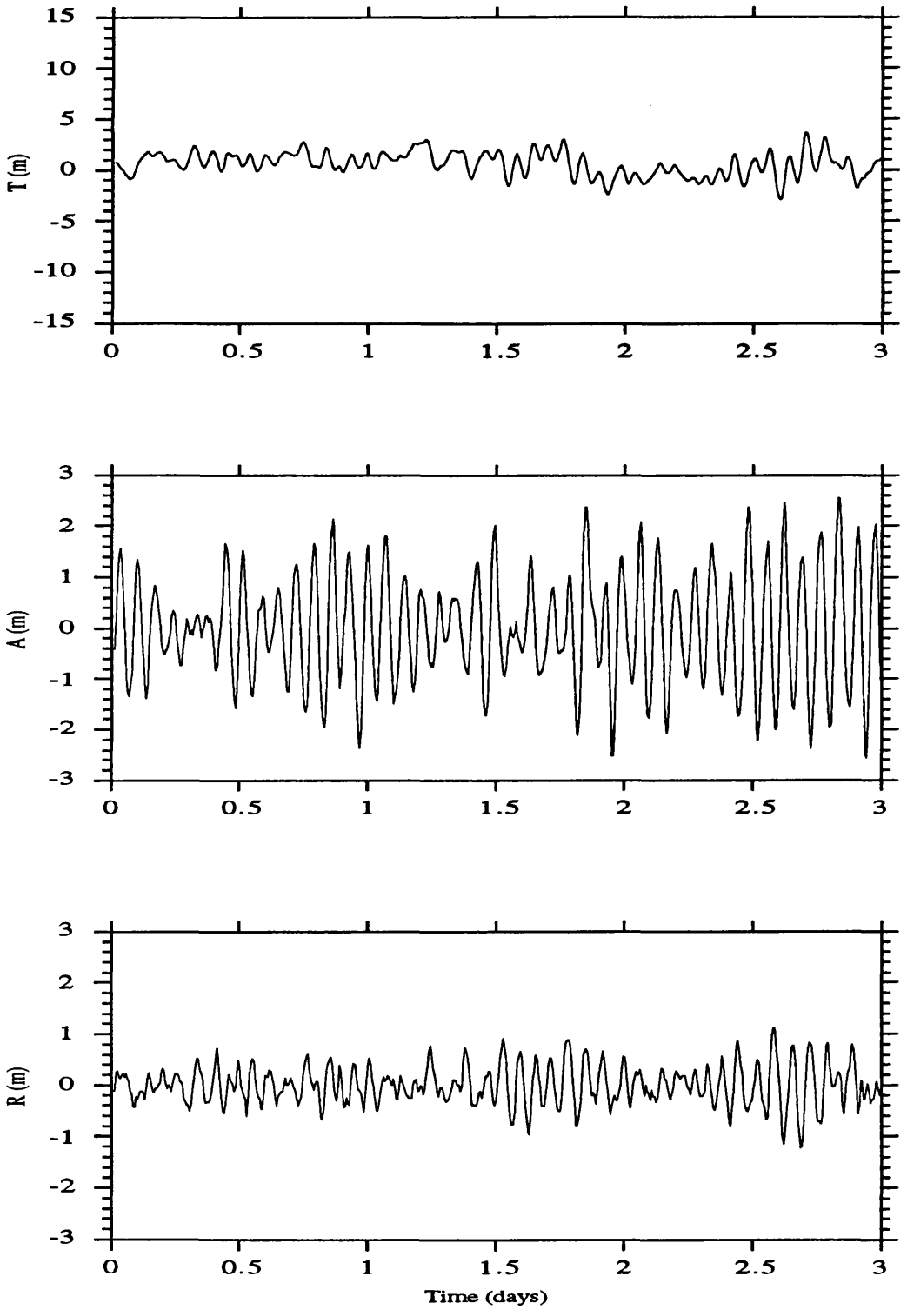

Figure 8.14 - TAR differences between orbits L1 and P3A

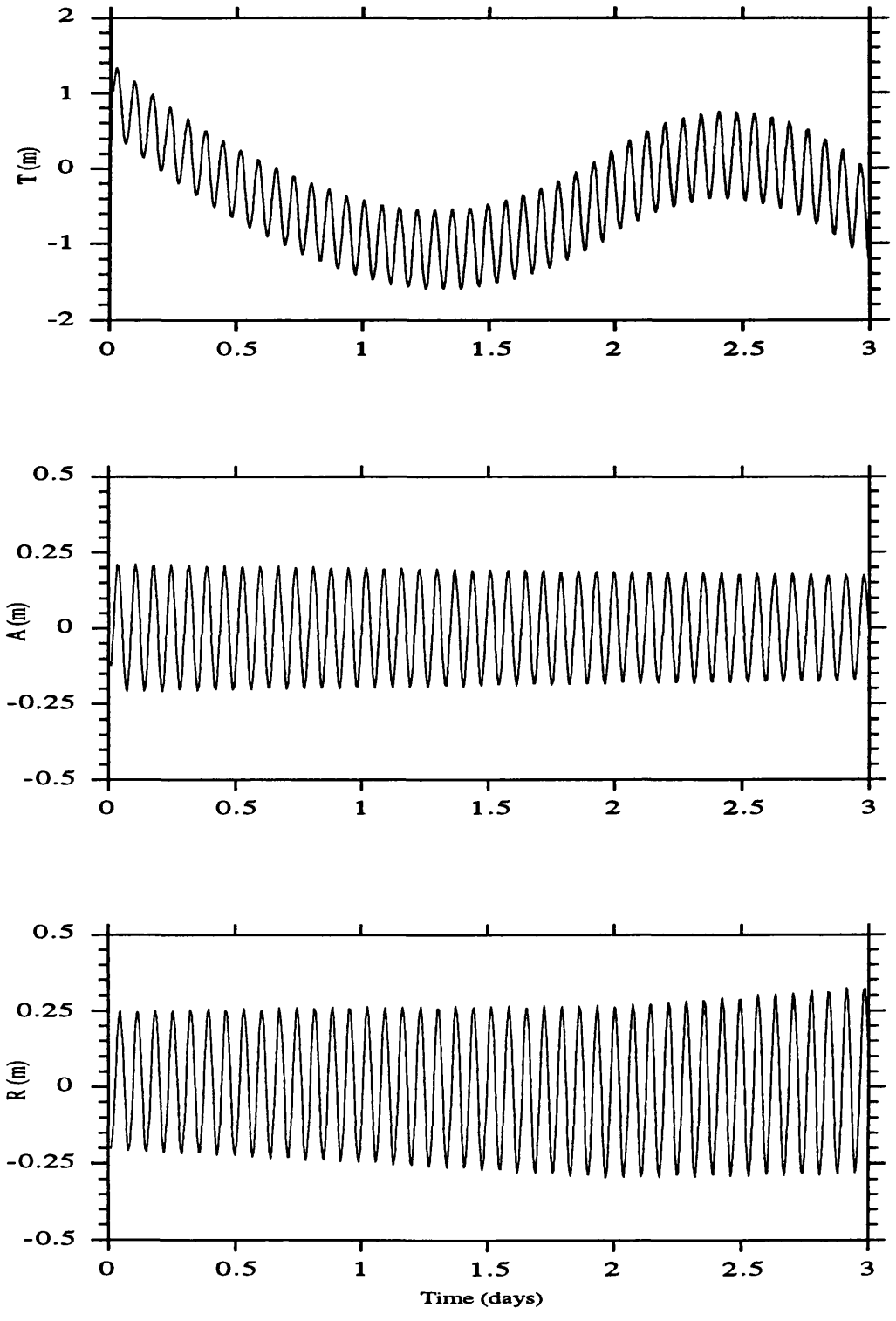

Figure 8.15 - TAR differences between orbits P3A and P3B.

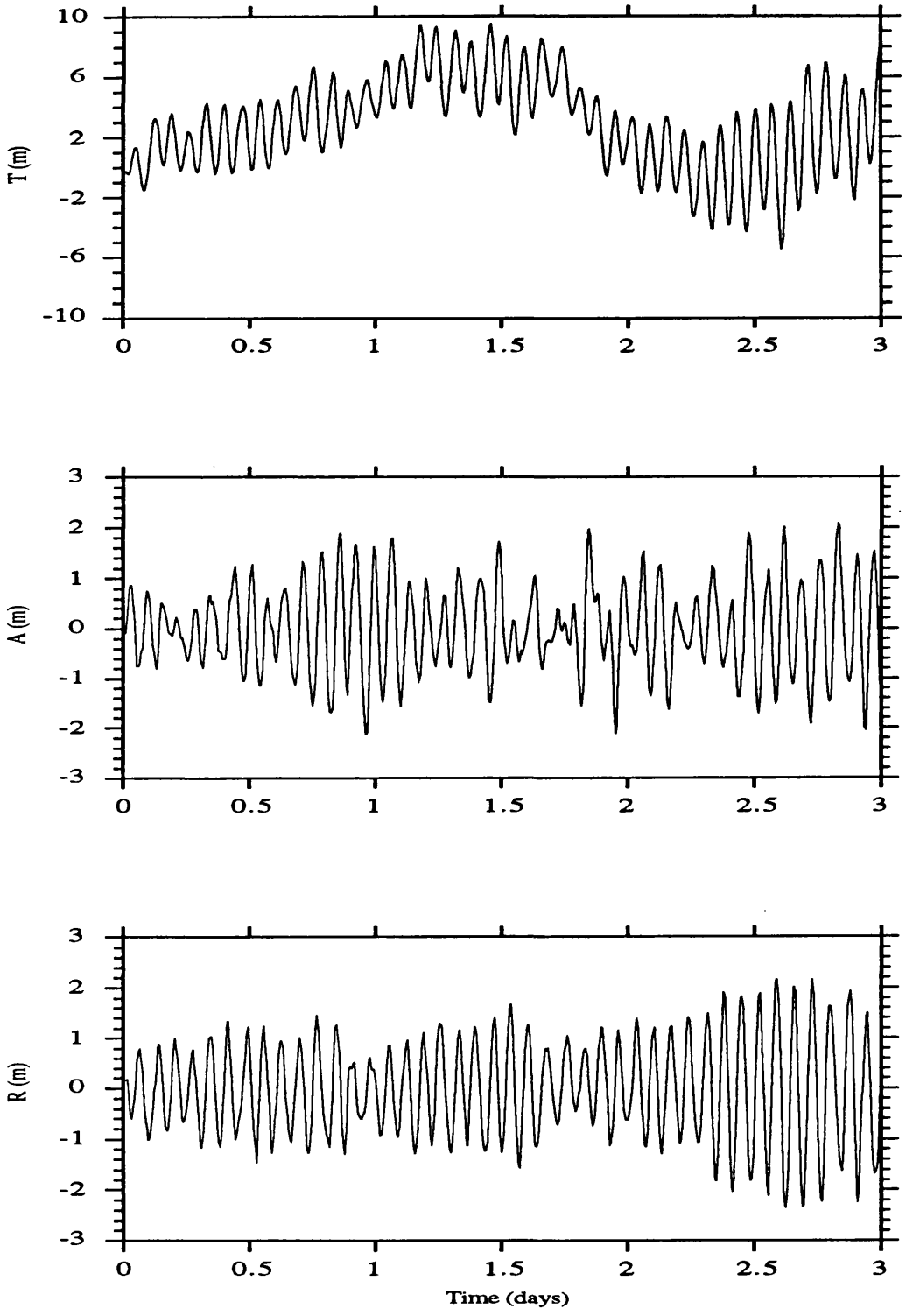

Figure 8.16 - TAR differences between orbits L1 and P4.

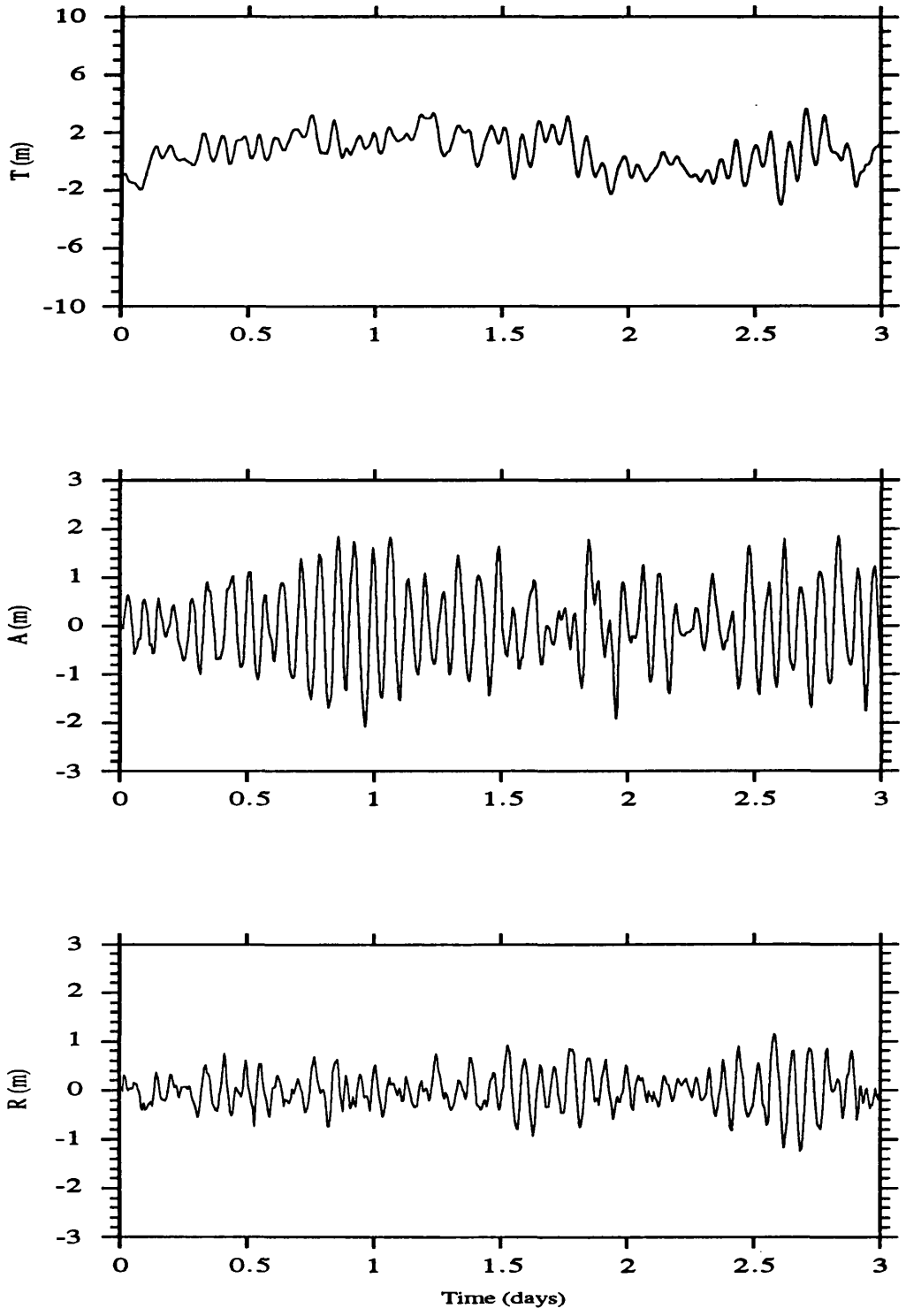

Figure 8.17 - TAR differences between orbits L1 and P4A.

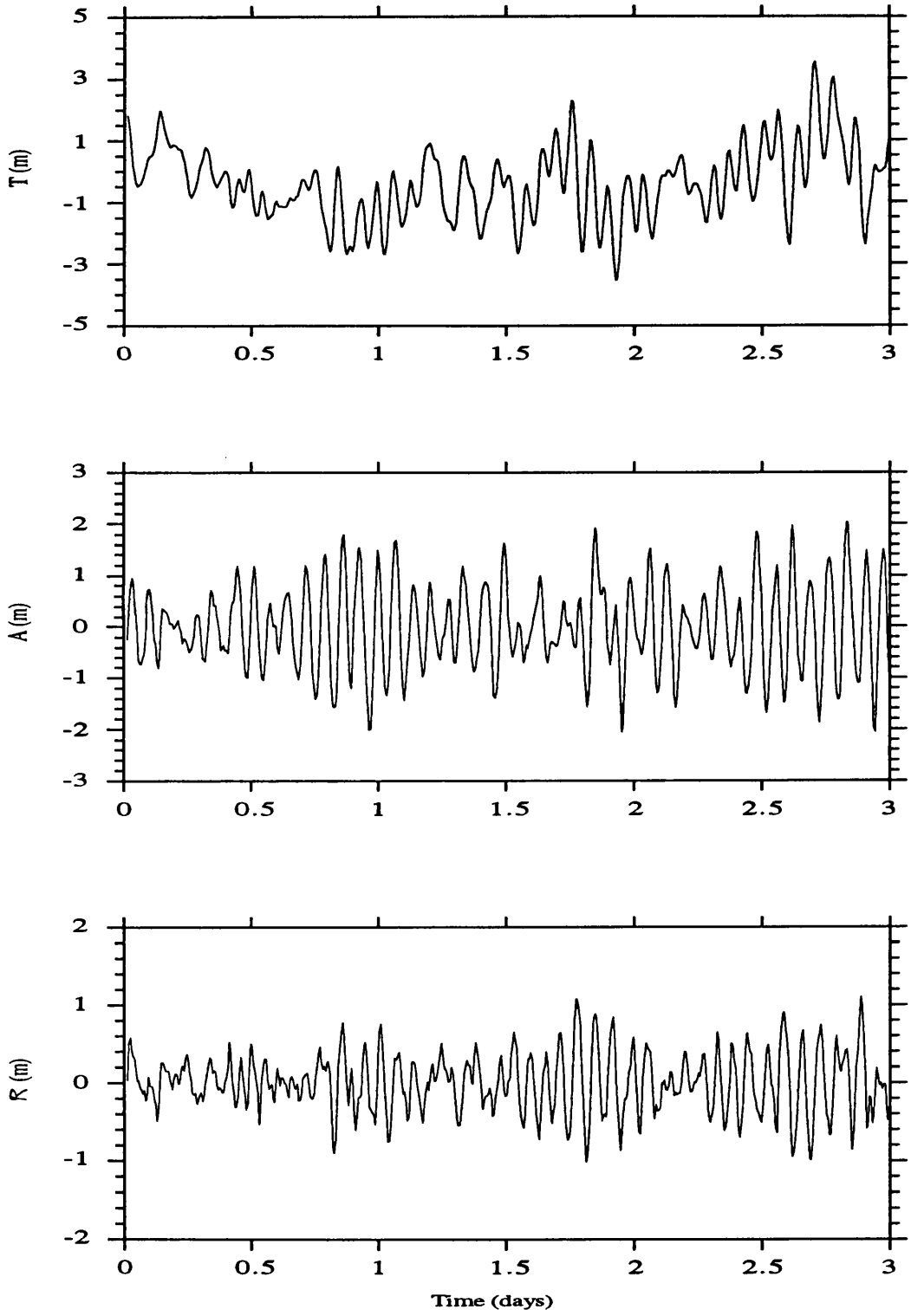

Figure 8.18 - TAR differences between orbits L1 and P5.

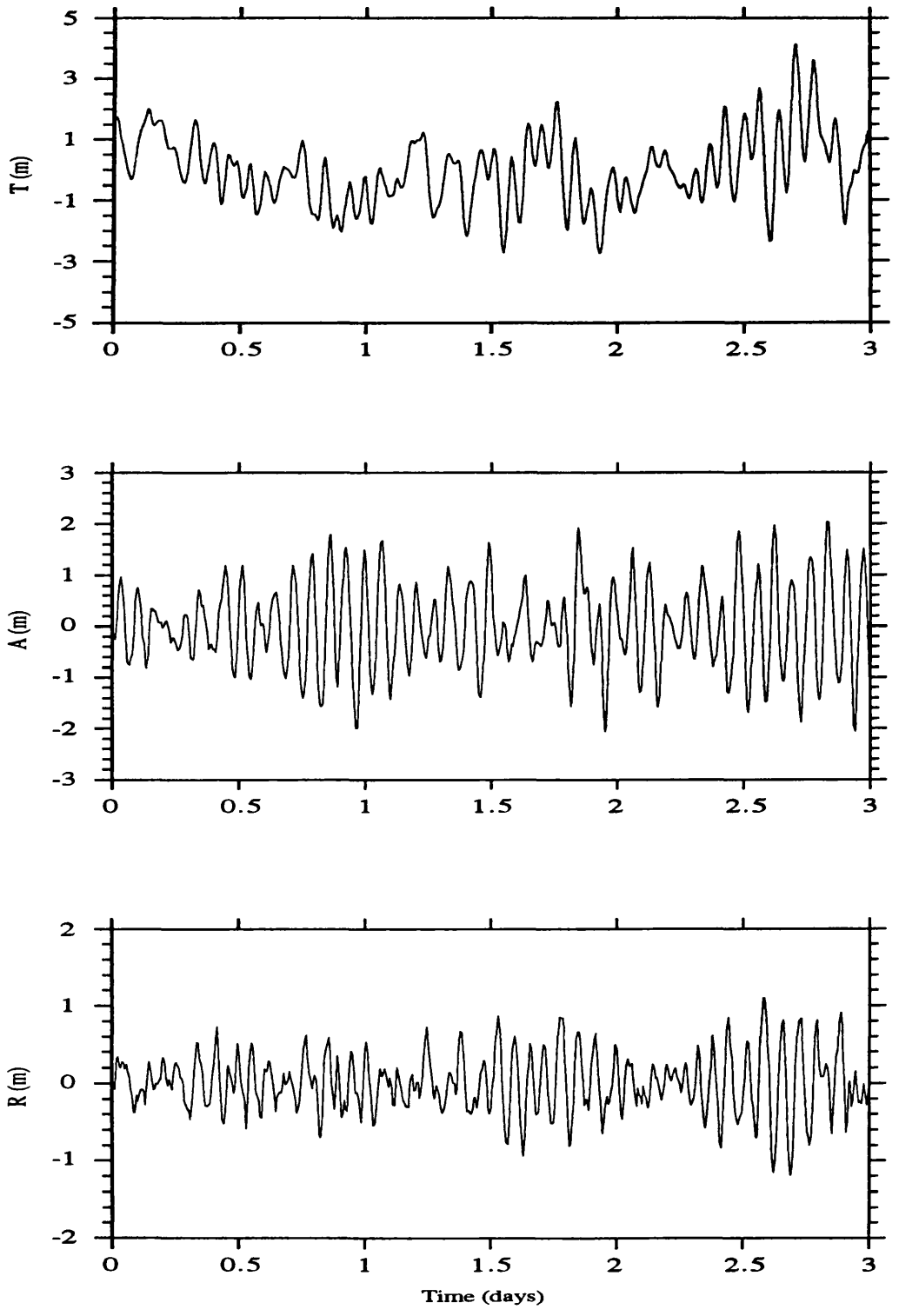

Figure 8.19 - TAR differences between orbits L1 and P5A

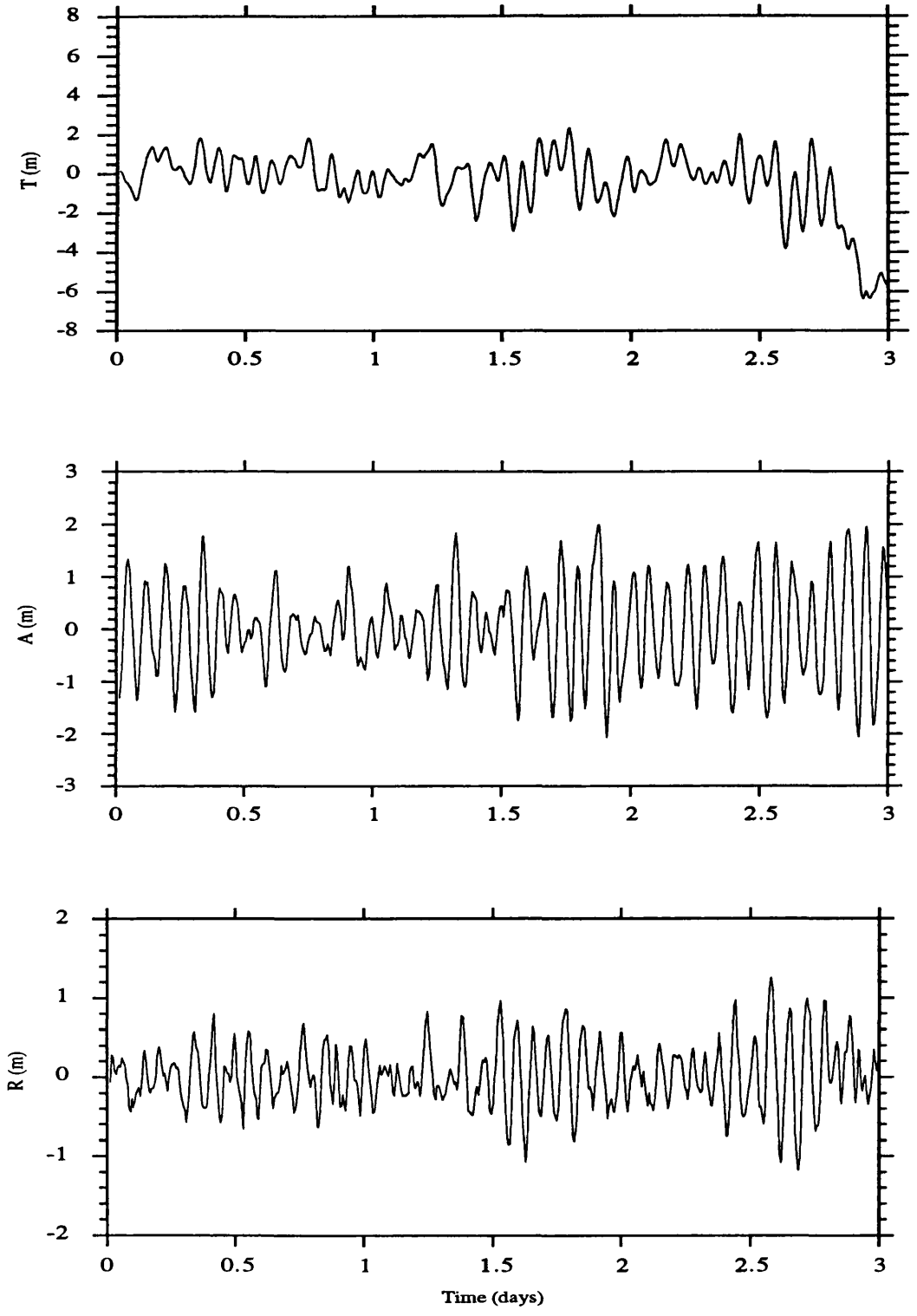

Figure 8.20 - TAR differences between orbits L1 and P6

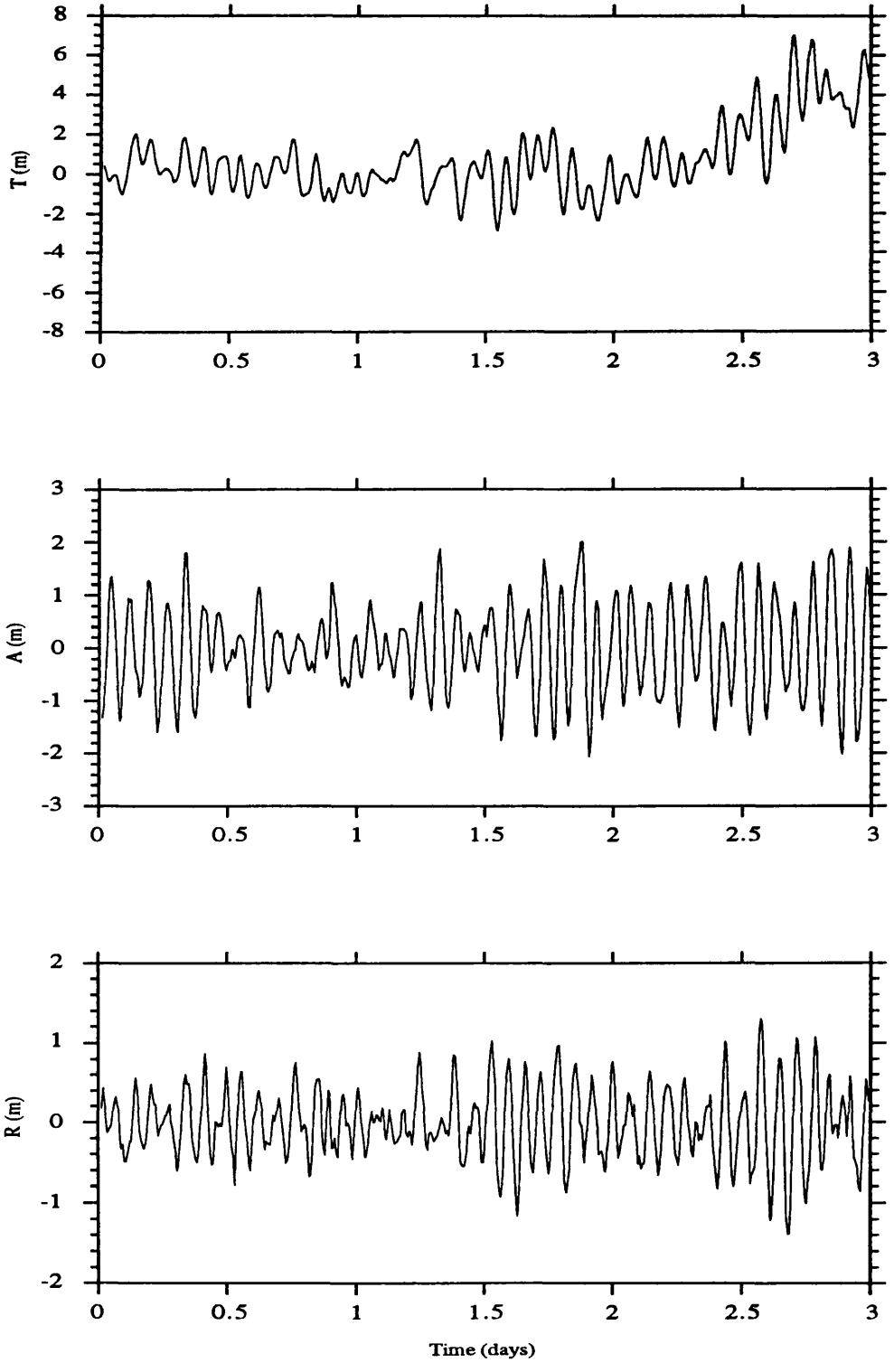

Figure 8.21 - TAR differences between orbits L1 and P6A

when altimeter data are mixed with reduced networks of range data, the fewer range data points are used, the smaller should be the value of altimeter sigma, i. e., the larger should be the altimeter weight so that the solution becomes more constrained.

To understand the influence of the data standard deviations in the solution we have to remember that each altimeter measurement is multiplied by a weight factor $\omega_a = 1/\sigma_a^2$, and each PRARE measurement is multiplied by a factor $\omega_P = 1/\sigma_P^2 = 1/(0.07m)^2 \cong 200$. Therefore if $\sigma_a = 1$ m each PRARE measurement has a weight 200 times larger than each altimeter measurement. In the case of the PRARE3 data set, composed of 54 points, the PRARE data will have a weight equal to 200 x 54 = 10 800 , much larger than the 2900 altimeter measurements. In the solution P3A where $\sigma_a = 0.3$ m the total altimeter weight becomes $2900 / (0.3^2) \cong 32000$ therefore dominating the solution.

3 - The third configuration is composed of 7 passes from two stations, 3011 and 7834 (PRARE4), maintaining a gap of about two days during which no tracking data are available (Figure 8.8). The solution computed with only these data (P4) is very similar to the previous solution computed with 5 passes from only one station. The differences to the reference orbit reveal the same along-track pattern with larger errors in the area with no tracking data (Figure 8.16). Again the addition of altimetry (P4A) reduces the errors by a factor of 3 in both T and R directions removing the along track error pattern in the middle of the arc (Figure 8.17).

4 - The fourth configuration is constituted by 8 passes from the same stations (Figure 8.9). The main difference relative to the previous configuration is that now the largest interval during which there are no tracking data is reduced to about one day. The orbit computed with only this PRARE data (P5) is now much better determined with a uniform error distribution along the arc (Figure 8.18). The addition of altimetry (P5A) apparently does not improve the accuracy of the solution (Figure 8.19), but the solved-for parameters are better determined, revealing smaller correlations between them. In this solution a slightly larger altimeter sigma was used (0.5 m), but the solution with sigma = 0.3m is equivalent.

5 - The last configuration is formed by 8 passes from station 3003, the last pass being at the beginning of the third day (Figure 8.10). Therefore there are no tracking data for the last 22 hours of the arc. An orbit was computed with only these tracking data (P6), solving for the start vector, solar radiation coefficient and two drag coefficients, one for the first day and another for the last two days. The differences of this solution to the

reference orbit are presented in Figure 8.20. It is evident that the errors increase very quickly towards the end of the arc, showing that these solutions are not reliable at any time after the time corresponding to the last pass. This confirms a well known result that ephemerides computed by fitting to tracking data cannot be extrapolated outside the tracking interval.

The addition of altimeter data (P6A) does not solve the problem (Figure 8.21). As in the previous solution the along-track errors have a large increase towards the end of the arc. The conclusions are that altimetry data are a very helpful tracking data type to fill gaps of range data but not to extrapolate range data for more than a few hours after the last pass.

To assess the feasibility of using altimeter data alone, a solution was computed using altimetry data alone and using a set of starting values giving range rms of 280 metres and an altimeter rms (filtered residuals) of 2.14 m. After the adjustment to altimetry data alone the rms became 306 m for range and 0.59 m for altimeter. The differences of this solution to the reference are as large as 0.6 km along-track and 1.3 km across-track. However the radial difference is only 0.75 m. These results leave no doubt about the weakness of the along track and total absence of across-track information in altimeter data.

From these results several conclusions can be withdrawn.

Altimeter data alone cannot be used as tracking data for orbit determination. In spite of the weakness of this data type when used alone, only a few passes of range data are sufficient to add the necessary along-track information to obtain a stable and reliable solution.

The results show that altimetry can fill gaps of range data covering periods as long as two days. It is important to note that these gaps should be between passes of range data and not for example at the end of the arc. This means that altimetry can only be used to interpolate range data, but not to extrapolate.

The application to ERS-1 of these results obtained for SEASAT, is limited to the existence of a suitable geopotential model for this satellite. This model should produce ERS-1 orbits with similar accuracy to SEASAT orbits derived with GEMT1. This means that the rms range residuals for a 3-day arc tracked by a suitable network of laser stations, should be about 0.6m. If the actual model gives an rms of fit larger than this by a certain amount, the results will have to be scaled by the same amount.

The results presented in chapter 9 show that the present models for ERS-1 yield orbits with rms range residuals about three times these figures ($\approx$ 1.5 m). This constitutes a serious limitation for the scientific applications of ERS-1 data requiring satellite positions

at decimetre accuracy. This indicates the need for the development of short arc techniques whereby precise orbits can be obtained over regions of particular interest that are tracked by several stations. This is the subject of chapter 10 where the research carried out during this project on the development of short arc methods is presented.

Chapter 9

ERS-1 long arcs

9.1 Introduction

This chapter describes the work done on the computation of the orbit of ERS-1. The aim of this exercise is twofold. First to assess the accuracy of ERS-1 long arc ephemerides computed with the existing models. Second, to develop techniques to improve these solutions. Some aspects of the modelling of the two main forces affecting satellite's motion (the gravitational attraction and atmospheric drag) are investigated.

In these computations laser data were the unique tracking data type used. At the time of this study the only altimeter data available were the altimeter fast delivery URA product. The time tag of the altimeter measurements in the URA product is 1 millisecond. Since the satellite velocity is 7 km/s, during 1 millisecond the satellite moves 7 metres in the along-track direction. By comparison, since the maximum radial velocity is 10 m/s, the maximum radial displacement during the same time is only 1 cm. Therefore the addition of these altimeter data to range data would improve the orbit in the radial direction, but certainly not in the along-track direction.

Another reason for not using these altimeter data is that the URA product does not provide the geophysical corrections, namely the corrections due to Earth and Ocean tides. For the first effect, it is straightforward to write an algorithm for computing the radial displacement of a point due to Earth tides. The effect of ocean tides is much more difficult to model, requiring a knowledge of the phenomenon that is out of the scope of this thesis.

9.2 Computational model

At this stage the SATAN programs were set up for the computation of SEASAT orbits. The adaptation of the programs for the computation of the orbit of the ERS-1, required the conversion and rewriting of some of the algorithms. This section describes the main aspects of the computation model which had to be particularised for ERS-1. This model is summarised in Table 9.1.

Table 9.1

Summary of the computation model used in ERS-1 orbits

Periods of study	ARC_A - from 6 h February 4 to 9.6 h February 11 MJD ∈ [48656.25, 48661.4] ARC_B - from 19.2 h February 12 to 0 h February 16 MJD ∈ [48664.80, 48668.0]	
Celestial Reference System	J2000	
Precession	IAU, 1976	
Nutation	IAU, 1980	
Earth Tides	Wahr, 1980	
Ocean tides	Schwiderski, 1980	
Atmospheric Drag	Jacchia 1972 atmospheric model A/m = Variable	
Radiation Pressure	A/m = 0.01 (m^2/kg)	
Ephemerides	JPL DE-2000. Effects of Sun, Moon, Venus, Mars, Jupiter and Saturn included	
Adjusted parameters	Start vector, daily drag coefficients, radiation pressure coefficient	
Step length for integration	1.25 minutes for long arcs 0.50 minutes for short arcs	
Laser data	10° cut-off elevation Marini-Murray tropospheric correction Centre of mass correction	
Geopotential	GEMT1, GEMT2	GRIM4_C2
Terrestrial Reference System	GEMT1 system	GRIM4 system
Earth Parameters	a=6378137 m 1/f = 298.257 GM = 398600.436 c = 299792.458 km/s	a=6378136 m 1/f = 298.257 GM = 398600.4368 c = 299792.458 km/s
Laser Station Coordinates	ITRF91 stations transformed to GEMT1 No plate motion applied	ITRF91 stations transformed to GRIM4 Plate motion: NUVEL1 NNR
Pole coordinates	IERS coordinates transformed to GEMT1 system	IERS coordinates transformed to GRIM4 system

9.2.1 Reference systems

In all ERS-1 computations that used the GEMTn models, the adopted time scale and reference systems were the same adopted for SEASAT. In the solutions computed with the GRIM4_C2 geopotential model, the adopted system is the terrestrial reference system associated with the GRIM models. This is the same terrestrial system adopted in all station and geopotential model solutions produced at the Deutsches Geodaetisches Forschungsinstitut (DGFI) in Germany.

The main difference between the IERS and GRIM/DGFI systems is a shift in the pole position. The pole origin used by the GRIM models is the position of the mean pole averaged over the period 1/1980 to 10/1986. The position of the GRIM pole origin with respect to the CIO/IERS pole is (Reigber et al., 1992):

$$\begin{aligned} \Delta xp &= 45 \text{ mas} \\ \Delta yp &= 286 \text{ mas} \end{aligned} \qquad (9.1)$$

The BIH polar motion series were referred to the GRIM4 pole origin by applying a simple translation:

$$\begin{aligned} xp_{GRIM4} &= xp_{CIO} - \Delta xp \\ yp_{GRIM4} &= yp_{CIO} - \Delta yp \end{aligned} \qquad (9.2)$$

The Earth parameters used with GRIM4 are the parameters associated with this model (Table 9.1).

In addition to the complete set of coefficients up to degree 50, for the epoch 1984.0, the GRIM4 solution includes the rate of change of the C_{20} coefficient, $\dot{C}_{20}$. Therefore the value of C_{20} used (C_{20} =0.48416514x10^{-3}), is the calculated value for the epoch of the computations (1992.1), taking into account this rate of change. Another solved-for parameter of the GRIM4_C2 model is the value of C_{00} = 0.999999992. This value should be multiplied by the a priori GM constant used in the model (GM_0 = 3986400.440) to give the final value associated with GRIM4_C2 (GM = 3986400.4368).

9.2.2 Laser station coordinates

The positions of the laser stations were extracted from the ITRF91 (IERS Terrestrial Reference Frame 91) solution (IERS, 1992) and (Boucher et al., 1992). The ITRF are

annual solutions computed and published by the IERS. These ITRF91 coordinates were transformed to the GRIM4 and GEMT1 systems using the following procedures:

A - Transformation ITRF91 → GRIM4

• The ITRF91 solution gives the list of the station coordinates referred to the IERS system, for the epoch 1988.0 ([IERS, 1992] and [Boucher et al., 1992]).

• The IERS gives the 7 transformation parameters from the ITRF91 to the individual Sets of Station Coordinates (SSC) used in the ITRF91 solution, at the epoch 1988.0. Amongst these SSCs it is the DGFI 92 L 01 solution which uses the same frame as the GRIM4 model (Reigber et al., 1992).

• The transformation parameters from the ITRF91 to the DGFI/GRIM4 system were computed for epoch 1992.1 using the formula (IERS, 1992):

$$T_{1992.1} = T_{1988.0} + \dot{T}\,(1992.1\text{-}1988.0) \qquad (9.3)$$

$T_{1998.0}$ are the transformation parameters at epoch 1988.0

$\dot{T}$ are the rate of change of the translation and rotation parameters. They refer to the annual station displacements according to the NUVEL1 NNR plate motion model (DeMets et al., 1990).

• The final parameters for the epoch 1992.1 (T_1, T_2, T_3, D, R_1, R_2, R_3) were used in the Bursa-Worf transformation, to obtain the station coordinates in the GRIM4 system referred to epoch 1992.1:

$$\begin{bmatrix} X \\ Y \\ Z \end{bmatrix}_{\substack{GRIM4 \\ (1992.1)}} = \begin{bmatrix} X \\ Y \\ Z \end{bmatrix}_{\substack{ITRF91 \\ (1988.0)}} + \begin{bmatrix} T_1 \\ T_2 \\ T_3 \end{bmatrix} + \begin{bmatrix} D & -R_3 & R_2 \\ R_3 & D & -R_1 \\ -R_2 & R_1 & D \end{bmatrix} \begin{bmatrix} X \\ Y \\ Z \end{bmatrix}_{\substack{ITRF91 \\ (1988.0)}} \qquad (9.4)$$

These parameters are presented in Table 9.2.

Finally, when necessary, eccentricities were applied to the station coordinates so that they refer to the optical centre of the laser.

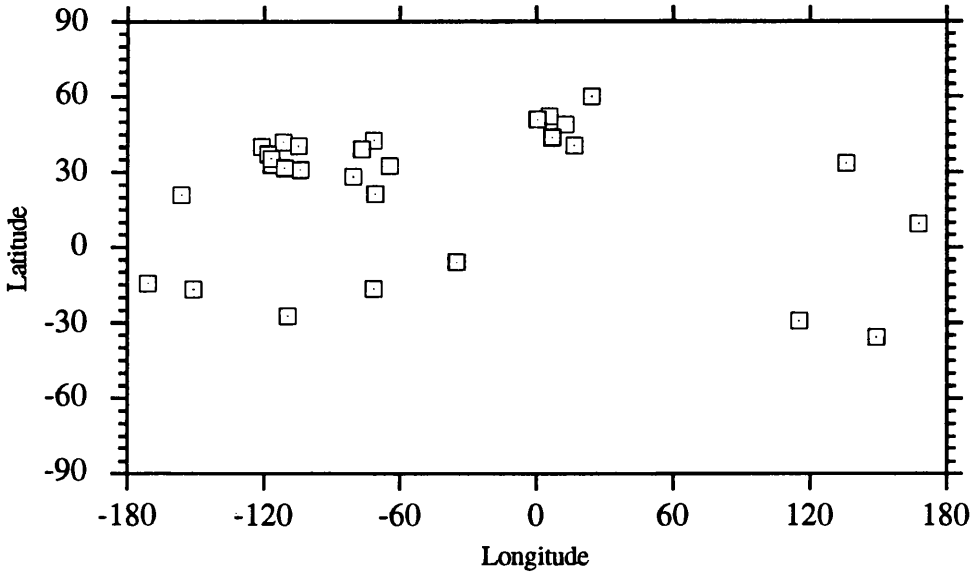

Figure 9.1 - Laser stations used in the transformation between the ITRF91 and the GEMT1 system.

Table 9.2

Parameters of the Bursa-Worf transformation between ITRF91 and various systems

System	T_1 m	T_2 m	T_3 m	D 10-8	R_1 0.001"	R_2 0.001"	R_3 0.001"
GRIM4 (1988.0)	0.007	-0.030	0.000	-0.37	-284.4	-44.5	5.7
GRIM4 (1992.1)	0.023	-0.016	-0.020	-0.37	-284.2	-45.0	5.3
GEMT1	0.080	-0.048	-0.115	-0.44	-267.1	-33.4	-10.2

B - <u>Transformation ITRF91 → GEMT1</u>

In this case, since no transformation parameters were available, they were computed using the following procedure:

• A set of 38 stations common to the ITRF91 and GEMT1 (Marsh et al., 1987) solutions, with a fairly good geographical distribution, was chosen (Figure 9.1).

• Using the coordinates of these 38 stations, the 7 parameters of the transformation between the two systems were computed. These parameters are presented in Table 9.2.

• These parameters were then used to transform the ERS-1 laser station coordinates, taken from the ITRF91 solution, to the GEMT1 system.

In this transformation no plate motion was applied, since no plate motion model is associated with the GEMT1 (Marsh et al., 1987) stations.

9.2.3 Centre of mass correction for laser data

The centre of mass correction for a laser Range $= |\vec{S} - \vec{T}|$ is computed as (Zhu and Reigber, 1991):

$$\delta\text{Range} = M \cdot (\vec{G} - \vec{L}) \cdot \frac{\vec{S} - \vec{T}}{|\vec{S} - \vec{T}|} \tag{9.5}$$

where

• $\vec{L} = [\, x_L,\ y_L,\ z_L \,]$ are the coordinates of the optical centre of the laser retro-reflector in the Satellite Fixed Reference Frame (SFRF) (Figure 5.7).

• $\vec{G} = [\, x_G,\ y_G,\ z_G \,]$ are the coordinates of the satellite centre of mass in the same frame.

• $\vec{S}$ and $\vec{T}$ are the satellite and station geocentric vectors in the same Inertial System, for example the True of Date System (the geocentric inertial system defined by the true equator and equinox of date) or the J2000 system (CIS).

• M is the transformation matrix between the SFRF and the Inertial System

The numerical value of $\vec{L}$ is:

$$\vec{L} = [\, -2.8504,\ -0.700,\ -0.950 \,] \tag{9.6}$$

The value of $\vec{G}$ at the beginning of the mission was:

$$\vec{G} = [\, -1.8133,\ 0.0116,\ 0.0120 \,] \tag{9.7}$$

When the satellite is in the yaw steering mode, the Satellite Fixed Reference System points the Z axis towards the local vertical, the Y axis opposite to the direction of the instantaneous ground velocity vector and the X axis completing the right-handed system (Figure 5.7).

The matrix M has the following form:

$$M = M_3 \,.\, M_2 \,.\, M_1 \tag{9.8}$$

The product $M_2 \,.\, M_1$ is the transformation matrix between the SFRF and the so-called Local Orbital Reference Frame (LORF). M_1 is a simple rotation of 180° about the Z axis.

$$M_1 = \begin{bmatrix} -1 & 0 & 0 \\ 0 & -1 & 0 \\ 0 & 0 & 1 \end{bmatrix} \tag{9.9}$$

The form of the matrix M_2 depends on the satellite mode performance:

$$M_2 = \begin{cases} \text{I (identity matrix) - in the fine pointing mode} \\ R_3(-\Delta\zeta)\, R_2(-\Delta\eta)\, R_1(-\Delta\xi) \text{ - in the yaw steering mode} \\ R_2(\beta) \text{ - in the roll - tilt mode} \end{cases} \tag{9.10}$$

where

$$\begin{aligned} &\text{pitch: } \Delta\xi \cong -0.335°\sin U \cos U \\ &\text{roll: } \Delta\eta \cong 0.050° \sin U \\ &\text{yaw: } \Delta\zeta \cong \arctan(0.0683 \cos U) \end{aligned} \tag{9.11}$$

U is the satellite true anomaly and β is the roll angle in the roll-tilt mode, maximum $|\beta|$ will be around 9.5°.

The Local Orbit Reference Frame is defined by the directions of the unit vectors:

$$\vec{C}: \frac{(\dot{\vec{S}} \times \vec{S})}{|\dot{\vec{S}} \times \vec{S}|} \text{ in the across track direction} \tag{9.12}$$

$$\vec{D}: \frac{\vec{S} \times (\dot{\vec{S}} \times \vec{S})}{|\vec{S} \times (\dot{\vec{S}} \times \vec{S})|} \text{ which is close to the direction of the instantaneous} \tag{9.13}$$

velocity vector (along-track).

$$\vec{R}: \frac{\vec{S}}{|\vec{S}|}, \text{ the satellite radial direction.} \tag{9.14}$$

Note that these vectors are closely related with the T, A, R vectors defined in equation 8.17. In fact $\vec{R}$ is common to both systems, $\vec{C} = -\vec{A}$ and $\vec{D}$ is very close to $\vec{T}$. If the orbit was circular $\vec{D}$ and $\vec{T}$ would be the same.

Finally, M_3 is the transformation matrix between the local orbit reference frame and the inertial system:

$$M_3 = \left[\vec{C} , \vec{D} , \vec{R} \right] = \begin{bmatrix} C_X & D_X & R_X \\ C_Y & D_Y & R_Y \\ C_Z & D_Z & R_Z \end{bmatrix} \tag{9.15}$$

It is very important that the centre of mass correction is adequately computed and applied to data since for ERS-1 this correction has a large variation. For example, for the observations processed in the computations described in section 9.3 this correction takes values in the interval [-0.5 m , 1.5 m].

9.2.4 Modelling of the cross-sectional area for Drag and Radiation Pressure

For the purpose of computing the satellite cross-sectional area in any direction, the spacecraft can be divided into three main areas (Figure 9.2):

• The satellite main body (platform + payload) which is roughly a box with dimensions: 2 x 2 x 3 m^3.

• The solar array which rotates about the satellite **A** (or **X**) axis, making an approximately constant angle with the direction normal to the orbit plane (**A** axis) of 68°± 5°. The size of the array is 12 x 2.4 m^2.

• The SAR antenna, aligned with the direction of the satellite movement (**T** axis) and making an angle of 67° with the **R** axis. Its area is 10 x 1 m^2.

The vectors T, A, R shown in figure 9.2 are as defined in equation 8.17.

A - Atmospheric drag

For the computation of the force due to atmospheric drag on the satellite, the area that needs to be considered is the projected area on the plane perpendicular to the satellite movement: plane ($\vec{R}$, $\vec{A}$). There are two main areas to consider:

• A constant area, the face of the satellite main box that is perpendicular to the direction of the movement: 3 x 2 = 6 m^2.

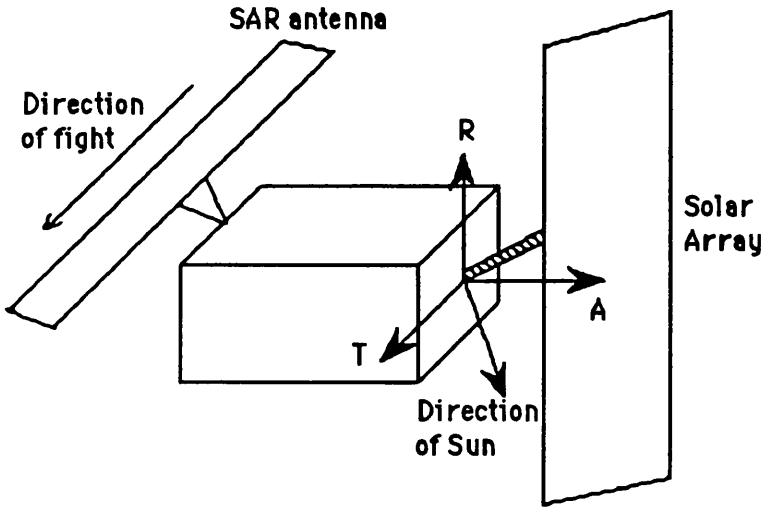

Figure 9.2 - Satellite main areas for atmospheric drag and radiation pressure.

• A variable area, the projection of the solar array, rotating 360° around the A axis, on plane $(\vec{R},\vec{A})$: $28.8\left|\cos(\vec{T}.\vec{\mu}_{sun})\right|$, where $\vec{\mu}_{sun}$ is the unit vector in the direction of the Sun, expressed in the same system as the T, A, R vectors.

The cross-sectional area for atmospheric drag is modelled as:

$$A_D = 6 + 28.8\left|\cos(\vec{T}.\vec{\mu}_{sun})\right| \quad m^2 \tag{9.16}$$

It is clear from this expression that this area has a strong variation with minimum 7 m^2 and maximum 32 m^2. In this analysis the satellite is considered to be in fine pointing mode. When the satellite is in the yaw steering mode, the vectors T, A, R have small oscillations with respect to the satellite. These oscillations induce small area variations of the same order of the neglected areas such as some spacecraft instruments and appendages. Therefore they can be neglected when compared to the total area.

The area-to-mass ratio for atmospheric drag is computed as $\frac{A_D}{m}$ where **m** is the satellite total mass (2157 kg).

B - <u>Radiation Pressure</u>

For direct solar radiation the area that needs to be considered is the projected area on the plane perpendicular to the direction of the Sun.

Three main areas can be considered:

• The solar panel which is always perpendicular to the Sun direction, with an area of 28.8 m^2.

• The projection of the 3 sides of the satellite main box :

$$\begin{aligned} &6\left|\cos(\vec{T}.\vec{\mu}_{sun})\right| \ m^2 \\ &4\left|\cos(\vec{A}.\vec{\mu}_{sun})\right| \ m^2 \\ &6\left|\cos(\vec{R}.\vec{\mu}_{sun})\right| \ m^2 \end{aligned} \qquad (9.17)$$

• The projection of the SAR antenna:

$$3.9\left|\cos(\vec{A}.\vec{\mu}_{sun})\right| + 9.2\left|\cos(\vec{R}.\vec{\mu}_{sun})\right| \ m^2 \qquad (9.18)$$

The total cross-sectional area for direct solar radiation (A_{DSR}) is the sum of all these partial areas. It is found to vary between a minimum value of 38 m^2 and a maximum of 47 m^2. This is a simple algorithm which does not take into account detailed spacecraft geometry. This leads to an overestimate of the area since not all these areas are simultaneously visible by the Sun. To consider the shadow effect of some of the instruments over another, the relative position of all the satellite instruments would have to be accurately known.

For Earth Albedo and Infra-red Radiation the area to be considered is the projected area in the plane perpendicular to the **R** direction, the plane ($\vec{T}$, $\vec{A}$):

• Main box: 6 m^2

• Solar array: $28.8\left|\cos(\vec{R}.\vec{\mu}_{sun})\right|$

• SAR antenna: 9.2 m^2

• Altimeter antenna: 1.13 m^2

The total area for Albedo and IR (A_{AIR}) is the sum of all these partial areas. It is found to vary between a minimum of 20 m^2 and a maximum of 45 m^2.

The area-to-mass ratio for each of the perturbations is computed by dividing each of the areas A_{DSR} and A_{AIR} by the satellite mass.

9.3 ERS-1 solutions with laser data

The period of study used on all ERS-1 computations is a 15 day period, from 1 to 16 February 1992, MJD ∈ [48653.0, 48668.0]. This corresponds to a period during which ERS-1 was flying on a 3-day repeat cycle (first ice phase). During this period two manoeuvre dates occurred: on February 04 at 02h 17m and 03h 08m and on February 11 at 02h 33m. From this period two arcs where selected: ARC_A covering 5.15 days and ARC_B covering 3.2 days (Table 9.3).

Laser data for ERS-1 were kindly supplied by RGO in the form of normal points. One parameter supplied with each normal point is the standard deviation of the normal point. In the formation of the normal points, when this standard deviation is greater than a certain value, it is set to a constant value of 0.5 m. Therefore all the points with standard deviation equal to 0.5m were rejected.

Using the previous criterion, the tracking data for ARC_A are reduced to 15 passes from 8 stations (Table 9.4). This laser data set for ARC_A is named LASER1. The spatial distribution of these 8 laser stations is presented in Figure 9.3. The total number of normal points for this arc is 207, corresponding to a number of 6851 raw laser observations. The temporal distribution of these passes is displayed in Figure 9.5. In this figure, together with the passes that contribute to the solution, rejected passes using the above criterion are also plotted.

Table 9.3
Arcs used on ERS-1 solutions

Arc name	Start and end date (MJD)		Length (days)	Tracking data		
				Stations	Passes	Normal points
ARC_A	48656.25	48661.40	5.15	8 (LASER1)	15	207
ARC_B	48664.80	48668.00	3.20	6 (LASER2)	14	282

Table 9.4

ERS-1 laser data for the period MJD ∈ [48656.25 , 48661.40] - LASER1

Station	Symbol	Location	Longitude (° E)	Latitude (°)	Height (m)	Passes	Normal Points
1181	POT	Potsdam, GDR	13.06538	52.38025	147.8	1	20
7090	YAR	Yarragadee, Australia	115.34675	-29.04658	244.5	1	4
7097	EAS	Easter Island, Chile	250.61645	-27.14775	119.0	1	17
7109	QUI	Quincy, USA	239.05526	39.97506	1109.5	1	7
7210	MAU	Maui, Hawaii	203.74407	20.70724	3068.3	4	42
7835	GRS	Grasse, France	6.92119	43.75469	1322.8	3	32
7839	GRZ	Graz, Austria	15.49344	47.06712	539.4	2	44
7840	RGO	Hertmonceux, UK	0.33621	50.86739	75.3	2	41

Table 9.5

ERS-1 laser data for the period MJD ∈ [48664.8 , 48668.0] - LASER2

Station	Symbol	Location	Longitude (° E)	Latitude (°)	Height (m)	Passes	Normal Points
7097	EAS	Easter Island, Chile	250.61645	-27.14775	119.0	1	21
7810	ZIM	Zimmerwald, Switzerland	7.46530	46.87722	951.0	1	9
7835	GRS	Grasse, France	6.92119	43.75469	1322.8	3	55
7838	SIM	Simosato, Japan	135.93701	33.57763	101.5	1	28
7839	GRZ	Graz, Austria	15.49344	47.06712	539.4	5	114
7840	RGO	Hertmonceux, UK	0.33621	50.86739	75.3	3	55

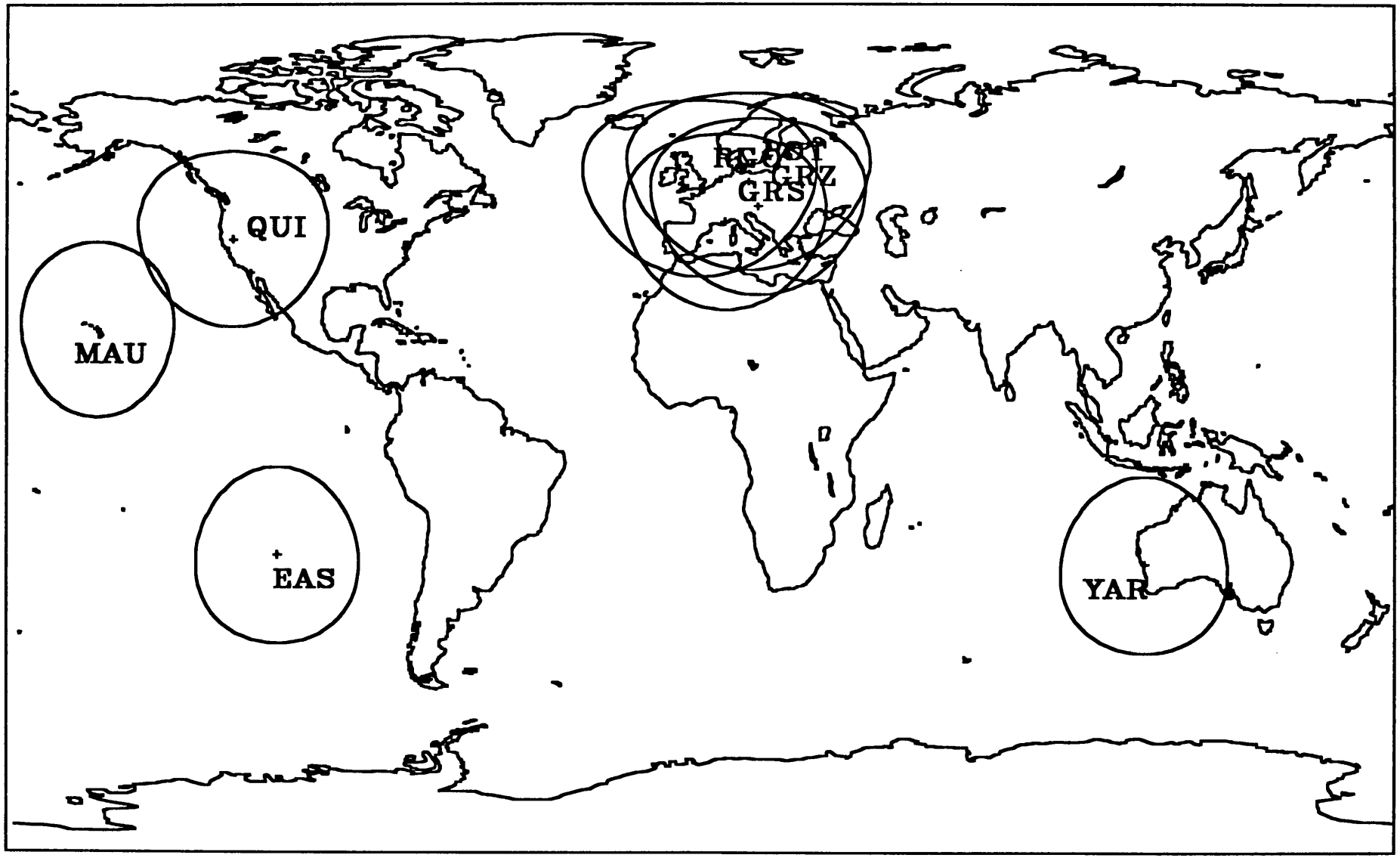

Figure 9.3 - Spatial distribution of ERS-1 laser stations for ARC_A (LASER1).

Figure 9.4 - Spatial distribution of ERS-1 laser data for ARC_B (LASER2).

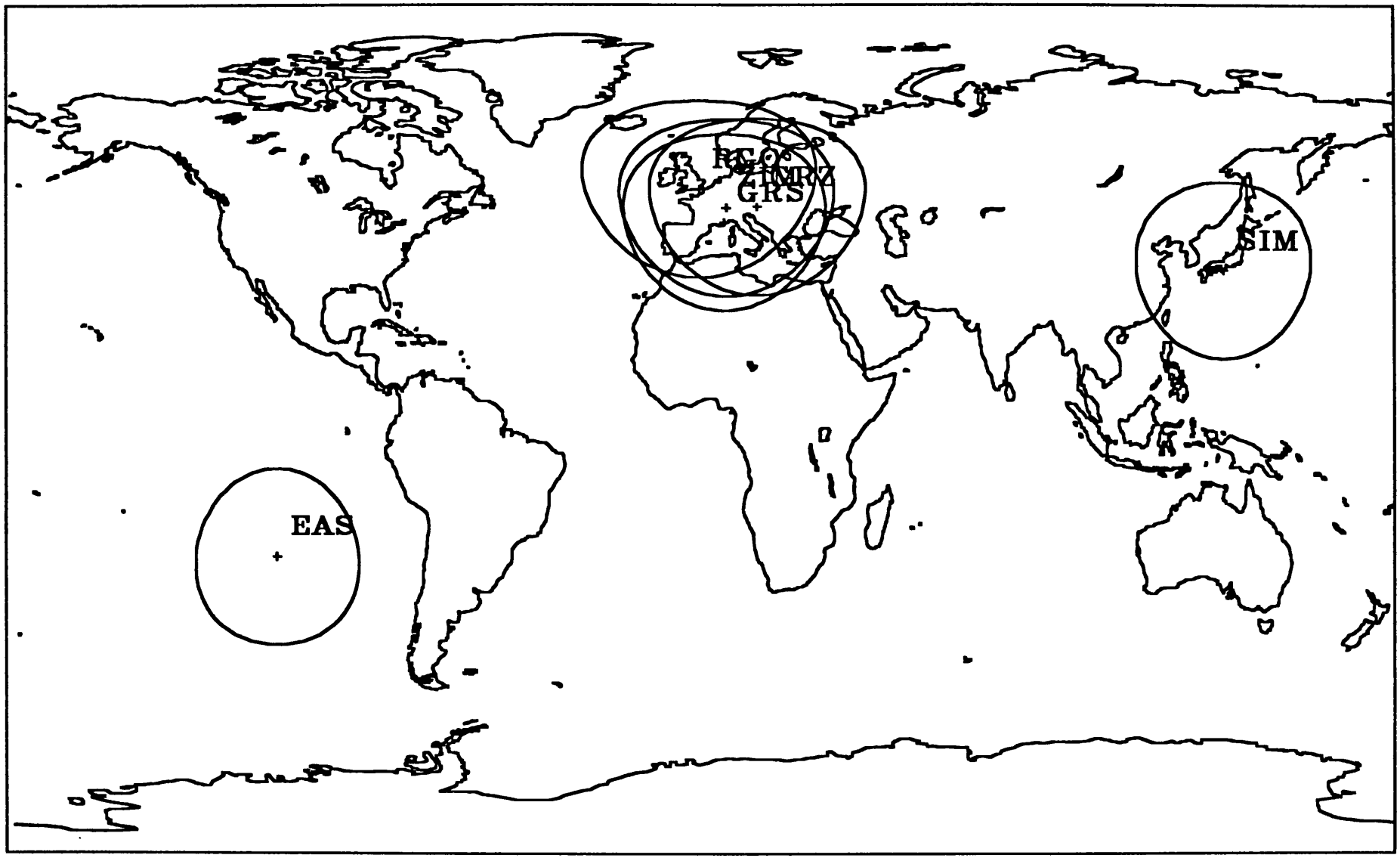

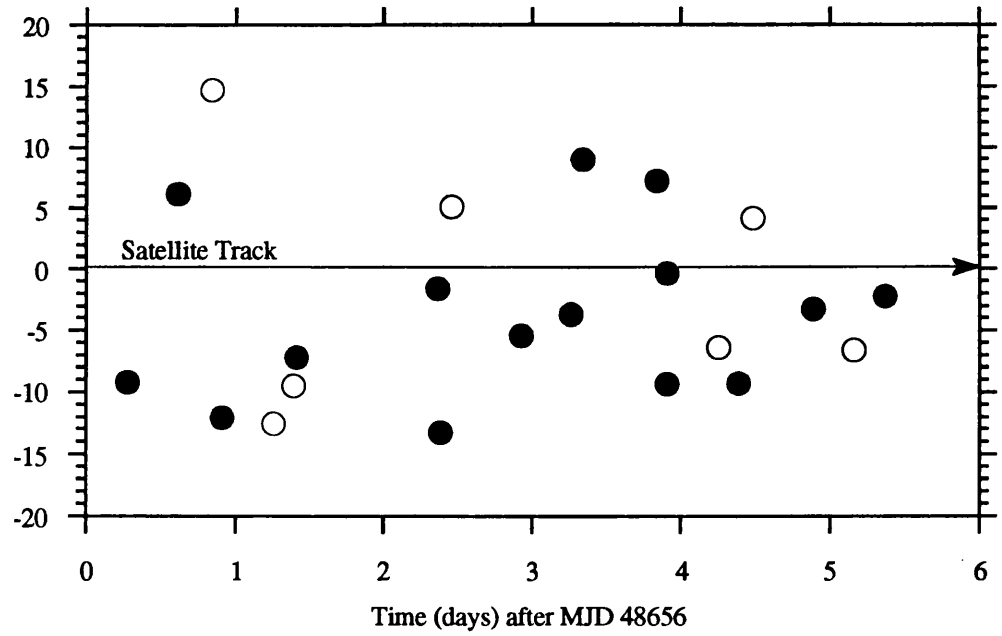

Figure 9.5 - Temporal distribution of laser data for ARC_A (LASER1). Each circle represents one pass. For each pass the Y axis represents the minimum angular distance between the satellite and the tracking station. If the station is on the left or on the right of the satellite track, the angular distance is considered respectively positive or negative. The white circles represent rejected passes.

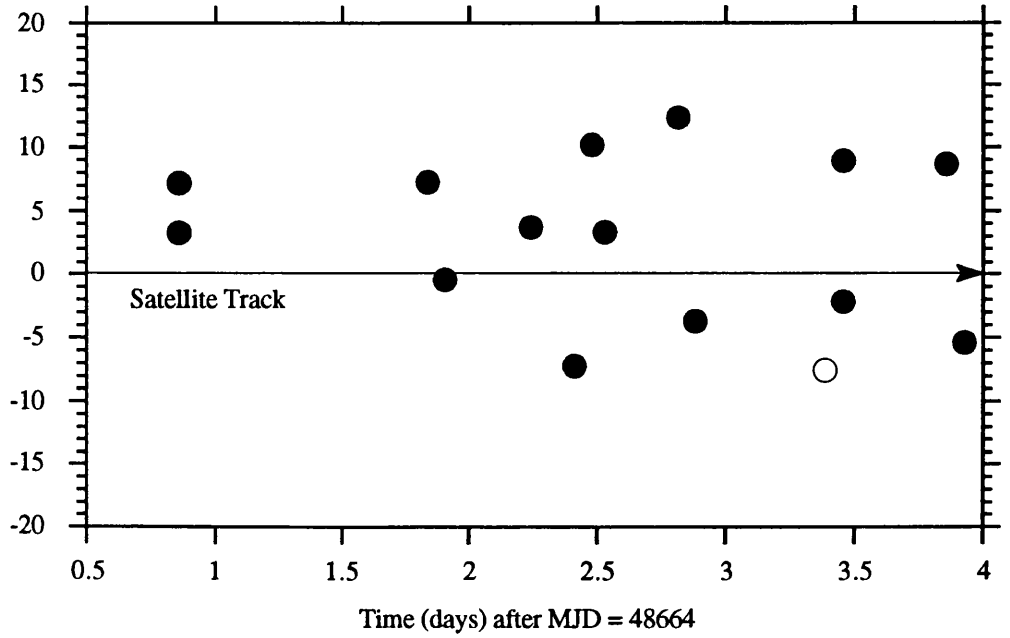

Figure 9.6 - Temporal distribution of laser data for ARC_B (LASER2). The white circle represents a rejected pass.

ARC_B is a shorter arc of 3.2 days, for which, after applying the same rejection criterion, there are 14 passes from 6 stations (Table 9.5). This laser data set for ARC_B is named LASER2. The spatial distribution of these 6 laser stations is presented in Figure 9.4. These data comprise 282 normal points, corresponding to a total of 7359 raw laser observations. The temporal distribution of these passes is presented in Figure 9.6.

Comparing the tracking data for both arcs, it is evident that ARC_A has a better geographical distribution. Most of the data for this arc come from a station in Hawaii (7210) and a set of 4 stations in Europe. On the contrary, all data for ARC_B are from stations in Europe, apart from two passes, one from Easter Island and one from Simosato in Japan.

Solutions for ARC_A are named A1, to A5 and the corresponding solutions for ARC_B B1 to B5.

Since no "satellite truth" is available, the only way of assessing the accuracy of the different solutions is to compare them with solutions computed using different models. To study the influence of the different perturbations on the orbit, several solutions were computed for both arcs using different models. The computation model used on the first solution computed for each arc (A1 and B1) is called the "base model" and is described in Table 9.6.

Table 9.6
Computation model used in solutions A1 and B1 (base model)

geopotential	GRIM4_C2 and associated stations coordinates and Earth parameters
Solved-for parameters	• start vector • radiation pressure coefficient • drag coefficients: - ARC_A : 6 coefficients, one for each day - ARC_B : 3 coefficients one for the first 1.2 days and one for each of the last two days.
Area-to-mass ratio	• atmospheric drag - variable, as described in section 9.2.4 • radiation pressure - constant = 0.01 (m^2/kg)

The models used in all the other solutions differ from the base model by only one characteristic as described in Tables 9.7 and 9.8. Apart from the property specified in these tables, all the other characteristics are common to the base model. For example, the computation model used in solutions A2 and B2 is equal to the base model except for the geopotential, where GEMT2 is adopted instead of GRIM4_C2.

Table 9.7
Solutions computed for ARC_A

Orbit	Model (differences relative to the base model)	Residuals (m)		Residuals on rejected points	
		rms	max	rms	max
A1	———	1.58	5.78	5.16	11.74
A2	GEMT2	1.47	6.22	3.68	6.09
A3	Variable cross-sectional area for Radiation Pressure	1.58	5.74	5.12	11.70
A4	Constant cross-sectional area for Atmospheric Drag	1.61	5.86	5.08	11.24
A5	Solving for a constant drag coefficient	48.65	171.28	69.03	188.01

Table 9.8
Solutions computed for ARC_B

Orbit	Model (differences relative to the base model)	Residuals (m)	
		rms	max
B1	———	1.44	3.49
B2	GEMT2	3.33	6.98
B3	Variable cross-sectional area for Radiation Pressure	1.43	3.51
B4	Constant cross-sectional area for Atmospheric Drag	1.42	3.51
B5	Solving for a constant drag coefficient	3.68	13.00

Tables 9.7 and 9.8 present the laser residuals (rms and maximum values) for each solution. For ARC_A a significant number of passes (seven) had been rejected because of the size of the standard deviation of the normal point. Since these observations were not used in the computations, they can be used to test the orbit accuracy outside the

tracked areas. For this reason, at the end of each solution the residuals at these points are computed and presented in the last column of Table 9.7. This is not done for ARC_B since there is only one rejected pass for this arc (Figure 9.6).

The differences between each solution and the solution computed with the base model are also computed and presented in Tables 9.9 and 9.10. The plots of these differences are presented in Figures 9.7 to 9.14. To make the comparison between the different solutions easier, the same scale was used in the plots, whenever possible. However the magnitude of the differences has such a wide variation that is not possible to adopt a uniform scale for all graphs.

Table 9.9
TAR differences for orbits in ARC_A

Orbits	Total (m)		T (m)		A (m)		R (m)	
	rms	max	rms	max	rms	max	rms	max
A1 - A2	7.45	21.84	7.01	21.74	2.01	6.42	1.54	4.17
A1 - A3	0.12	0.30	0.08	0.27	0.09	0.21	0.02	0.06
A1 - A4	2.53	6.64	2.41	6.63	0.11	0.30	0.74	1.90
A1 - A5	216.7	937.4	206.2	936.7	26.5	48.0	61.1	173.9

Table 9.10
TAR differences for orbits in ARC_B

Orbits	Total (m)		T (m)		A (m)		R (m)	
	rms	max	rms	max	rms	max	rms	max
B1 - B2	7.54	19.31	7.11	19.23	2.09	5.23	1.81	4.61
B1 - B3	0.12	0.34	0.10	0.32	0.07	0.20	0.03	0.08
B1 - B4	1.00	2.74	0.96	2.74	0.05	0.13	0.27	0.75
B1 - B5	9.95	21.38	8.81	21.38	0.78	1.32	1.59	3.77

To have an idea of the order of magnitude of the different forces acting on the satellite, the rms, minimum and maximum values of each force were computed for ARC_A and ARC_B. These are presented in Tables 9.11 and 9.12.

It is clear from these tables that the gravitational forces are dominant. However the main component of these forces comes from Newton's central force which is modelled very accurately. Also the planetary perturbations and effects due to tides are modelled with high accuracy. Therefore the main uncertainty in the gravitational forces comes from errors in the geopotential coefficients. With respect to the surface forces, drag is the dominant force in ARC_A, with larger amplitude of variation, but for ARC_B radiation pressure has the same amplitude of variation with a larger rms.

Table 9.11
Acceleration caused by different perturbations, for ARC_A
(Units are m/s^2)

Perturbation	Minimum	RMS	Maximum
Geopotential	7.75	7.78	7.79
Tides + Third Bodies	$0.3x10^{-6}$	$1.1x10^{-6}$	$1.5x10^{-6}$
Drag	$0.9x10^{-8}$	$10.0x10^{-8}$	$37.2x10^{-8}$
Radiation Pressure	$1.0x10^{-8}$	$7.8x10^{-8}$	$10.8x10^{-8}$
Direct Solar Radiation	0.0	$8.3x10^{-8}$	$11.1x10^{-8}$
Albedo + IR radiation	$0.9x10^{-8}$	$1.7x10^{-8}$	$2.7x10^{-8}$

Table 9.12
Acceleration caused by different perturbations, for ARC_B
(Units are m/s^2)

Perturbation	Minimum	RMS	Maximum
Geopotential	7.75	7.78	7.79
Tides + Third Bodies	$0.7x10^{-6}$	$1.2x10^{-6}$	$1.8x10^{-6}$
Drag	$0.6x10^{-8}$	$5.2x10^{-8}$	$10.6x10^{-8}$
Radiation Pressure	$1.0x10^{-8}$	$9.0x10^{-8}$	$12.3x10^{-8}$
Direct Solar Radiation	0.0	$9.7x10^{-8}$	$12.9x10^{-8}$
Albedo + IR radiation	$0.9x10^{-8}$	$1.9x10^{-8}$	$2.9x10^{-8}$

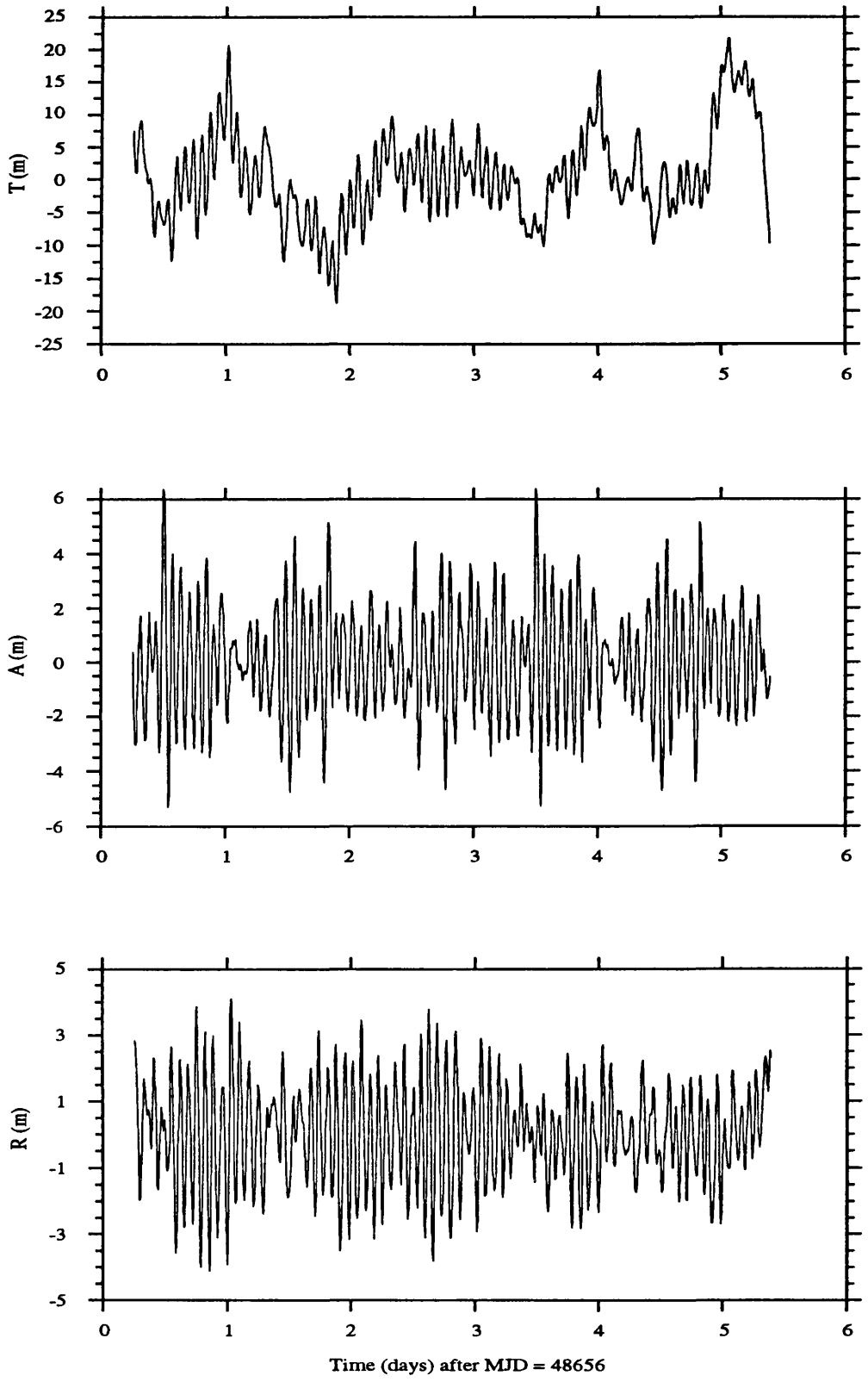

Figure 9.7 - TAR differences between orbits A1 and A2 (GRIM4_C2 versus GEMT2)

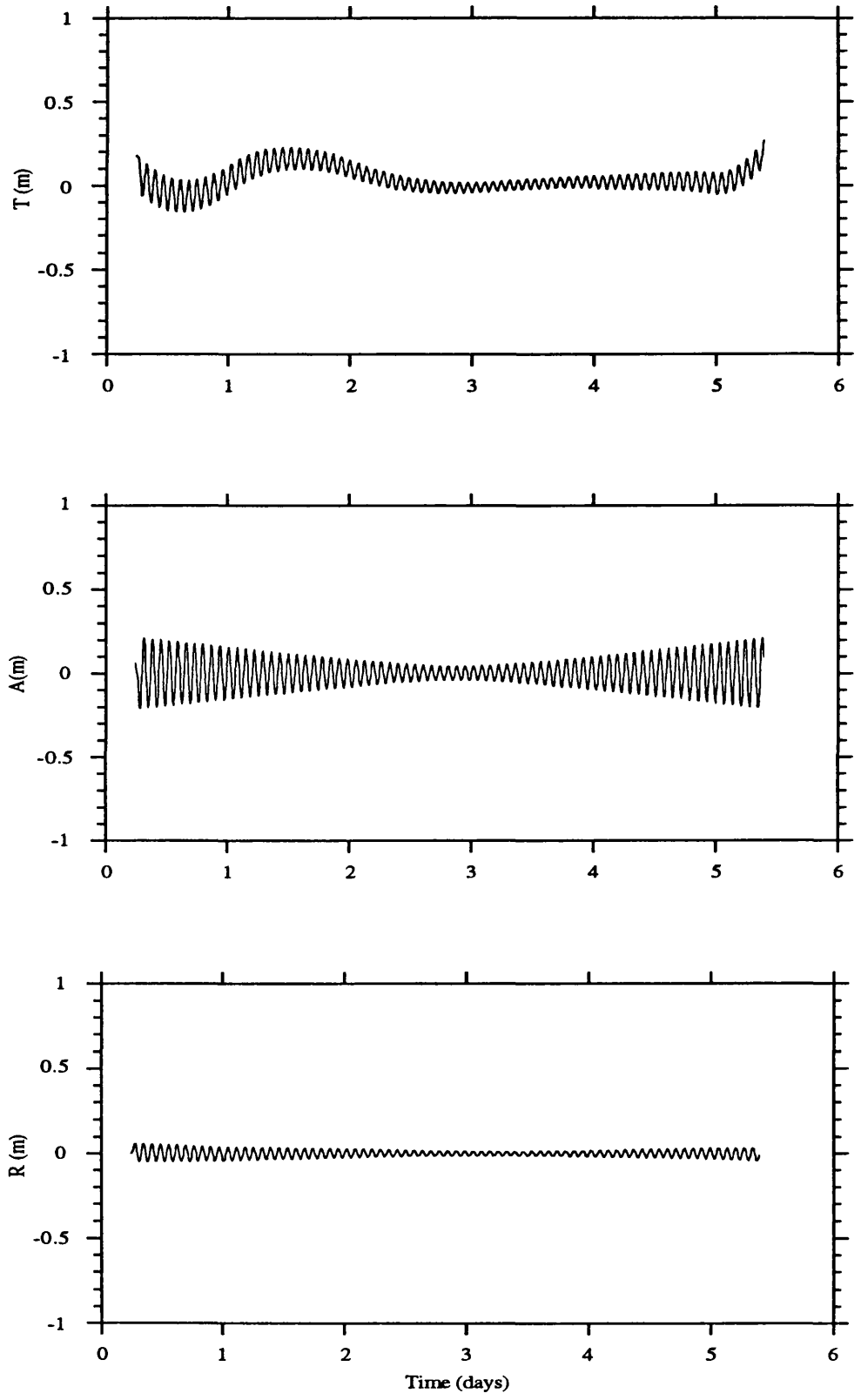

Figure 9.8 - TAR differences between orbits A1 and A3 (constant versus variable cross-sectional area for Radiation Pressure)

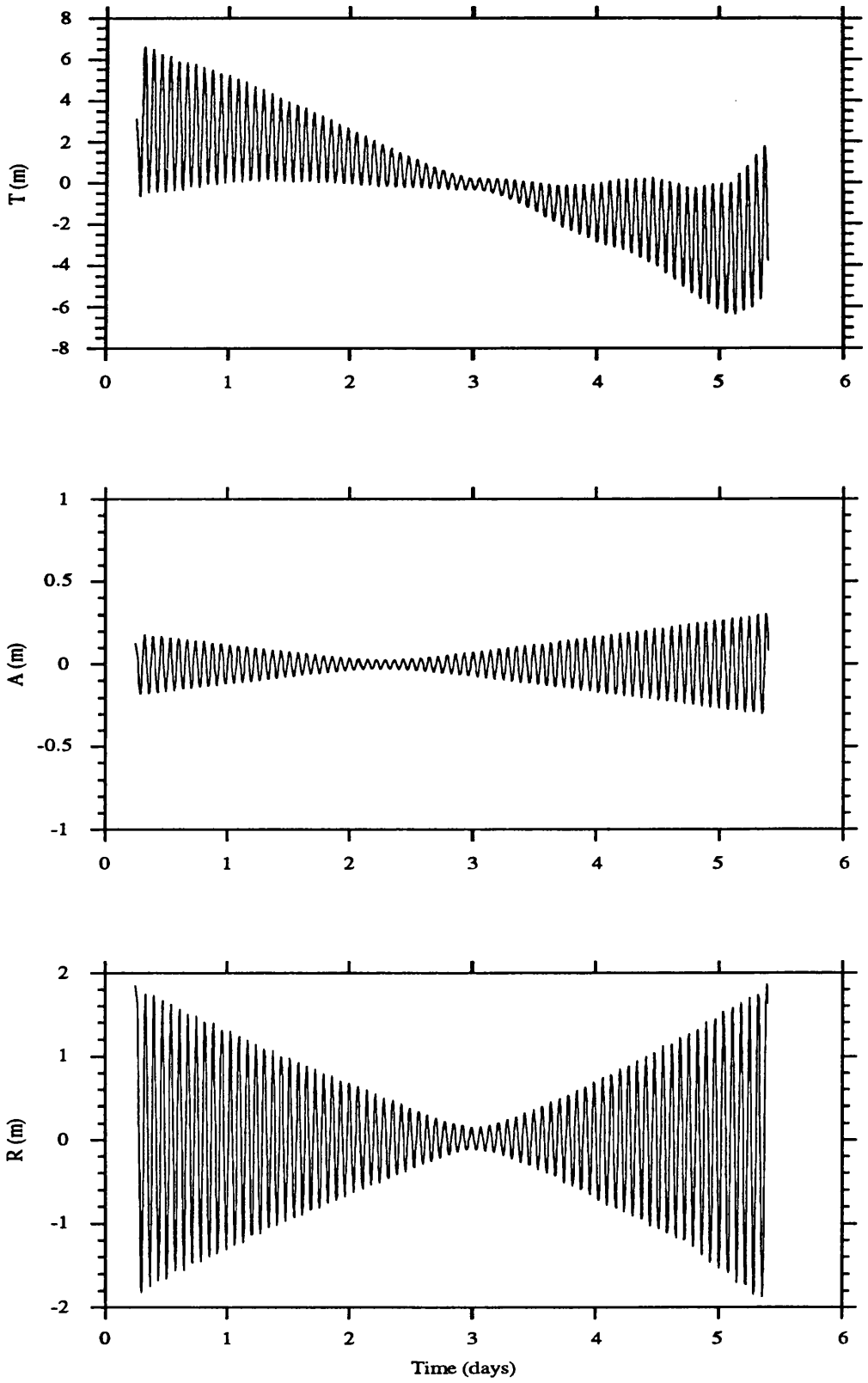

Figure 9.9 - TAR differences between orbits A1 and A4 (constant versus variable cross-sectional area for Atmospheric Drag)

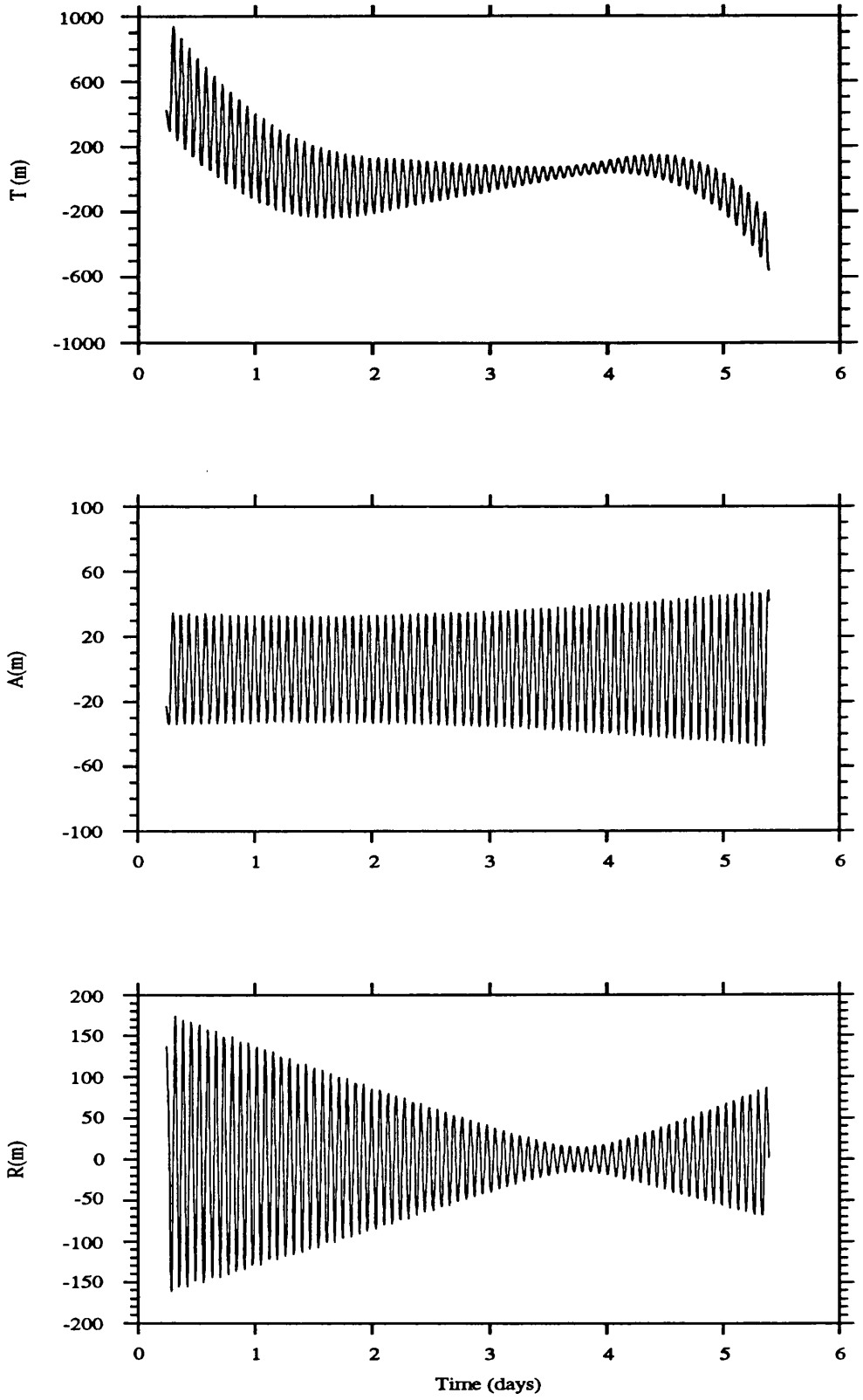

Figure 9.10 - TAR differences between orbits A1 and A5 (solving for 6 drag coefficients versus one coefficient)

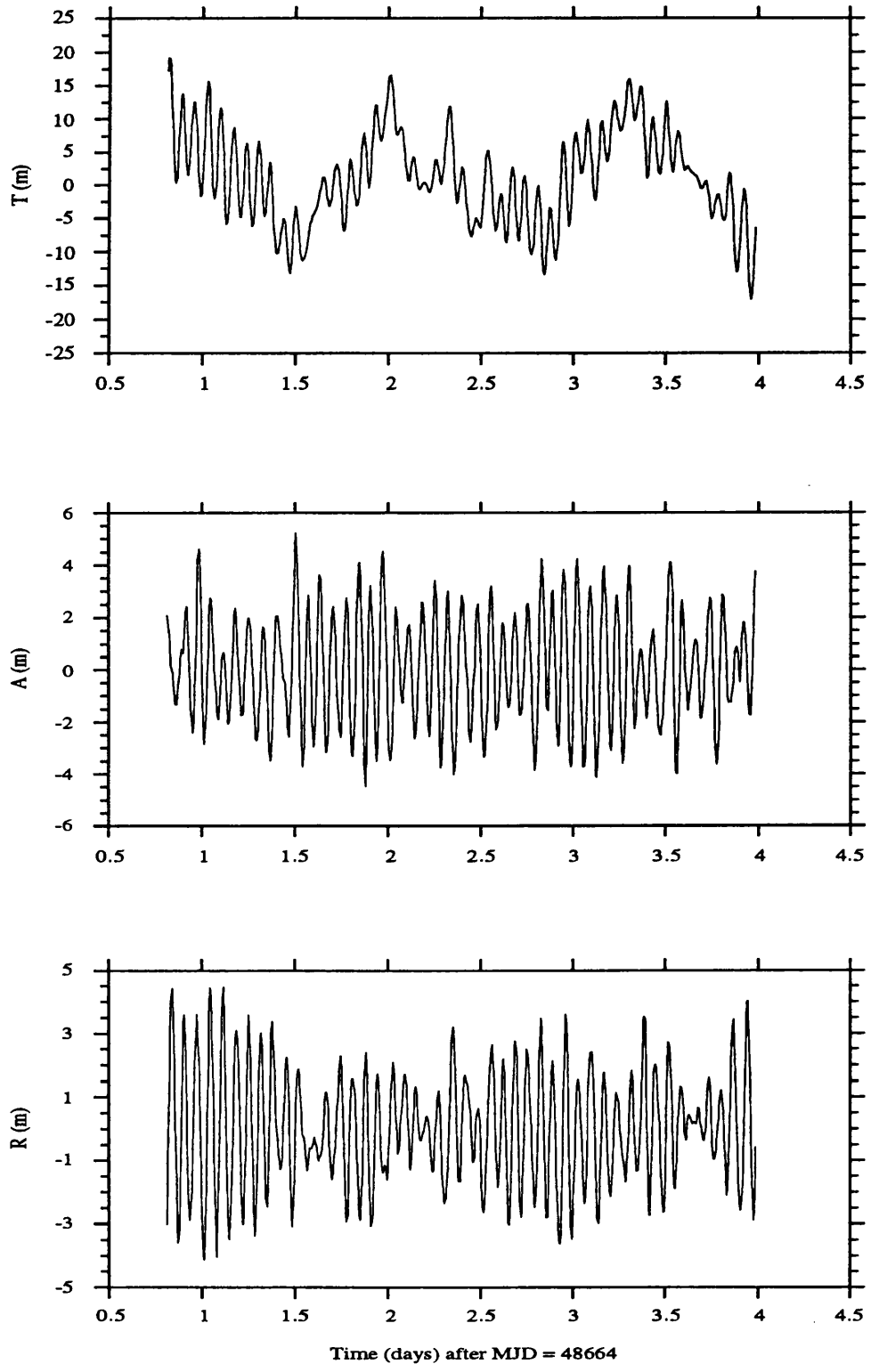

Figure 9.11 - TAR differences between orbits B1 and B2 (GRIM4_C2 versus GEMT2)

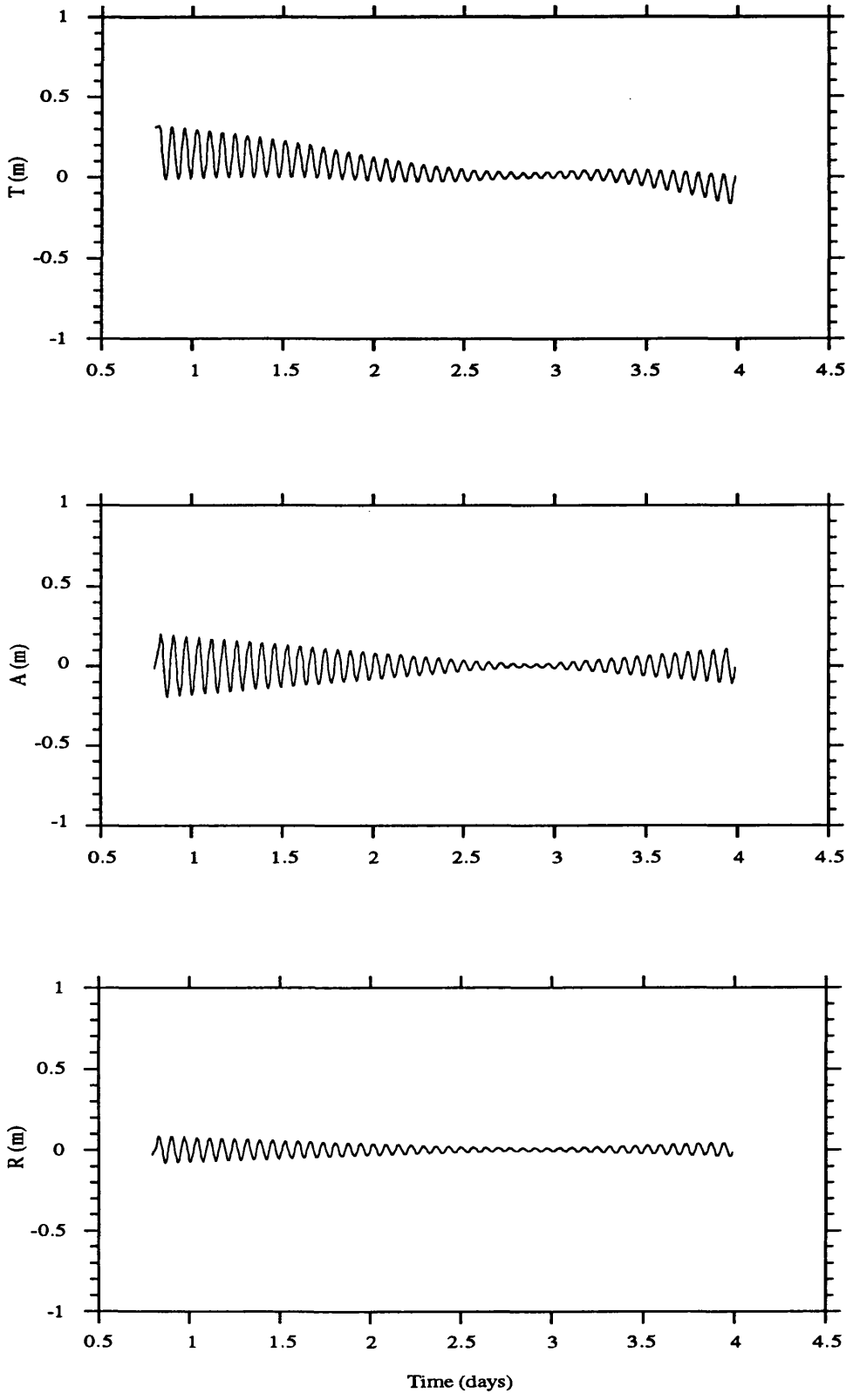

Figure 9.12 - TAR differences between orbits B1 and B3 (constant versus variable cross-sectional area for Radiation Pressure)

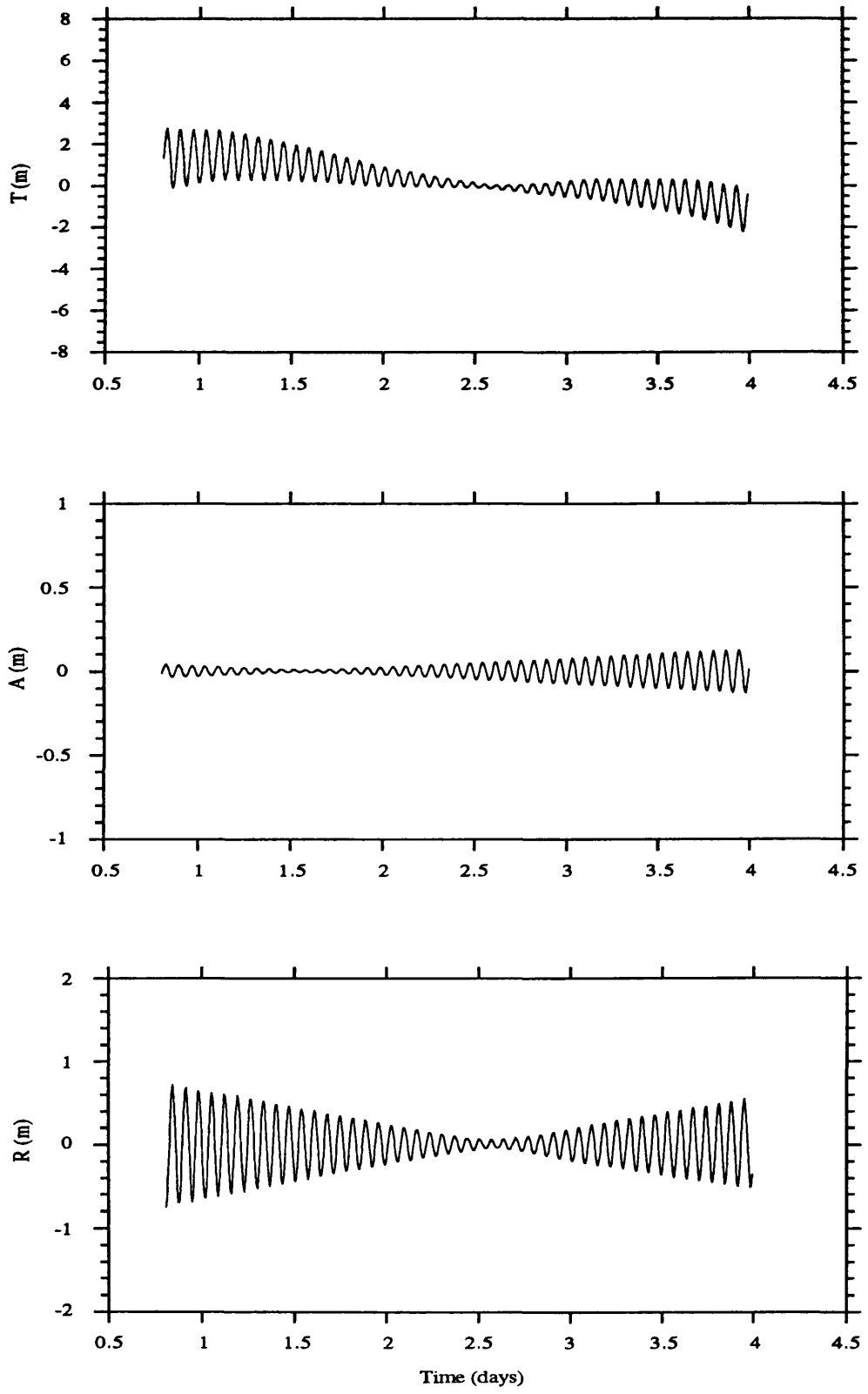

Figure 9.13 - TAR differences between orbits B1 and B4 (constant versus variable cross-sectional area for Atmospheric Drag)

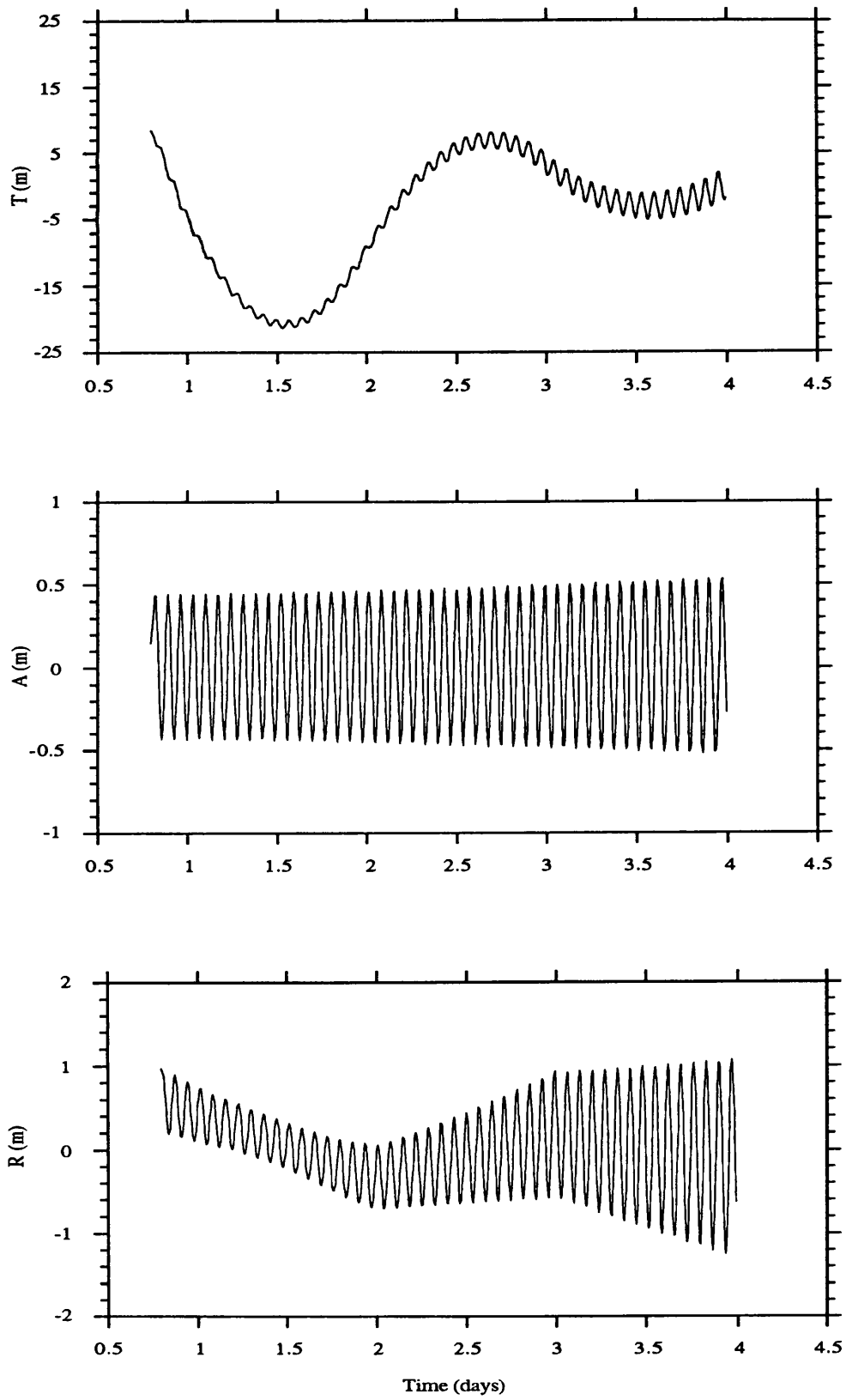

Figure 9.14 - TAR differences between orbits B1 and B5 (solving for 3 drag coefficients versus one coefficient)

From the analysis of these results the following conclusions can be withdrawn.

1 - Errors due to radiation pressure are not dominant in these ERS-1 orbits. In fact the solution is not sensitive to the modelling of the cross-sectional area in the direction of the Sun or the Earth. Solutions computed with a constant area show the same rms of fit as solutions computed with a variable area. The differences between these solutions (A1-A3 and B1-B3) are at decimetre level in the along-track component and at centimetre level in the other two directions. The dominant shape of these differences is the bow-tie pattern with errors that are minimum at the middle of the arc and increase towards the ends, with a superimposed one cycle per revolution signal (Figures 9.8 and 9.12).

2 - Comparing orbits A4 and B4, computed by using a constant area-to-mass ratio for atmospheric drag (of 0.01 m^2/kg), with orbits A1 and B1 where a variable area had been used (according to the model described in section 9.2.4), the rms of fit of these orbits is of the same order. By the analysis of these residuals, the orbit does not seem to be sensitive to the modelling of a variable cross-sectional area for atmospheric drag.

However the differences between orbits computed using different models for the drag cross-sectional area (A1-A4 and B1-B4) reveal the dominant bow-tie pattern superimposed to a one cycle per revolution signal (Figures 9.9 and 9.13). The amplitude of these differences at the start and end of the arc reach several metres in the T and R components. This indicates that drag errors are large for these solutions, ARC_A errors being twice as large as errors on ARC_B.

These results do not necessarily imply that the area model is wrong. The satellite cross-sectional area is a strong function of latitude, since the solar array makes a complete rotation during one revolution. The tracking data can only sense this variation if they come from stations well distributed in latitude. However in both arcs, all stations have latitudes within a narrow range. In particular, all ARC_B stations except one are at latitudes close to 40°. The same argument applies to radiation pressure. The main difference is that the cross-sectional area for atmospheric drag has a wider variation (7 to 32 m^2) than that for direct solar radiation (38 to 47 m^2). Therefore the orbit is more sensitive to the modelling of the first area than to the second one. The modelling of the area for Albedo and IR radiation has an even smaller effect since these perturbations are about one order of magnitude smaller than drag and direct solar radiation (Tables 9.11 and 9.12).

Drag errors are the dominant errors in ARC_A. This is because there is a strong geomagnetic activity during this period. The 3 hour geomagnetic index Kp measures this

geomagnetic activity. The indexes Kp plotted in Figure 9.18 experience strong variations during the ARC_A period, taking values in the interval [0.7 , 7.0] with an amplitude of 6.3. On the contrary, the amplitude of the variation of the Kp index for ARC_B is about half of the previous arc, with values in the interval [0.3 , 3.7]. During the same periods, the solar flux are high values but with smoother variations (Figure 9.17). Again the amplitude of the variation for the first arc (25) is more than twice the amplitude for the second arc (10). The range of the solar flux values is [219 , 244] for ARC_A and [195 , 205] for ARC_B.

Figure 9.15 plots the density variations function of the Kp index, for different values of the solar flux. For ARC_A, considering an average flux of 230, when the Kp takes values in the interval [0.7, 7.0] the density trebles its value, going from 6.6×10^{-14} Kg/m^3 to 1.7×10^{-13} Kg/m^3 . These changes in density induce proportional variations in the drag force and therefore in the satellite perturbation.

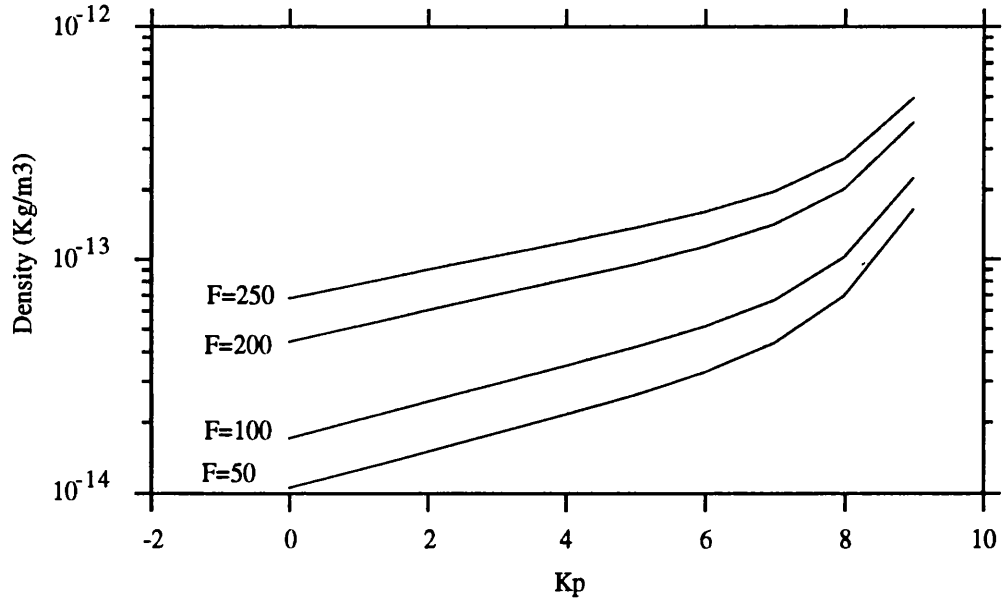

Figure 9.15 - Density variation functions of the Kp index, for different values of the solar flux

These strong solar and geomagnetic activities cause serious perturbations in the satellite orbit which are not modelled by a simple model for the drag force as described by equation 3.13. This becomes evident when orbits are computed by solving for a single drag coefficient (C_D) for the whole arc. Solution A5, computed by solving for a single C_D, has huge residuals with an rms of 48 m. By comparison the same solution for ARC_B, B5, has an rms of only 3.7 m. Considering the poor quality of these single C_D solutions it is remarkable the improvement obtained when solving for multiple drag coefficients as in orbits A1 and B1. The differences between these solutions is of the

order of hundreds of metres for ARC-A (Figure 9.10) but only a few metres for ARC_B (Figure 9.14).

The use of multiple drag coefficients is therefore an indispensable technique for the computation of ERS-1 orbits. However it does not solve completely the problem of modelling the perturbations caused on the satellite by strong solar and geomagnetic activity. This topic will be further discussed in section 9.4.

3 - GRIM4_C2 seems to be a better model for ERS-1 than GEMT2. This is not surprising since it incorporates DORIS data from SPOT2, a satellite with an orbit very similar to ERS-1's, with a height of 832 km and an inclination of 98.7°. On the contrary, in the generation of GEMT2 there were no data from satellites with height close to ERS-1's and inclinations within 10 degrees of ERS-1's inclination (Marsh et al., 1990a).

For ARC_A, solutions computed with different geopotential models (A1 and A2) have rms of fit of the same order. By contrast, for ARC_B the rms of fit of GEMT2 orbit (B2) is twice as large as the corresponding GRIM4_C2 orbit (B1). However, the differences between the solutions (A1-A2 and B1-B2) are of the same order for both arcs (Figure 9.7 and 9.11).

The interpretation of these results is not straightforward. The dominant errors for ARC_B seem to be the geopotential errors while for ARC_A drag errors are dominant. By solving for multiple drag coefficients a great part of the along-track errors, including long period errors of gravitational origin, are absorbed.

It remains to be explained why for ARC_B the GEMT2 orbit (B2) has an rms more than twice as large as the corresponding solution for ARC_A (A2). Concerning the geopotential perturbation, the main difference between these two arcs is the different geographical distribution of the tracking stations. Most of ARC_A data come from North America, while the data for ARC_B are mainly from stations in Europe. The tracking data used on geopotential modelling come from a wide range of techniques, but in the past there was a concentration of tracking stations in North America. For this reason, the geopotential models derived from these data are better defined in that region, than for example in Europe, where the number of stations used to be substantially smaller. This argument is corroborated by the results obtained for SEASAT. In fact SEASAT orbits computed with GEMT2 have very small rms of fit partly because almost all the SEASAT laser data come from stations concentrated in the United States. The SEASAT laser data used in the solutions described in Chapter 8 all come from North American stations, apart from one station in South America and one in Europe (Figure 8.4 and Table 8.4). SEASAT solution L1 computed using these data and GEMT2 has an overall rms of fit of

only 0.3 m but the rms of fit of the two passes from the European station is as large as 0.7 metres.

In conclusion, ERS-1 solutions computed using the base model described in Table 9.6 have rms range residuals of 1.5 metres. According to the differences between these solutions and solutions computed with GEMT2, the radial accuracy of these ephemerides should be better than 1.5 metres, and the across-track accuracy only slightly smaller, around 2 metres. However the along track component can reach several metres ($\approx$ 7 m rms).

9.4 Influence of solar flux and geomagnetic data

The accuracy of ERS-1 orbits described in the previous section is far from ideal. This developed a strong motivation for research on methods to improve these results.

During a period of high solar activity, the drag force is a dominant perturbation of satellite motion. Strong variations in solar and geomagnetic activity cause large variations in the atmospheric density at satellite heights and consequently in the drag force exerted on the satellite by the surrounding atmosphere. Therefore the atmospheric model plays an important role in the computation of these ephemerides.

In this study some aspects concerning the modelling of the atmospheric density are investigated, in particular the use of actual measurements of solar flux and geomagnetic data.

9.4.1 Structure of the upper atmosphere

If the atmosphere were isothermal and of homogeneous composition, the density would decay exponentially with height. The real situation is much more complicated.

Nicolet (1960) showed that above 250 km the observed density profiles could be reproduced, if for each of them the temperature was assumed to be a constant, and the composition varied with height according to the law of diffusion in a gravitational field. The constant temperatures above 250 km range from 650 K to about 2000 K or higher, depending on the solar activity and time of the day.

Figure 9.16 shows different temperature profiles corresponding to different levels of solar activity. The region from the beginning of the temperature rise, at about 90 km, to where the rise stops, is called the thermosphere. The height at which this stop occurs is

called the thermopause. This threshold is shifted higher and higher with increasing solar activity.

The sharp increase in temperature in the region between 100 km and 250 km is due to the extreme ultraviolet radiation (e.u.v.) from the Sun that is absorbed just in that region.

The atmosphere can be considered homogeneous in composition from sea level until about 90 km, the so-called homosphere. From this height onwards several changes in composition occur, and above 120 km the atmosphere can be considered in diffusion equilibrium. This means that the density of each constituent varies with height independently from all the other constituents. This region in which the atmospheric constituents behave differently from each other is called the heterosphere.

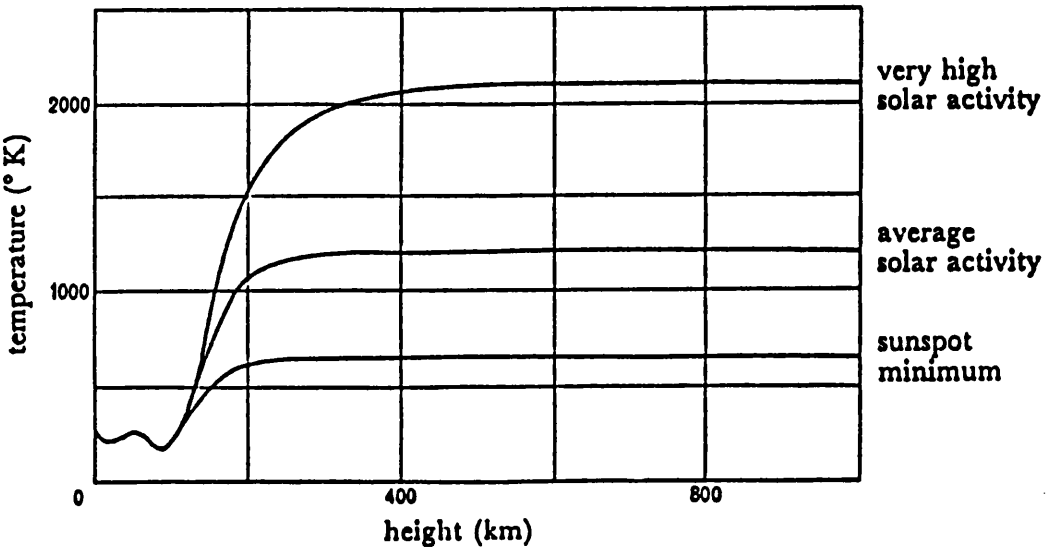

Figure 9.16 - Atmospheric temperature profiles for three stages of solar activity. From (Jacchia, 1972).

As the height increases the heavy constituents are left behind giving way to lighter constituents.

Most of the recent atmospheric models assume that the atmosphere is in diffuse equilibrium above 120 km and then construct models for different temperature profiles assuming certain boundary conditions at the 120 km.

In the atmospheric model used in this study (Jacchia, 1972), the boundary conditions are applied to a lower height of 90 km and the exponential shape of the temperature profiles is replaced by other analytical expressions.

9.4.2 Density variations of the upper atmosphere

The structure of the upper atmosphere varies due to a variety of phenomena. Four main distinct types of variations can be considered (Jacchia, 1972):

- Variations with solar activity
- Variations with geomagnetic activity
- The diurnal variation
- The semi-annual variation

A - Variations with solar activity

In the variations with solar activity one must distinguish between a slow variation due to the 11-year solar cycle and day-to-day variations. These are usually explained by considering that the ultraviolet solar radiation that heats the upper atmosphere consists of two components, one related to active regions on the solar disk (sunspots) and the other to the disk itself. The day-to-day variation is caused not only by the sunspots but also by their appearing and disappearing in the solar disk due to the Sun's rotation with a period of 27 days. The 11-year solar cycle is associated with the slower variation of the disk component.

In the Jacchia_72 model the variations with solar activity are input into the models by means of daily values of solar flux at 10.7 cm, observed with a radio telescope at Ottawa, the so-called $F_{10.7}$. This solar flux is generally adopted as a serviceable index of solar activity. There is a remarkable parallelism between its variation and those of the upper atmosphere.

The $F_{10.7}$ solar flux consists of a disk component and an active-area component which are not easily separable. However the disk component is linearly related to the flux averaged over 4 to 5 solar rotations ($\overline{F}_{10.7}$).

The temperature variations in the atmosphere occur with a time lag with respect to those of the solar flux. Different authors provide different values for this time lag from 0.5 days (Jacchia and Briggs, 1963) to 2.3 days (McDonald, 1963). The Jacchia_72 model uses a time lag of 1.71 days.

B - Variations with geomagnetic activity

In addition to varying due to solar activity, the Earth's atmosphere shows another type of variation, which is correlated with variations in the magnetic field of the Earth. Intense magnetic storms occur when clouds of charged particles, ejected from the Sun in the course of a solar flare, collide with the Earth's atmosphere. A solar flare is a short-lived phenomenon that usually lasts an hour or less. During these magnetic storms the temperature and density of the upper atmosphere increase. The temperature increase during a magnetic disturbance is, on average, enhanced at high latitudes.

The duration of the atmospheric perturbation matches that of the magnetic storm but lags some 6 to 7 hours behind it. The time lag seems to be a little bigger at low and middle latitudes and smaller in the auroral zones.

The value of this time lag has been determined by different authors. In a study using drag analysis of 4 satellites, Jacchia et al. (1967) found an average value of 6.7 ± 0.3 hours. This is the value adopted in the Jacchia_72 model. By drag analysis of the satellite Explorer 9, Roemer (1966) determined a mean value of 5.2 ± 0.4 hours.

During magnetic storms the temperature variations seem to be linearly related with the planetary geomagnetic index Ap, while during quieter periods the relation is linear with the planetary index Kp, which is the logarithmic counterpart of Ap (Jacchia et al., 1967). These indices are the average of measurements, at a 3-hour interval, at 11 sub-auroral zone observatories located mainly in Europe (NGDC, 1992) and are widely used by the present atmospheric models to describe the irregular variations in the geomagnetic field.

Apart from the magnetic storms, small variations in the magnetic field of the Earth, such as are observed during magnetically quiet days, also affect the temperature and density in the upper atmosphere.

C - The diurnal variation

The diurnal variation is caused by the variations in the solar e.u.v. radiation due to the day/night change. The e.u.v. radiation is a major source of upper atmospheric heating. Therefore the temperature goes up after sunrise and falls at night, and atmospheric densities follow the same variation. Due to this effect, atmospheric densities reach a minimum around 4 a.m. and a maximum around 2 p.m. The temperature range is large at the equator and progressively decreases towards the poles.

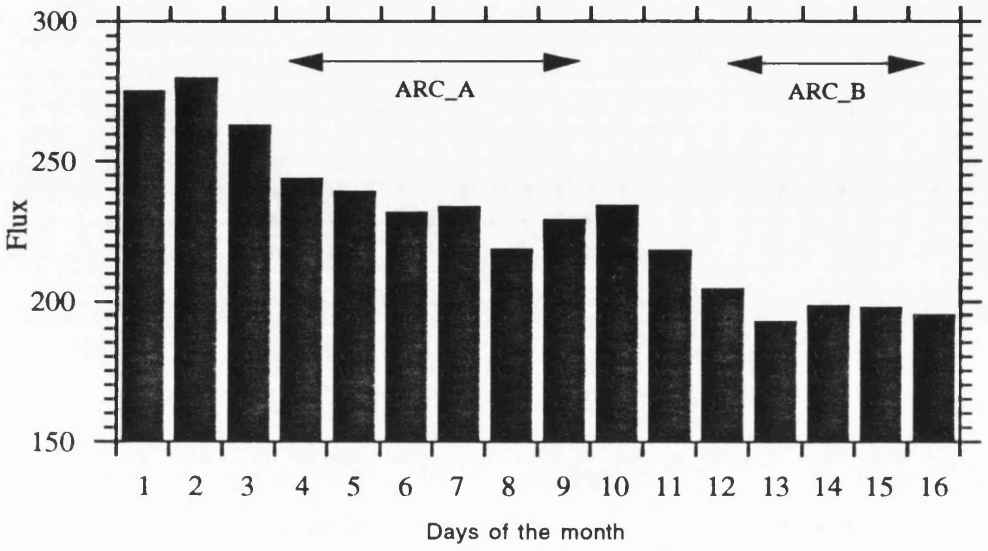

Figure 9.17 - Flux data for the first 16 days of February 1992

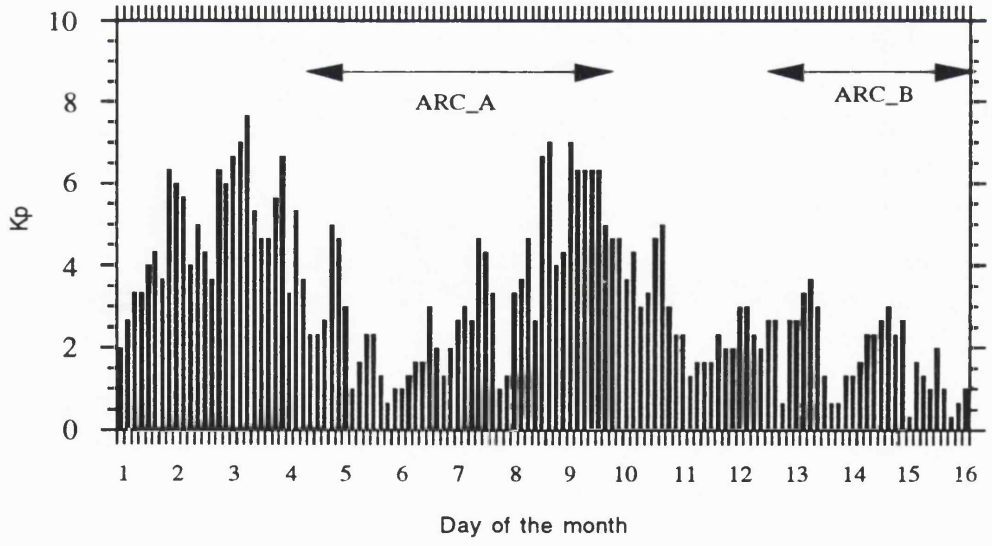

Figure 9.18 - Geomagnetic index Kp for the first 16 days of February 1992

D - The semi-annual variation

This is the least understood of all the variations. The density of the upper atmosphere shows a deep minimum in July followed by a high maximum in October. In January there is a secondary minimum, followed by a secondary maximum in April.

9.4.3 Influence of $F_{10.7}$ and Kp time lags on the orbit

During the period corresponding to ARC_A there are very strong variations of the geomagnetic index Kp. These indices are input into the model for computing the atmospheric density at a specified time. High variations in the Kp indices induce high variations in the computed density and therefore in the drag force (Figure 9.15).

As explained before, the Kp indices are input into the model with a certain time lag with respect to the time of the computation. Therefore, such sharp variations in the Kp index as occurred during ARC_A, if they are not "in phase" with the actual satellite perturbation as sensed by the tracking data, result in a poor orbit adjustment with high residuals. The belief that the orbit adjustment is a function of this time lag was the motivation for research on the influence of this parameter on orbit accuracy.

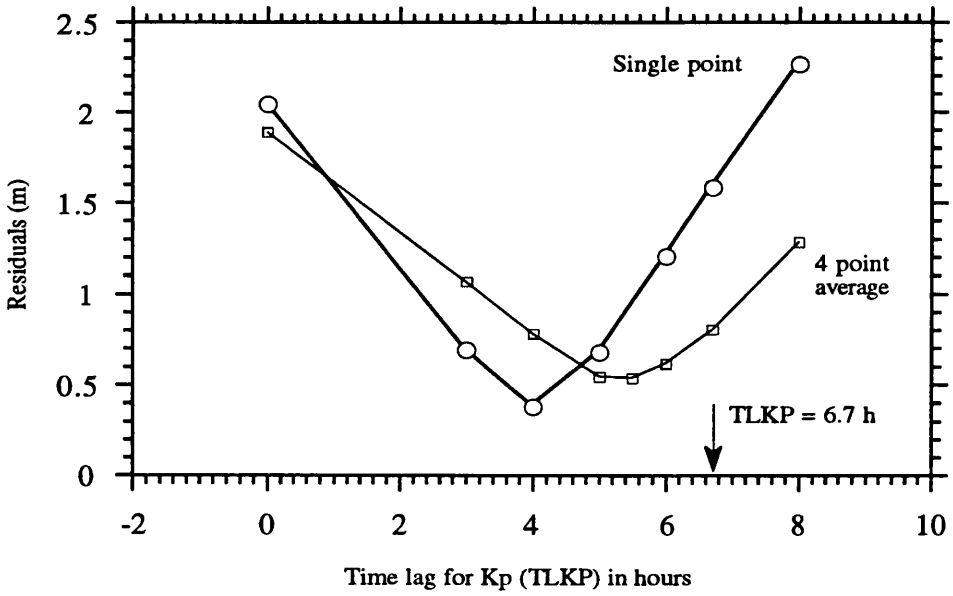

Figure 9.19 - Rms of orbit residuals as function of TLKP for ARC_A

For this purpose, orbits A1 and B1 described in section 9.3 were recomputed using different values for the Time Lag of the Kp index (TLKP). In all computations the same base model was used, the only difference between the various solutions being the TLKP value. The results are plotted in Figure 9.19 for ARC_A and 9.23 for ARC_B, in the thicker curves labelled as "single-point".

An orbit was computed for each TLKP value corresponding to each circle point in the graphs. The Y axis represents the rms of fit to range data in metres.

Table 9.13
Solutions computed for ARC_A using different TLF and TLKP

Orbit	TLF (days)	TLKP (hours)	Interpolation method	Residuals (m)		Residuals on rejected points	
				rms	max	rms	max
A1	1.71	6.7	single point	1.58	5.78	5.16	11.74
A6	1.71	4.0	single point	0.38	1.01	2.34	8.41
A7	1.71	6.7	4-point average	0.80	3.25	3.92	11.42
A8	1.71	5.5	4-point average	0.54	2.20	3.26	9.98
A9	1.00	4.0	single point	0.45	1.46	2.32	8.59

Table 9.14
TAR differences for orbits in ARC_A using different TLF and TLKP

Orbits	Total (m)		T (m)		A (m)		R (m)	
	rms	max	rms	max	rms	max	rms	max
A1 - A6	9.05	29.34	8.66	29.32	1.60	2.59	2.10	3.90
A1 - A7	5.96	20.57	5.65	20.57	1.11	1.76	1.54	3.30
A7 - A8	2.49	6.30	2.38	6.30	0.44	0.69	0.58	1.06
A6 - A8	5.97	28.84	5.95	28.83	0.08	0.17	0.50	2.36
A6 - A9	0.79	3.26	0.77	3.26	0.11	0.18	0.10	0.37

Using the TLKP adopted in the atmospheric model (6.7 h) the solution obtained for ARC_A has an rms of 1.58 m (solution A1). By using TLKP values from zero up to

eight hours, it is found that the rms of fit has a clear minimum for a TLKP around 4 hours, reaching an rms value of only 0.38 metres (solution A6 in Table 9.13). This means that a difference in the TLKP value of 2.7 hours generates orbits with rms range residuals of more than one metre difference.

The same test was done for the Time Lag of the solar Flux (TLF). Now orbit A6 was recomputed keeping a TLKP = 4.0 hours, but using different values for the TLF. The result for TLF = 1 hour is presented in Table 9.13. As expected, the solution is less sensitive to the variations of the TLF value than to those of the TLKP. This is because the amplitude of the solar flux variation is less than that of the Kp indices. The solar flux is input as daily values and as averages for four solar rotations. Therefore a change in the time lag of these values by one or two days does not significantly affect the solution. The time lag adopted in the atmospheric model (TLF = 1.71 days) seems to be appropriate. In fact the rms of fit increases when this value is either increased or decreased, proving that the time lag corresponding to the minimum residuals is close to the adopted value by the atmospheric model. The difference between solutions computed with different TLFs (A6 and A9 in Tables 9.13 and 9.14) is small, revealing that this parameter does not significantly affect the solution.

In all these computations the Kp index for each time **t** was computed by interpolation from the 4 nearest 3-hour values, by using 4-point Lagrange interpolation. This process is referred to in the tables and in the graphs as the "single-point" method. The previous results show that the orbit adjustment is poor when the time lag of the Kp indices is not "in phase" with the induced orbital perturbation. This suggests that, instead of using the measured indices, it might be preferable to use a smooth function of these values, so that the sharp changes that occur during this period become smoother.

To study this effect, the previous computations were repeated, using for each time **t** the average of the 4 nearest 3-hour Kp values. This procedure is referred to as the "4-point average" method. The results for ARC_A are show in Table 9.13 and in Figure 9.19 (thinner line).

As before, the orbit was computed for a range of TLKP from zero to eight hours. On average the rms residuals of these solutions are smaller than the corresponding solutions using a "single-point" Kp value. For example, comparing solutions A1 and A7 for which the model adopted TLKP = 6.7 hours was used, the rms residuals for the second orbit (0.80 m) are about half of the rms residuals for the first solution (1.58 m). This means that the satellite senses the sharp variations in the atmospheric density caused by strong geomagnetic activity in a smoother way. The time lag (TLKP) that corresponds to the minimum rms of fit (5.5 hours) is larger than the value found on "single point" solutions:

4 hours. The difference between these minimum values is due to the different shape of the Kp curves in both cases (Figure 9.20).

There is no doubt that solutions with smaller rms (A6 and A8) are better than the others. This statement is further proved by the values of the rms residuals at the rejected points, which are smaller for these solutions (last column of Table 9.13).

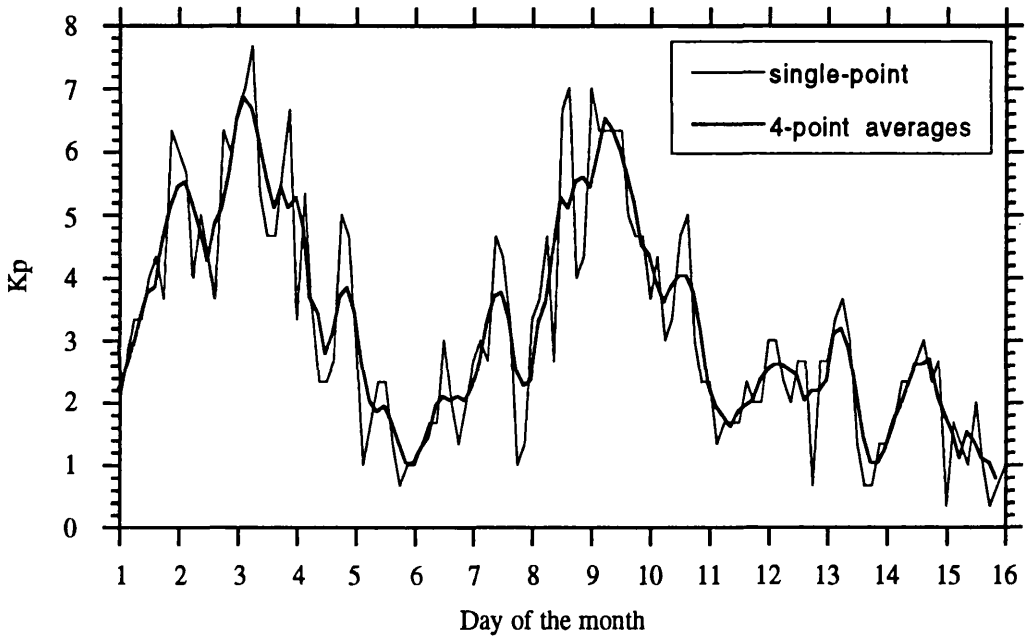

Figure 9.20 - Single-point Kp indexes versus 4-point averages.

The differences between these solutions reveal a great deal of information which is not detectable by the analysis of the fitting residuals. Table 9.14 presents some of these differences. Comparing orbit A1 and A6, both computed using "single-point" Kp values, they have very large differences, particularly in the along-track component (Figure 9.21). However the differences between the corresponding solutions using "4-point averages" (A7 and A8) is are much smaller, revealing that these are smoother solutions which are not as sensitive to the TLKP value as the "single-point" orbits.

Surprisingly large are the differences between orbits A6 and A8, both giving very small residuals of fit. These differences are particularly large at the end of the arc, during the last half day. This means that at this part of the arc the orbit is poorly determined. This is mainly due to two reasons. The first is due to the fact that at this part of the arc there are

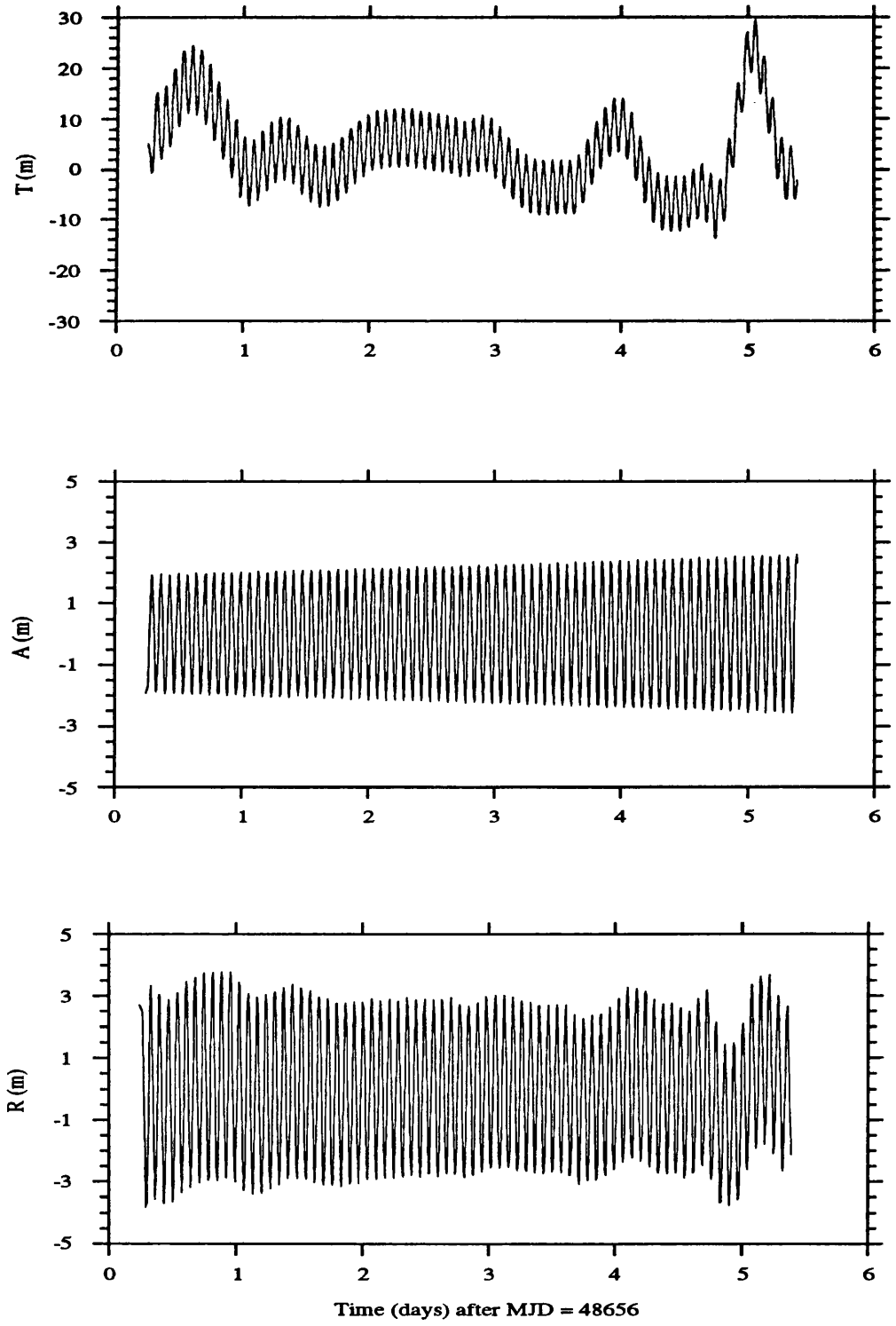

Figure 9.21 - T, A, R differences between orbits A1 and A6 (TLKP = 6.7 h versus TLKP = 4 h)

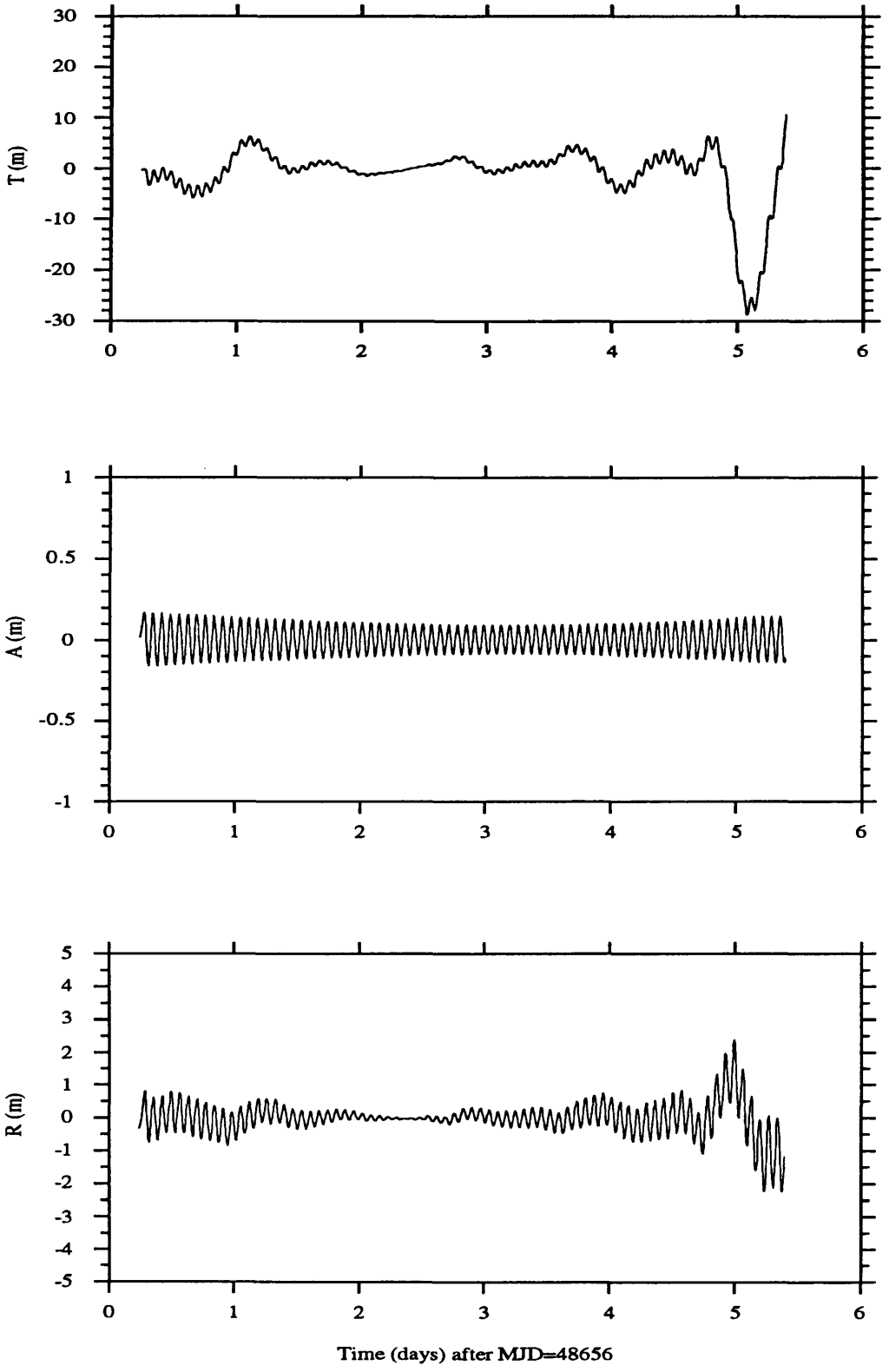

Figure 9.22 - T, A, R differences between orbits A6 and A8 ("single-point" versus "4-point average" Kp data

very large variations in the Kp index, inducing very sharp changes in the drag acceleration.

The second reason is related to the way the drag coefficients are solved-for. For this arc, one coefficient was adjusted for each day. However in the last day there is only one pass of tracking data, which is not enough to provide a good determination of the Cd coefficient for this day.

The results presented in Chapter 8 show that the addition of altimeter data would help to fill the data gap existing at the end of the arc and would lead to a better determined solution. A posteriori, it seems that with the laser data available for this arc, it would have been preferable to have cut the arc at the end of the 5th day, after the last pass for this day.

Similar computations were performed for ARC_B. The results are shown in Figure 9.23 and Tables 9.15 and 9.16.

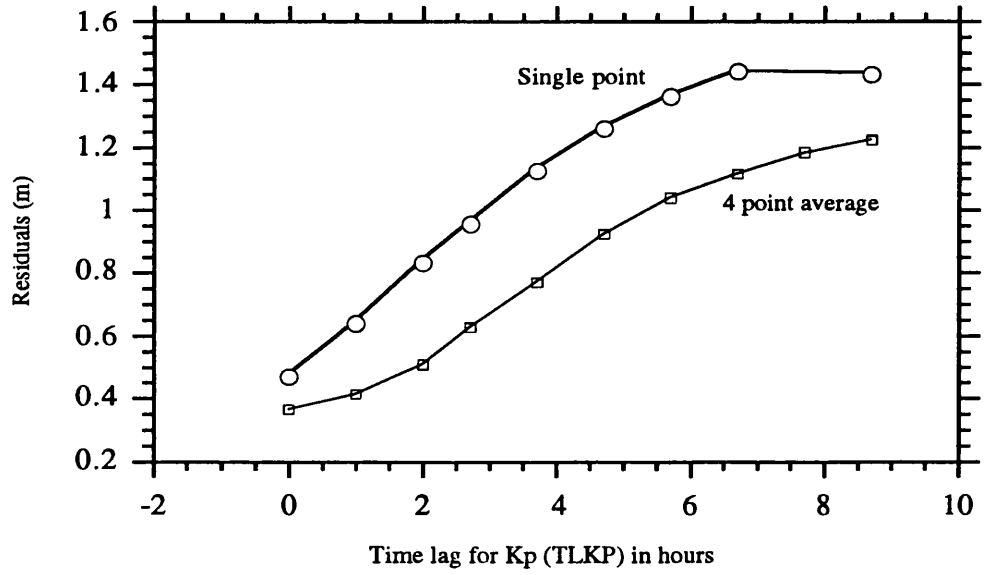

Figure 9.23 - Rms of orbit residuals as function of TLKP for ARC_B

As for ARC_A, the rms of fit of orbits computed using 4-point average Kp values is smaller than the corresponding single-point solution by about one metre. The influence of the value of TLF is less than the influence of the TLKP value. The Jacchia_72 adopted value of 1.71 days proves again to be adequate.

The main difference in these results relative to the results obtained for ARC_A is the different value found for the TLKP corresponding to the best orbit adjustment. For ARC_B this value is equal to zero, both in the "single point" and in the "4-point average" solutions.

Table 9.15
Solutions computed for ARC_B using different TLF and TLKP

Orbit	TLF (days)	TLKP (hours)		Residuals (m) rms	max
B1	1.71	6.7	single point	1.44	3.49
B6	1.71	0.0	single point	0.47	1.12
B7	1.71	6.7	4-point average	1.12	2.52
B8	1.71	0.0	4-point average	0.36	1.15
B9	1.00	0.0	single point	0.53	1.19

Table 9.16
TAR differences for orbits in ARC_B using different TLF and TLKP

Orbits	Total (m)		T (m)		A (m)		R (m)	
	rms	max	rms	max	rms	max	rms	max
B1 - B6	7.33	20.45	7.22	20.44	0.57	0.98	1.15	2.78
B1 - B7	1.69	4.27	1.64	4.27	0.18	0.31	0.36	0.87
B7 - B8	4.94	13.25	4.37	13.24	0.59	0.99	1.16	2.85
B6 - B8	3.14	8.89	3.11	8.89	0.20	0.32	0.39	0.92
B6 - B9	0.52	1.11	0.50	1.11	0.06	0.09	0.12	0.26

It is difficult to analyse these results, since the phenomena that cause this time lag between a magnetic storm and the induced change in the atmospheric density at satellite height are not well understood. There is no clear explanation for the heating experienced by the upper atmosphere during geomagnetic disturbances and it is not known how the heating is distributed in height. It is known, however, that density variations during magnetic storms are observed at heights as low as 200 km (Jacchia ,1965), which are in

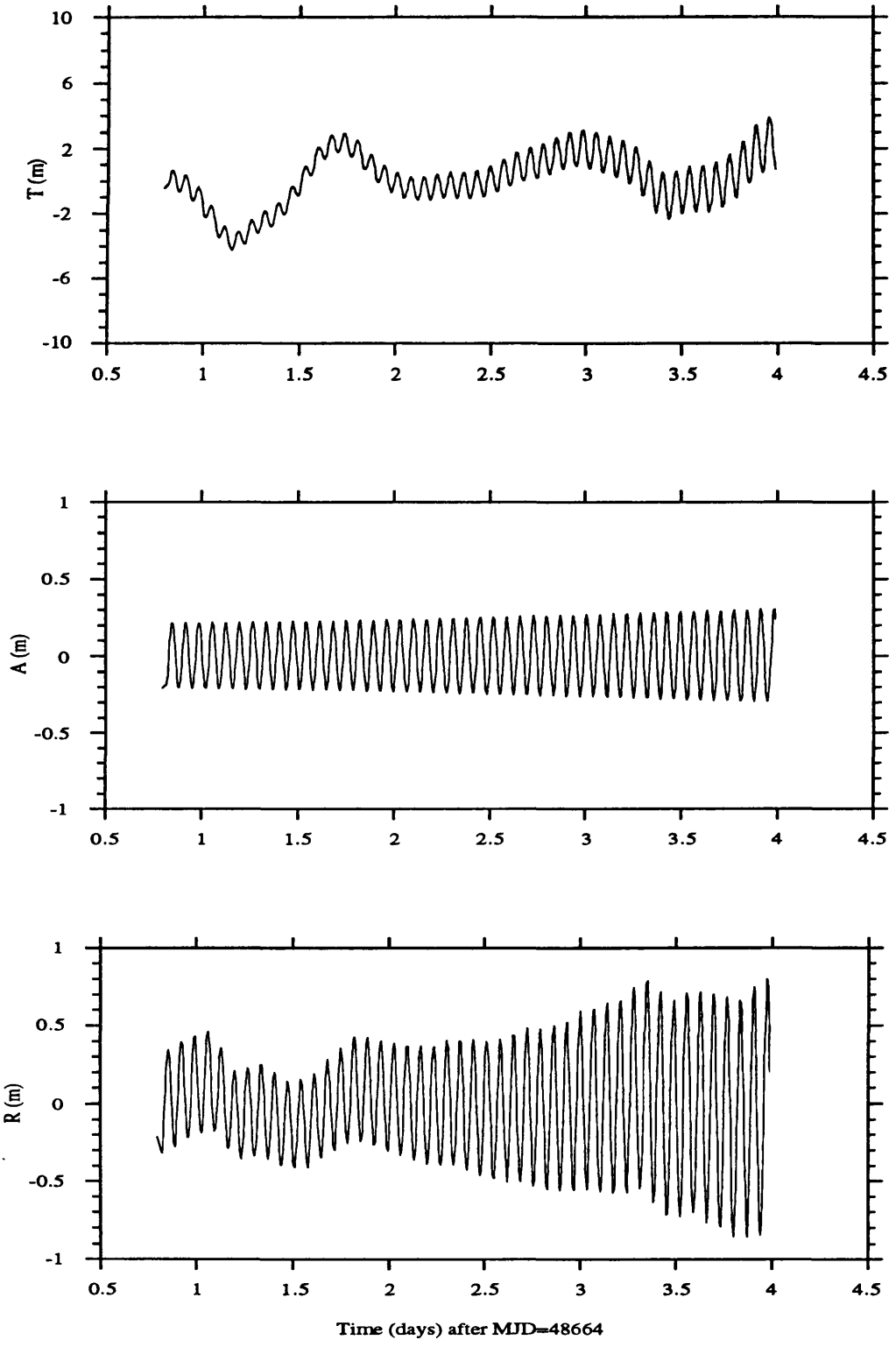

Figure 9.24 - T,A,R differences between orbits B1 and B7 ("single-point" versus "4-point average" for a TLKP = 6.7h)

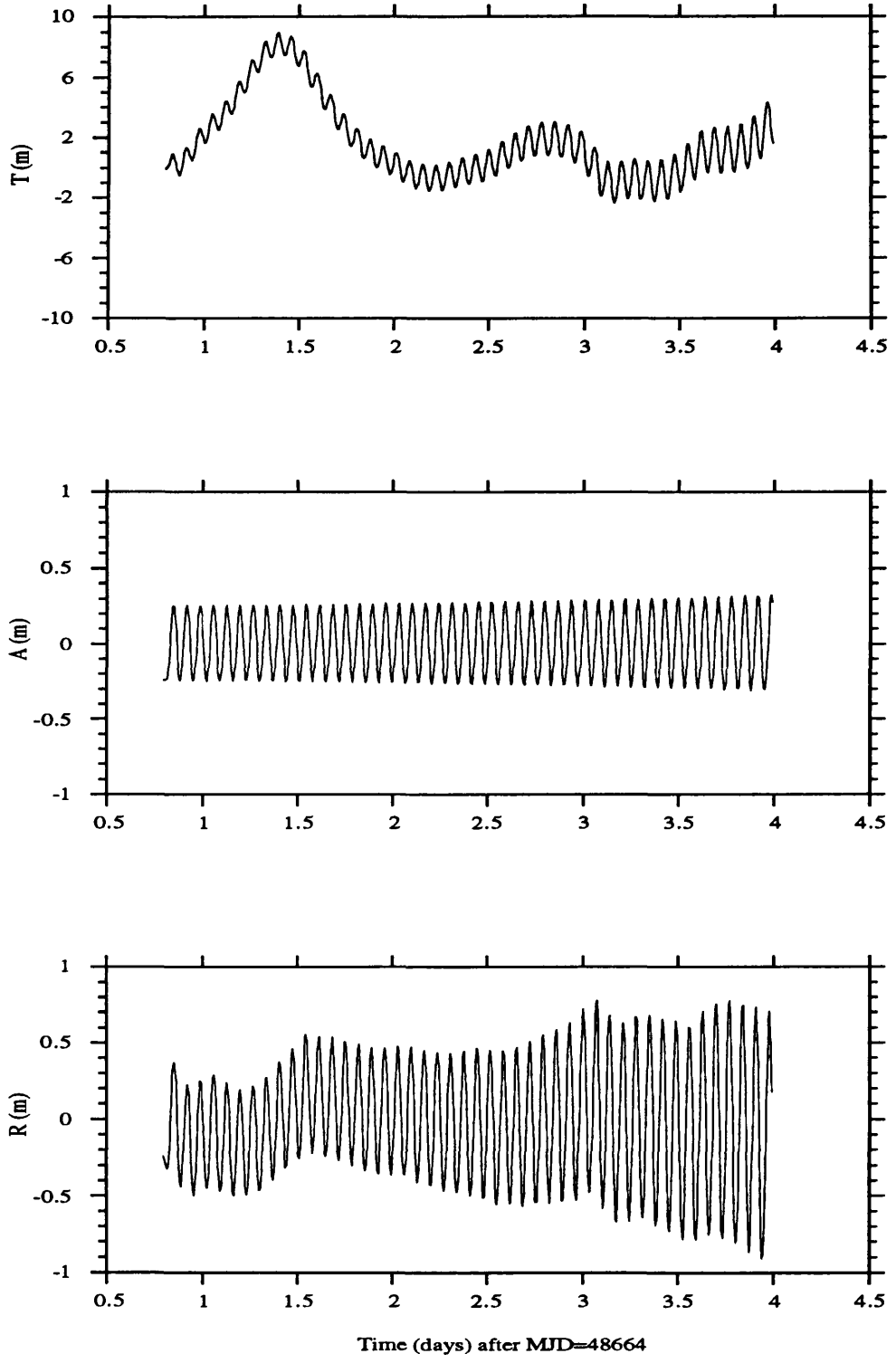

Figure 9.25 - T, A, R differences between orbits B6 and B8 ("single-point" versus "4-point average" Kp data.

phase with density variations at higher levels. The fact that the temperature (and therefore the density) variations show a time lag with respect to the geomagnetic (Kp) variations, could be interpreted as conduction time, if it is assumed that most of the energy is dissipated at heights of 120-130 km.

The time lag adopted by the Jacchia-72 model was determined by drag analysis of 4 satellites. Three of these satellites (Injun 3, Explorer 19 and Explorer 24) had highly eccentric orbits with perigee heights from 250 to 550 km and apogee heights around 2400 km. The fourth satellite (Explorer 17) had an orbit with smaller eccentricity with perigee height of 270 km and apogee height of 800 km. In this analysis the time lag obtained for the last satellite (5.2 hours) is about two hours smaller than the average obtained for the first three (7.0 hours). Jacchia et al. (1967) claim that no clear indication of any variation of the time lag with the satellite perigee height was found. This is in contradiction with the explanation mentioned above, that the time lag is related to conduction time, if most of the heating caused by the magnetic storm occurs at low altitudes. If this was true then the higher the satellite, the greater should be the time lag. If the average satellite height is considered, then the lower this height, the smaller the value of the time lag. However for highly eccentric orbits the average height is not a relevant parameter since the orbit is mostly affected within a small section of orbit around the perigee.

By analysis of the histograms of the various time lags determined by Jacchia et al, (1967) and Roemer (1966) from drag analysis on a number of satellites, we conclude that the "observed" time lags have a large variation, taking values in the interval [0, 12] hours.

Therefore, the time lag found to correspond to a best fit orbit for ARC_A (4 hour for the "single-point" method and 5.5 h for the 4-point average method) is in agreement with the variability quoted for this parameter. The value found for ARC_B (0 h) is more difficult to explain. Although this value is within the quoted variability, the curve in Figure 9.23 does not indicate a clear minimum but rather a linear variation. This value seems too low to correspond to any physical phenomenon, since it is unlikely that the satellite would sense the perturbation exactly at the same time that it occurs. Then how can the results represented in Figure 9.23 be explained ?

Figures 9.18 and 9.20 show that the index Kp during ARC_B has a variation that closely follows a one cycle per day signal. This variation can easily be absorbed by the daily drag coefficients provided that it is "in phase" with the intervals specified for each coefficient. In this case the best fit is achieved for a value of the TLKP of 0 hours, but this does not mean that this solution is better than the others. It only means that the induced perturbation fits better to the tracking data. This is confirmed if we compare the two orbits computed with TLKP = 6.7 h (B1 and B7) with the two orbits computed using a TLKP =

0h (B6 and B8). The difference between these solutions is presented in Figures 9.24 and 9.25. The difference between the first two solutions (B1 - B7 in Figure 9.24) is smaller than the difference between the second ones (B6 - B8 in Figure 9.25). It seems that the last two solutions are poorly determined in the along-track component.

In particular during the first 1.2 days of the arc, where a single drag coefficient is solved for this period, the difference between these solutions is large, reaching about 9 metres.

In conclusion, the value of TLKP = 0h, found to correspond to a best orbit adjustment is too small. The results for ARC_A suggest that a value around 5h should be used instead of the Jacchia_72 value of 6.7 h.

One important conclusion is that the accuracy of ERS-1 orbits computed for periods of high geomagnetic activity are strongly dependent on the time lag introduced in the Kp data. One solution could be to adjust this parameter within the orbit computation. However, to solve for TLKP together with multiple drag coefficients might lead to high correlations between these coefficients, since the TLKP would be another along-track parameter. Therefore this is only possible if enough tracking data are available. In this adjustment some constraint would have to be applied to force the TLKP to take values within a certain interval, for example [3h, 7h].

9.4.4 Use of predicted solar flux data

Precise orbit determinations as described in the previous sections are dependent on the acquisition of several types of data, which can only be assessed some time after their collection. The data needed by the SATAN programs to compute an accurate orbit for a satellite such as ERS-1 are:

- Pole coordinates - These are published in bulletin A of the IERS with a delay of one or two weeks after data collection.

- Tracking data - In principle laser data should be available soon after their collection, if not from a great number of stations, at least from a few.

- Geomagnetic and solar flux data - They are available from the National Geophysical Data Centre, in the USA, within a few weeks of data collection. However the adopted atmospheric model uses the values of the solar flux for a period of two solar rotations (54 days) around the time of the computation. Therefore to use this model, the orbit can only be computed at least two months after data collection.

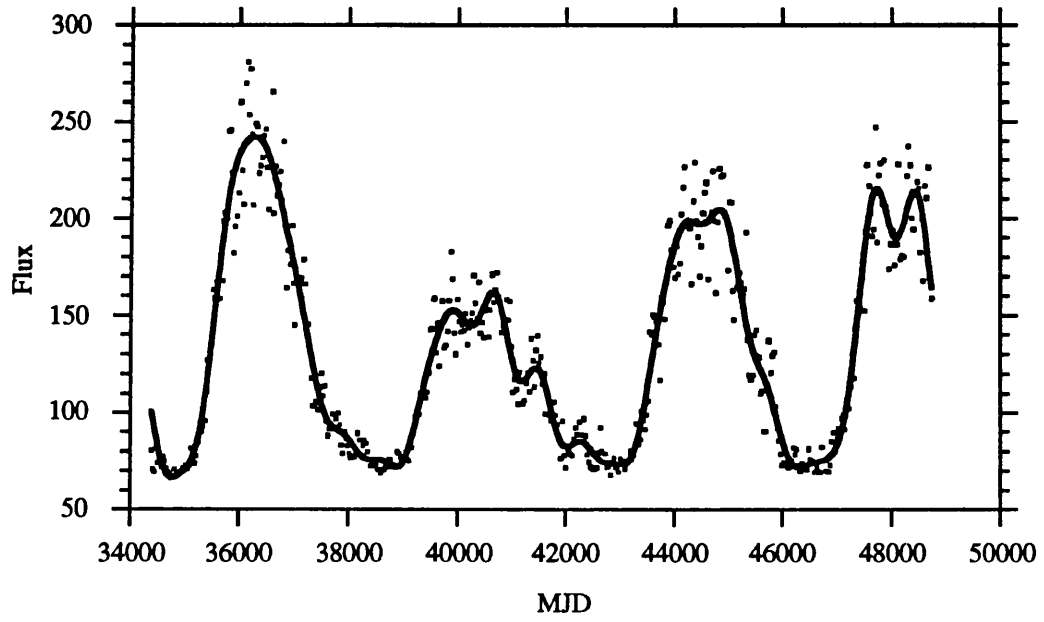

Figure 9.26 - Monthly averages of solar flux from January 1953 to January 1992

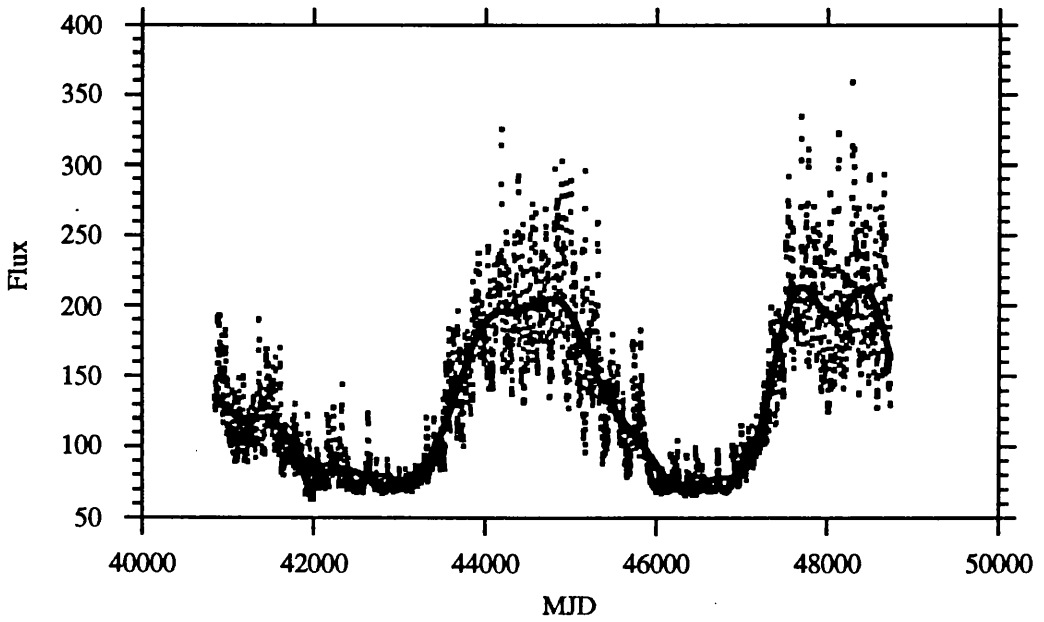

Figure 9.27 - Daily values of solar flux from 1970 October 1 to 1992 April 30

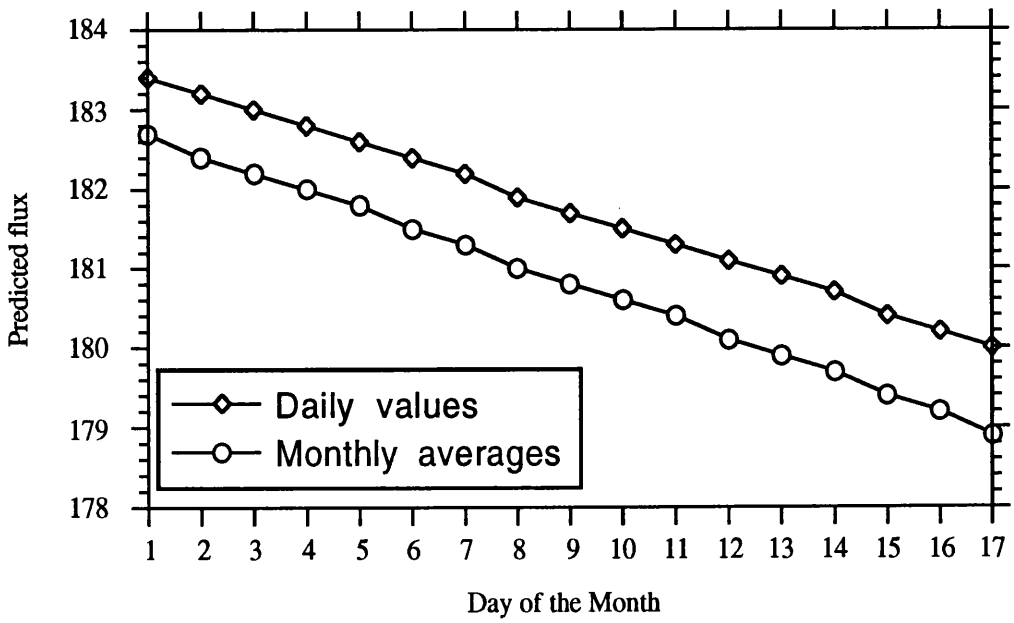

Figure 9.28 - Predicted flux using daily values and monthly averages.

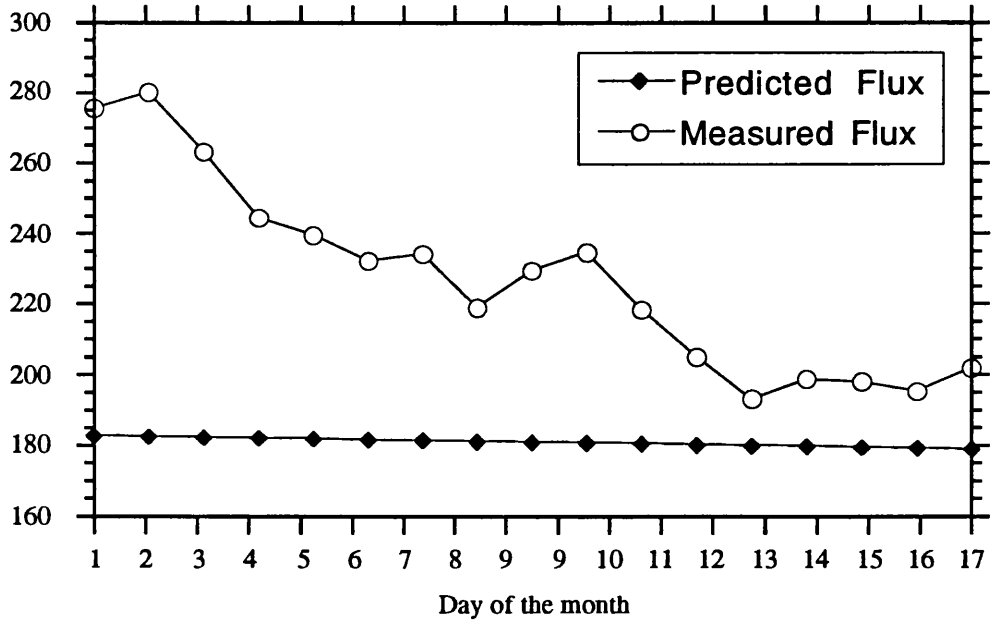

Figure 9.29 - Measured flux and predicted flux using monthly averages.

One of the aims of this study is to be able to compute precise ERS-1 orbits as close as possible to real time. Therefore the use of predicted solar flux instead of actual measurements is investigated.

For this analysis two sets of solar flux data are used.

The first set is composed of daily values of the $F_{10.7}$ solar flux for a period of 22 years (two solar cycles). The analysis of this data set (Figure 9.27) shows that points are very scattered and that the only predictable signal is the long wavelength component. The dominant frequency corresponds to the 11-year solar cycle. Superimposed to this main frequency there are other signals with much smaller amplitudes with periods from 2 to 5.3 years, which are particularly noticeable at the solar maximums. Therefore a cut-off frequency was used such that only those signals with periods longer than two years are kept. In fact a sharper cut-off could have been used, keeping only the 11-year component. In any case the resulting curve will just keep the long-wavelength trend of the phenomenon. This curve, represented in Figure 9.27 is used to predict flux values for the next 4 months after the last point in the curve.

Table 9.17
Solutions computed for ARC_A using predicted flux

Orbit	Flux data (TLF = 1.71 days)	Kp indexes (TLKP = 4h)	Residuals (m)		Residuals on rejected points	
			rms	max	rms	max
A6	Actual data	Actual data	0.38	1.01	2.34	8.41
A10	Predicted data	Actual data	0.45	1.42	2.76	8.87
A11	Predicted data	All zero	1.19	5.85	8.25	27.54

Table 9.18
TAR differences for orbits in ARC_A using predicted flux

Orbits	Total (m)		T (m)		A (m)		R (m)	
	rms	max	rms	max	rms	max	rms	max
A6 - A10	2.63	10.73	2.56	10.73	0.31	0.56	0.50	1.67
A6 - A11	12.50	68.77	16.44	68.77	0.38	1.00	1.43	6.14

A second set of solar flux measurements was used. These data consist of monthly averages for a period of 39 years (3.5 solar cycles), from 1953 to 1992. This covers all the available measurements until present (Figure 9.26). The dominant frequencies are close to those detected using the first data set. Using the same cut-off frequency, the resulting smooth curve is represented in Figure 9.26.

Table 9.19
Solutions computed for ARC_B using predicted flux

Orbit	Flux data (TLF = 1.71 days)	Kp indexes (TLKP = 0h)	Residuals (m) rms	max
B6	Actual data	Actual data	0.47	1.12
B10	Predicted data	Actual data	0.71	1.42
B11	Predicted data	All zero	0.55	1.73

Table 9.20
TAR differences for orbits in ARC_B using predicted flux

Orbits	Total (m)		T (m)		A (m)		R (m)	
	rms	max	rms	max	rms	max	rms	max
B6 - B10	1.42	3.62	1.35	3.62	0.19	0.28	0.39	0.75
B6 - B11	12.60	33.83	12.59	33.83	0.21	0.34	0.57	1.29

These two curves were used to predict the solar flux for the first 4 months of 1992, covering the period of the computations. Figure 9.28 compares the results obtained from the two curves. For such a short period of time as 15 days, the predicted flux is just a straight line. The two predictions differ by a small constant bias, but the linear trend is similar. When these predicted values are plotted together with the actual measurements, the prediction is nearly equivalent to assuming a constant flux for the whole period. Both predictions will give equivalent solutions since this bias will be absorbed by the drag coefficients.

If it is acceptable to predict the long wavelength trend of the solar flux, for the geomagnetic indexes that is not possible at all, since the geomagnetic activity is not a regular and predictable phenomenon.

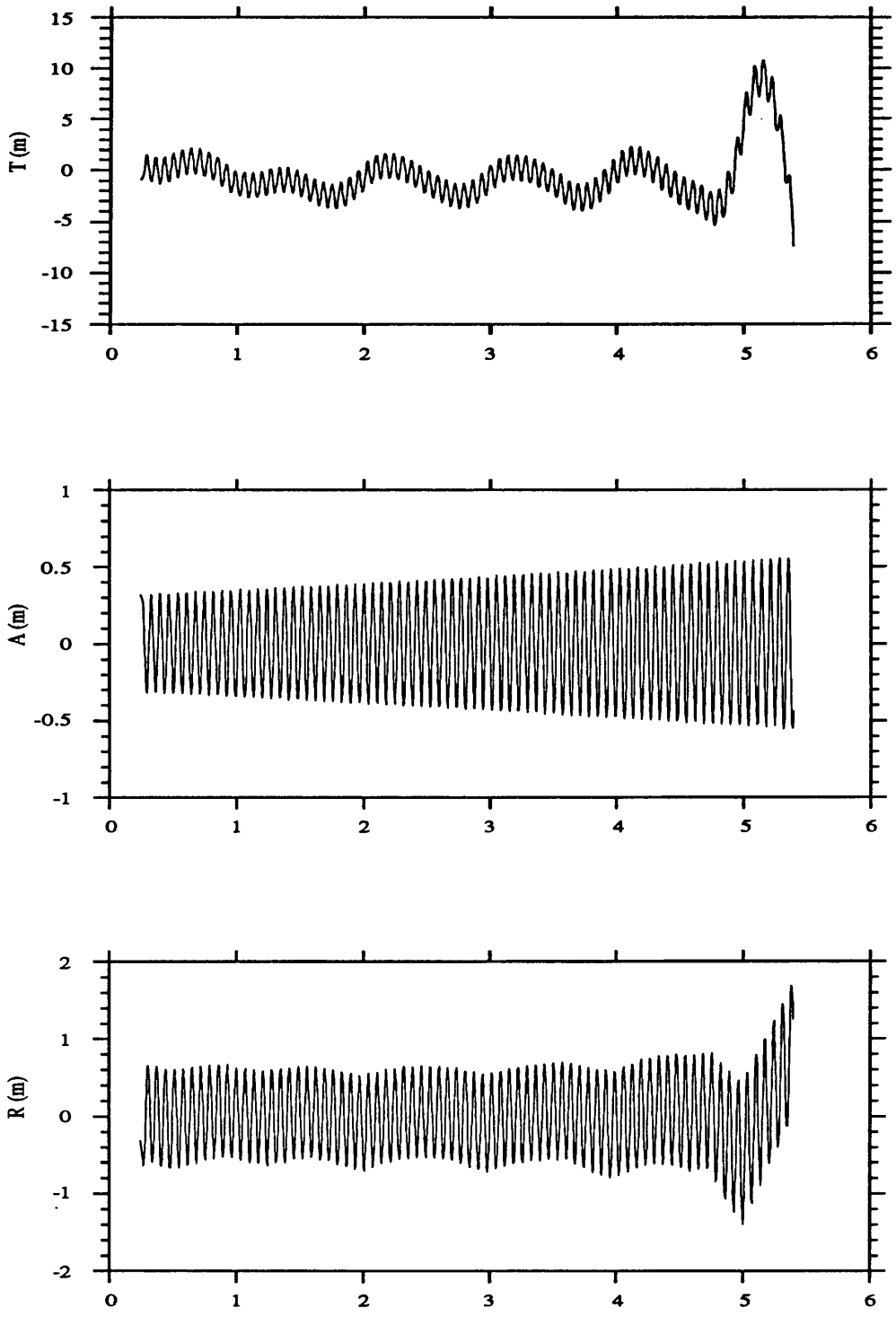

Figure 9.30 - T,A,R differences between orbits A6 and A10 (measured flux versus predicted flux)

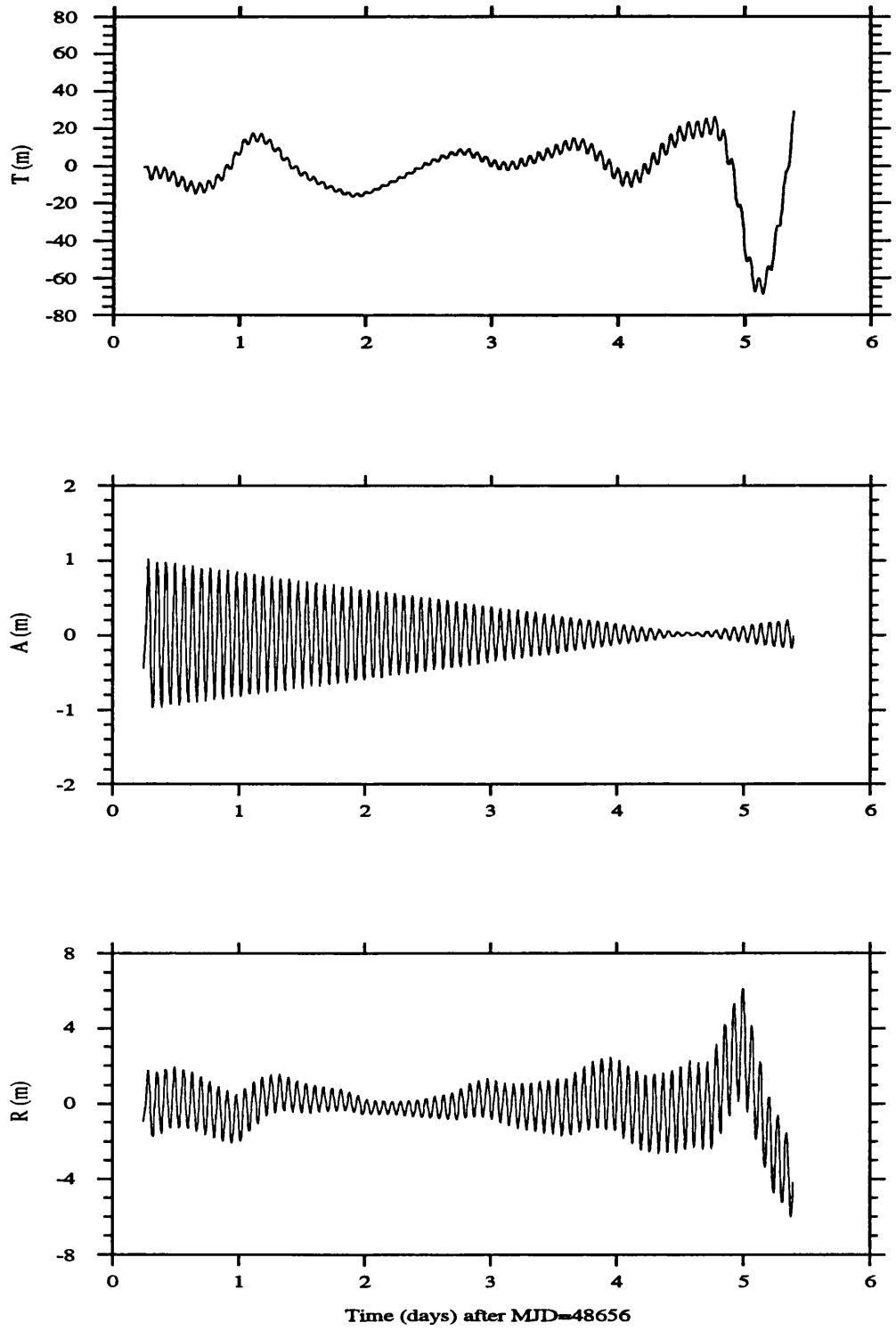

Figure 9.31 - T,A,R differences between orbits A6 and A11 (measured flux and Kp data versus predicted flux and no Kp data)

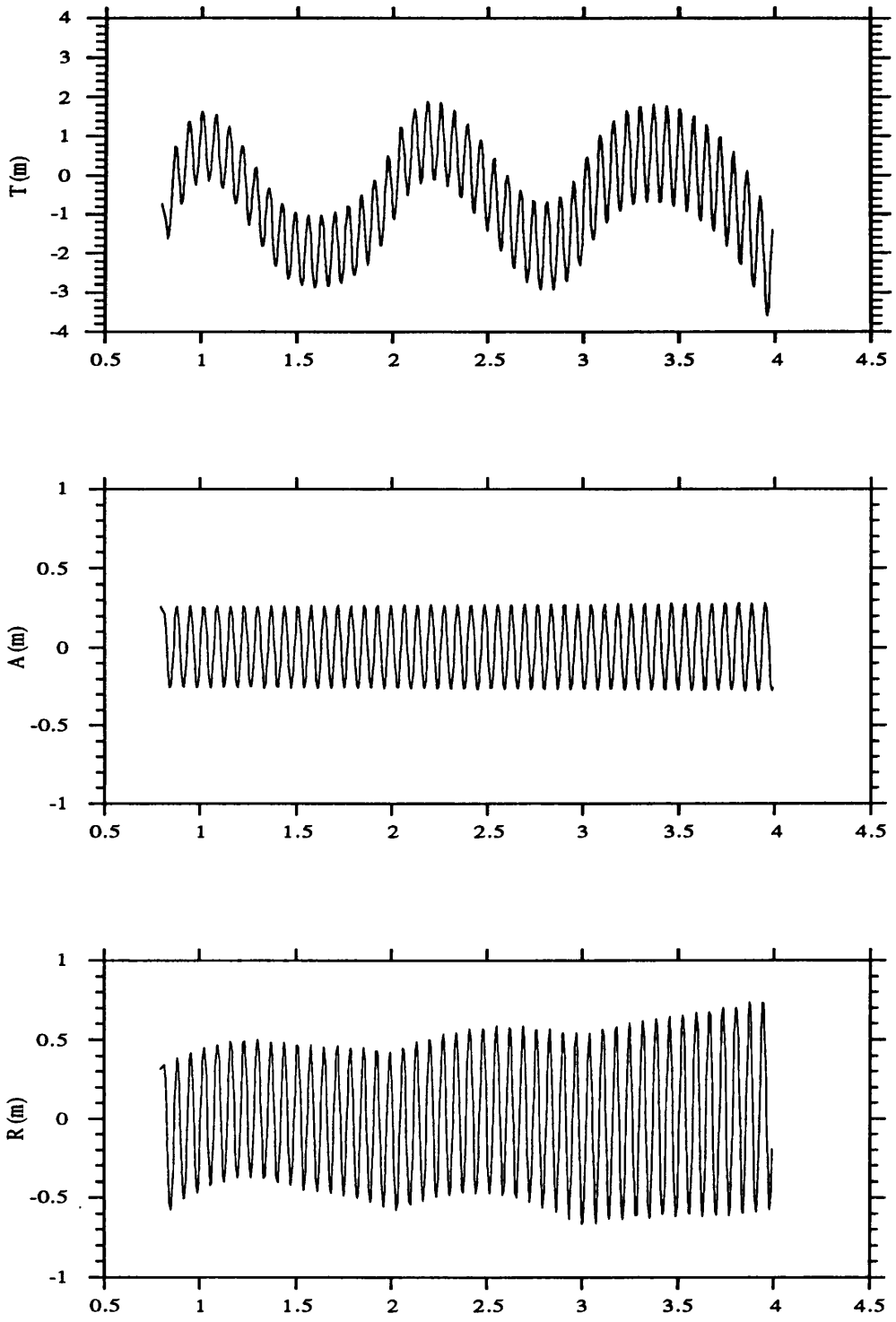

Figure 9.32 - T,A,R differences between orbits B6 and B10 (measured flux versus predicted flux)

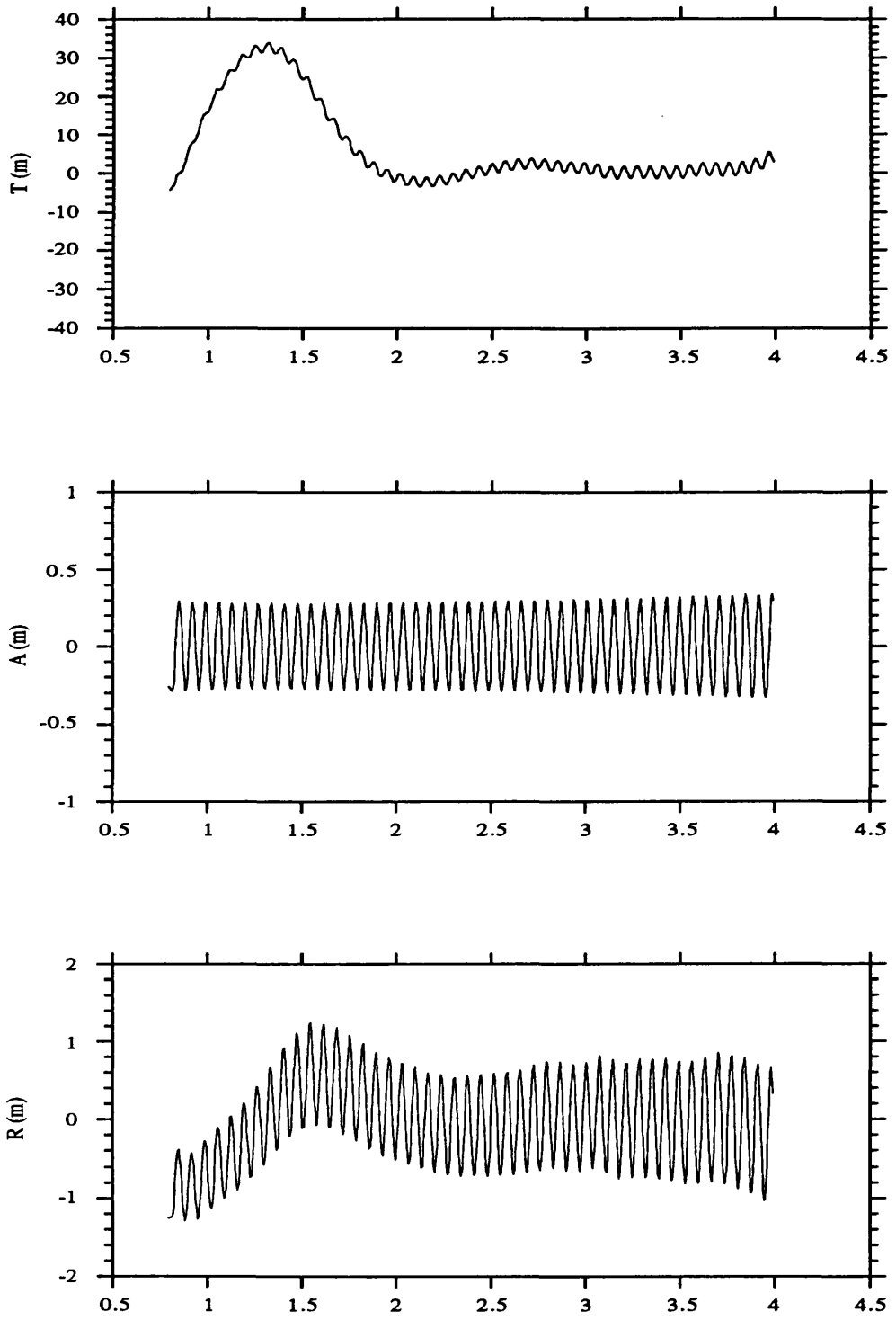

Figure 9.33 - T,A,R differences between orbits B6 and B11 (measured flux and Kp data versus predicted flux and no Kp data)

Using the predicted values of the solar flux two solutions where computed for ARC_A as described in Table 9.17. In the first solution, called A10, the solar flux used is the predicted flux but the actual Kp indexes are kept. In this solution the values adopted for the TLKP were the values corresponding to the minimum residuals in Table 9.13, i.e., TLKP = 4 h, keeping the value of TLF = 1.71 days. The reason for computing this solution is because the only data that actually need to be predicted for a long period are the flux data. The Kp indexes are only needed for the time of the computation and therefore can usually be obtained within a few weeks of data collection.

The second solution, called A11, uses predicted solar flux and neglects completely the geomagnetic data, attributing a value of zero to all Kp indexes. The difference between these solutions and the solution computed using actual data (A6) is presented in Table 9.18 and Figures 9.30 and 9.31.

Considering the actual accuracy of all these solutions, the differences between orbits A6 and A10 is not significant apart from the last half day of the arc. It had already been noticed that this arc is not well determined in this region and therefore the solution should only be considered up to the last pass of the 5th day. Apart from this region the rms of the differences between these solutions is only 1.6 m, 0.3 m and 0.5 m in the T, A and R components respectively. Therefore the use of predicted solar flux does not significantly degrade the solution.

The same is not true if the geomagnetic indices are not used as in solution A11. Now this solution departs considerably from solution A6, showing along-track differences with amplitudes as large as 20 m in the first 5 days of the arc. In the last half day the amplitude of the differences is again as large as in all the previous results.

Similar computations were repeated for ARC_B, the results being presented in Tables 9.19 and 9.20, and Figures 9.32 and 9.33. The results are similar to those obtained for ARC_A only the amplitude of the differences is smaller, since the geomagnetic activity for this arc is also smaller.

In conclusion, the use of predicted solar flux together with actual geomagnetic indices does not significantly degrade the solution. Since the solar flux has a daily variation, this effect is absorbed by the drag coefficients. However the use of the geomagnetic indices is fundamental. The effect of neglecting these measurements is proportional to the amplitude of the geomagnetic activity along the arc and can reach several metres.

9.5 - Adjustment of geopotential coefficients

As part of the effort to develop improved ERS-1 orbits with the existing models, the adjustment of geopotential coefficients is considered.

The development of gravity field models involves the processing of large amounts of data and powerful computers to run the programs. The SATAN package is a set of relatively simple programs which are intended to run on a medium machine. The aim is therefore to implement on those programs a simple algorithm for the adjustment of a selected set of gravity field coefficients, and investigate how this procedure can help in the computation of more precise ERS-1 ephemerides. Since the only tracking data available was the reduced laser data set referred to throughout this chapter, it was known in advance that with these data it would not be possible to get a refined geopotential model that would give improved orbit accuracy for all parts of the arc. This exercise must therefore be regarded as a preparation for future research by using a better data set.

9.5.1 Orbit errors due to geopotential coefficients errors.

In the expression of the geopotential in terms of spherical harmonics, each term containing the coefficients of degree ℓ, $(C_{\ell m}, S_{\ell m})$ is multiplied by factor $\left[\frac{r_o}{r}\right]^{\ell}$ where r_o is the Earth's equatorial radius and r the geocentric distance to the satellite (equation 3.3). Because of this altitude attenuation factor, the higher the degree of a spherical harmonic coefficient, or of its error, the less its effect on the potential and the gravitational acceleration on the satellite.

The errors in the coefficients of present models increase with ℓ and m until they reach about 100% of the coefficient itself at about degree and order 30. Above this, the combined effect of all the estimated coefficients might reproduce the data used in the geopotential modelling, but their individual values may be 100% in error.

Using analytical theory it may be shown that many different terms in the gravity field lead to the same orbit perturbations. It is therefore possible to select a set of geopotential coefficients which may be adjusted relative to an existing gravity model, in order to achieve an improvement in the accuracy of this model for a particular satellite.

The analysis of satellite orbit errors due to a geopotential model is usually based on Kaula's theory.

The frequencies of the orbit errors due to a spherical harmonic of degree ℓ and order m are (Kaula, 1966), (Colombo, 1984):

$$\psi_{\ell mpq} = (\ell - 2p+q)(\dot{\omega} + \dot{M}) - q\dot{\omega} + m(\dot{\Omega} - \dot{\theta}) \qquad (9.19)$$

where: • $p = 0,1, ..., \ell$

• q can take any values from $-\infty$ to $+\infty$ but for near circular orbits it is sufficient to consider $|q|<2$, i.e., only 3 values: $0, \pm 1$.

• $\dot{\omega}$ is the apsidal frequency of a complete revolution of the perigee.

• $\dot{\Omega} - \dot{\theta}$ is the frequency of a complete rotation of the Earth with respect to the precessing orbital plane.

• $\dot{M}$ is the rate of change of the mean anomaly (approximately one cycle per revolution).

Each of these frequencies is a linear combination of the orbital frequency $\dot{\omega} + \dot{M}$ (one cycle per revolution), the apsidal frequency $\dot{\omega}$ and the frequency $\dot{\Omega} - \dot{\theta}$.

When the frequency is zero, the amplitude of the perturbation becomes infinite. In this case the orbit is said to be in a "perfect resonance".

At a height of about 1000 km a spacecraft completes a number of 13 to 14 revolutions in one "nodal day", the time $T_D = \left| \frac{2\pi}{\dot{\Omega} - \dot{\theta}} \right|$ taken by the Earth to do a complete revolution with respect to the precessing orbital plane. Calling this number N_R, and assuming that $\dot{\omega} = 0$, there are always combinations of ℓ, **m** and **q** such that

$$(\ell - 2p+q)\dot{M} + m(\dot{\Omega} - \dot{\theta}) = 0 \qquad (9.20)$$

for all coefficients of order $m = k N_R$, $k=0,1,2, ...$

If N_R is very close to an integer, the perturbations are large but periodic, with long periods, the so-called "deep resonance".

For altimeter satellites flying in frozen orbits $\dot{\omega}$ is quite small (in theory should be zero) and N_R differs considerably from an integer, being about 14.3. In this case, the errors from coefficients whose order **m** comes closest to satisfy the resonance condition, can still produce long period effects much larger than those of the others. These terms are

called "shallow resonant" terms. Altimeter satellites have orbits with shallow resonance at orders close to the whole multiples of 13 or 14.

For ERS-1 $N_R = 14.3$ and therefore the resonant terms are:

k=0 all zonals
k=1 m=14,15
k=2 m=28,29
k=3 m=43

After the resonant terms, the terms for which $(\ell - 2p+q) = 0$ come next in importance. In this case the frequency reduces to $- q\dot{\omega} + m(\dot{\Omega} - \dot{\theta})$. For altimeter satellites this frequency is quite small compared to the dominant "once per revolution frequency" $\dot{\omega} + \dot{M}$. Provided that **q** and **m** are small integers, these terms are much smaller than any other terms where $(\ell - 2p+q) \neq 0$. Since $\dot{\omega}$ is very small when compared to $(\dot{\Omega} - \dot{\theta})$, the corresponding frequencies will be close to **m** cycles per day, the corresponding terms being called "m-dailies".

The total amplitude of the oscillation associated with a particular frequency is a sum of all terms for which **(ℓ-2p)**, **q** and **m** are constant. Terms of the same order **m**, and degree ℓ of the same parity (even, odd), contribute to the same frequency. For example (16,14) and (14,14) produce errors of the same type and the same happens with (15,14) and (17,14). For altitudes of 1000 km, $|q|<2$ and these perturbations are more significant for terms with $\ell<10$.

9.5.2 Choice of the coefficients to adjust

The adjustment of a sub-set of geopotential coefficients for a particular satellite has been analysed by several authors. Wakker et al, (1983b) adjusted a set of 7 pairs of C and S coefficients of the already tuned SEASAT model PGS-S4. The adjusted coefficients were all shallow resonant coefficients. During the present study it was found that some of these shallow resonant coefficients, leading to errors of the same frequency, (all terms of the same order and same degree parity) reveal very high correlations when solved together. For example, (14,14) and (16,14) cause approximately the same type of errors and therefore only the dominant term (14,14) should be solved.

The geopotential model selected for this adjustment was GEMT2. Figure 9.35 represents the rms errors per degree of the GEMT2 coefficients. From this figure, the coefficients with largest uncertainties lie within a band $12 \leq \ell \leq 30$. Figure 9.34 shows the estimated error for each individual coefficient. According to this figure, the coefficients with the

Figure 9.34 - Estimated error for GEMT2 coefficients. Errorx10^{-9}. Extracted from (Marsh et al., 1990a).

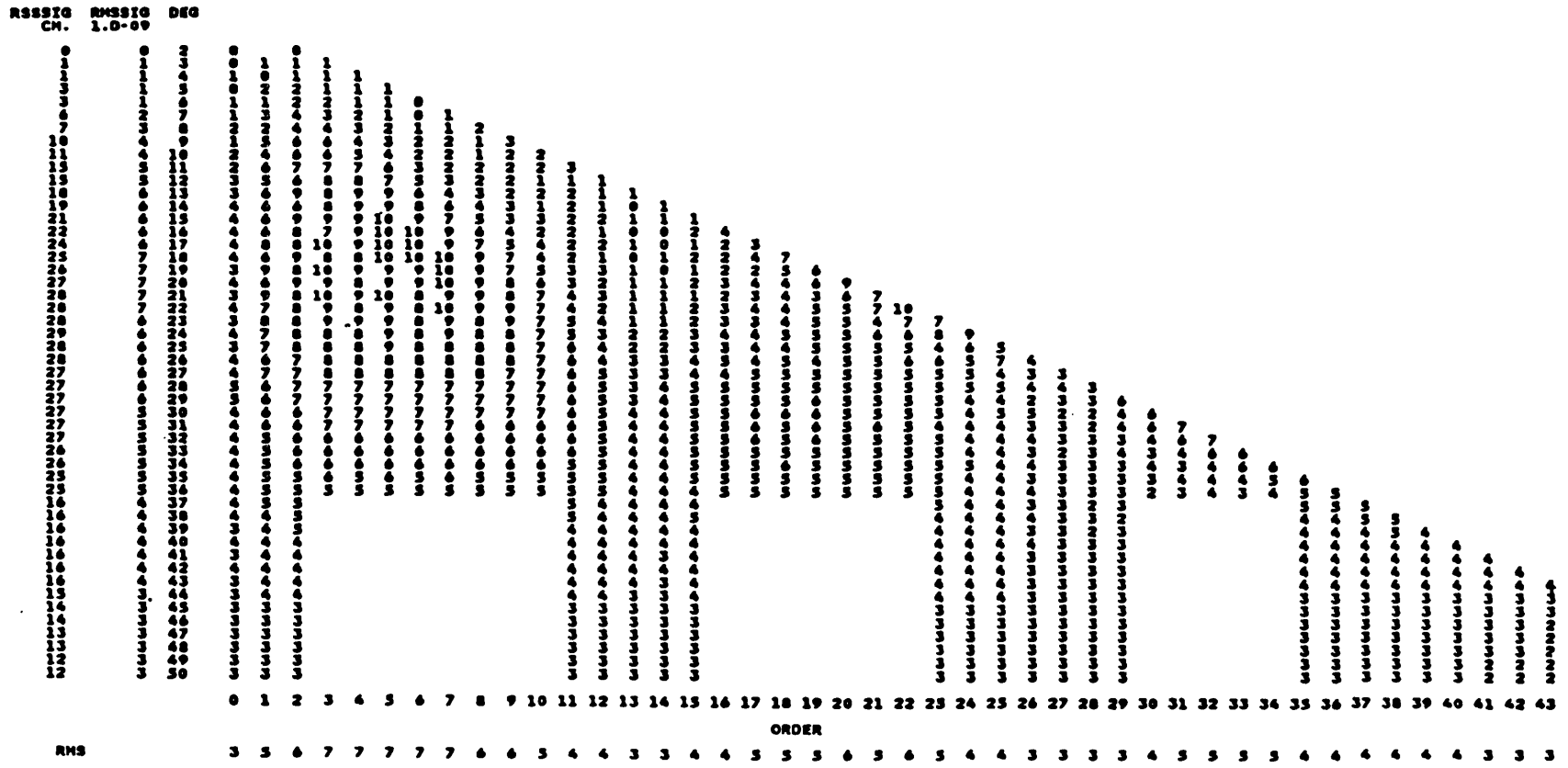

largest errors are situated within a band with degree $13 \leq \ell \leq 25$ and order $1 \leq m \leq 9$. The blank squares in this figure represent the coefficients which are not modelled in GEMT2.

To determine the set of coefficients to adjust, instead of using the rather complicated Kaula formulation (Kaula, 1966), (Rosborough and Tapley, 1987), a simpler procedure was developed for this project. The algorithm implemented in program ORBIT for the adjustment of geopotential coefficients includes the computation of the partial derivatives of satellite position, (X, Y, Z), with respect to each geopotential coefficient. These are computed by numerical integration as explained in section 3.5.1. These partials can be used to compute the effect of a certain coefficient on the position of the satellite, during a specified time interval and therefore to determine which coefficients have more influence on the orbit accuracy. The adopted procedure is explained.

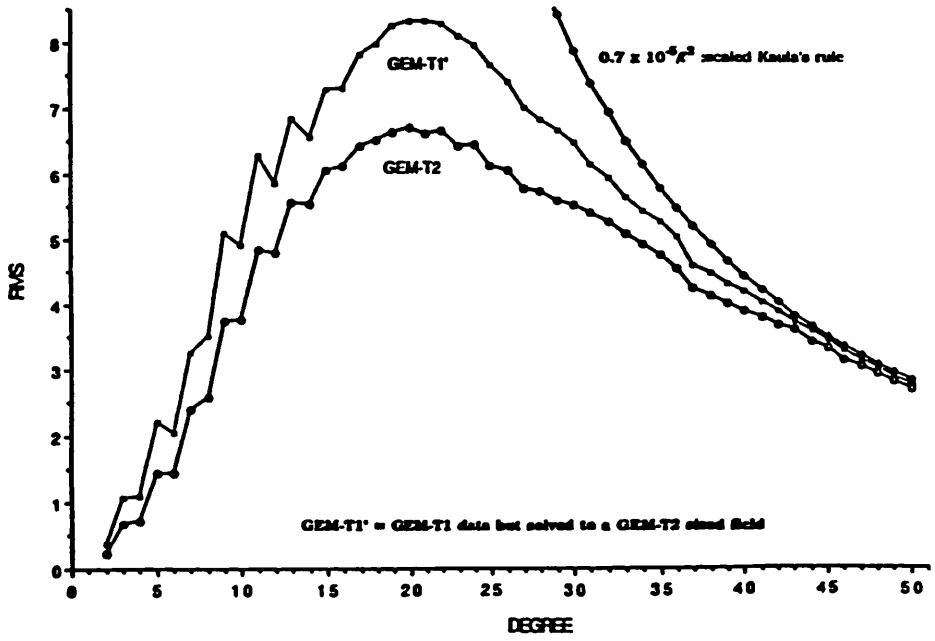

Figure 9.35 - RMS of coefficient errors per degree for GEMT2. From (Marsh et al., 1990a)

For each coefficient of degree ℓ and order **m**, program ORBIT computes the partial derivatives of (X, Y, Z) with respect to each pair $(C_{\ell m}, S_{\ell m})$. These partials can be used to compute the errors on (X, Y, Z), $(\Delta X, \Delta Y, \Delta Z)$, caused by errors on $(C_{\ell m}, S_{\ell m})$,

$(\Delta C_{\ell m}, \Delta S_{\ell m})$. The formulae are given for the $C_{\ell m}$ coefficients. Similar expressions hold for $S_{\ell m}$.

$$\begin{bmatrix} \Delta X \\ \Delta Y \\ \Delta Z \end{bmatrix} = \begin{bmatrix} \frac{\partial X}{\partial C_{lm}} \\ \frac{\partial Y}{\partial C_{lm}} \\ \frac{\partial Z}{\partial C_{lm}} \end{bmatrix} \Delta C_{lm} \tag{9.21}$$

For these computations $\Delta C_{\ell m}$ were assumed to be equal to the value of the coefficients themselves, using Kaula's Rule of Thumb:

$$\Delta C_{\ell m} = C_{\ell m} = \frac{10^{-5}}{\ell^2} \tag{9.22}$$

This method gives an overestimate of the errors for the coefficients of the lowest degrees, but this does not constitute a problem since according to Figures 9.34 and 9.35 only coefficients above degree 12 will be considered.

These errors in (X, Y, Z) are then transformed into errors in the (T,A,R) directions, by applying the transformation:

$$\begin{bmatrix} \Delta T \\ \Delta A \\ \Delta R \end{bmatrix} = \begin{bmatrix} T_X & T_Y & T_Z \\ A_X & A_Y & A_Z \\ R_X & R_Y & R_Z \end{bmatrix} \begin{bmatrix} \Delta X \\ \Delta Y \\ \Delta Z \end{bmatrix} \tag{9.23}$$

The matrix in the above formula is formed by the components of the (T,A,R) vectors in the (X, Y, Z) frame (the J2000 frame).

For a 3-day ERS-1 orbit, these errors were computed, at each step of the integration (1.25 minutes), for each coefficient. At the end of the integration the rms values of these errors are computed. Table 9.21 presents the coefficients with degree ≥13 with the 10 largest errors for each component. These errors are the sum of the errors caused by $C_{\ell m}$ and $S_{\ell m}$.

To be able to compare the relative influence of each coefficient on the orbits of both satellites, the same procedure was repeated for a 3-day SEASAT orbit. Since GEMT2 is a precise geopotential model for SEASAT, in principle, a coefficient which gives much larger errors for ERS-1 than for SEASAT should be adjusted.

Table 9.21
GEMT2 coefficients with the 10 largest errors for ERS-1 (for degree ≥13)

T	A	R
(15,14)	(15,14)	(14,14)
(15,15)	(17,14)	(16,15)
(17.14)	(15,15)	(16,14)
(13,13)	(13,13)	(18,14)
(13, 3)	(19,14)	(13, 1)
(13, 2)	(13,12)	(14,13)
(13,12)	(17,15)	(20,14)
(14, 3)	(21,14)	(18,15)
(15, 3)	(14, 1)	(15,14)
(14, 2)	(19,15)	(15, 1)

Table 9.22
GEMT2 coefficients giving larger errors for ERS-1 than for SEASAT
(meaning of rows as explained in the text)

T	(13,2) (13,3) (14,3) (14,4) (15,5) (19,4) (19,18) (23,6) (24,24) (25,8) (26,26) (28,28) (31,6) (34,6) (35,7) (43,43) (45,43)
A	(13,12) (13,13) (14,2) (15,13) (15,14) (15,15) (17,14) (17,16) (18,1) (19,14) (30,29)
R	(13,1) (14,14) (16,14) (16,15) (18,14)

From this comparison, a set of coefficients is found to induce substantially larger errors on ERS-1 than on SEASAT. These coefficients are presented in Table 9.22, classified in three classes:

- T - the only component with significant errors is the along-track (T) component.

• A - Apart from the T errors, A errors are also very significant, being much larger than R errors.

• R - Apart from the T errors, R errors are very significant, being much larger than A errors.

Combining all this information a set of coefficients was selected. In this selection the following criteria were adopted:

• Only terms above degree 13 (inclusive) are considered.

• Because coefficients that induce errors at the same frequency will have very high correlations, only those which produce the highest errors are chosen. For example terms (14,14), (16,14) and (18,14) produce very similar errors in the R component. In this case only the dominant term (14,14) is solved-for.

• Terms which induce long-period errors are given preference relative to short period terms. This is because the available tracking data for these ERS-1 arcs do not have a good geographical distribution. Therefore if short period terms are solved-for, the resulting field would reproduce the data, but would be very poor over the untracked parts.

• The dominant resonant terms are included.

9.5.3 Orbits computed by adjusting a selected set of geopotential coefficients

Due to the poor distribution of the tracking data it was known in advance that only a small set of coefficients could be adjusted. From a careful analysis of the above results and after removing some highly correlated coefficients, a set of 14 pairs (C, S) were selected as indicated in Table 9.23.

One orbit was computed for ARC_A by solving for the usual parameters (start vector, daily drag coefficients, solar radiation coefficient) plus this set of 28 coefficients. The residuals after fit of this solution (called A12) have an rms of 0.48 metres with a maximum of 2.01 metres. Apparently this is an improvement with respect to solution A2 computed with the initial GEMT2 model.

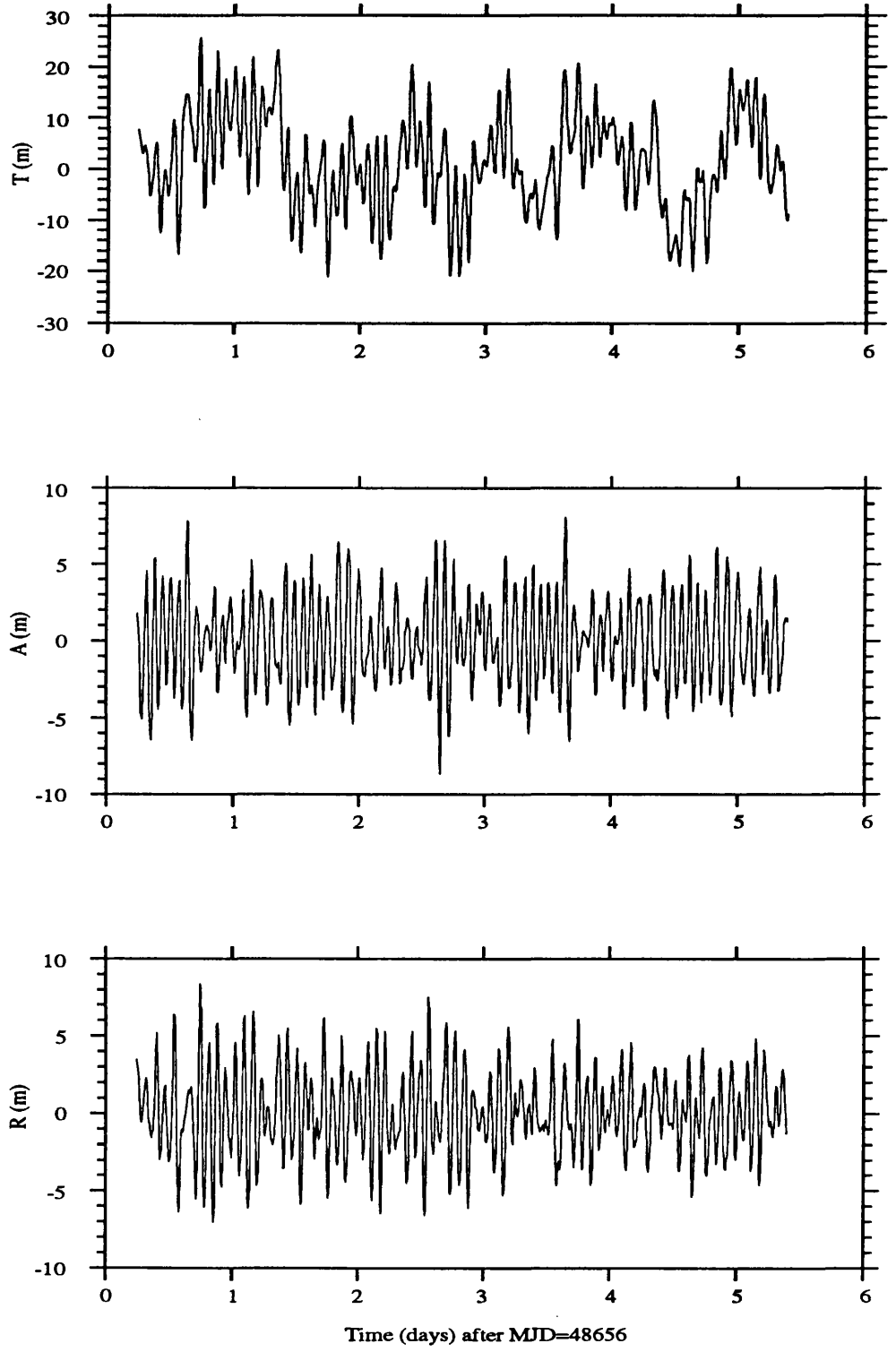

Figure 9.36 - T, A, R differences between orbits A1 and A12 (GRIM4_C2 versus adjusted GEMT2 model)

Using this adjusted model to compute an orbit for ARC_B, a solution is obtained with an rms of 3.1 metres, which is a slight improvement with respect to orbit B2 computed with the original GEMT2.

Table 9.23
Set of adjusted GEMT2 coefficients used in solution A11

(13,3) (13,13) (14, 2) (14, 4) (14,14) (15, 5) (15,14) (15,15) (17,16) (19,18)
(23, 6) (26,26) (31, 6) (35, 7)

However when solution A12 is compared with orbits computed with GRIM4_C2 large differences exist between these orbits. A comparison with orbit A1 is plotted in Figure 9.36 (A1 - A12). When this figure is compared with Figure 9.7 we can see that there is no real improvement. On the contrary, the differences in the A and R components are slightly larger.

Other combinations of geopotential coefficients were used with similar results.

It is evident from these results that this technique cannot be applied to arcs of this length (approximately 5 days) by using data from a small number of stations with poor geographical distribution, such as the laser data set used in this study. Another important factor is that, during this period the drag perturbation is very high and therefore this arc is unsuitable for the adjustment of geopotential coefficients. In fact if we try to solve for geopotential coefficients with only a single drag coefficient for the whole arc, the adjustment is very poor, revealing that the adjusted coefficients cannot absorb the along-track drag errors.

However this technique can certainly be applied if a larger data set is available, covering a much longer interval. When the fully corrected ERS-1 altimeter data are available, these data can certainly help in this type of computation, by filling the long gaps existing in laser data. As pointed out by Zandbergen et al. (1988), for the adjustment of geopotential coefficients it will probably be better to use crossover points instead of the global filtered altimeter heights, to avoid the aliasing of the sea surface topography into the recovered model.

In conclusion, more research needs to be done on the implementation of the above explained procedure for the adjustment of a selected set of geopotential coefficients. To obtain more reliable results, the method should be applied to a much longer arc, in order to get a better determination of the resonant coefficients. This determination should take place during a period of quiet solar and geomagnetic activity, so that errors due to the mismodelling of the drag force are not absorbed by the geopotential coefficients.

9.6 Conclusions

The best geopotential model for ERS-1, at present seems to be GRIM4_C2. ERS-1 orbits determined with this model by adjusting for daily drag coefficients have rms range residuals of 1.5 m. The radial and across-track accuracy of these orbits is of the same order, but the along-track errors are about 3 times larger.

During periods of low solar and geomagnetic activity, these errors are mainly of gravitational origin (e.g. ARC_B), but for arcs where this activity is high, manifested in sharp variations of the geomagnetic index Kp (e.g. ARC_A), the errors due to drag mismodelling become more important. The long wavelength component of these errors can be absorbed by solving for daily drag coefficients. When the tracking data are sparse, with long gaps close to one day, the choice of the intervals to which each of the coefficients will apply is very important. In principle the intervals should be daily intervals, starting and ending at the start and end of each new day, since there are a number of perturbations that have a daily variation. Each coefficient will be determined solely by the tracking data available for that interval. Therefore if, for example during that day there is only one pass, the coefficient will not be well determined, and if there are sharp fluctuations of the drag force during the same period, the orbit will have large errors in this area.

The rms of fit of the computed ephemeris is strongly dependent on the value used for the time lag introduced in Kp data (TLKP). It was found, that for ARC_A a difference of about 2 hours in the TLKP value makes the rms of fit to laser ranges go from 1.6 metres to only 0.4 metres. If adequate data are available, this parameter should be adjusted within the solution. If such adjustment is impossible instead of the original Kp indices, it seems preferable to use a smoother representation of the same indices. In this study a simple 4-point average filter was applied, but further research is needed to determine a more appropriate smoothing function.

By contrast with the results obtained for the TLKP, the time lag introduced in the solar flux indices $F_{10.7}$, (TLF) seems to have a minor influence in the solution. These indices

model daily and longer wavelength variations of the atmospheric density. Therefore any error in these indices is absorbed by the daily drag coefficients, provided adequate tracking data are available. A consequence of this result is that if predicted values of solar flux are used, by just modelling the long wavelength component of their variation (mainly the 11-year solar cycle), the resulting ephemeris does not depart from the solution that would be obtained by using the actual measured indices. In this case the resulting adjusted drag coefficients will exhibit unrealistic values, to account for the effect of a bias on each daily index $F_{10.7}$.

The same is not true if the geomagnetic indices are neglected. In this case the Kp indices cannot be predicted, since they model irregular unpredictable variations of the geomagnetic field. The errors induced by neglecting the geomagnetic indices depend on their variability over the interval considered. For arcs with sharp Kp variations, these errors may reach several metres. This constitutes a limitation to the generation of precise and rapid ephemerides. It is therefore crucial to have access to these measurements, as soon as they are released by the NGDC, in the United States.

In order to reduce the errors of gravitational origin, the adjustment of a selected set of geopotential coefficients was considered. Due to the few data passes that were available for this exercise, and the large drag errors existing in this arc, the results are not very conclusive. The same technique should be applied to a much longer arc, during a period of reduced solar activity. This subject needs further research into an appropriate choice of the coefficients to adjust and determination of "a priori" constraints to reduce the high correlations existing between some of the parameters, in particular the resonant coefficients.

Chapter 10

Short arcs

10.1 Introduction

ERS-1 long arc orbits computed with the present models (Chapter 9) have an accuracy which are about one order of magnitude below the accuracy required for most applications. In particular, the full exploitation of satellite altimetry for oceanographic or geodetic purposes, requires a knowledge of the satellite radial position to within the accuracy of the altimeter measurement: from 5 to 10 cm.

At present this accuracy can only be achieved for short arcs that are intensively tracked by a number of stations.

The most widely used short arc technique is probably the TAR method referred to in section 4.2 (Sinclair, 1985, 1989), whereby corrections along the T, A and R directions are applied to a previously computed long arc solution. This method is very useful for very short arcs of up to 10 minutes (1/10 of a revolution). Its main disadvantage is that it is non-dynamic, i.e., the corrected track is no longer an exact solution of the equations for the satellite motion. The accuracy of this method depends on the accuracy of the initial long arc solution. To obtain a radial accuracy of the order of 10 cm, the initial long arc solution should exhibit range rms residuals of about 0.6 m.

The restrictive application of this method to only very short arcs was the motivation for research on alternative methods, valid for a substantially longer arc. The basic idea behind this is the following. Consider an arc of up to about one revolution that is tracked on both ends of the arc. By fitting an orbit to these observations, in principle the solution will be well determined at both ends, in the tracked areas, but large errors may exist in the middle of the arc, where no tracking data are available. Thinking in terms of the "equilibrium" of the solution we may imagine it as a line that is suspended at both ends but sagging in the middle. To reduce this catenary effect the line could be stretched by reducing its length. The equivalent to stretching the line in a computed solution is reducing the number of degrees of freedom of the solution. In other words, if an orbit is well defined at the ends of the arc, it should be possible to constrain the solution so that the errors in the middle of the arc are reduced.

This idea evolved into the development for this project of two dynamic methods for short arc computation, which will be called "Constrained" and "Bayesian" methods.

This chapter describes the research done on the development of these short arc techniques. In addition to the two methods mentioned above, the TAR method is also analysed with regard to its application to longer arcs.

The most important factors in short arc solutions are the geometrical configuration of the tracking data along the arc and the accuracy of the station coordinates. Provided the length of the arc is short enough, the accuracy of the force model is of slight importance. To be able to study the effect of station configuration, a data set of PRARE range data was generated for SEASAT, for the first three revolutions of day September 18, 1978 (MJD = 43769). This data set comprises 27 passes for 14 stations, a total of 1931 measurements with an interval between observations of 5 seconds. The procedure used in this simulation was described in section 6.3.

The fact that SEASAT is used instead of ERS-1, does not invalidate the application of the results obtained for the former to the latter. This is because the force model does not significantly affect the accuracy of these solutions. Since both data types are similar, the results obtained with PRARE range data are applicable to laser data, with the advantage that most of the present lasers have an accuracy even better than the assumed PRARE accuracy (7 cm).

The reference orbit used to simulate these data was described in section 8.3. This orbit was generated with the best available model for SEASAT and GEMT2 (orbit L1 in Chapter 8). This solution will be referred to throughout this chapter as the reference orbit (REF). For the analysis of these data the force model was changed by using GEMT1 instead of GEMT2. The computation model used in all the short arc solutions is the same used in all SEASAT long arc solutions (Table 8.1), except for the number of solve for parameters. The integration step length used is 0.5 minutes.

Since all computations use simulated data, the accuracy of these solutions is assessed by computing their difference to the reference orbit (REF) used to generate the observations. This orbit represents the "true path" of the satellite relative to which all observations "fit exactly", in the sense that the rms of fit of the reference orbit to the tracking data is equal to the accuracy of the data themselves (7 cm).

10.2 Constrained method

In this method it is assumed that some good quality passes of range data are available at least from two stations one at the beginning and one at the end of the arc.

As in long arc computations, an orbit is generated by numerical integration and fitted to the observations. The main difference relative to a long-arc solution is that only the 6 parameters of the start vector are solved for.

Instead of the classical formulation in terms of position and velocity ($X, Y, Z, \dot{X}, \dot{Y}, \dot{Z}$), the start vector is expressed in terms of the 6 osculating elements ($a, e, i, M, \omega, \Omega$) where

- a - semi-major axis
- e - eccentricity
- i - inclination
- M - mean anomaly
- ω - argument of perigee
- Ω - right ascension of the ascending node

For near circular orbits, such as ERS-1's, a change in the value of the argument of the perigee ω is almost equivalent to a change in the mean anomaly **M**. Using this formulation the parameters **M** and ω are highly correlated, when solved together their correlation being very nearly 1. Therefore an alternative equivalent formulation is adopted whereby, instead of ($\mathbf{M}, \omega$), the pair ($\mathbf{M}+ \omega , \omega$) is solved for.

The set of 6 solved-for parameters becomes:

$$(a, e, i, M+ \omega, \omega, \Omega)$$

Solving for these elements is perfectly equivalent to solving for the classical 6 osculating elements, with the advantage that smaller correlations exist between the parameters.

It is well known that the existing error in a computed ephemeris has a variety of periods, but when expressed in the TAR variations they are close to the orbital period. Therefore the dominant shape of the error is a one cycle per revolution signal.

Depending on the distribution of the tracking data along the arc, the orbit will be more or less well determined along each of the T, A and R directions. If the short arc is tracked by only one or two stations, by solving for all 6 osculating elements mentioned above, usually leads to high correlations between some of the parameters. These solutions can be very ill-conditioned, i.e., the errors may have very large variations, within a short interval. This problem can be resolved, by either reducing the number of parameters solved for, or by constraining the solution in some way.

The reduction of the number of parameters is difficult, since each parameter influences the orbit in a different way. The method considered here overcomes this problem by applying constraints to the solved-for parameters.

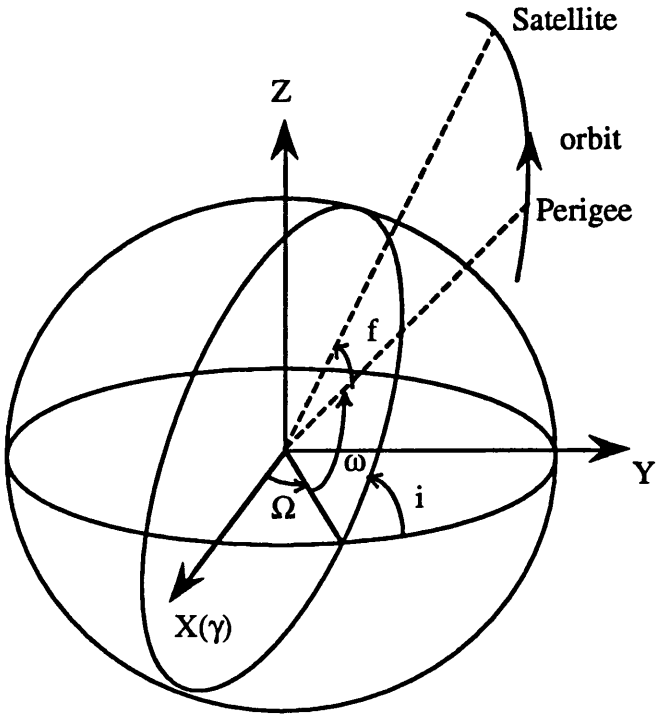

Figure 10.1 - Satellite osculating orbital elements

For very short arcs it would usually be sufficient to solve for only one parameter along each of the three T, A and R directions. However, the equations of motion are expressed in terms of position and velocity and it is not straightforward to write simple transformations to express them in terms of T, A, R elements. Instead, it is preferable to use the formulation in terms of the 6 osculating elements and apply certain constraints to these elements, these constraints being related to the TAR variations of the osculating elements.

By simple geometrical considerations, for near circular orbits, the 6 osculating elements can be grouped into three categories, according to which of the TAR components the element is more related to:

1 - (M, ω) - The argument of perigee locates the orbit relative to the ascending node and the mean anomaly M locates the position within the orbit relative to the perigee (Figure 10.1). Therefore the sum of these two parameters locate the position of the

satellite relative to the ascending node. For orbits of low eccentricities, a small change in either M or ω hardly affects the satellite radial position. Therefore a change in either of these parameters is equivalent to a linear change in the along-track (T) component. Furthermore, the effect is very nearly the same if it is due to a change in M or a change in ω.

If the solution is ill-conditioned in the T direction, applying a simple constraint of the form $dM+d\omega = 0$ it is equivalent to solving for only one along-track parameter, keeping the position of the ascending node unchanged.

2 - (i, Ω) - These parameters orient the orbit plane relative to the inertial space. A small change in any of these parameters forces a small rotation of the orbit plane as a whole and therefore affects mainly the across-track position (A). Nevertheless, the effects are not equivalent. In fact a change in Ω produces a displacement of the across-track component (dA_Ω), which is maximum at the ascending and descending nodes and is zero at the middle points half way between the nodes (Figure 10.2). If the orbit is near polar, a change in the inclination **i** produces similar changes (dAi), but with a phase difference of half of revolution, i.e., they are zero at the nodes and maximum at the halfway points.

In very simple terms if **t** is the time elapsed since the ascending node crossing then the across track displacements dA_i and dA_Ω caused by variations di and $d\Omega$ can be written as:

$$dAi = di \,.\, K.\, \sin\left[\frac{2\pi\, t}{T}\right] \tag{10.1}$$

$$dA_\Omega = -\, d\Omega \,.\, K.\, \cos\left[\frac{2\pi\, t}{T}\right] \tag{10.2}$$

where T is the satellite period (100 minutes) and K is a units conversion constant.

By applying the constraint $di + d\Omega = 0$ the total across-track displacement becomes:

$$dA = dAi + dA_\Omega = di \;.\; K.\left[\sin\left[\frac{2\pi\, t}{T}\right] + \cos\left[\frac{2\pi\, t}{T}\right]\right] \tag{10.3}$$

The geometrical interpretation of these formulae is presented in Figure 10.2. It can be seen that this constraint forces the total across-track variation to be sinusoidal with an amplitude equal to 1.5 times the amplitude of each individual variation. This method is therefore equivalent to solving for only one across-track parameter.

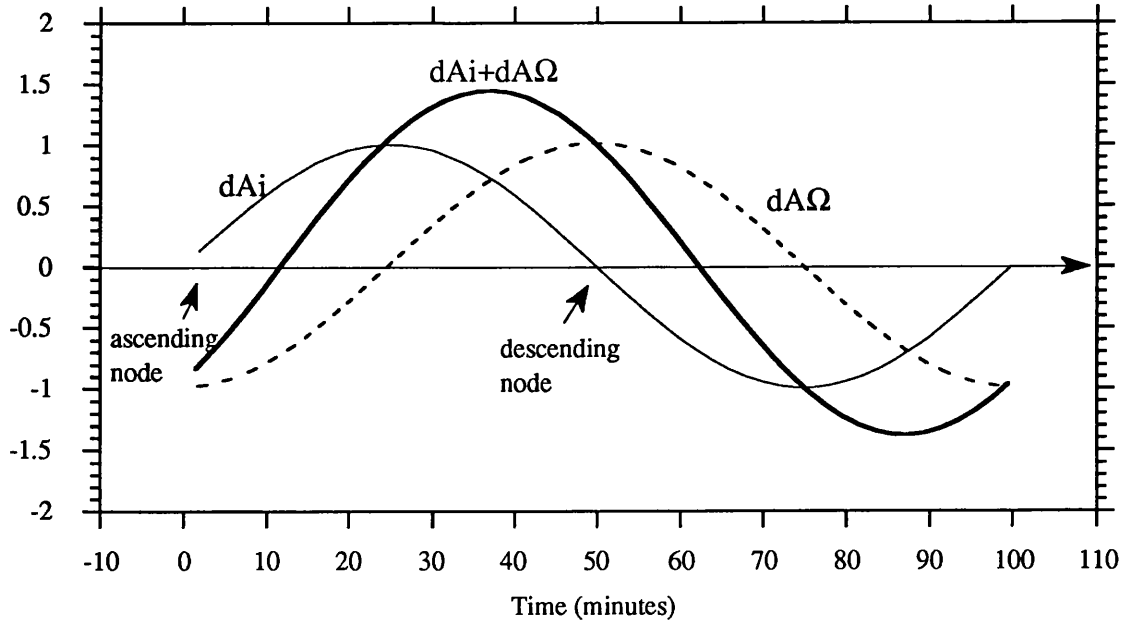

Figure 10.2 - Approximate form of the across-track error when the constraint ($di + d\Omega = 0$) is applied.

3 - (a, e) - These parameters define the size and shape of the orbital ellipse. A change in any of these parameters induces changes only in the radial component (R). Since the orbit is nearly circular, a variation in **a** produces a change in the satellite radial position which is approximately constant for all points. On the contrary, a change in the eccentricity causes a variation in R which is maximum at perigee and apogee, and zero at the halfway points.

These variations can be derived using only the in-plane equations of motion, by considering only the Keplerian movement. For the Keplerian movement, the geocentric radial distance of the satellite is :

$$r = a (1 - e \cos E) \qquad (10.4)$$

where E is the eccentric anomaly.

A variation **da** in **a** causes a variation $\mathbf{dR_a}$ in **R**, given by:

$$dR_a = da (1 - e \cos E) \qquad (10.5)$$

Since **e** is very small ($\cong 10^{-3}$) this variation is approximately constant at all points.

A variation **de** in **e** causes a variation $\mathbf{dR_e}$ in **R**, given by:

$$dR_e = - a\, de \cos E \qquad (10.6)$$

This variation is maximum at apogee (= a de) and at perigee (= -ade) and zero at the halfway points where E=± 90°.

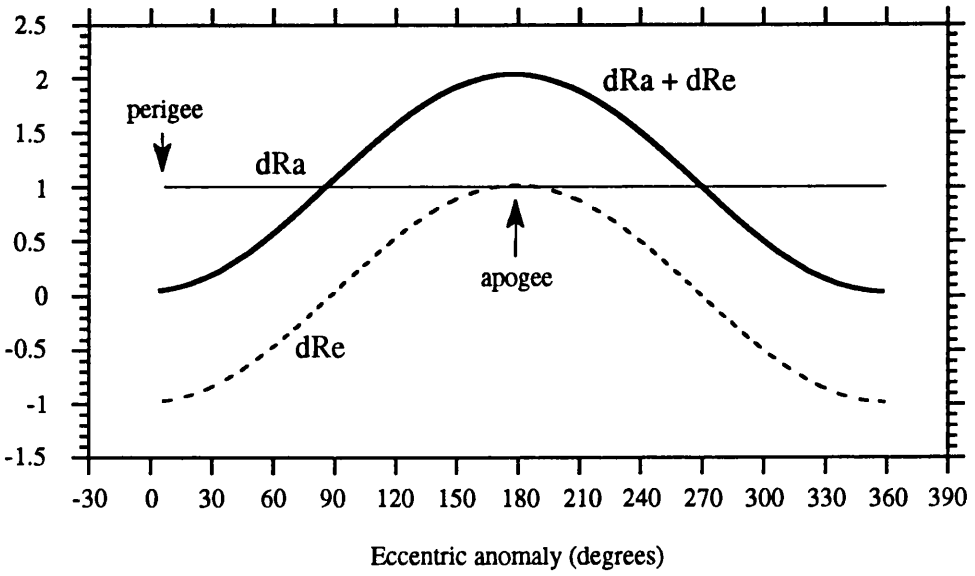

Figure 10.3 - Approximate form of the radial error when the constraint (da - a de = 0) is applied.

By applying a constraint of the form da - a de = 0 (da = a de) then the total radial displacement is a sinusoidal function as plotted in Figure 10.3, being minimum (zero) at perigee and maximum (2 da) at apogee. This is therefore equivalent to solving for only one radial parameter, keeping the perigee unchanged.

By using this method a number of 8 tracking configurations were studied. These configurations, named from **1** to **8** are described in Table 10.1 and Figures 10.4 to 10.11. In these figures each line represents one pass. For each pass the Y axis represents the minimum angular distance between the satellite and the tracking station. If the station is on the left or on the right of the satellite track, the angular distance is considered respectively positive or negative.

For each configuration one solution is first computed by solving for all 6 osculating elements (a, e, i, M+ ω, ω, Ω). These first solutions are named S1, S2, ... S8,, meaning Short-arc solution for arc/configuration 1, 2, ... 8.

For each solution, the rms/max residuals of fit and the parameters exhibiting the highest correlations are present in Table 10.2. By analysis of the geometry of the tracking configuration and depending on the parameters which exhibit higher correlations, the decision is taken on which constraints should be applied for each solution. For each configuration Table 10.2 presents the results for the best solution and the constraints that have been applied. These constrained solutions are called SC1, SC2, ... SC8, meaning Constrained Solution for configuration 1, 2, ... 8.

The first four arcs have very similar configurations. For all of them there are 4 stations, two at each end of the arc, one on each side of the track (Figures 10.4 to 10.7). The main difference between them is the arc length.

The first arc has a length of only 32 minutes, about 1/3 of a revolution. For such a short arc, the solution obtained by solving for all 6 osculating elements (S1), although high correlations exist between several parameters, has a very small difference relative to the reference orbit. This means that, for such a short interval, this type of configuration determines a solution with the same accuracy of the observations (Figure 10.12). The application of some constraints to the parameters does not significantly affect the solution, although the individual parameters may be better determined. Solution SC1 computed by applying the constraint ($dM + d\omega = 0$) is equivalent to the previous solution (Figure 10.13)

Arc 2 has a similar configuration but a length of 66 minutes (2/3 of a revolution). By solving for the 6 elements (solution S2), the highest correlations exist between the pair (i, Ω). By applying the constraint $di + d\Omega = 0$, the orbit substantially improves in the across-track direction as is evident from Figures 10.14 and 10.15. The rms error of the constrained solution is about 10 cm in all components.

As the length of the arc increases, the errors become larger, in particular in the T direction, being minimum at the extremes of the arc, close to the tracked areas, and maximum in the middle.

The solution computed for arc 3, by solving for the 6 parameters (S3) has very large errors of more than one metre in the middle of the arc (Figure 10.16). The simple application of the constraint ($dM + d\omega = 0$), forces these errors to decrease to a level of 20 cm rms (solution SC3 in Figure 10.17).

The first solution (S4) computed for arc 4 (with a length of 130 minutes), has similar type of errors (Figure 10.18). However the application of the same constraint ($dM + d\omega = 0$) does not reduce the error by any appreciable amount (Figure 10.19). It seems that the same techniques applied to arcs with lengths up to one revolution do not have the same applicability to longer arcs. In this case, the applied constraints, although not

degrading the solution, cannot improve it either. These solutions can only be improved if some tracking data exist in the middle of the arc, as in configuration 8 (Figure 10.11). In fact this last arc is similar to arc 4, with the addition of an extra pass in the middle of the arc. In this case a better solution is obtained by comparison to the S4 solution. Again, the application of the constraint (di + $d\Omega$ = 0) to the highest correlated parameters, reduces the across-track error from 37 to 11 cm (Figures 10.26 and 10.27).

The next two arcs (5 and 6) have the same type of configuration, with two stations, one at each end of the arc, on opposite sides of the track (Figures 10.8 and 10.9).

The first has a length of 32 minutes. A solution computed with only these two passes, by solving for all 6 osculating elements (S5) is very ill-conditioned with several parameters exhibiting correlation close to 1. The difference of this solution relative to the reference orbit amounts to several metres. In particular, the across-track and radial components are very poorly determined with errors up to 10 metres. (Figure 10.20).

Table 10.1 Tracking configurations considered in short arcs

Configuration	Spatial distribution	Arc Length (minutes)
1	4 stations, 2 at each end of the arc, one on each side of the track	32
2	"	66
3	"	100
4	"	130
5	2 stations one at each end of the arc, on opposite sides of the track	32
6	"	100
7	2 stations one at each end of the arc, on the same side of the track	100
8	5 stations, 2 at beginning 2 at the end and one in the middle of the arc.	130

Table 10.2 - Short arc constrained solutions

Orbit	Constraints applied to parameters	Residuals rms	Residuals max	Maximum correlations
S1	—	0.07	0.23	(a , e) = 0.99 (a , M+ω) = 0.96
SC1	dM+ dω = 0	0.07	0.23	—
S2	—	0.07	0.22	(i , N) = 0.96
SC2	di+ dΩ = 0	0.08	0.21	—
S3	—	0.08	0.21	(e , M+ω) = 0.81
SC3	dM+ dω = 0	0.14	0.34	—
S4	—	0.07	0.24	(M+ ω, ω) = 0.89
SC4	dM+ dω = 0	0.13	0.36	—
S5	—	0.06	0.12	(M+ ω, N) = 1 (a , e) = 1 (i , ω) = 1
SC5	dM+ dω = 0 di+ dΩ = 0 -da + ade = 0	0.09	0.30	—
S6	—	0.07	0.20	(a , i) = 1 (e, i) = 0.99
SC6	dM+ dω = 0 -da + ade = 0	0.07	0.22	—
S7	—	0.07	0.23	(e , i) = 1 (a, e) = 1 (i , M+ω) = 0.99
SC7	dM+ dω = 0 di+ dΩ = 0 -da + ade = 0	0.11	0.31	—
S8	—	0.13	0.35	(i , N) = 0.75
SC8	di+ dΩ = 0	0.14	0.38	—

Table 10.3

TAR differences between the reference orbit and short arc constrained solutions

Orbits	Total (m)		T (m)		A (m)		R (m)	
	rms	max	rms	max	rms	max	rms	max
REF - S1	0.10	0.14	0.04	0.08	0.05	0.12	0.07	0.11
REF - SC1	0.09	0.13	0.04	0.07	0.05	0.12	0.07	0.11
REF - S2	0.22	0.37	0.09	0.17	0.16	0.28	0.12	0.25
REF - SC2	0.17	0.26	0.10	0.20	0.08	0.12	0.12	0.26
REF - S3	1.01	1.69	0.94	1.69	0.08	0.19	0.35	0.64
REF - SC3	0.30	0.46	0.20	0.38	0.10	0.17	0.19	0.36
REF - S4	0.69	1.14	0.56	1.13	0.31	0.49	0.25	0.48
REF - SC4	0.64	1.13	0.54	1.06	0.25	0.47	0.24	0.57
REF - S5	8.97	15.36	1.27	1.93	6.95	12.31	5.53	9.02
REF - SC5	0.40	0.45	0.27	0.37	0.21	0.36	0.21	0.29
REF - S6	2.25	3.14	1.87	3.11	0.91	1.31	0.88	1.82
REF - SC6	0.29	0.51	0.15	0.45	0.17	0.33	0.17	0.29
REF - S7	2.01	2.82	1.77	2.81	0.65	0.95	0.70	1.39
REF - SC7	0.49	0.82	0.40	0.82	0.15	0.30	0.23	0.48
REF - S8	0.48	0.72	0.24	0.43	0.37	0.60	0.20	0.47
REF - SC8	0.32	0.60	0.30	0.57	0.11	0.27	0.19	0.41

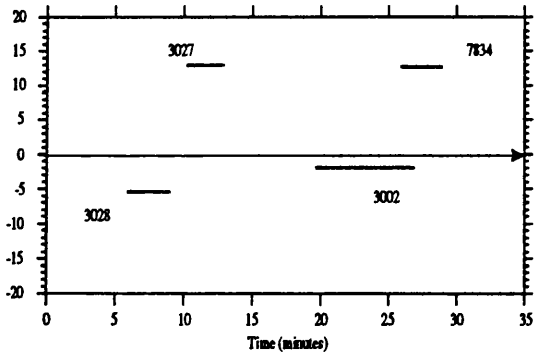

Figure 10.4 - Configuration 1. In all figures from 10.4 to 10.11 the Y axis repreaents the angular distance (in degrees) between satellite and station (see also figure 8.3)

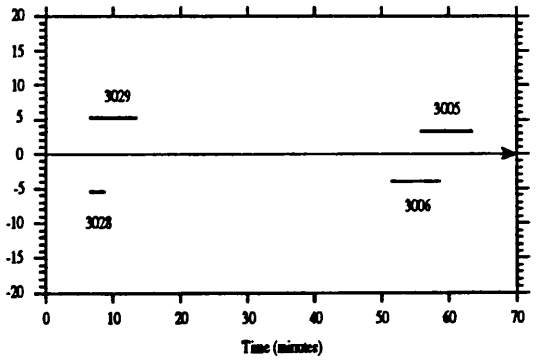

Figure 10.5 - Configuration 2

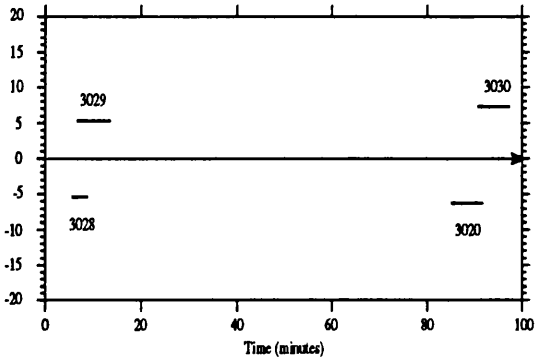

Figure 10.6 - Configuration 3

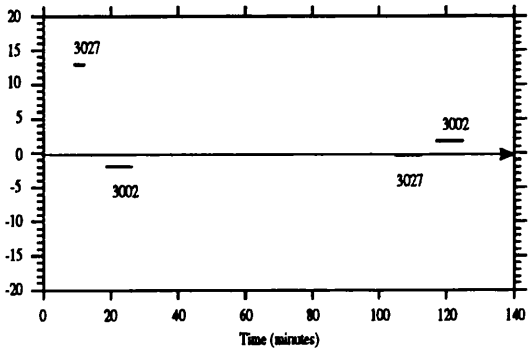

Figure 10.7 - Configuration 4

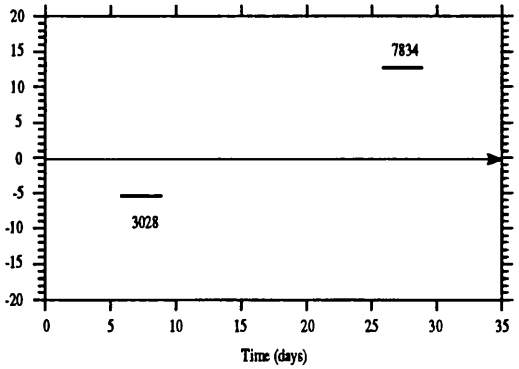

Figure 10.8 - Configuration 5

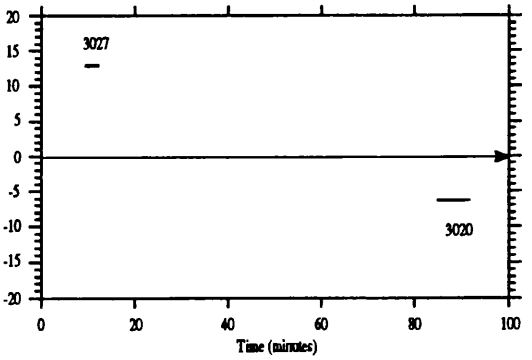

Figure 10.9 - Configuration 6

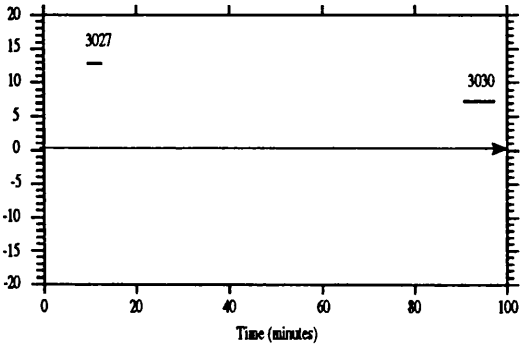

Figure 10.10 - Configuration 7

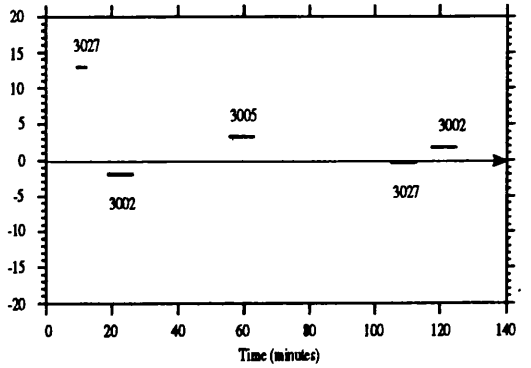

Figure 10.11 - Configuration 8

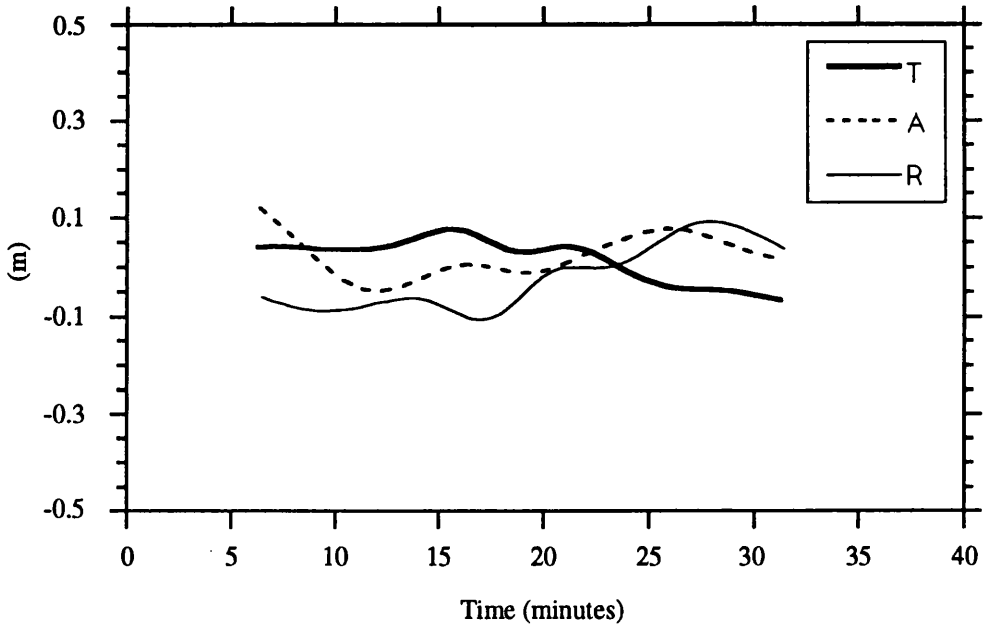

Figure 10.12 - T, A, R differences between reference and orbit S1

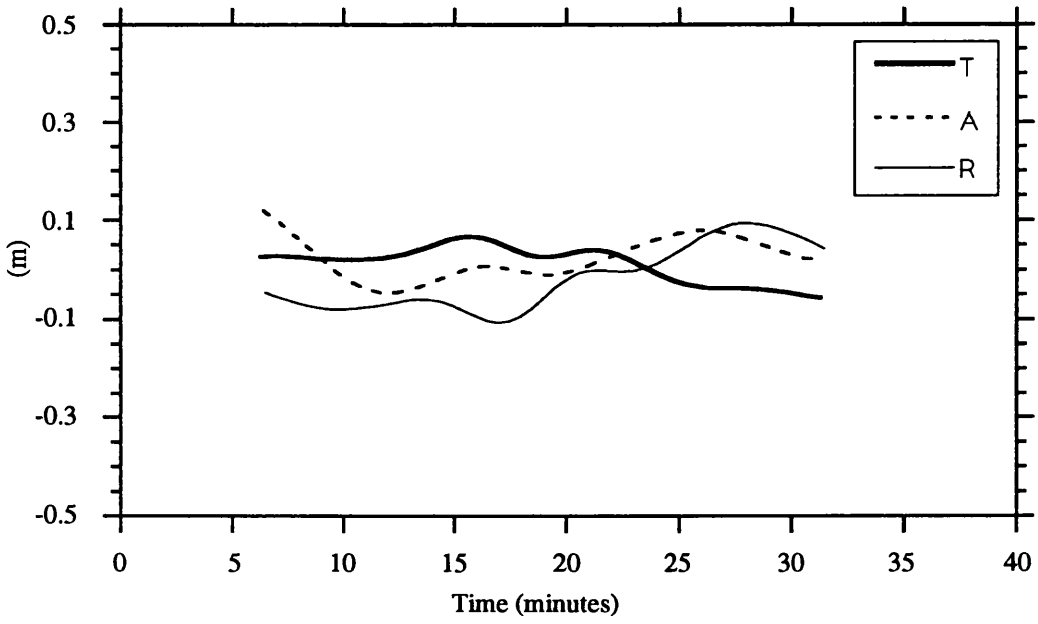

Figure 10.13 - T, A, R differences between reference and orbit SC1

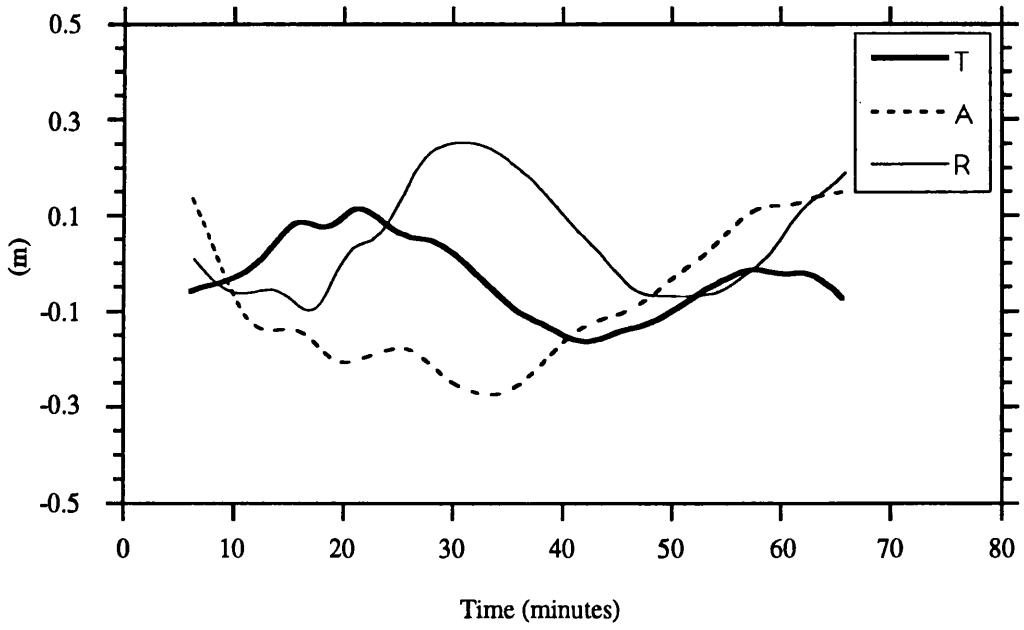

Figure 10.14 - T, A, R differences between reference and orbit S2

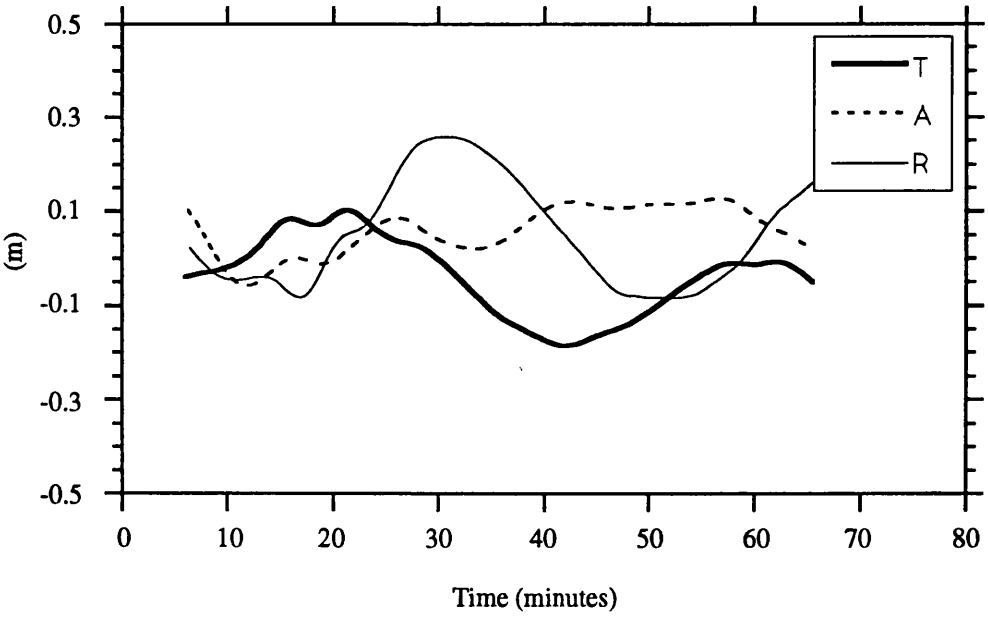

Figure 10.15 - T, A, R differences between reference and orbit SC2

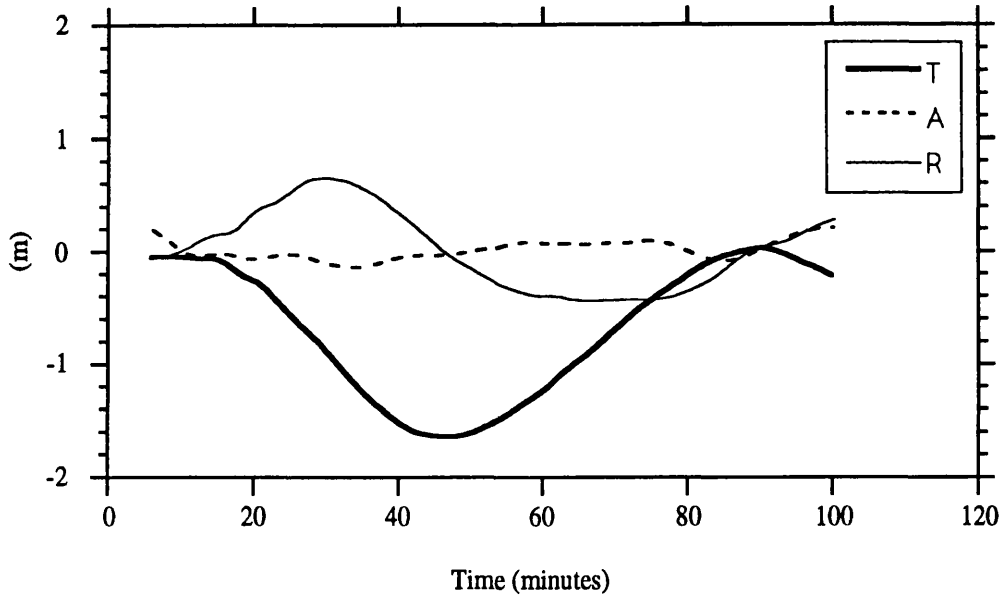

Figure 10.16 - T, A, R differences between reference and orbit S3

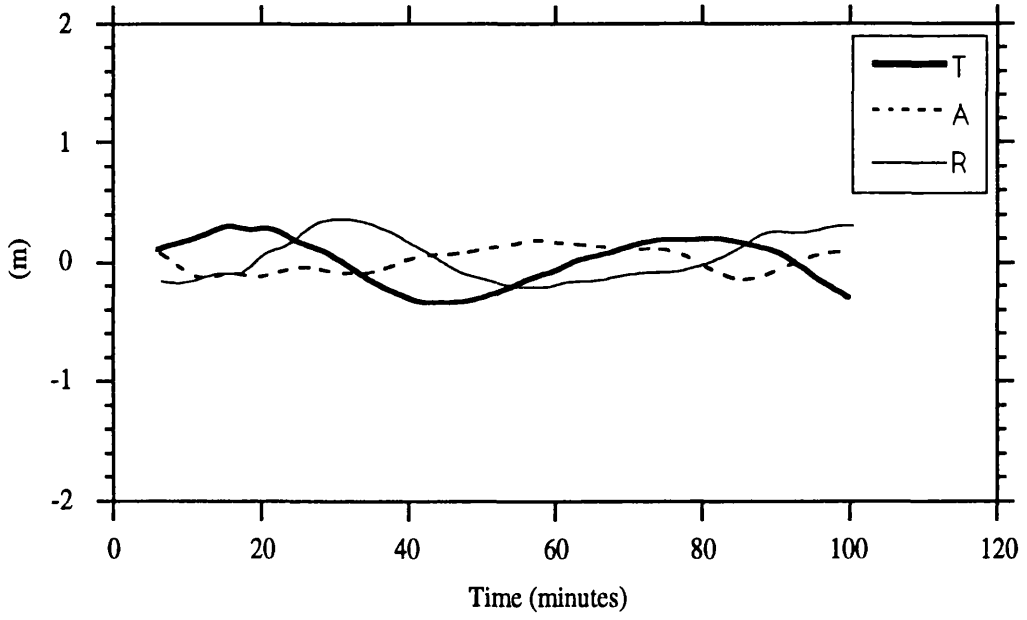

Figure 10.17- T, A, R differences between reference and orbit SC3

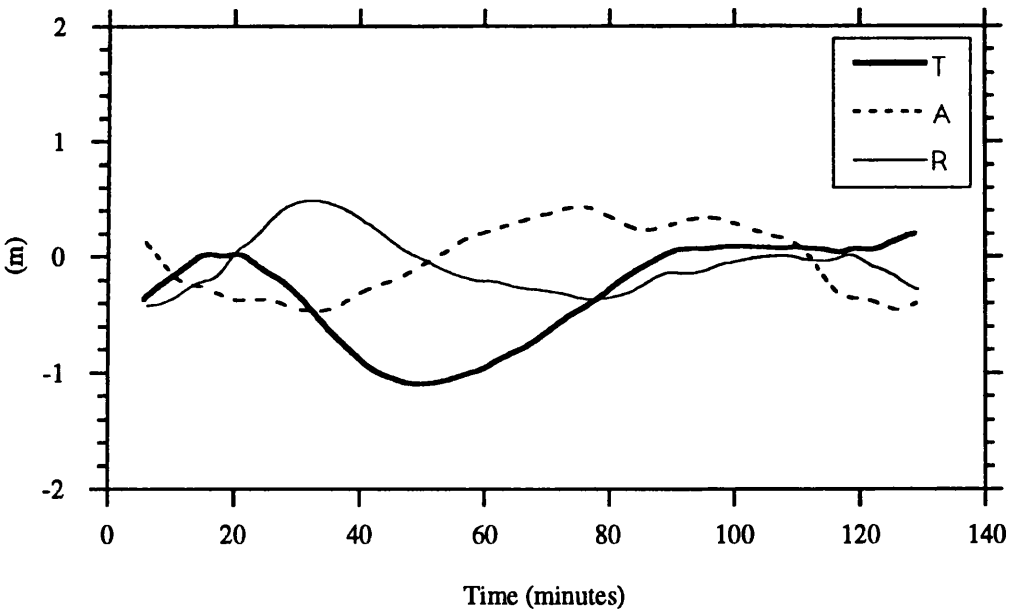

Figure 10.18 - T, A, R differences between reference and orbit S4

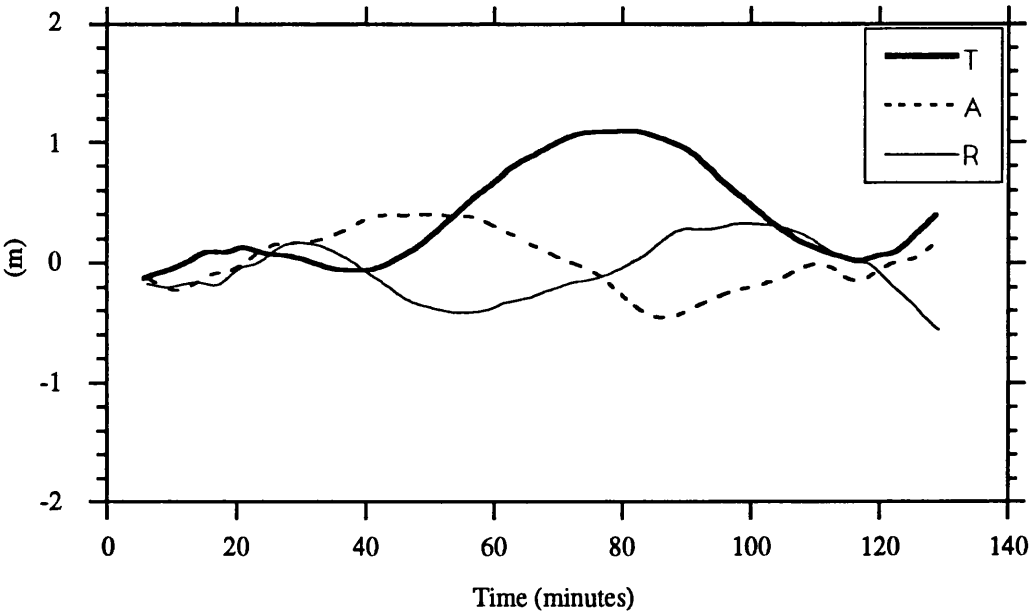

Figure 10.19 - T, A, R differences between reference and orbit SC4

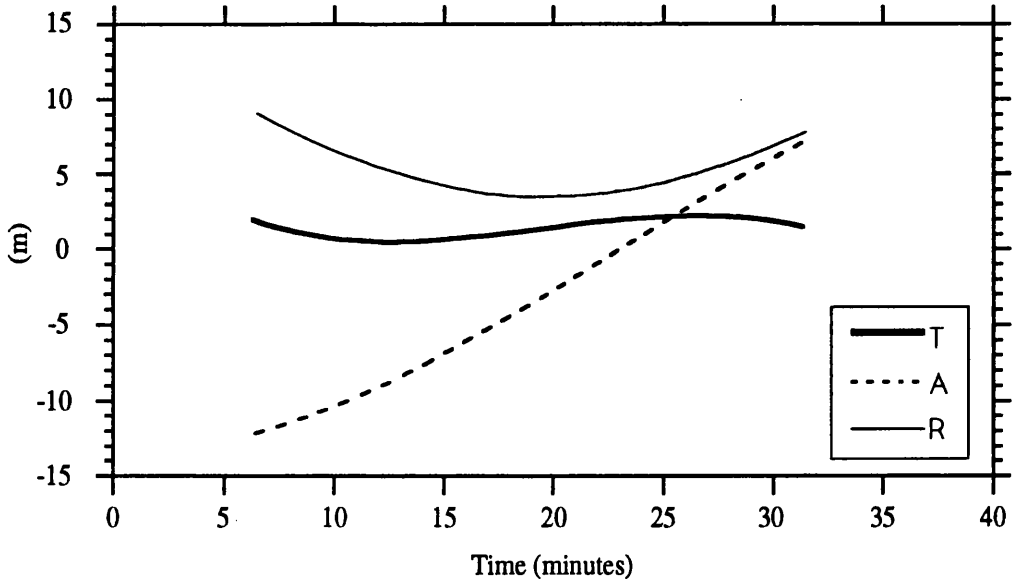

Figure 10. 20- T, A, R differences between reference and orbit S5

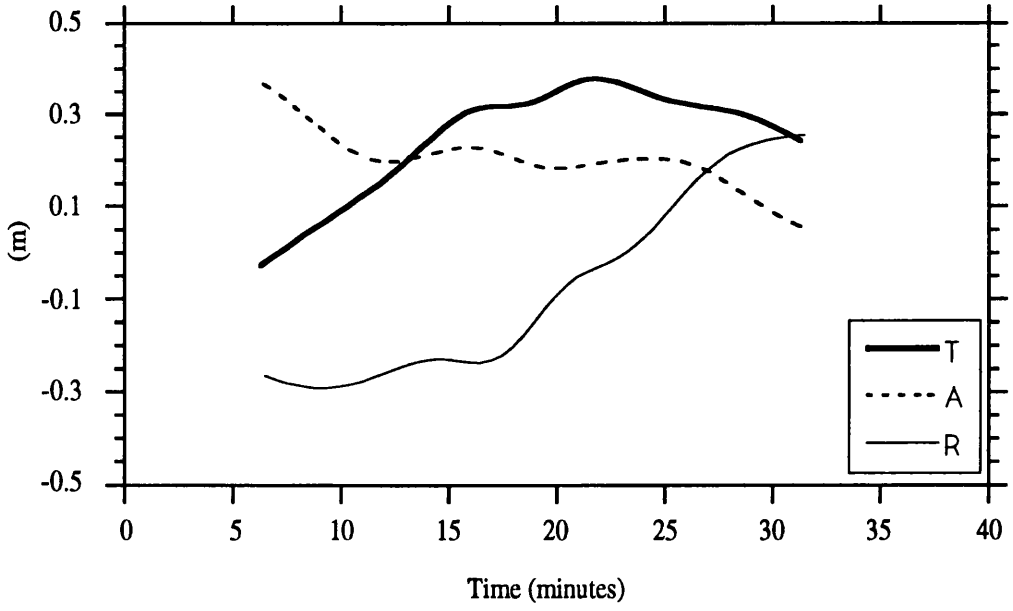

Figure 10.21 - T, A, R differences between reference and orbit SC5

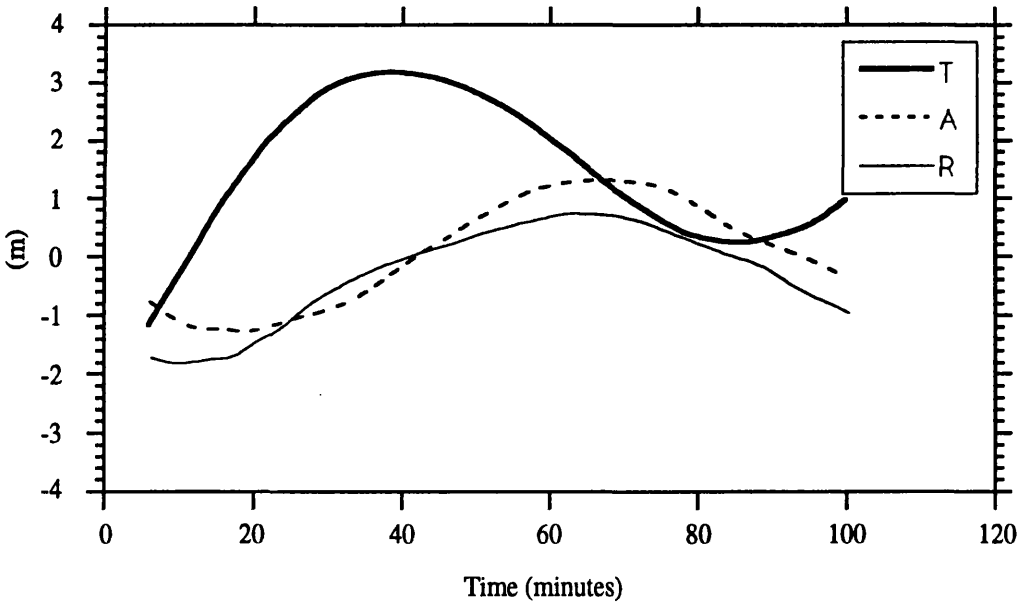

Figure 10.22 - T, A, R differences between reference and orbit S6

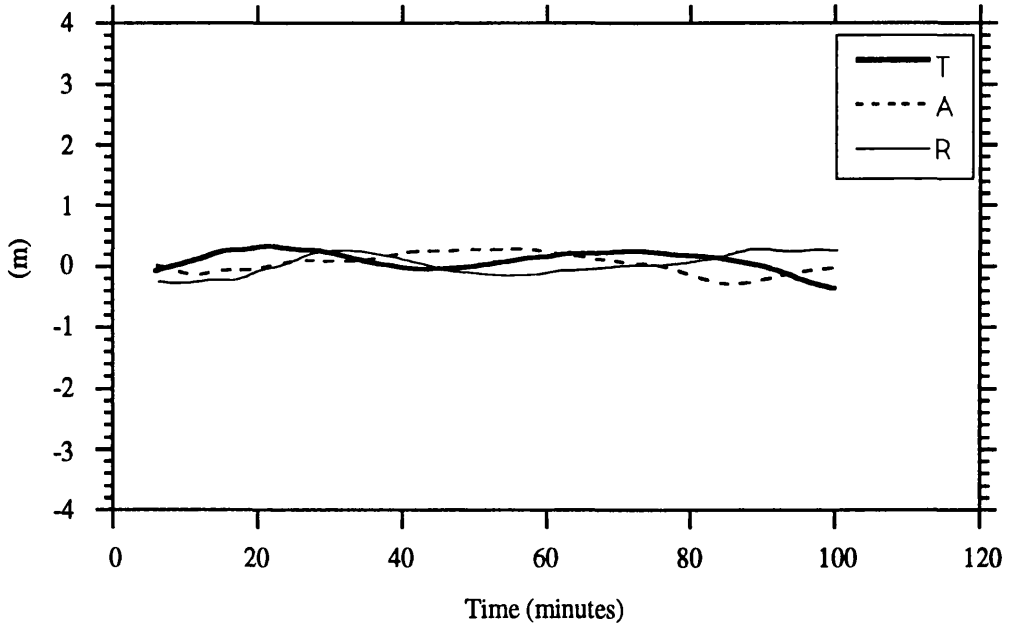

Figure 10.23 - T, A, R differences between reference and orbit SC6

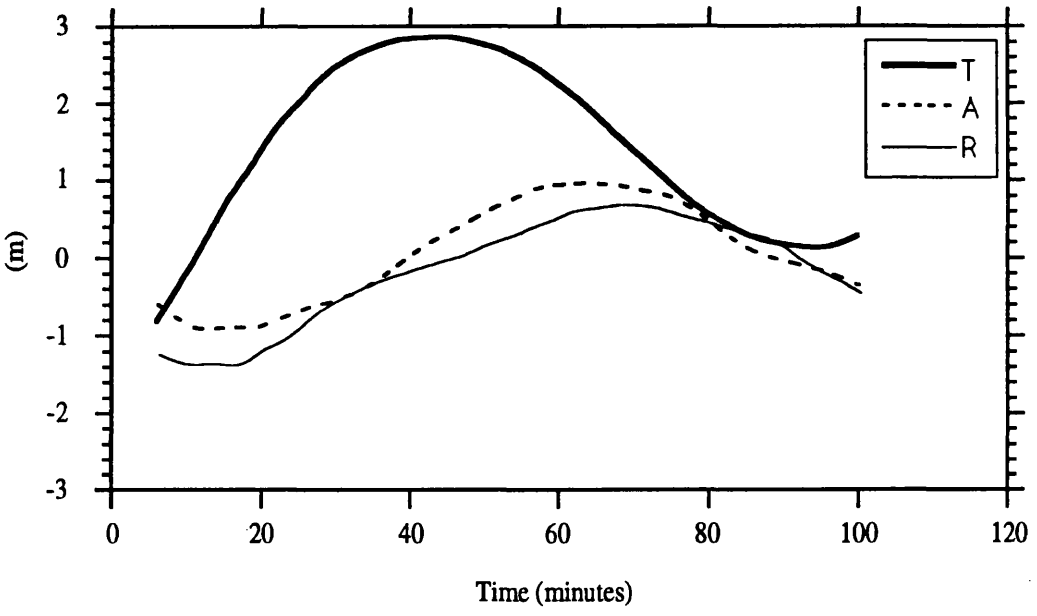

Figure 10. 24- T, A, R differences between reference and orbit S7

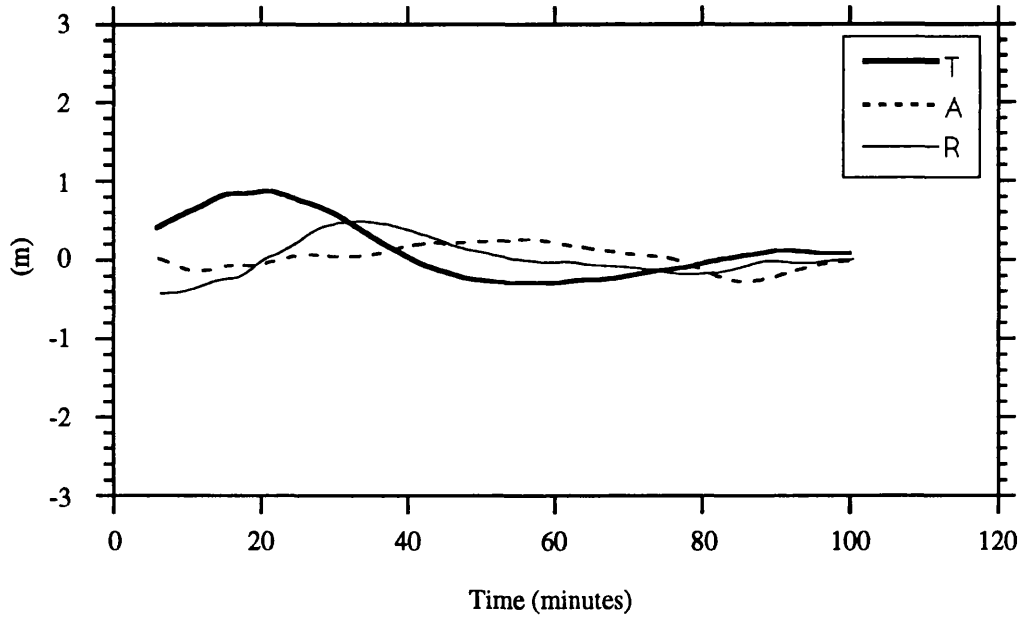

Figure 10.25 - T, A, R differences between reference and orbit SC7

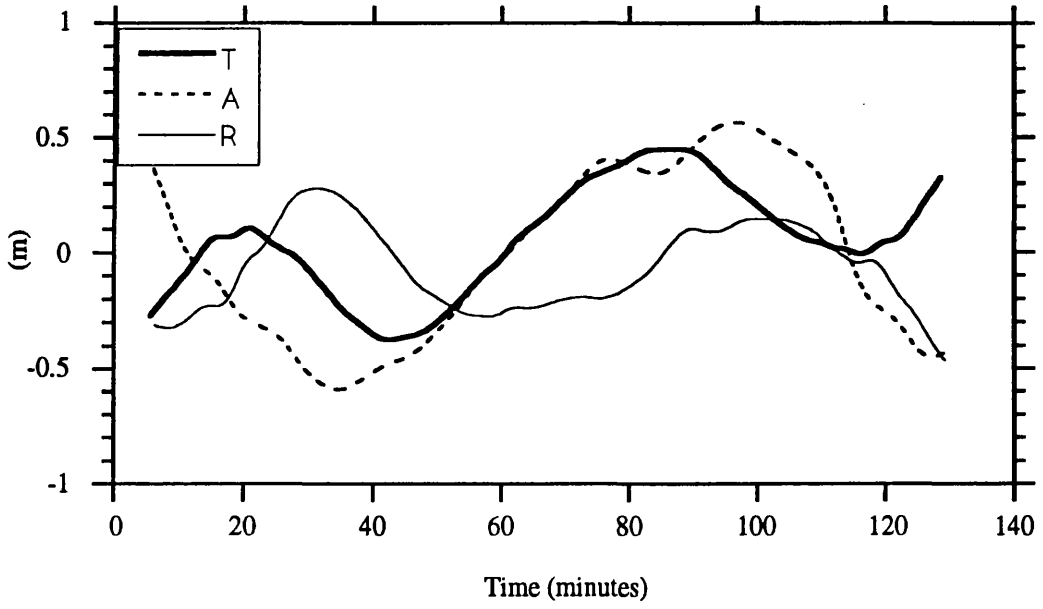

Figure 10.26 - T, A, R differences between reference and orbit S8

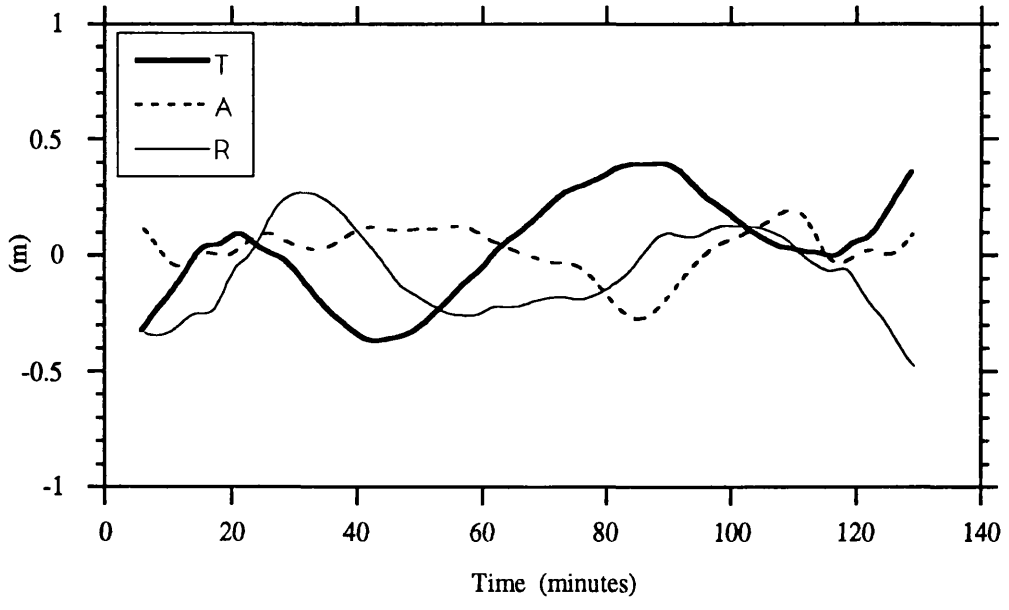

Figure 10.27 - T, A, R differences between reference and orbit SC8

With such a poor configuration a solution is only possible if strong constraints are applied to the parameters. In solution SC5, 3 constraints have been applied, one along each of the three TAR directions. In this way, the errors are reduced from a level of several metres to about 20 to 25 cm rms in all components (Figure 10.21).

Arc 6 is similar to arc 5 but three times longer (100 minutes). Although the errors for solution S6 are not as large as those for S5, they still amount to several metres in the middle of the arc. (Figure 10.22). Again, by applying constraints, this time in the T and R directions, these errors are reduced to a level of 15 cm in all components (solution SC6 in Figure 10.23).

Finally one last arc (arc 7) is considered, with a length of 100 minutes and only two passes, both on the same side of the track. This time high correlations exist between several parameters. The shape of the errors for the solution computed by solving for all 6 osculating elements (S7) is very similar to those of solution S6. The application of constraints to this solution reduces the error by a factor of 4 (Figures 10.24 and 10.25).

In conclusion, the application of simple constraints to the solved for osculating elements allows the computation of very precise short-arc orbits. The accuracy of these solutions depends on the tracking configuration and the length of the arc. Generally, the shorter the arc, the higher the accuracy. For arcs of about 33 minutes these solutions have the same accuracy of the tracking data ($\cong$ 10 cm). Between this length and one revolution, the accuracy may be slightly poorer, depending on the tracking configuration.

The choice of constraints to be applied to each individual solution is made by taking into account the correlations existing between the various parameters.

This is therefore a very useful technique, with application to much longer arcs than the TAR method. Its application to arcs longer than one revolution is less reliable, since as the arc length increases, the error in the force model starts to influence the solution.

10.3 Bayesian method

In most of the cases, before computing a short arc solution, a long arc has already been computed, which includes the short arc. Therefore if the initial set of parameters comes from another solution, then the associated covariance matrix can be used as "a priori" information to constrain the new (short arc) solution.

This procedure was explained in section 3.4.3. The usual least squares algorithm determines the solution for which

$$v^T W v = \text{minimum} \qquad (10.7)$$

where v are the residuals and W the inverse of the observations' covariance matrix.

If X_0 is the set of initial parameters, X the corresponding corrected set after the adjustment, and W_X the inverse of the "a priori" covariance matrix associated with the parameters X_0, the Bayesian solution for X is the solution which minimises

$$v^T W v + (X_0 - X)^T W_X (X_0 - X) = \text{minimum} \qquad (10.8)$$

This solution can be interpreted as a combination of two separate solutions:

- A - the "a priori" solution which determined the set of parameters Xo and associated covariance matrix $B_X = W_X^{-1}$ (usually a long arc solution)

- B - the "single short-arc" solution that would be obtained if no "a priori" information is available

If N is the normal matrix of solution B then the normal matrix of the combined Bayesian solution is $N + W_X$. Therefore, if no relative weights are applied, the combined solution corresponds to an "average" of the two separate solutions.

This method is particularly useful when the normal matrix of the short arc solution, N, is ill-conditioned. In this case, the addition of W_X to the normal equations acts as a constraint to the solution.

In practice this constraint should be more or less strong depending on the quality of the single short arc solution. Therefore, a weighting factor K is introduced, to control the influence of W_X relative to N. Instead of W_X, the scaled matrix $K.W_X$ is then applied.

This method was applied to solutions S5 and S7 referred to in the previous section. The "a priori" solution was a 3-day arc solution computed with observations from two PRARE stations. The rms of this solution for the 3-day observations was 0.39 metres. The solved for parameters and associated covariance matrix were then used in each of the short-arc Bayesian solutions.

In all these Bayesian solutions the solved for parameters are the 6 osculating elements in the form (a, e, i, M+ ω, ω, Ω).

The results are presented in Tables 10.4 and 10.5. For comparison, Table 10.5 also presents, for each configuration, the differences of the two separate solutions ("a priori" and "single short-arc") relative to the reference orbit.

Table 10.4 - Short arc Bayesian solutions

Orbit	Scaling factor (K)	Residuals		Maximum correlations
		rms	max	
S5	—	0.06	0.12	(M+ ω, N) = 1 (a , e) = 1 (i , ω) = 1
SB5	0.01	0.06	0.17	—
S7	—	0.07	0.23	(e , i) = 1 (a, e) = 1 (i , M+ω) = 0.99
SB7	0.01	0.09	0.23	—

Table 10.5

TAR differences between the reference orbit and short arc Bayesian solutions

Orbits	Total (m)		T (m)		A (m)		R (m)	
	rms	max	rms	max	rms	max	rms	max
REF - "a priori" (ARC 5)	0.99	1.09	0.27	0.40	0.88	1.02	0.36	0.54
REF - S5	8.97	15.36	1.27	1.93	6.95	12.31	5.53	9.02
REF - SB5	0.23	0.29	0.15	0.19	0.15	0.26	0.07	0.14
REF - "a priori" (ARC 7)	1.16	1.55	0.89	1.28	0.70	1.01	0.27	0.54
REF - S7	2.01	2.82	1.77	2.81	0.65	0.95	0.70	1.39
REF - SB7	0.59	0.83	0.40	0.76	0.35	0.56	0.25	0.53

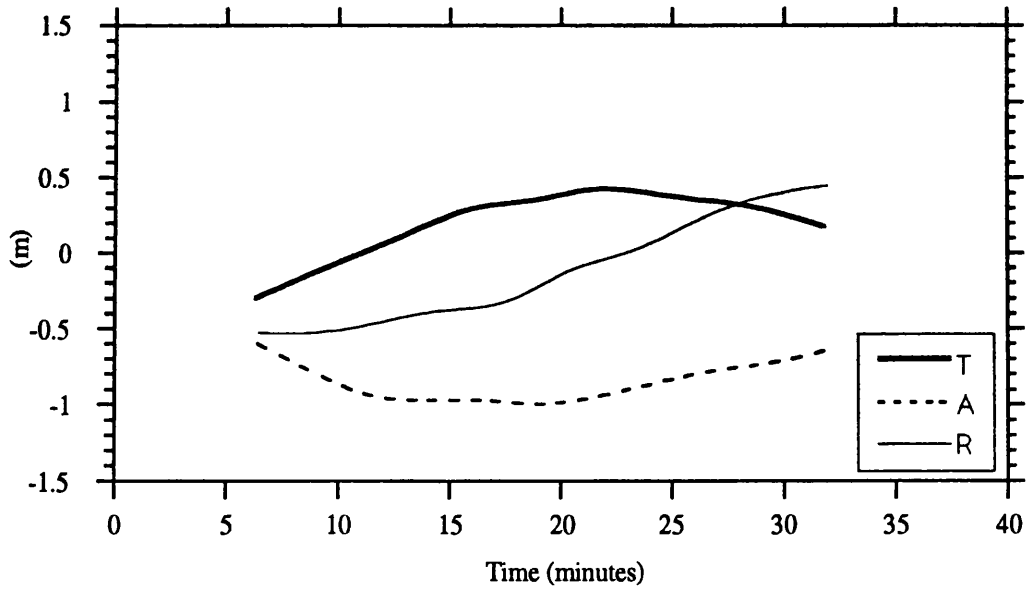

Figure 10.28 - TAR differences between the reference and the "a priori" orbit for ARC 5

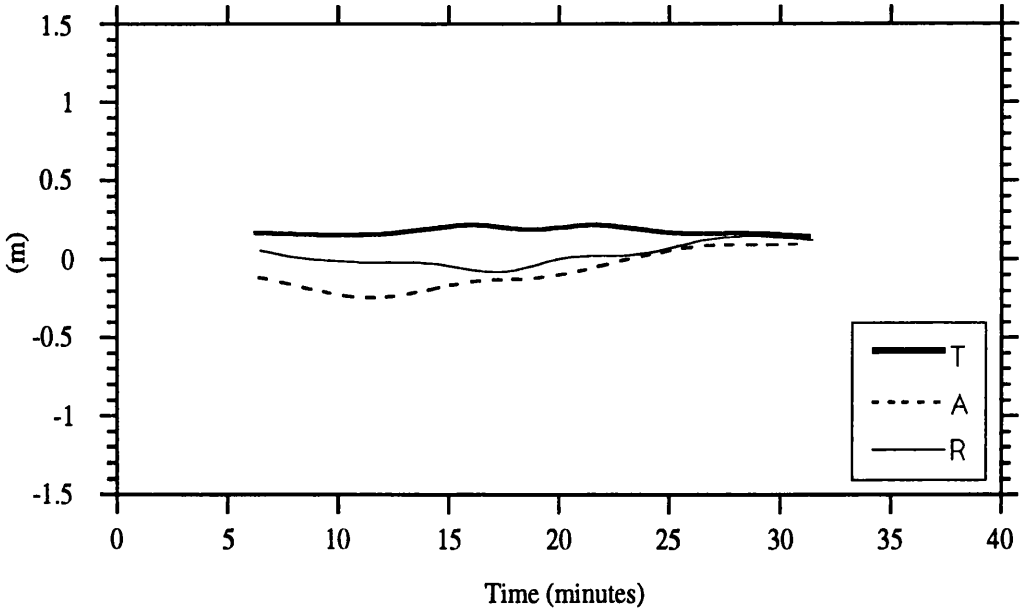

Figure 10.29 - TAR differences between the reference orbit and orbit SB5

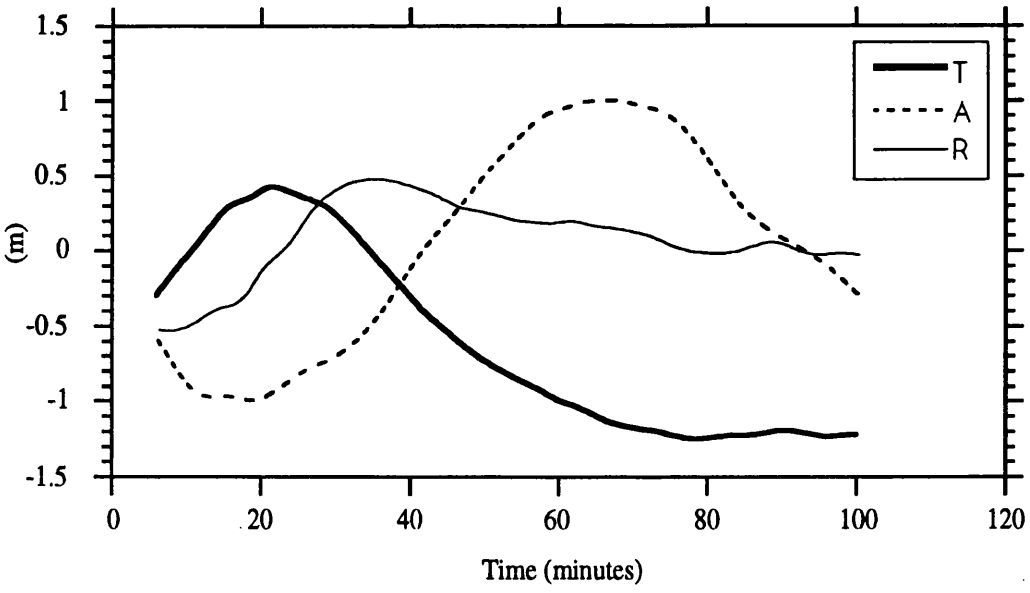

Figure 10.30 - TAR differences between the reference orbit and the "a priori" orbit for ARC 7

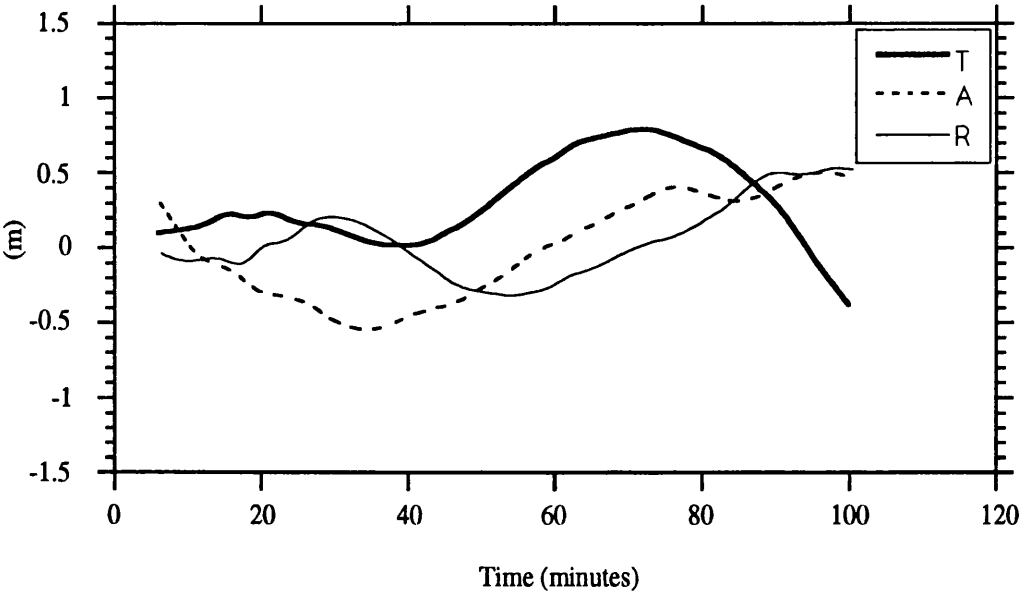

Figure 10.31 - TAR differences between the reference orbit and orbit SB7

For the arc 5 interval, the "a priori" solution has a global rms difference of about 1 metre (Figure 10.28). The dominant errors of this solution, during this interval, are in the across-track component. The error for the "single short-arc solution", S5, computed by solving for all 6 elements is very large, amounting to several metres (Figure 10.20). The Bayesian Solution SB5, resulting from the combination of these two, using a scaling factor K=0.001, has very small errors of 15 cm rms in the T and A components and 7 cm in R.

For arc 7 similar results are obtained. The errors of the Bayesian solution SB7 are considerably smaller that those for each of the individual solutions (compare Figures 10.24, 10.30, and 10.31).

By applying the same technique to other arcs, it is concluded that the accuracy of these combined solutions depends on the accuracy of each of the separate solutions. However, in all the tested arcs, the Bayesian solution was always better than any of the two solutions computed separately. In fact if the "a priori" solution is a long arc solution, it acts as a smoothing constraint to the unstable "single short-arc" solution, and therefore their combination leads to a better short arc orbit than any of the individual solutions.

10.4 TAR methods

As opposed to the two previously described "Constrained" and "Bayesian" methods, TAR techniques developed by Sinclair (1985, 1989) are non-dynamical methods, where "a posteriori" corrections are applied to a previously computed long arc orbit, along each of the three T, A and R directions. This technique proved to be very efficient for certain types of configurations, for short intervals up to 10 minutes.

The application of these techniques to longer arcs up to one revolution was investigated. These corrections are modelled by one of the following expressions:

1 - A simple polynomial function in time. For example the correction ΔT in the along-track component is given by:

$$\Delta T = T_0 + T_1 t + T_2 t^2 + T_3 t^3$$

where T_0, T_1 ,T_2 ,T_3 are solved for parameters and **t** is time difference relative to the middle of the arc.

2 - Periodic functions of the satellite orbital period, with constant amplitudes. The form of these functions for the T component is:

$$\Delta T = T_0 \cos\omega t + T_1 \sin\omega t + T_2 \cos 2\omega t + T_3 \sin 2\omega t$$

where ω is the orbital frequency (one cycle per revolution).

3 - Periodic functions of the satellite orbital period, with constant and time varying amplitudes. The form of these functions for the T component is:

$$\Delta T = T_0 \cos\omega t + T_1 \sin\omega t + T_2\, t \cos\omega t + T_3\, t \sin\omega t$$

Similar expressions hold for A and R.

The reason for using these formulations is due the spectrum exhibited by the orbital errors as described in section 4.6.

These techniques were applied to some of the configurations considered above. It was found that the first and third methods give in general better results than the second.

Table 10.6 - Short arc TAR solutions

Orbit	Method used	Solved for parameters	Residuals rms	Residuals max	Maximum correlations
T1A	Polynomial (1)	$T_0, A_0, R_0, T_1, A_1, R_1$	0.08	0.30	$(T_1, R_1) = 0.75$
T1B	Periodic with constant and time varying amplitudes (3)	$T_0, A_0, R_0, T_1, A_1, R_1$,	0.08	0.27	$(T_1, R_1) = 0.76$
T5A	Polynomial (1)	T_0, A_0, R_0	0.09	0.27	$(T_0, R_0) = 0.76$
T5B	Periodic with constant and time varying amplitudes (3)	T_0, A_0, R_0	0.09	0.27	$(A_0, R_0) = 0.77$

Some of the results obtained for arcs 1 and 5 are presented in Tables 10.6 and 10.7. Both arcs have a length of 35 minutes. The "a priori" long arc solution relative to which the corrections are solved for and applied to, is the same "a priori" solution used in the Bayesian method.

For the first configuration (arc 1), by solving for the first 6 parameters using either the method 1 or 3, solutions are obtained (T1A and T1B), which depart from the reference

orbit by only 10 to 15 cm (Table 10.7). To be able to assess the improvement achieved by these solutions with respect to the "a priori" solution, the difference between these and the reference orbit are also given in Table 10.7.

Table 10.7
Differences between the reference orbit and short arc TAR solutions

Orbits	Total (m)		T (m)		A (m)		R (m)	
	rms	max	rms	max	rms	max	rms	max
REF - "a priori" (ARC 1 and ARC 5)	0.99	1.09	0.28	0.40	0.88	1.01	0.36	0.54
REF - T1A	0.23	0.52	0.14	0.40	0.12	0.25	0.14	0.26
REF - T1B	0.15	0.33	0.11	0.29	0.06	0.13	0.08	0.15
REF - T5A	0.56	0.86	0.35	0.49	0.30	0.55	0.33	0.67
REF - T5B	0.65	0.86	0.25	0.38	0.48	0.55	0.36	0.70

For arc 5 only three parameters were solved, since very high correlations occur between various parameters. In this case the corrected track departs from the reference orbit by 30 to 40 cm on each component with a global rms differences of about 60 cm. These results are worse than the corresponding results obtained with both the constrained and the Bayesian methods for the same arc.

For arcs longer than 30 minutes the TAR technique is no longer applicable. For these lengths the corrected track is highly dependent on the accuracy of the initial long arc solution.

10.5 Conclusions

Both the Constrained and the Bayesian methods described above, are very useful short arc techniques that can be applied to substantially longer arcs than the TAR method. This last method gives very good results for very short arcs up to 10 minutes with particular station configurations as mentioned by Sinclair (1989), but for arcs longer than 30 minutes they are no longer applicable.

By properly applying a number of constraints to the solved for parameters, the constrained method allows precise orbit determinations, even for configurations as poor as configuration 5 (only one station at each end of the arc). For arcs of about 30 minutes (1/3 of a revolution) the accuracy of these solutions is at decimetre level. For longer arcs, the accuracy decreases as the length of the arc increases, up to about one revolution. For arcs longer than one orbital revolution (100 minutes) this technique is no longer applicable. At this length the force model errors become noticeable and it is not possible to eliminate them by smooth solutions as the described above.

The Bayesian method can be very useful for particularly unstable configurations. The final accuracy of the solution depends both on the degree of instability of the short arc solution, and the quality of the long-arc ephemeris over that particular region. In any case the combined solution is a weighted average of the two separate solutions, and therefore more reliable than any of the individual solutions separately. The choice of the relative weights that should be applied, depends on the instability of the tracking configuration. This is detected by analysing the correlations between the solve for parameters. High correlations usually imply an ill-determined short-arc solution. Therefore the higher these correlations the more weight should be given to the long-arc solution.

Chapter 11
Conclusions and Recommendations

The SATAN software package, originally designed to process laser data, has been expanded to process two additional types of tracking data: direct altimeter measurements and PRARE range data.

PRARE data were simulated using the data format as specified by the German PAF for ERS-1. An efficient algorithm was developed for the processing of altimetry data. The altimeter measurements are transformed into residual sea surface heights, by using an appropriate geoid model. Prior to being used in the orbit adjustment, residual sea surface heights are processed by a spectral analysis subroutine, where only the frequencies below a specified cut-off (usually two cycles per revolution) are kept. This spectral analysis is efficiently performed by using Fast Fourier Transform techniques. Therefore a large number of points can be processed without any substantial increase in computing time. These smoothed sea surface heights are then used as tracking data residuals in the orbit adjustment. In the fitting process any sampling interval can be specified, to balance the weight of altimeter data relative to other types of tracking data used in the solution.

In the altimeter processing the partial derivatives of the "observed" altimeter height above ellipsoid, with respect to cartesian satellite coordinates (X,Y,Z), were computed using new formulae derived by the author of this thesis. These formulae are exact and very simple when compared to the expressions used in the GEODYN program (Eddy et al, 1990) or the formulae presented by Rothwell (1989).

Throughout this project several additional facilities were introduced into the programs. These new algorithms allow the determination of more flexible solutions by either solving for additional parameters or by constraining the normal equations matrix. A number of algorithms were added for the specific computation of ERS-1 orbits including the centre of mass correction for laser ranges and the modelling of the cross-sectional area for drag and radiation pressure.

Software validation was achieved using laser, altimetry and simulated PRARE for SEASAT and laser from ERS-1. ERS-1 altimetry data have not been used, due to the poor accuracy of the Fast Delivery Product available. However the software modifications required to process ERS-1 altimetry are straightforward.

SEASAT orbits computed with the SATAN programs, exhibited rms laser range residuals of 0.3 metres or less. These figures are in agreement with published results for SEASAT. The best geopotential models for this satellite were found to be GEMT2 and GRIM4_C2, both yielding similar results. In the computation of the GRIM4_C2 orbit, the GEMT2 reference system and station coordinates were used, since the GEMT2 and the GRIM4 systems are very close (see sections 8.2.1 and 9.2.1). However the use of pole and station coordinates, properly referred to the GRIM4 system, should slightly improve the orbit computed with this model.

The accuracy of the orbits computed with these two gravity field models has been assessed by analysis of their differences. GEMT2 and GRIM4_C2 come from two independent solutions. Since they yield orbits with the same rms of fit, the differences between these orbits are a clear indication of the global accuracy of the ephemerides generated by these two geopotential models. These differences amount to 0.7, 0.6 and 0.3 m in the TAR directions respectively, with a global rms of 1 metre. The same solutions computed with GEMT1 have an rms of 0.5 to 0.6 metres, with differences relative to the two previous solutions about 1.5 times larger than the figures quoted above.

In all SEASAT computations a constant cross-sectional area for drag and radiation pressure was adopted, and daily drag coefficients were solved for. The SEASAT NASA area tables for modelling the cross-sectional areas for drag and radiation pressure have not been used, since it had been shown (Rothwell, 1989) that the use of constant areas and multiple drag coefficients would give equivalent results. This is probably due to the limited geographical distribution of the SEASAT laser data, that could not sense large variations in the cross-sectional area.

It has been demonstrated that orbits computed with PRARE data have similar accuracy to orbits computed with an equivalent network of laser data. The advantage of having used simulated instead of real data, is that the effect of the amount and distribution of tracking data can be studied. The results show that the rms of fit to tracking data is an optimistic indicator of the global accuracy of long arc ephemerides. This is because actual tracking networks usually have poor geographical coverage.

The results obtained with altimeter data confirm that these data alone cannot be used for orbit determination, since they improve the orbit only in the radial direction. Despite the weakness of this data type when used alone, only a few passes of range data are sufficient to add the necessary along-track information.

Investigation into the extent to which altimetry can replace range data, revealed that altimetry data can fill gaps of range data covering periods as long as two days. However,

these gaps should be between passes of range data and not for example at the end of the arc. This means that altimetry can only be used to interpolate range data, but not to extrapolate. In fact, if an arc containing a few passes of range data is extended by using altimeter data, the solution will be well determined until a few revolutions after the last pass of range data; the along-track errors will linearly increase and, half a day later, will amount to several metres.

The application to ERS-1 of the results obtained for SEASAT, is constrained by the lack of a geopotential model for the former satellite with suitable accuracy. In SEASAT computations the geopotential model errors were modelled as the differences between GEMT1 and GEMT2. Hence to obtain the same results for ERS-1, this model should yield ERS-1 orbits with similar accuracy to SEASAT orbits derived with GEMT1. This means that the rms range residuals for a 3-day arc tracked by an appropriate network of laser stations, should be about 0.5 to 0.6m. Since the present best models for ERS-1 give an rms of fit three times as large as this, these results have to be scaled accordingly.

ERS-1 orbits were determined using state of the art models and several algorithms developed during this project. The geopotential model that was found to yield the best overall results is GRIM4_C2. ERS-1 ephemerides determined with this model by adjusting for daily drag coefficients have rms laser range residuals of 1.5 m. By comparison, the rms of fit of the same orbits computed with GEMT2, was of the same order on one arc, but about twice as large (3.3 m) on another arc. The incorporation of DORIS data from SPOT (which has an inclination very close to that of ERS-1) on GRIM4_C2 seems to have led to a slight model improvement. However these figures are still three times as large as the corresponding results for SEASAT. This means that the GRIM models are an improvement over GEMT2 but are still a long way from the required accuracy. The radial and across-track differences of the orbits computed with GRIM4_C2 and GEMT2 is of the order of 1.5 and 2 metres respectively, but the along-track errors are about 3 times larger (7 metres). Since these differences reveal mostly information on the less accurate model, the global accuracy of GRIM4_C2 solutions should be slightly better than these figures.

The main errors in ERS-1 solutions occurring during periods of quiet geomagnetic activity are of gravitational origin, but for arcs corresponding to periods of high geomagnetic activity, manifested in sharp variations of the geomagnetic index Kp, the errors due to drag mismodelling become more important.

To reduce the errors of gravitational origin, the adjustment of a selected set of geopotential coefficients has been investigated. Due to the reduced data set that was available for this project, and the large drag errors existing in this arc, the results are not very conclusive. The method developed in this study needs to be applied to a much

longer arc, or a series of arcs. To avoid the absorption of drag errors into the adjusted geopotential coefficients this adjustment should take place during a period of reduced geomagnetic activity. Further research needs to be done in this subject, into an appropriate choice of the coefficients to adjust and determination of "a priori" constraints to reduce the high correlations existing between some of the parameters, in particular the resonant coefficients.

With regard to drag effects, the influence of solar flux and geomagnetic data used in the computation of atmospheric density has been thoroughly investigated. The rms of fit of ERS-1 ephemerides are a strong function of the value used for the time lag introduced in geomagnetic Kp indices (TLKP). It was found that a difference of about 2 hours in the TLKP value causes the rms of fit to laser ranges to vary from 1.6 metres to only 0.4 metres. During periods of strong geomagnetic activity, the 3-hour Kp indices exhibit very sharp variations within periods of a few hours. These variations cause similar variations in the computed density and therefore in the induced perturbation on the satellite. If the Kp variations are not "in phase" with the satellite perturbation sensed by the tracking data, the orbit adjustment will be poor with large rms of fit.

These results suggest that this parameter should be adjusted within the solution. This a topic that needs further investigation. However it can be anticipated that this adjustment is only possible if sufficient data are available. A change in the time lag is equivalent to an along-track shift in the satellite perturbation. Without good widely distributed tracking data, high correlations may exist between this parameter and the drag coefficients, since they both determine along-track corrections. If such adjustment is not possible, instead of the original Kp indices, it is preferable to use a smoother representation of the same indices. A simple 4-point average filter used in this study was found to yield overall orbit adjustments better than the single-point ones. Further research should be carried out to determine a more appropriate smoothing function.

Similar investigation has been carried out to determine the influence of the time lag introduced in the solar flux indices $F_{10.7}$, (TLF). Results show that, as opposed to TLKP, this parameter has a minor influence in the solution. The solar flux indices model daily and longer wavelength variations of the atmospheric density and any error in these indices is absorbed by the daily drag coefficients. This result is very important to understand the overall influence of the solar flux data in the orbit accuracy. Therefore if adequate tracking data are available, allowing a good recovery of the drag coefficients, any mismodelling in the flux indices will be absorbed by the corresponding drag parameters.

Ephemerides were computed by using predicted values of solar flux, by just modelling the long wavelength component of their variation (mainly the 11-year solar cycle). It was

found that these orbits do not depart significantly from the solutions that would be obtained by using the actual measured indices. Any bias in these indices is absorbed by the corresponding drag coefficients which will exhibit meaningless values, either too large or too small. Unlike the solar flux indices, the geomagnetic indices cannot be predicted since they model irregular variations of the geomagnetic field. The errors induced by neglecting the geomagnetic indices depend on their variability over the interval considered. For arcs with sharp Kp variations, these errors may reach several metres. This creates a restriction to the generation of precise and quick ephemerides. Therefore for the generation of rapid and accurate orbits it is essential to have access to these measurements, as soon as they are released by the NGDC.

The geometric models derived to compute the cross-sectional area for drag and radiation pressure did not seem to improve the solution relative to the use of a simple constant area model. These areas (in particular the drag area) are strong functions of latitude. Since the tracking data available for this study come from stations all at very close latitudes, these data cannot sense large changes in the cross-sectional area. To determine the actual accuracy of these models a larger tracking data set should be used, with stations exhibiting a wide range of latitudes.

For two arcs occurring on periods of different levels of solar and geomagnetic activity, minimum, maximum and rms values for the acceleration due to the main forces that act on the satellite have been computed. Results show that for the arc occurring during a period of strong geomagnetic disturbances the acceleration due to drag has a much larger variation than the acceleration due to radiation pressure. However during the quieter period drag and radiation pressure exhibit similar variations, the rms of radiation pressure acceleration having a larger amplitude. In this study the effect of radiation pressure has not been investigated, but these results show that those effects cannot be neglected and they should be the subject of future research. From the forces that contribute to radiation pressure, the most important, and therefore the one that should be investigated in more detail, is the force arising from the direct solar radiation. Compared to this, the effects of albedo and IR radiation together are about one order of magnitude smaller, and can therefore be regarded as second order effects.

In all ERS-1 solutions the use of multiple drag coefficients is crucial. The algorithm implemented in the SATAN programs during this project proved to be very efficient. By solving for daily drag coefficients the long wavelength component of the along track errors can be absorbed. When the tracking data are sparse, with large gaps close to one day, the choice of the intervals to which each of the coefficients will apply is most important. Since there are a number of perturbations that have a daily variation, in principle the intervals should be daily intervals, starting and ending at the start and end of

each new day. Each coefficient is determined solely by the tracking data available for that interval. Therefore if for example during a particular day there is only one pass, the coefficient will not be well determined, and if there are sharp fluctuations of the drag force during the same period, the orbit will have large errors in this area.

Two new short arc techniques (Constrained and Bayesian) have been investigated and compared to the TAR method.

On the constrained method, constraints are applied to the solved-for parameters, therefore reducing the number of degrees of freedom of the solution and forcing it to become smoother. The choice of the constraints to be applied to each individual solution is made by taking into account the correlations existing between the various parameters. By an appropriate choice of the constraints, this method allows very precise orbit determinations, even when applied to poor configurations such as two passes, one at each end of the arc. For arcs of about 30 minutes the accuracy of these solutions is at decimetre level. For longer arcs, the accuracy gradually diminishes as the length of the arc increases until about one orbital revolution. For arcs longer than one orbital revolution (100 minutes) this method is no longer appropriate. At this length the force model errors start to manifest and smooth solutions of this type are no longer capable of absorbing these errors.

The Bayesian method has been shown to be very advantageous for particularly unstable configurations. By using this method the final orbit is a combined result of two separate solutions: the single short arc solution that would be obtained by just fitting the orbit to the observations in the short arc, and the "a priori" solution, usually a long arc ephemeris. The accuracy of the combined solution depends both on the degree of instability of the short arc solution, and the quality of the long-arc ephemeris over that particular region. It is therefore a weighted average of these two orbits. The choice of the relative weights that should be applied to each of them, depends on the stability of the tracking configuration revealed by the correlations between the solve for parameters. Since high correlations usually imply ill-determined short-arc solutions, generally the higher these correlations the more weight should be given to the long-arc solution.

This study shows that short arc techniques as described above can be an alternative for computing ephemerides with decimetre accuracy. By using short-arc methods very precise and rapid ephemerides can be obtained, provided adequate tracking data are available. Since most of the applications do not require an orbit over a long arc, but within a local region, it is hoped that these techniques will play an important role in the development of scientific applications of ERS-1 data.

A number of factors have conditioned the derivation of some of the results presented in this thesis, which otherwise could have been improved or expanded.

The first serious limitation was due to computing time. During most of this project the software was running on a μVAX 2000. For a 3-day arc the average CPU time taken to perform an iteration in this computer was approximately 30 minutes. This means that in the very unrealistic situation that only these programs were running on the machine, a full 3-arc run of two iterations would take about one hour. Fortunately towards the end of this project the programs were implemented on a much faster computer, a VAX Station 4060, where the CPU time of each run is reduced to one or two minutes.

Due to the limited time allocated for a project of this nature, and because in science nothing is definite, this thesis has left open several areas that need further study.

An interesting topic of research is the inclusion of the TLKP as an adjusted parameter. To do this the addition of altimetry data to ERS-1 solutions is essential, due to the limited coverage of the present laser tracking network.

The performance of altimetry data on ERS-1 orbits, using the algorithm developed during this project, needs to be investigated. For this purpose the complete altimeter ocean product, including all the geophysical corrections, has to be used.

The accuracy of the geometric algorithms developed in this study for the computation of ERS-1 cross-sectional areas for atmospheric drag and radiation pressure need to be assessed. This can either be done by comparing these algorithms with the ESA derived models, or by using a network of stations well distributed in latitude. If such a configuration is not possible, simulated data could be used in a similar fashion to the simulation study done on this project with SEASAT PRARE data.

Parallel to the effort to improve the modelling of the surface forces, the adjustment of a set of geopotential coefficients needs further investigation. This might be essential while a complete tuned model for ERS-1 has not been determined.

Appendix A

Partial derivatives of height above ellipsoid with respect to (X, Y, Z)

A.1 Introduction

For the implementation of the altimeter algorithm developed during this study (Chapter 7), the partial derivatives of the height h of a point above some reference ellipsoid with respect to the associated cartesian coordinates (x, y, z) are required. Since h cannot be expressed as an explicit function of (x, y, z) only, the derivation of analytical formulae for these partials is not a simple task. An alternative is to use approximate formulae.

In this thesis very simple and exact formulae for these partial derivatives were derived. These formulae and their derivation are the subject of this appendix.

A.2 Spherical Coordinates

When the Earth is approximated by a sphere, instead of the usual geodetic coordinates (φ, λ, h) we have the spherical coordinates (ϕ, λ, r) (see Figure 7.4).

The relationship between (x, y, z) and the spherical angular coordinates (ϕ, λ, r) is:

$$\begin{cases} x = r\cos\phi\,\cos\lambda \\ y = r\cos\phi\,\sin\lambda \\ z = r\sin\phi \end{cases} \tag{A.1}$$

where ϕ is geocentric latitude, r is geocentric distance and λ is longitude. Inversely,

$$\begin{cases} \lambda = \arctan\left(\dfrac{y}{x}\right) \\ \phi = \arctan\left(\dfrac{z}{\sqrt{x^2 + y^2}}\right) \\ r = \sqrt{x^2 + y^2 + z^2} \end{cases} \tag{A.2}$$

In this case the computation of the partial derivatives of (x, y, z) with respect to the geocentric distance **r** can be done by using the expressions:

$$\begin{cases} \dfrac{\partial x}{\partial r} = \cos\phi\cos\lambda = \dfrac{x}{r} \\ \dfrac{\partial y}{\partial r} = \cos\phi\sin\lambda = \dfrac{y}{r} \\ \dfrac{\partial z}{\partial r} = \sin\phi = \dfrac{z}{r} \end{cases} \tag{A.3}$$

Inversely, the computation of the partial derivatives of **r** with respect to (x, y, z) is straightforward:

$$\begin{cases} \dfrac{\partial r}{\partial x} = \dfrac{2x}{2\sqrt{x^2 + y^2 + z^2}} = \dfrac{x}{r} \\ \dfrac{\partial r}{\partial y} = \dfrac{2y}{2\sqrt{x^2 + y^2 + z^2}} = \dfrac{y}{r} \\ \dfrac{\partial r}{\partial z} = \dfrac{2z}{2\sqrt{x^2 + y^2 + z^2}} = \dfrac{z}{r} \end{cases} \tag{A.4}$$

Comparing these two formulae we get an interesting result: the partials of (x, y, z) with respect to **r** are equal to the partials of **r** with respect to (x, y, z).

$$\begin{cases} \dfrac{\partial r}{\partial x} = \dfrac{\partial x}{\partial r} = \cos\phi\cos\lambda \\ \dfrac{\partial r}{\partial y} = \dfrac{\partial y}{\partial r} = \cos\phi\sin\lambda \\ \dfrac{\partial r}{\partial z} = \dfrac{\partial z}{\partial r} = \sin\phi \end{cases} \tag{A.5}$$

A.3 Geodetic Coordinates

A.3.1 Relationship between cartesian (x, y, z) and geodetic angular coordinates (φ, λ, h)

For most of the geodetic applications we are interested in using geodetic instead of spherical angular coordinates.

Reviewing the relationship between cartesian (x, y, z) and angular (φ, λ, h):

$$\begin{cases} x = (\nu + h)\cos\varphi\cos\lambda \\ y = (\nu + h)\cos\varphi\sin\lambda \\ z = \left[\nu(1-e^2) + h\right]\sin\varphi \end{cases} \qquad (A.6)$$

where **a** and **e** are the semi-major axis and eccentricity of the reference ellipsoid, φ is geodetic latitude, and ν is radius of curvature in prime vertical:

$$\nu = a\left(1 - e^2\sin^2\varphi\right)^{-1/2} \qquad (A.7)$$

Inversely, one would like to obtain expressions of (φ, λ, h) in terms of (x, y, z). For λ a simple relationship can be written as in the case of spherical coordinates (equation A.2), since λ is the same in both coordinate systems (spherical and geodetic):

$$\lambda = \arctan\left(\frac{y}{x}\right) \qquad (A.8)$$

The same cannot be established for φ and **h**. In fact φ is computed by iteration using the expression

$$\tan\varphi = \frac{z + e^2\nu\sin\varphi}{\sqrt{x^2 + y^2}} \qquad (A.9)$$

This iteration can be started by using the spherical approximation given by equation A.2. Once φ has been computed then **h** can be obtained by:

$$h = \frac{\sqrt{x^2 + y^2}}{\cos\varphi} - \nu \qquad (A.10)$$

A.3.2 Partial derivatives of (x, y, z) with respect to (φ, λ, h).

The partial derivatives of (x, y, z) with respect to (φ, λ, h) can be deduced by differentiating equations A.6 with respect to (φ, λ, h):

$$J = \begin{bmatrix} \frac{\partial x}{\partial \varphi} & \frac{\partial x}{\partial \lambda} & \frac{\partial x}{\partial h} \\ \frac{\partial y}{\partial \varphi} & \frac{\partial y}{\partial \lambda} & \frac{\partial y}{\partial h} \\ \frac{\partial z}{\partial \varphi} & \frac{\partial z}{\partial \lambda} & \frac{\partial z}{\partial h} \end{bmatrix} = \begin{bmatrix} A\cos\lambda & -B\sin\lambda & \cos\varphi\cos\lambda \\ A\sin\lambda & B\cos\lambda & \cos\varphi\sin\lambda \\ -A\frac{\cos\varphi}{\sin\varphi} & 0 & \sin\varphi \end{bmatrix} \qquad (A.11)$$

where

$$A = \left[\frac{\partial \nu}{\partial \varphi}\cos\varphi - (\nu + h)\sin\varphi\right]$$

$$B = (\nu + h)\cos\varphi \qquad (A.12)$$

$$\frac{\partial \nu}{\partial \varphi} = \frac{\nu^3}{a^2} e^2 \sin\varphi\cos\varphi$$

The matrix J is called the Jacobean of the transformation $(x, y, z) \xrightarrow{f} (\varphi, \lambda, h)$.

A.3.3 Partial derivatives of (φ, λ, h) with respect to (x, y, z) using numeric matrix inversion.

Since no explicit form exists for φ and h in terms of (x, y, z), one alternative form for computing the partial derivatives of (φ, λ, h) with respect to (x, y, z) is by matrix inversion of Jacobean J. In fact if J is the Jacobean of the transformation

$$(x, y, z) \xrightarrow{f} (\varphi, \lambda, h) \qquad (A.13)$$

as defined in equation A.11, then the Jacobean of the inverse transformation

$$(\varphi, \lambda, h) \xrightarrow{f^{-1}} (x, y, z) \qquad (A.14)$$

is J^{-1}, the inverse of matrix J

$$J^{-1} = \begin{bmatrix} \frac{\partial\varphi}{\partial x} & \frac{\partial\varphi}{\partial y} & \frac{\partial\varphi}{\partial z} \\ \frac{\partial\lambda}{\partial x} & \frac{\partial\lambda}{\partial y} & \frac{\partial\lambda}{\partial z} \\ \frac{\partial h}{\partial x} & \frac{\partial h}{\partial y} & \frac{\partial h}{\partial z} \end{bmatrix} = \begin{bmatrix} \frac{\partial x}{\partial\varphi} & \frac{\partial x}{\partial\lambda} & \frac{\partial x}{\partial h} \\ \frac{\partial y}{\partial\varphi} & \frac{\partial y}{\partial\lambda} & \frac{\partial y}{\partial h} \\ \frac{\partial z}{\partial\varphi} & \frac{\partial z}{\partial\lambda} & \frac{\partial z}{\partial h} \end{bmatrix}^{-1} \qquad \text{(A.15)}$$

Therefore, for each point the computation of these partials requires the inversion of a (3x3) matrix. This can be computationally expensive if a large number of points has to be processed as in the case of altimeter analysis.

A.4 Exact formulae for the partial derivatives of (φ, λ, h) with respect to (x, y, z)

In this section it will be demonstrated that very simple expressions exist for the partial derivatives of h with respect to (x, y, z), similar to the expressions found for r in the case of spherical coordinates (equations A4 and A5). These formulae are:

$$\begin{cases} \frac{\partial h}{\partial x} = \frac{\partial x}{\partial h} = \cos\varphi\cos\lambda \\ \frac{\partial h}{\partial y} = \frac{\partial y}{\partial h} = \cos\varphi\sin\lambda \\ \frac{\partial h}{\partial z} = \frac{\partial z}{\partial h} = \sin\varphi \end{cases} \qquad \text{(A.16)}$$

i.e., as in the case of spherical coordinates, the partials of h with respect to (x, y, z) are equal to the partials of (x, y, z) with respect to h. The demonstration of these formulae is done in two steps:

1. Computation of the determinant of the Jacobean J , det(J).

$$\det(J) = \frac{\partial x}{\partial \varphi}\frac{\partial y}{\partial \lambda}\frac{\partial z}{\partial h} + \frac{\partial y}{\partial \varphi}\frac{\partial z}{\partial \lambda}\frac{\partial x}{\partial h} + \frac{\partial z}{\partial \varphi}\frac{\partial x}{\partial \lambda}\frac{\partial y}{\partial h} - \frac{\partial z}{\partial \varphi}\frac{\partial y}{\partial \lambda}\frac{\partial x}{\partial h} - \frac{\partial y}{\partial \varphi}\frac{\partial x}{\partial \lambda}\frac{\partial z}{\partial h} - \frac{\partial x}{\partial \varphi}\frac{\partial z}{\partial \lambda}\frac{\partial y}{\partial h} \qquad \text{(A.17)}$$

Since $\frac{\partial z}{\partial \lambda} = 0$ only 4 terms are left which can be arranged as:

$$\det(J) = \frac{\partial x}{\partial \varphi}\frac{\partial y}{\partial \lambda}\frac{\partial z}{\partial h} + \frac{\partial z}{\partial \varphi}\left[\frac{\partial x}{\partial \lambda}\frac{\partial y}{\partial h} - \frac{\partial y}{\partial \lambda}\frac{\partial x}{\partial h}\right] - \frac{\partial y}{\partial \varphi}\frac{\partial x}{\partial \lambda}\frac{\partial z}{\partial h} \qquad \text{(A.18)}$$

Now substituting each of the partials by their expressions in terms of (φ, λ, h), given in equation A.11.

$$\det(J) = A\,B\,\sin\varphi\cos^2\lambda - A\,\frac{\cos\varphi}{\sin\varphi}\left[-B\,\cos\varphi\sin^2\lambda - B\,\cos\varphi\cos^2\lambda\right]$$

$$+ A\,B\,\sin\varphi\sin^2\lambda$$

$$= A\,B\,\sin\varphi - A\,\frac{\cos\varphi}{\sin\varphi}\left[-B\,\cos\varphi\right] = \frac{A\,B}{\sin\varphi}\left[\sin^2\varphi + \cos^2\varphi\right]$$

The final expression of det(J) is:

$$\det(J) = \frac{A\,B}{\sin\varphi} \qquad \text{(A.19)}$$

2. Explicit computation of $\left(\frac{\partial h}{\partial x}, \frac{\partial h}{\partial y}, \frac{\partial h}{\partial z}\right)$

$\left(\frac{\partial h}{\partial x}, \frac{\partial h}{\partial y}, \frac{\partial h}{\partial z}\right)$ being elements of J^{-1} , they can be computed in terms of the elements of J (equation A.15).

$$
\begin{cases}
\dfrac{\partial h}{\partial x} = \dfrac{\dfrac{\partial y}{\partial \varphi}\dfrac{\partial z}{\partial \lambda} - \dfrac{\partial z}{\partial \varphi}\dfrac{\partial y}{\partial \lambda}}{\det(J)} = \dfrac{\dfrac{A\,B\cos\varphi\cos\lambda}{\sin\varphi}}{\dfrac{A\,B}{\sin\varphi}} = \cos\varphi\cos\lambda \\[2ex]
\dfrac{\partial h}{\partial y} = \dfrac{\dfrac{\partial z}{\partial \varphi}\dfrac{\partial x}{\partial \lambda} - \dfrac{\partial x}{\partial \varphi}\dfrac{\partial z}{\partial \lambda}}{\det(J)} = \dfrac{\dfrac{A\,B\cos\varphi\sin\lambda}{\sin\varphi}}{\dfrac{A\,B}{\sin\varphi}} = \cos\varphi\sin\lambda \\[2ex]
\dfrac{\partial h}{\partial z} = \dfrac{\dfrac{\partial x}{\partial \varphi}\dfrac{\partial y}{\partial \lambda} - \dfrac{\partial y}{\partial \varphi}\dfrac{\partial x}{\partial \lambda}}{\det(J)} = \dfrac{A\,B\left[\cos^2\lambda + \sin^2\lambda\right]}{\dfrac{A\,B}{\sin\varphi}} = \sin\varphi
\end{cases}
\tag{A.20}
$$

Equations A.16 have therefore been proved. Apart from the advantage of being exact, these formulae are very simple when compared to the expressions used in the GEODYN program (Eddy et al, 1990) or the formulae presented by Rothwell (1989).

A.5 Transformation of the partial derivatives from CTS to CIS

All the formulae derived above, hold in any cartesian geocentric (x, y, z) terrestrial system, in particular the Conventional Terrestrial System (CTS). For use in program RGODYN the partial derivatives in equation A.16 have to be transformed into the Conventional Inertial System (CIS).

Let (x, y, z) be a position of a point in the CTS, (X, Y, Z) the corresponding position in the CIS and R the transformation matrix between the two systems:

$$
\begin{bmatrix} X \\ Y \\ Z \end{bmatrix}_{CIS} = R \begin{bmatrix} x \\ y \\ z \end{bmatrix}_{CTS} \tag{A.21}
$$

Differentiating with respect to h we get:

$$\begin{bmatrix} \frac{\partial X}{\partial h} \\ \frac{\partial Y}{\partial h} \\ \frac{\partial Z}{\partial h} \end{bmatrix}_{CIS} = \frac{\partial R}{\partial h} \begin{bmatrix} x \\ y \\ z \end{bmatrix}_{CTS} + R \begin{bmatrix} \frac{\partial x}{\partial h} \\ \frac{\partial y}{\partial h} \\ \frac{\partial z}{\partial h} \end{bmatrix}_{CTS} \qquad (A.22)$$

The form of matrix R is given in equation 2.10. This matrix does not depend on the point considered. It is only a function of time. Therefore $\frac{\partial R}{\partial h} = 0$ and we obtain:

$$\begin{bmatrix} \frac{\partial X}{\partial h} \\ \frac{\partial Y}{\partial h} \\ \frac{\partial Z}{\partial h} \end{bmatrix}_{CIS} = R \begin{bmatrix} \frac{\partial x}{\partial h} \\ \frac{\partial y}{\partial h} \\ \frac{\partial z}{\partial h} \end{bmatrix}_{CTS} \qquad (A.23)$$

And since

$$\begin{bmatrix} \frac{\partial h}{\partial x} \\ \frac{\partial h}{\partial y} \\ \frac{\partial h}{\partial z} \end{bmatrix}_{CTS} = \begin{bmatrix} \frac{\partial x}{\partial h} \\ \frac{\partial y}{\partial h} \\ \frac{\partial z}{\partial h} \end{bmatrix}_{CTS} \qquad (A.24)$$

we finally get

$$\begin{bmatrix} \frac{\partial h}{\partial X} \\ \frac{\partial h}{\partial Y} \\ \frac{\partial h}{\partial Z} \end{bmatrix}_{CIS} = R \begin{bmatrix} \frac{\partial h}{\partial x} \\ \frac{\partial h}{\partial y} \\ \frac{\partial h}{\partial z} \end{bmatrix}_{CTS} \qquad (A.25)$$

Appendix B
Brief description of software included in the SATAN programs

The SATAN software package was originally written by A. Sinclair and G. Appleby at the Royal Greenwich Observatory. This appendix gives a list of this software with a brief description of each program unit and the alterations that have been introduced into the programs during this project.

The SATAN package consists of two main programs, ORBIT and RGODYN and a relatively large set of subroutines. These are described in tables B.1 to B.4.

Table B.1
Description of program ORBIT

Program name	Description	Alterations introduced during this project
ORBIT	Computes satellite position and velocity at specified observation dates by numerical integration of the equations of motion. It also calculates the partial derivatives of satellite position and velocity with respect to the solve-for parameters that affect the orbit. The integration method used is an eighth order Gauss-Jackson method with an iterative starting scheme. The force model includes effects due to : • The Earth's Gravitational field • Gravitational attraction of the sun moon and planets • Atmospheric drag • Radiation pressure • The solid Earth and ocean tides	Implementation of the solution for multiple drag coefficients and for a selected set of geopotential coefficients.

Table B.2
Description of program RGODYN

Program name	Description	Alterations introduced during this project
RGODYN	Determines corrections to the parameters that define the orbit by fitting it to observations. The original program processed only laser data. The fitting algorithm is the least squares method of observation equations. The original program could be run in one of two modes: • long-arc mode whereby a normal solution is obtained by determining corrections to a set of orbital parameters. • short-arc mode whereby the orbit is adjusted to observations within a short arc by solving for corrections along the TAR directions.	• Processing of PRARE data • Processing of altimetry data • Solution for multiple drag coefficients. • Solution for osculating orbital elements instead of position and velocity. • Solution for a user selected set of geopotential coefficients. • Bayesian least squares in addition to conventional least squares. • Possibility of applying constraints to the solve-for parameters. • TAR solutions using additional formulae for the corrections.

Table B.3
List of subroutines that were kept in their original form,
as written by A Sinclair and G. Appleby,
by alphabetic order.

Subroutine name	Description
ALBPIR	Evaluates albedo and infrared force per unit area (PIR). Cf. equation 3.16. (Vonder Haar and Suomi, 1971).
CAD	Computes atmospheric density using Jacchia-72 model (Jacchia, 1972). See equation 3.13
CL3	Determines coefficients for cubic Lagrangean Interpolation
DCHOLS	Double precision Choleski matrix inversion
DERIV	Computes partials of position and velocity wrt osculating elements in the order (a, e,i , M+ω, ω, Ω)
EARTH	Computes matrix to transform from true equator and equinox of epoch to a conventional terrestrial system (equation 2.16)
ELEMTS	Converts position and velocity to osculating elements
FLUX	Returns solar flux and Kp indices at a specified time by interpolation
FLUXDATA	Sets up solar fluxes and geomagnetic indices for the interval of the computations
GEOC	Converts geodetic (φ,λ,h) to geocentric (X,Y,Z). Cf equation A.6
KEPLER	Converts osculating elements to position and velocity
MARINI	Computes one-way refraction delay for laser ranges (equation 6.5)
PREPROC	Reads SLR observation file in either MERIT I or MERIT II formats
SUPRES	Suppresses the solution for a particular parameter, given its position in the normal matrix
TIDEFQ	Computes corrections to tesserals due to frequency-dependence of Love number K2 for solid Earth tides. Also applies ocean tide perturbations (Melbourne at al., 1983)
TIDES	Computes station displacement due to solid Earth tides (equation 3.22)
UTPOLE	Gets pole coordinates, UT1-UTC data and time conversion factors
XGEO	Converts geocentric (X,Y,Z) to geodetic (φ,λ,h). Cf equations A.7 to A.10

Table B.4

List of subroutines that were written or modified during this thesis, by alphabetic order.

Subroutine name	Description	Comments
ALTIM	Reads SEASAT altimeter data in the GDR format	written by J. Fernandes
CMERS1	Computes centre of mass correction for ERS-1 (Laser or Altimeter)	written by J. Fernandes
DERIV2	Computes partials of position and velocity wrt osculating elements in the order (a, e,i , M, ω, Ω)	adapted from subroutine DERIV
DFFT	Evaluation of the discrete Fast Fourier Transform of a real unevenly spaced array of size N	written by J. Fernandes
DRAG	Computes acceleration due to atmospheric drag. Cf. equation 3.13.	use of multiple drag coefficients and modelling of a variable cross-sectional area for ERS-1 have been introduced
FOUR1	Computes the FFT or the inverse FFT of a complex array of size $N=2^k$ (Press et al, 1986)	introduced by J. Fernandes
MATINV	Double precision matrix inversion by the Gaussian method	introduced by J. Fernandes
MATVET	Multiplies a matrix by a vector	written by J. Fernandes
PRARERAN	Reads PRARE range data file according to ESA format	written by J. Fernandes
PRODMAT	Multiplies two matrixes	written by J. Fernandes
REALFT	Compute the FFT or the inverse FFT of a real evenly spaced array of size $N=2^k$ (Press et al, 1986)	introduced by J. Fernandes
ROTATION	Defines rotations R_i (α) of angle α about axis i (equation 2.12)	written by J. Fernandes
SHRINK	Reverses "extirpolation" performed by SPREAD	written by J. Fernandes
SOLRAD	Computes acceleration due to solar radiation pressure, albedo and IR radiation (Equation 3.15).	modelling of a variable cross-sectional area for ERS-1 has been introduced
SPREAD	"Extirpolates" an array of length N into an expanded array of size NDIM (Press and Rybicki, 1989)	introduced by J. Fernandes

References

Allan, A. L., 1993 - Practical Surveying and Computations - Buttherworth-Heinemann

Biancale, R., G. Balmino, B. Moynot, J. M. Lemoine, J. C. Marty, F. Barlier, Y. Boudon, P. Schwintzer, Ch. Reigber, W. Barth, F. H. Massmann, J. C. Raimondo, M. Gerstl, A. Bode, H. Li, 1993 - GRIM4 : Un modele de champs de gravite de la terre - personal comunication

Born, G. H., J. A. Dunne and D. B. Lame, 1979 - SEASAT overview mission - *Science*, Vol 24

Boucher, C. and J. Dufour, 1992 - The DORIS tracking system - A progress report - Institut Geographique National, France

Boucher, C. and Z. Altamini, 1992 - The IERS Terrestrial Reference System - Institut Geographique National, France

Boucher, C., Z. Altamini, and L. Duhem, 1992 - ITRF 91 and its associated velocity field - *IERS Technical Note* No 12

Charlot, P. (ed), 1992 - Earth Orientation, reference frames and atmospheric excitation functions submitted for the 1991 IERS Annual Report - *IERS Technical Note* No 11

Colombo, O. L., 1984 - Altimetry, Orbits and Tides - NASA Technical Memorandum 86180

Cross, P. A., 1983 - Advanced least squares applied to position-fixing - North East London Polytechnic, Working Paper No 6

DeMets, C., R. G. Gordon, D. F. Argus and S. Stein, 1990 - Current Plate Motions - *Geophysical Journal International*, 101, 425-478

Doherty, G. M., 1992 - ERS-1 Data Products Validation Status - presentation at ERS-1 PI meeting ESRIN: 17-19 March 1992

Duchossois, G., 1991 - The ERS-1 Mission Objectives - *ESA Bulletin* no 65

Eddy, W. F., J. J. McCarthy, D. E. Pavlis, J. A. Marshall, S. B. Luthcke, L. S. Tsaoussi, G. Leung and D. A. Williams, 1990 - GEODYN systems description, NASA, GSFC

Engelis, T. and P. Knudsen, 1989 - Orbital Improvement and Determination of the Ocean Geoid and Topography from 17 days of Seasat data - *Manuscripta Geodaetica*, Vol 14, 193-201

Engelis, T., 1988 - On the simultaneous improvement of a satellite orbit and determination of sea surface topography using altimeter data - *Manuscripta Geodaetica*, Vol 13, 180-190

ESA, 1986 - Anouncement of Opportunity for ERS-1- Technical Annex: ERS-1 System Description

ESA, 1992 - The CD Guide to ERS-1 - ESA SP-1155

Fernandes, M. J., 1988 - Use of Altimeter data to improve radial ephemeris - MSc thesis, University College London

Francis, R., G. Graf, P. G. Edwards, M. McCaig, C. McCarthy, P. Dubock, A, Lefebvre, B. Pieper, P. Y. Pouvreau, R. Wall, F. Wechsler, J. Louet and R. Zobl, 1991 - The ERS-1 Spacecraft and Its Payload - *ESA Bulletin* no 65

Goad, C. C,, B. C. Douglas and R. W. Agreen, 1980 - On the use of satellite altimeter data for radial ephemeris improvement- *The Journal of the Astronautical Sciences*, Vol XXVIII No 4 , 419-428

Haar V. T. H. and V. E. Suomi, 1971 - Measurements of the Earth's radiation budget from satellites during a five-year period - *Journal of Atmospheric Sciences*, Vol 28, No 3, 305 - 314

Hartl, Ph., W. Schäfer, Ch Reigber and H. Wilmes, 1984 - The Precise Range and Range Rate Equipment (PRARE) and its possible support to the radar altimeter measurements for ERS-1 - ESA SP-221

Hauck, H. and K. Herzberger, 1986. - A numerical comparison between long-arc and short-arc techniques using laser observations - *Advances in Space Research*, Vol 6, No 9, 63-65

Hauck, H., 1988 - A short-arc technique with orbit control - *Manuscripta Geodaetica*, Vol 3, 313-322

International Earth Rotation Service, 1992 - 1991 IERS Annual Report - Central Bureau of IERS, Observatoire de Paris

Jacchia, L. G. and R. E. Briggs, 1963 - Smithsonian Contribution to Astrophysics, 6, 13

Jacchia, L. G., J. Slowey and F. Verniani, 1967 - Geomagnetic Perturbations and Upper-Atmosphere Heating - *Journal of Geophysical Research*, Vol 72, No 5

Jacchia, L.G., 1972 - Atmospheric models in the region from 110 to 2000 km - COSPAR International Reference Atmosphere, Akademie-Verlag, Berlin

Jacchia,L. G., 1965 - Atmospheric structure and its variations at heights above 200 km - CIRA, COSPAR International Reference Atmosphere, North-Holland Publication Co., Amsterdam

Jet Propulsion Laboratory, NASA, 1980 - Seasat: Geophysical Data Record (GDR) Users Handbook, Altimeter. Seasat: Altimeter Geophysical Algorithms Specifications

Kaula, W. M., 1966 - Theory of Satellite Geodesy - Blaisdell Publishing Company, Waltham, Massachusetts

King, R. W., E. G. Masters, C. Rizos, A. Stolsz and J. Collins, 1985 - Surveying with GPS - Monograph 9, School of Surveying, The University of New South Wales, Kensington, Australia

King-Hele, D., 1964 - Theory of satellite orbits in an atmosphere - Buttherworths, London

Louet, J. and Francis, R.,1992 - ERS-1: - The First Months in Orbit - *ESA Bulletin* no 70

MacDonald, G. J., 1963 - *Reviews of Geophysics* I, 305

Marini, J. W. and C. W. Murray, 1973 - Correction of Laser Range Tracking Data for Atmospheric Refraction at Elevations Above 10 Degrees - NASA GSFC X-591-73-351

Marsh, J. G., C. J. Koblinsky, F. Lerch, S. M. Klosko, J. W. Robbins, R. G. Williamson and G. B. Patel, 1990b - Dynamic Sea Surface Topography, Gravity and Improved Orbit Accuracy From the Direct Evaluation of Seasat Altimeter data - *Journal of Geophysical Research*, Vol 95, No C8

Marsh, J. G., F. J. Lerch, B. H. Putney, D. C. Christodoulidis, D. E. Smith, T. L. Felsentreger, B. V. Sanches, S. M. Klosko, E. C. Pavlis, T. V. Martin, J. W. Robbins, R. G. Williamson, O. L. Colombo, D. D. Rowlands, W. F. Eddy, N. L. Chandler, K. E. Rachlin, G. B. Patel, S. Bhati and D. S. Chinn, 1988 - A new gravitational model for the Earth from satellite tracking data: GEM-T1 - *Journal of Geophysical Research*, Vol 93, No B6, 6179 - 6215

Marsh, J. G., F. J. Lerch, B. H. Putney, D. C. Christodoulidis, D. E. Smith, T. L. Felsentreger, B. V. Sanches, S. M. Klosko, E. C. Pavlis, T. V. Martin, J. W. Robbins, R. G. Williamson, O. L. Colombo, D. D. Rowlands, W. F. Eddy, N. L. Chandler, K. E. Rachlin, G. B. Patel, S. Bhati and D. S. Chinn,, 1987 - An improved model of the Earth's gravitational field: GEM-T1 - NASA Technical Memorandum 4019

Marsh, J. G., F. J. Lerch, B. H. Putney, T. L. Felsentreger, B. V. Sanches, S. M. Klosko, G. B. Patel, J. W. Robbins, R. G. Williamson, T. L. Engelis, W. F. Eddy, N. L. Chandler, D. S. Chinn, S. Kapoor, K. E. Rachlin, L. E. Braatz and E. C. Pavlis, 1990a - The GEM-T2 Gravitational Model - *Journal of Geophysical Research*, Vol 95, No B13, 22043 - 22071

McCarthy, J. J. and T. V. Martin, 1977 - A computer efficient model of Earth albedo satellite effects - E G & G Wash. Anal. Services Center, Washington, Report 012 -77

McCarthy, D.(ed.), 1992 - IERS Standards 1992 - Central Bureau of IERS, Observatoire de Paris

Melbourne, W., R. Anderle, M. Feissel, R. King, D. McCarthy, D. Smith, B. Tapley, R. Vicente, 1983 - Project Merit Standards - U. S. Naval Observatory Circular No 167

Melchior, P., 1978 - The Tides of the Planet Earth - Pergamon Press

Merson, R. H. and A. W. Odell, 1975 - Skynet Orbit Determination, Program SPOD2 - RAE TR. 75093

Moore, P. and D. A. Rothwell, 1990 - A study of gravitational and non-gravitational modelling errors in crossover differences - *Manuscripta Geodaetica*, No 15

Moore, P., 1987 - Orbital perturbations for low Earth satellites - Summer school in Space and Terrestrial Geodesy, Nothingham University

Moritz, H., 1979 - Concepts in Geodetic Reference Frames- OSU Report No. 294, The Ohio State University

Moritz, H., 1980 - Geodetic Reference System 1980, *Bulletin Geodesique*, Vol 54, No 3 , pp 395-405

Mueller, I. I., 1981 - Reference Coordinate Systems for Earth Dynamics: a Preview - in Reference Coordinate Systems for Earth Dynamics, edited by Gaposhkin, E. M. and Kolaczek, B.

Mueller, I. I., 1988 - Reference Coordinate Systems: an update - OSU Report No. 394, The Ohio State University

Mueller, I. I., S. Y. Zhu and Y. Bock, 1982 - Reference Frame Requirements and the MERIT Campain - OSU Report No. 329, The Ohio State University

NGDC, 1992 - Geomagnetic Indices Bulletin - Monthy publication of the National Geophysical Data Center, Boulder, Colorado

Nicolet, M., 1960 - *Space Research I* (edited by H. Kallmann-Bijl), 46-89, Amsterdam

Oliver, W. L., 1982 - A procedure for the efficient calculation of atmospheric density - COSPAR paper II.2.8, Ottawa

Press, W. H. and G. B Rybicki, 1989 - Fast algorithm for spectral analysis of unevenly sampled data - *The Astrophysical Journal*, 338, 277-280

Press, W. H. et al, B. P. Flannery, S. A. Teukolsky and W. T. Vetterling, 1986 - Numerical Recipes, the Art of Scientific Computing - Cambridge University Press

Rapp, R. H. and N. K. Pavlis, 1990 - The Development and Analysis of Geopotential Coefficient Models to Spherical Harmonic Degree 360 - *Journal of Geophysical Research*, Vol 95, No B13, 21885-21911

Rapp, R., 1987 - An estimate of equatorial gravity from terrestrial and satellite data - *Geophysical Research Letter* 14, 730-732

Reigber Ch., Ch. Foerste, P. Schwintzer, F. H. Massman, H. Mueller, 1992 - Earth Orientation and Station Coordinates Computed From 11.75 Years of Lageos Observations, DGFII 92 L 01 - *IERS Technical Note* No 11

Robinson, I. S., 1985 - Satellite Oceanography - Ellis Horwood

Roemer, M. 1966 - Atmospheric densities and temperatures from precisely reduced observations of the Explorer IX satellite - Smithsonian Astrophysical Observatory - Special Report No 199

Roemer, M., 1971 - *Space Research XI*, Akademie-Verlag, Berlin

Rosborough, G. W. and B. D. Tapley, 1990 - Radial, transverse and normal satellite position perturbations due to the geopotential - *Celestial Mechanics* 40, 429-421

Rosengren, M. 1992 - ERS-1 - An Earth Observer that Exactly Follows Its Chosen Path - *ESA Bulletin* no 72

Rothwell, D. A.,1989 - Precise Orbit Determination and Analysis from Satellite Altimetry and Laser ranging - PhD Thesis - University of Aston, Birmingham

Schwiderski, E. W., 1980 - Ocean tides. Part I: Global ocean equations. Part II: A hydrodynmical interpolation model - *Marine Geodesy* , Vol 3, 161-255

Sinclair, A. T. and G. M. Appleby, 1986 - SATAN programs for the determination and analysis of satellite orbits from SLR data - SLR Technical Note no 9, Royal Greenwich Observatory

Sinclair, A. T., 1985 - The radial accuracy of orbits determined from SLR data - SLR Technical Note no 7

Sinclair, A. T., 1987 - Earth Rotation and Reference Systems - Summer School in Space Geodesy , Nottingham

Sinclair, A. T., 1988 - Mathematical description of the SATAN programs - personal communication

Sinclair, A. T., 1989 - The determination of orbit corrections by short-arc techniques with application to ERS-1 - *Manuscripta Geodaetica* 14, 238-246

Stewart, R. H., 1985 - Methods of Satellite Oceanography, University of California Press, Berkely

Tapley, B. D. and G. H. Born, 1980 - The SEASAT precision orbit determination experiment, *Journal of the Astronautical Sciences*, 28, 371-390

Tapley, B. D. and G. W. Rosborough, 1985 - Geographically correlated orbit error and its effect on satellite altimetry missions - *Journal of Geophysical Research* , Vol 90 No C6, 11817-11831

Tapley, B. D., G. H. Born and M. E. Parke, 1982 - The SEASAT altimeter data and its accuracy assessment - *Journal of Geophysical Research* , Vol 87 No C5, 3179-3188

Wagner, C. A., 1985 - Radial variations of a satellite orbit due to gravitational errors: implications for satellite altimetry - *Journal of Geophysical Research* , Vol 90 No B4, 3027-3036

Wahr, J. M., 1981- The forced nutation of an elliptical, rotating elastic and oceanless earth - *Geophysical Journal of the Royal Astronomical Society,* Vol 64, 705-727

Wakker, K. F., B. A. C. Ambrosius and L. Aardoom, 1983a - Precise orbit determination for ERS-1 - ESOC contract 5227/82/D/IM(SC), Delft University, Neitherlands

Wakker, K. F., B. A. C. Ambrosius and T. V der Ploeg, 1983b- SEASAT orbit determination from laser range observations - in Satellite Microwave Remote Sensing - T. D. Allan (ed)

Wakker, K. F., R. C. A. Zandbergen and B. A. C. Ambrosious, 1987 - SEASAT orbit determination experiments in preparation for the ERS-1 altimetry mission - *Astrodynamics*, Vol 65

Wilkins, G. A. and I. I Mueller, 1986 - On the Rotation of the Earth and The Terrestrial Reference System - *Bulletin Geodesique*, No 60, 85-100

Wilmes, H. , C. H. Reigber, W. Schäfer and Ph Hartl, 1987 - Precise Range and Range Rate Equipment, PRARE, on board ERS-1. Orbitography in support to the radar altimetry and tool for precise geodetic positioning - XIX I.U.G.G. General Assembly, International Association of Geodesy, Vancover, Canada

Zandbergen, R. C. A., K. F. Wakker and B. A. C. Ambrosious, 1988 - Application of satellite altimeter data to orbit error correction and gravity model adjustment - 27th COSPAR meeting, Espoo

Zhu, S. Y and Ch. Reigber, 1991 - ERS-1 Standards at D_PAF, ERS-D-STD-31101, Deutsches Geodaetisches Forchungsinstitut, Abt. I